

**KARADENİZ TECHNICAL UNIVERSITY
THE GRADUATE SCHOOL OF NATURAL AND APPLIED SCIENCES**

DEPARTMENT OF CHEMISTRY

**DEVELOPMENT OF DOPED TiO₂ PHOTOCATALYST PREPARED ON α -Al₂O₃
CERAMIC SUBSTRATE AND THEIR USE IN THE DEGRADATION OF
IBUPROFEN, CAFFEINE, AND CARBAMAZEPINE AS MODEL
CONTAMINANTS OF EMERGING CONCERN (CECs)**

DOCTORATE THESIS

Chukwuka Bethel ANUCHA

**JANUARY 2022
TRABZON**



KARADENİZ TECHNICAL UNIVERSITY
THE GRADUATE SCHOOL OF NATURAL AND APPLIED SCIENCES

DEPARTMENT OF CHEMISTRY

**DEVELOPMENT OF DOPED TiO₂ PHOTOCATALYST PREPARED ON α -Al₂O₃
CERAMIC SUBSTRATE AND THEIR USE IN THE DEGRADATION OF IBUPROFEN,
CAFFEINE, AND CARBAMAZEPINE AS MODEL CONTAMINANTS OF EMERGING
CONCERN (CECs)**

Chukwuka Bethel ANUCHA

**This thesis is accepted to give the degree of
DOCTOR OF PHILOSOPHY**

**By
The Graduate School of Natural and Applied Sciences at
Karadeniz Technical University**

The Date of Submission : 18 / 12 / 2021

The Date of Examination : 13 / 01 / 2022

Thesis Supervisor : Prof. Dr. Emin BACAŞIZ

Co Supervisor Prof. Dr. Vassilis N. STATHOPOULOS

Trabzon 2022

FOWARD

The presented study in this thesis was carried out at the Analytical Chemistry Laboratory of the Department of Chemistry, Faculty of Science, Karadeniz Technical University, Trabzon, Turkey.

This study has received funding from the European Union's Horizon 2020 research and innovation programme under the Marie Skłodowska-Curie Action with grant agreement No 765860.

Firstly, a huge thank you to the Almighty God who gave life.

It is with high pleasure that I wish to express my profound gratitude to my supervisor Prof. Dr. Emin Bacaksiz for giving me an all-round support throughout the course of this study. Without him, it would have been most difficult. My special thanks go to my co-supervisor; Prof. Dr. Vassilis N. Stathopoulos whose assistance co-supervising this work could not go unnoticed. A very big thank you to Dr. Ilknur Altin for her sound advice getting the work through. It is worth mentioning the special assistance I had received during this work from various people including Prof. Dr. Tayfur Kucukomeroglu, Prof. Dr. Ismail Polat, Assistant Researcher Abdullah Karaca, and a whole lot of others. They assisted me utmost in technical areas of the work and made sure the devices I used worked. The Chemistry and Physics department personnel gave me wonderful platform to execute my assignments during my study. From the University of Turin (UNITO), I wish to thank Professors Paola Calza, Debora Fabbri, and Guiliana Magnacca and all who have facilitated me during my secondment training at UNITO. A special thank you to the entire personnel at Materials Industrial Research and Technology Centre (MIRTEC) S.A., Chakilda, Greece. A special thank you to Ms. Zoi Tatoudi, and Mr. Elias Georgiopoulos for their wonderful support to me during my secondment training at MIRTEC and thank you Dr. Pavlos K. Pandis. They all provided and assisted me with some of the materials which happen to form part of this work. Special thanks to all my friends, and entire AQUAlity team.

Finally, my heartfelt gratitude goes to my family and especially the love of my life, my wife who not only kept the house but also gave me so much strength to go on these last 3 years.

Chukwuka Bethel ANUCHA

Trabzon 2022

STATEMENT OF ETHICS

By this statement, I hereby declare that the Ph.D. thesis titled “Development of Doped TiO₂ Photocatalyst Prepared on α -Al₂O₃ Ceramic Substrate and Their Use in The Degradation of Ibuprofen, Caffeine, and Carbamazepine as Model Contaminants of Emerging Concern (CECs)” has been accomplished by me Chukwuka Bethel ANUCHA under the supervision of Prof. Dr. Emin BACAŞIZ. I also declare that I have personally completed the experiments/analysis, generated the data at the indicated laboratory and have observed the highest ethical and scientific standards during the course of developing the thesis. I have also avoided plagiarism and acknowledged fully the work of others to which I have referred in the thesis. I admit and accept all the legal consequences should there be any proven false claim associated with this declaration. 31/01/2022

Chukwuka Bethel ANUCHA

TABLE OF CONTENTS

	<u>Page No</u>
FORWARD	III
STATEMENT OF ETHICS	IV
TABLE OF CONTENTS	V
SUMMARY	IX
ÖZET	X
LIST OF FIGURES	XI
TABLE INDEX	XX
ABBREVIATIONS	XXII
1. GENERAL INFORMATION	1
1.1. Introduction	1
1.2. Advanced Treatment Methods	8
1.2.1. Advanced Oxidation Processes (AOPs)	9
1.2.1.1. Solar Driven TiO ₂ Based Heterogeneous Photocatalysis	15
1.3. Modification Strategies	17
1.3.1. Heteroatom Doping	18
1.3.1.1. Metal Cation Doping	19
1.3.1.2. Non-metal Anion Doping	20
1.3.1.3. Composite Catalyst Doping	22
1.3.2. Metal Oxide Semiconductor Coupling	22
1.3.3. Heterojunction Constructions	26
1.3.3.1. Conventional Heterojunctions	27
1.3.3.2. New Generation Heterojunctions	30
1.3.3.2.1. p-n Heterojunctions	30
1.3.3.2.2. Surface Heterojunctions	31
1.3.3.2.3. Z-scheme/Direct Z-scheme Heterojunctions	32
1.3.3.2.4. Semiconductor-based Carbonaceous Materials Heterojunction	33
1.3.4. Sensitization	36
1.3.4.1. Inorganic/Organic Metal/Metal-Free Dye Anchoring	37
1.3.4.2. Nobel Metal Loading	39
1.3.5. Surface Morphology and Regulation	39
1.3.5.1. Zero-Dimensional Nanoparticles (0D)	40
1.3.5.2. One-Dimensional Nanofibres/Nanorods (1D)	40

1.3.5.3.	Two-Dimensional Nanosheets (2D)	41
1.3.5.4.	Three-Dimensional Frameworks (3D).....	41
1.3.6.	Nanomaterial Hybrids.....	42
1.4.	Core Configuration of TiO ₂ /Semiconductor Based Photocatalyst Reaction System.....	43
1.4.1.	Ceramics.....	48
1.4.1.1.	Types of Ceramic Membranes.....	48
1.4.1.1.1.	Porous Ceramic Membranes.....	48
1.4.1.1.2.	Dense Ceramic Membranes.....	49
1.4.1.2.	Geometrical Configuration of Ceramic Membranes.....	49
1.4.1.3.	Development and Fabrication of Ceramic Membranes.....	50
1.4.1.4.	Commonly Used Immobilized Technique	52
1.4.1.4.1.	Sol-gel and Dip Coating as Versatile Applied Immobilization Technique.....	52
1.4.1.4.2.	Characterization of Membranes Support.....	55
2.	MATERIALS AND METHODS.....	58
2.1.	Chemical Reagents.....	58
2.2.	Methods and Instrumentation.....	59
2.2.1.	Chemical Reagents.....	59
2.2.2.	Titania Powder Materials.....	60
2.2.2.1.	Anatase Commercial TiO ₂ (HRTiO ₂).....	60
2.2.2.2.	Sol-gel Synthesized TiO ₂ (SynTiO ₂).....	61
2.2.2.3.	Sonochemical Decoration of HRTiO ₂ and SynTiO ₂	62
2.2.2.4.	Sensitization: Cobalt (II) Phthalocyanine (CoPc).....	63
2.2.5.	Material Characterization.....	64
2.2.6.	Determination of pH Point of Zero Charge (pH _{pzc}) of Catalyst Materials.....	65
2.2.7.	TiO ₂ Photocatalytic Measurements.....	65
2.2.8.	Immobilized Photocatalyst Material.....	69
3.	RESULTS	70
3.1.	α -Al ₂ O ₃ Ceramic Support Development.....	70
3.2.	α -Al ₂ O ₃ Coarse Particle Size Determination (PSD).....	71
3.3.	Determination of Porosity.....	71
3.4.	Process Development of α -Al ₂ O ₃ Substrate Ceramic Support.....	71
3.5.	TiO ₂ Base Powder Selection for Support Surface Coating: HRTiO ₂	72
3.6.	Dispersion and Stability of Powder Suspension.....	73
3.7.	Particle Size Distribution of HRTiO ₂ Powder Suspension.....	74

3.8.	Surface Topcoat Development with HRTiO ₂ Powder Suspension.....	77
3.9.	Powder Material Characterizations: HRTiO ₂ and SynTiO ₂ Sample Series.....	82
3.9.1.	Thermogravimetric Analysis-Differential Scanning Calorimetry (TGA- DSC) Measurement.....	82
3.9.2.	X-ray Diffraction (XRD) and Fourier Transform Infrared (FTIR) Measurements.....	84
3.9.3.	Surface Topcoat Development of W/HRTiO ₂ Powder Suspension.....	90
3.9.3.1.	XRD and FTIR Measurements of W/HRTiO ₂ Topcoated α -Al ₂ O ₃ Ceramic Support.....	90
3.9.4.	Transmission Electron Microscopy (TEM) Measurement and Scanning Electron Microscopy- Energy Dispersive X-ray Spectroscopy (SEM-EDS) Measurement Analysis.....	92
3.9.5.	Brunauer Emmet Teller (BET) and X-ray Photoelectron Spectroscopy (XPS) Analysis Measurement.....	96
3.9.6.	UV-Visible Diffuse Reflectance Spectroscopy (UV-vis/DRS) Mode Measurement Analysis.....	107
3.10.	Photocatalytic Test Measurement.....	110
3.10.1.	Target CECs Compounds.....	110
4.	DISCUSSION.....	112
4.1.	General Outlook on Material Sample Characterizations.....	112
4.2.	Photocatalytic Activity Evaluation of the HRTiO ₂ and Decorated Material Forms.....	112
4.2.1.	Photocatalyst Material Test Evaluation Over Ibuprofen (IBF).....	112
4.2.1.1.	Effect of pH.....	113
4.2.1.1.1.	pH Point of Zero Charge (pHpzc).....	113
4.2.1.2.	Effect of Catalyst Dosage and Initial IBF Concentration.....	116
4.2.1.3.	Effect of Chemical Scavengers.....	118
4.2.1.4.	Effect of Contaminant Ions (Cations and Anions), and Humic Acid (HA).....	119
4.2.1.5.	Effect of Hydrogen Peroxide (H ₂ O ₂).....	125
4.2.1.6.	Evaluation of Visible Light Photocatalytic Activity.....	126
4.2.1.7.	Possible Photocatalytic Degradation Process Mechanism.....	130
4.2.2.	Photocatalyst Material Test Evaluation Over Caffeine (CAF).....	132
4.2.2.1.	Effect of pH.....	133
4.2.2.2.	Effect of Catalyst Dosage and Initial CAF Concentration.....	135
4.2.2.3.	Effect of Chemical Scavengers.....	137
4.2.2.4.	Effect of Contaminants Ion (Cations and Anions), and Humic Acid (HA).....	138
4.2.2.5.	Effect of Hydrogen Peroxide (H ₂ O ₂).....	141
4.2.2.6.	Evaluation of Visible Light Photocatalytic Activity.....	143
4.2.2.7.	Possible Photocatalytic Degradation Process Mechanism.....	147
4.2.3.	Photocatalyst Material Test Evaluation Over Carbamazepine (CBZ).....	149
4.3.	Photocatalyst Activity Evaluation of SynTiO ₂ and Decorated Material Forms.....	155

4.3.1.	Photocatalyst Material Test Evaluation Over Ibuprofen (IBF).....	155
4.3.1.1.	Effect of pH.....	156
4.3.1.1.1.	pH Point of Zero Charge (pHpzc) Value.....	156
4.3.1.2.	Effect of Catalyst Dosage and Initial IBF Concentration.....	159
4.3.1.3.	Effect of Chemical Scavengers	161
4.3.1.4.	Effect of Contaminant Ions (Cations and Anions) and Humic Acid (HA).....	162
4.3.1.5.	Effect of Hydrogen Peroxide (H ₂ O ₂)	165
4.3.1.6.	Possible Photocatalytic Degradation Process Mechanism.....	169
4.3.2.	Photocatalyst Material Test Evaluation Over Caffeine (CAF).....	171
4.3.2.1.	Effect of pH.....	172
4.3.2.1.1.	pH Point of Zero Charge (pHpzc) Value.....	172
4.3.2.2.	Effect of Catalyst Dosage and Initial CAF Concentration	175
4.3.2.3.	Effect of Chemical Scavengers	177
4.3.2.4.	Effect of Contaminant Ions (Cations and Anions) and Humic Acids (HA).....	178
4.3.2.5.	Effect of Hydrogen Peroxide (H ₂ O ₂)	182
4.3.2.6.	Possible Photocatalytic Degradation Process Mechanism.....	186
4.3.3.	Photocatalytic Material Test Evaluation Over Carbamazepine (CBZ).....	188
4.4.	Photocatalyst Test Over Immobilized W/HRTiO ₂ on α -Al ₂ O ₃ Ceramic Support.....	191
5.	CONCLUSION	196
6.	RECOMMENDATION.....	197
7.	REFERENCES	198

CURRICULUM VITAE

Ph.D. Thesis

SUMMARY

DEVELOPMENT OF DOPED TiO₂ PHOTOCATALYST PREPARED ON α -Al₂O₃ CERAMIC SUBSTRATE AND THEIR USE IN THE DEGRADATION OF IBUPROFEN, CAFFEINE, AND CARBAMAZEPINE AS MODEL CONTAMINANTS OF EMERGING CONCERN (CECs)

Chukwuka Bethel ANUCHA

Karadeniz Technical University
The Graduate School of Natural and Applied Sciences
Chemistry Graduate Program

Supervisor: Prof. Dr. Emin BACAKSIZ

2022, 250 Pages

In this study, α -Al₂O₃ ceramic substrate was worked, characterized, and used as a support for an optimized W doped HRTiO₂ active layer. HRTiO₂ and SynTiO₂ were modified with 2 wt. % of either W and or Mo in the mono decorated materials and 1 wt. % each of W and Mo in the co-doped forms. Materials were characterized by TGA-DSC, XRD, FTIR, TEM, SEM-EDS, XPS, BET/BJH application method as well as UV-vis/DRS measurement. As part of the modification outcome in the improvement of the TiO₂ based photocatalysts materials; 2 wt % W/HRTiO₂ degraded 96 % of initial 50 mg/L IBF concentration, ~ 76 % of initial 100 mg/L CAF concentration, and ~ 100 % and 88 % of respective initial 50 mg/L and 100 mg/L CBZ concentrations after 1 h at 365 nm irradiation, and under natural (unmodified) initial pH conditions. In addition, the modified TiO₂ also showed enhanced performance activity under 450 nm irradiation. Effects of other parameters on the photocatalytic degradation process were also investigated and reaction mechanisms proposed. On the average, ~ 0.005 g (W/HRTiO₂) on ceramic support removed over 90 % of 5 mg/L initial IBF, CAF, and CBZ concentrations and sustained over 80 % removal for CAF and CBZ after successive 3 cycle test runs after 360 min of 365 nm irradiation under natural (unmodified) pH conditions. XRD and FTIR outcome showed topcoat surface stability thereafter.

Key Words: TiO₂, Semiconductors, phthalocyanines, doping, Sensitization, AOPs, Heterogeneous photocatalysis, CECs, Suspension, Immobilization, HPLC

ÖZET

SERAMİK α -Al₂O₃ ALTLIK ÜZERİNDE HAZIRLANAN KATKILI TiO₂
FOTOKATALİZÖRLERİN GELİŞTİRİLMESİ VE İBUPROFEN, KAFEİN VE
KARBAMAZEPİNİN GİBİ YAYGINLAŞAN ORGANİK KİRLETİCİLERİN
BOZUNDURULMASINDA KULLANILMASI

Chukwuka Bethel ANUCHA

Karadeniz Teknik Üniversitesi
Fen Bilimleri Enstitüsü
Kimya Anabilim Dalı
Danışman: Prof. Dr. Emin BACAĞSIZ
2022, 250 Sayfa

Bu çalışmada, α -Al₂O₃ seramik altlık malzemesi, optimize edilen HRTiO₂ aktif tabakası için destek materyali olarak kullanılmak üzere karakterize edildi. HRTiO₂ ve SynTiO₂ katalizörlerinin her birine katkı materyali ağırlıkça % 2 oranı, ortak katkı malzemelerde ise her bir katkı için % 1 oranı uygulandı. Malzemeler, UV-vis/DRS , TGA-DSC, XRD, FTIR, TEM, SEM-EDS, XPS, BET/BJH ölçümleri ile karakterize edildi. TiO₂ bazlı fotokatalitik malzemeye % 2 W katkılандığında, başlangıç doğal pH koşulları altında 60 dakika 365 nm dalga boyuna sahip lambayla ışınlama sonrası, 50 mg/L ibuprofen (IBF) derişiminde % 96'ı, 100 mg/L kafein (CAF) derişiminde % 76'ı ve 50 mg/L ve 100 mg/L karbamazepin (CBZ)'nin derişiminde ise sırasıyla % 100 ve % 88'i bozunduğu tespit edildi. Ayrıca, modifiye edilmiş TiO₂ katalizörü 450 nm ışınlama altında fotokatalitik aktivite gösterdiği belirlendi. Diğer deneysel parametrelerin bozunma süreci üzerindeki etkileri de araştırıldı ve reaksiyon mekanizmaları önerildi. Ortalama olarak, seramik destek üzerinde ~ 0,005 g W/HRTiO₂ ile 5 mg/L derişimlerinde IBF, CAF ve CBZ'nin % 90'ından fazlası bozunduğu ve 360 dakika ışınlama sonunda CAF ve CBZ'nin % 80'in üzerinde bozunmaya uğradığı belirlendi. Aynı malzemelerin benzer fotokatalitik çalışmalarda 3 kez kullanıldıktan sonra, malzemelerin en üst katmanının yüzey stabilitesi gösterdiği XRD ve FTIR ölçümleri ile tespit edildi.

Anahtar Kelimeler: TiO₂, Yarı iletkenler, ftalosiyanimler, Doping, duyarlılık, AOP'ler, Heterojen- fotokataliz, CEC'ler, Süspansiyon, Hareketsizleştirme, HPLC

LIST OF FIGURES

	<u>Page No</u>
Figure 1. Connection of synthetic chemicals and their interactive ways of transport into the environment [49]	7
Figure 2. Potential adverse consequential effects of emerging contaminants of high concern to humans [17]	8
Figure 3. Different form of AOPs classified based on phase types and sub classified based on the light requirement to operate.....	14
Figure 4. Basic mechanism of reactive species generation involved in semiconductor photocatalyst material.....	16
Figure 5. Different modification strategies for the realization of composite photocatalyst material [97, 104, 107]	18
Figure 6. Periodic table extract giving an outlook of level of study involving dopants for photocatalytic degradation of organic pollutants and other related applications [101]	20
Figure 7. Schematic pattern of illustration displaying photocatalysis mechanism of the three different heterojunction semiconductor photocatalyst: a) Type I, b) Type II, and c) Type III [191].....	28
Figure 8. Schematic display of the two different types of semiconductor materials: a) n-type semiconductors, and b) p-type semiconductors and their respective band positions [200]	31
Figure 9. Schematic display of charge separation mechanisms involved in modified semiconductor-based photocatalyst composites operating as: a) Schottky junction, b) Type II Heterojunction, c) p-n Heterojunction, or d) Direct-Z scheme Heterojunction [221].....	36
Figure 10. Different geometric configurations of ceramic membrane: a) Disk or tablet shaped, b) Plate and frame shaped, c) Tubular or straw shaped, d) Hollow shaped fibre, and e) Capillary shaped membranes [261].....	50
Figure 11. Basic protocol steps involved in ceramic membrane fabrication and development [261]	51
Figure 12. Schematic illustration of sol-gel method for the fabrication and development of ceramic membrane [261]	54
Figure 13. Illustration of a manually controlled dip coating of a typical photocatalyst material on α -Al ₂ O ₃ ceramic substrate	55
Figure 14. Schematic of thesis work outline	57

Figure 15. Optical property of the anatase and rutile phases of Huntsman tioxide (HRTiO ₂) pigment [269]	61
Figure 16. Stepwise approach for sol-gel preparation of titania (SynTiO ₂)	62
Figure 17. α -Al ₂ O ₃ ceramic substrate development process	72
Figure 18. Dispersion and stability control by visual inspection at 24 h of a) HRTiO ₂ , and b) P25 Degussa TiO ₂ powder suspensions without dispersant additive	73
Figure 19. Particle size distribution pattern of 15 wt. % HRTiO ₂ powder suspension formulated with: a) 1 wt. % Darvan C at 0 h milling, b) 1 wt. % Darvan C at 24 h milling, c) 2 wt. % Darvan C at 24 h milling, and d) 3.5 wt. % Darvan C at 24 h milling	76
Figure 20. Support coat deposition outcome of α -Al ₂ O ₃ ceramic support with diluted HRTiO ₂ powder suspension	79
Figure 21. SEM-EDS micrographs coated support surfaces with HRTiO ₂ diluted powder suspensions: a) 2 wt. %, b) 5 wt. %, and c) 10 wt. % concentrations	80
Figure 22. a), and b): SEM-EDS micrographs of coated support surfaces with HRTiO ₂ diluted at 1 wt. % suspension concentration, and c) topcoat cross-sectional image	81
Figure 23. TGA-DSC measurements of a) HRTiO ₂ , b) W/HRTiO ₂ , c) Mo/HRTiO ₂ , and d) W-Mo/HRTiO ₂ samples	83
Figure 24. TGA-DSC measurements of a) W/SynTiO ₂ , b) Mo/SynTiO ₂ , and c) W- Mo/SynTiO ₂ samples	84
Figure 25. a) XRD, and b) FTIR measurement of HRTiO ₂ and its decorated and sensitized forms	85
Figure 26. a) XRD, and b) FTIR measurement of SynTiO ₂ and decorated and sensitized forms	88
Figure 27. a) XRD, and b) FTIR measurements of W/HRTiO ₂ topcoat on α -Al ₂ O ₃ ceramic support annealed at 600 °C and in comparison with its base control components before photocatalytic test	91
Figure 28. TEM images of a) HRTiO ₂ , b) W/HRTiO ₂ , c) Mo/HRTiO ₂ , d) W-Mo/HRTiO ₂ , and e) W-Mo/HRTiO ₂ + 0.5CoPc	93
Figure 29. SEM-EDS measurement of a) HRTiO ₂ , b) W/HRTiO ₂ , c) Mo/HRTiO ₂ , d) W-Mo/HRTiO ₂ , e) W/HRTiO ₂ + 0.5CoPc, and f) W-Mo/HRTiO ₂ + 0.5CoPc	94

Figure 30. TEM images of a) SynTiO ₂ , b) W/SynTiO ₂ , c) Mo/SynTiO ₂ , and d) W-Mo/SynTiO ₂	95
Figure 31. SEM-EDS measurement of a) SynTiO ₂ , b) W/SynTiO ₂ , c) Mo/SynTiO ₂ , and d) W-Mo/SynTiO ₂	96
Figure 32. N ₂ adsorption -desorption isotherm measurements of a) HRTiO ₂ , b) W/HRTiO ₂ , c) Mo/HRTiO ₂ , d) W-Mo/HRTiO ₂ , e) W/HRTiO ₂ + 0.5CoPc, and f) W-Mo/HRTiO ₂ + 0.5CoPc	98
Figure 33. Pore size distribution obtained by BJH application method of a) HRTiO ₂ , b) W/HRTiO ₂ , c) Mo/HRTiO ₂ , d) W-Mo/HRTiO ₂ , e) W/HRTiO ₂ + 0.5CoPc, and f) W-Mo/HRTiO ₂ + 0.5CoPc	98
Figure 34. XPS survey spectrum of a) W/HRTiO ₂ , b) Mo/HRTiO ₂ , c) W-Mo/HRTiO ₂ , d) W/HRTiO ₂ + 0.5CoPc, and e) W-Mo/HRTiO ₂ + 0.5CoPc in comparison to HRTiO ₂ control sample.....	99
Figure 35. XPS spectra of W/HRTiO ₂ showing chemical elemental compositional peaks for a) Ti 2p, b) O 1s, and c) W 4f.....	100
Figure 36. N ₂ adsorption-desorption isotherm measurement of a) SynTiO ₂ , b) W/SynTiO ₂ , c) Mo/SynTiO ₂ , and d) W-Mo/SynTiO ₂	104
Figure 37. Pore size distribution obtained by BJH application method of a) SynTiO ₂ , b) W/SynTiO ₂ , c) Mo/SynTiO ₂ , and d) W-Mo/SynTiO ₂	104
Figure 38. XPS survey spectrum of a) W/SynTiO ₂ , b) Mo/SynTiO ₂ , c) W-Mo/SynTiO ₂ in relation to SynTiO ₂ control sample	105
Figure 39. XPS spectra of Mo/SynTiO ₂ showing elemental compositional peaks for: a) Ti 2p, b) O 1s, and c) Mo 3d	106
Figure 40. XPS spectra of W-Mo/SynTiO ₂ showing elemental compositional peaks for: a) Ti 2p, b) O 1s, c) Mo 3d, and d) W 4f.....	107
Figure 41. Energy band gap (E _g) estimates for: a) HRTiO ₂ (black line), and W/HRTiO ₂ (red line), b): Mo/HRTiO ₂ (light green line), and W-Mo/HRTiO ₂ (blue line), and c): W-Mo/HRTiO + 0.5CoPc (dark red line), and W-Mo/HRTiO + 1CoPc (dark green line).....	108
Figure 42. Energy band gap (E _g) estimates for a): SynTiO ₂ (black line) and W/SynTiO ₂ (red line), b): Mo/SynTiO ₂ (green line), and W-Mo/SynTiO ₂ (blue line)	110
Figure 43. a) Preliminary test for the photocatalytic degradation of ibuprofen (C ₀ = 50 mg/L, initial pH _{natural} (unmodified) condition under	

365 nm irradiation with HRTiO ₂ and decorated forms, b) corresponding photocatalytic degradation rate constant (k)	113
Figure 44. pH point of zero charge (pH _{pzc}) plot of 2 wt. % W/HRTiO ₂ photocatalyst material	115
Figure 45. a) pH effect on the photocatalytic degradation efficiency of W/HRTiO ₂ over IBF (C ₀ = 50 mg/L), and b) corresponding photocatalytic degradation rate constant (k)	115
Figure 46. a) Catalyst dosage effect on the photocatalytic degradation efficiency of W/HRTiO ₂ over IBF (C ₀ = 50 mg/L, initial pH _{natural} (unmodified) = ~ 5.13), and b) corresponding photocatalytic degradation rate constant (k)	117
Figure 47. a) Initial IBF concentration effect on the photocatalytic degradation efficiency of 1 g/L W/HRTiO ₂ at initial pH _{natural} (unmodified) = ~ 5.13, and b) corresponding photocatalytic degradation rate constant (k)	118
Figure 48. a) Chemical scavenger effect on the photocatalytic degradation efficiency of 1 g/L W/HRTiO ₂ over IBF (C ₀ = 50 mg/L, initial pH _{natural} (unmodified) = ~ 5.13), and b) photocatalytic degradation rate constant (k)	119
Figure 49. a) Cations effect on the photocatalytic degradation of 1 g/L W/HRTiO ₂ over IBF (C ₀ = 50 mg/L, initial pH _{natural} (unmodified) = ~ 5.13), b) corresponding photocatalytic degradation rate constant (k)	121
Figure 50. a) Anions effect on the photocatalytic degradation efficiency of 1 g/L W/HRTiO ₂ over IBF (C ₀ = 50 mg/L, initial pH _{natural} (unmodified) = ~ 5.13), and b) corresponding photocatalytic degradation rate constant (k)	123
Figure 51. a) Humic acid (HA) effect on the photocatalytic degradation efficiency of 1 g/L W/HRTiO ₂ over IBF (C ₀ = 50 mg/L, initial pH _{natural} (unmodified) = ~ 5.13), and b) corresponding photocatalytic degradation rate constant (k)	124
Figure 52. Hydrogen peroxide (H ₂ O ₂) effect on the photocatalytic degradation efficiency of 1 g/L W/HRTiO ₂ over IBF (C ₀ = 50 mg/L, initial pH _{natural} (unmodified) = ~ 5.13, and b) corresponding photocatalytic degradation rate constant (k)	125
Figure 53. Dark, photolysis, heat effect without catalyst and heat effect with catalyst test conditions at 1 g/L W/HRTiO ₂ , [IBF] ₀ = 50 mg/L, initial pH _{natural} (unmodified) = ~ 5.13 as applicable	126

Figure 54. a) Visible light photocatalytic evaluation of W/HRTiO ₂ , W/HRTiO ₂ + 0.5CoPc, and W/HRTiO ₂ + 1CoPc at 1 g/L each for IBF degradation (C ₀ = 10 mg/L, initial pH _{natural} (unmodified) = ~ 5.13), and b) corresponding photocatalytic degradation rate constant (k).....	127
Figure 55. Proposed photocatalytic degradation process mechanism for the removal of IBF by W/HRTiO ₂	132
Figure 56. a) Preliminary test for the photocatalytic degradation of caffeine (C ₀ = 100 mg/L, initial pH _{natural} (unmodified)) condition under 365 nm irradiation with HRTiO ₂ and decorated forms, and b) corresponding photocatalytic degradation rate (k)	133
Figure 57. a) pH effect on the photocatalytic degradation efficiency of W/HRTiO ₂ over CAF (C ₀ = 100 mg/L), and b) corresponding photocatalytic constant (k).....	135
Figure 58.a) Catalyst dosage effect on the photocatalytic degradation efficiency of W/HRTiO ₂ over CAF (C ₀ = 100 mg/L, initial pH _{natural} (unmodified) = ~ 5.48), and b) corresponding photocatalytic degradation constant (k)	136
Figure 59. a) Initial CAF concentration effect on the photocatalytic degradation efficiency of 1 g/L W/HRTiO ₂ (initial pH _{natural} (unmodified) = ~ 5.48), and b) corresponding photocatalytic degradation rate constant (k).....	137
Figure 60. a) Chemical scavenger effect on the photocatalytic degradation efficiency of 1 g/L W/HRTiO ₂ over CAF (C ₀ = 100 mg/L, initial pH _{natural} (unmodified) = ~ 5.48), and b) corresponding photocatalytic degradation rate constant (k)	138
Figure 61. a) Cation effects on the photocatalytic degradation efficiency of 1 g/L W/HRTiO ₂ over CAF (C ₀ = 100 mg/L, initial pH _{natural} (unmodified) = ~ 5.48), and b) corresponding photocatalytic degradation constant.....	139
Figure 62. a) Anion effect on the photocatalytic degradation efficiency of 1 g/L W/HRTiO ₂ over CAF (C ₀ = 100 mg/L, initial pH _{natural} (unmodified) = ~ 5.48), and b) corresponding photocatalytic degradation rate constant	140
Figure 63. a) Humic acid (HA) effects on the photocatalytic degradation efficiency of 1 g/L WHRTiO over CAF (C ₀ = 100 mg/L, initial pH _{natural} (unmodified) = ~ 5.48), and b) corresponding photocatalytic degradation rate constant (k)	141
Figure 64. a) Hydrogen peroxide (H ₂ O ₂) effect on the photocatalytic degradation efficiency of 1 g/L W/HRTiO ₂ over IBF (C ₀ = 100 mg/L, initial	

pH _{natural} (unmodified) = ~ 5.48), and b) corresponding photocatalytic degradation rate constant (k)	142
Figure 65. Dark, photolysis, heat effect without catalyst and heat effect with catalyst test at conditions of 1 g/L W/HRTiO ₂ , C ₀ = 100 mg/L, initial pH _{natural} (unmodified) = ~ 5.48 where applicable	143
Figure 66. Visible light photocatalytic evaluation of W/HRTiO ₂ , W/HRTiO ₂ + 0.5CoPc, and W/HRTiO ₂ + 1CoPc at 1 g/L each for CAF degradation (C ₀ = 10 mg/L) at initial pH _{natural} values (Table 21).....	144
Figure 67. Proposed photocatalytic degradation process mechanism for the removal of CAF by W/HRTiO ₂	149
Figure 68. Photocatalytic evaluation of 1 g/L W/HRTiO ₂ for CBZ degradation (C ₀ = 50 mg/L, and C ₀ = 100 mg/L) in comparison to unmodified pure anatase HRTiO ₂ under 365 nm irradiation and at initial pH _{natural} conditions (Table 22), and b) corresponding photocatalytic degradation rate constant (k)	150
Figure 69. Photocatalytic evaluation of 1 g/L Mo-W/HRTiO ₂ and 1 g/L Mo-W/HRTiO ₂ + 0.5CoPc for CBZ degradation (C ₀ = 10 mg/L) in comparison to unmodified pure anatase HRTiO ₂ under 450 nm irradiation and at initial pH _{natural} (unmodified) conditions (Table 22), and b) corresponding photocatalytic degradation rate constant (k).....	151
Figure 70. pH point of zero charge (pH _{pzc}) plot of 2 wt. % W/HRTiO ₂ + 0.5CoPc photocatalysts material.....	152
Figure 71. Photocatalytic evaluation of 1 g/L Mo-W/HRTiO ₂ + 0.5CoPc for CBZ degradation (C ₀ = 10 mg/L) under 450 nm irradiation at (initial pH _{natural} (unmodified) = 4, 9, and 11, Table 22), and b) corresponding photocatalytic degradation rate constant (k).....	153
Figure 72. a) Preliminary test for the photocatalytic degradation of ibuprofen (C ₀ = 10 mg/L, initial pH _{natural} (unmodified) conditions, Table 23) under 365 nm irradiation with SynTiO ₂ and decorated forms, and b) corresponding photocatalytic degradation rate constant (k).....	156
Figure 73. pH point of zero charge (pH _{pzc}) plot of 1 wt. % Mo-1 wt. % W/SynTiO ₂ photocatalyst material.....	157
Figure 74. a) pH effect on the photocatalytic degradation efficiency of Mo-W/SynTiO ₂ over IBF (C ₀ = 10 mg/L), and b) corresponding photocatalytic degradation rate constant (k)	158
Figure 75. a) Catalyst dosage effect on the photocatalytic degradation efficiency of Mo-W/SynTiO ₂ over IBF (C ₀ = 10 mg/L, initial	

pH _{natural} = ~ 9.87), and b) corresponding photocatalytic degradation rate constant (k)	159
Figure 76. a) Initial IBF concentration effect on the photocatalytic degradation efficiency of 1 g/L Mo-W/SynTiO ₂ initial pH _{natural} = ~ 9.87, and b) photocatalytic degradation rate constant (k)	160
Figure 77. a) Chemical scavenger effect on the photocatalytic degradation efficiency of 1 g/L Mo-W/SynTiO ₂ over IBF (C ₀ = 10 mg/L, initial pH _{natural} = ~ 9.87), and b) corresponding photocatalytic degradation rate constant (k)	161
Figure 78. a) Cation effects on the photocatalytic degradation efficiency of 1 g/L Mo-W/SynTiO ₂ over IBF (C ₀ = 10 mg/L, initial pH _{natural} = ~ 9.87), and b) corresponding photocatalytic degradation rate constant (k).....	163
Figure 79. a) Anion effect on the photocatalytic degradation efficiency of 1 g/L Mo-W/SynTiO ₂ over IBF (C ₀ = 10 mg/L, initial pH _{natural} = ~ 9.87, and b) corresponding photocatalytic rate constant (k).....	164
Figure 80. a) Humic acid (HA) effect on the photocatalytic degradation efficiency of 1 g/L Mo-W/SynTiO ₂ over IBF (C ₀ = 10 mg/L, initial pH _{natural} = ~ 9.87), and b) corresponding photocatalytic degradation rate constant (k)	165
Figure 81. a) Hydrogen peroxide (H ₂ O ₂) effect on the photocatalytic degradation efficiency of 1 g/L Mo-W/SynTiO ₂ over IBF (C ₀ = 10 mg/L, initial pH _{natural} = ~ 9.87), and b) corresponding degradation rate constant (k)	166
Figure 82. Dark, photolysis, heat effect without catalyst and heat effect with catalyst at test conditions of : 1 g/L Mo-W/SynTiO ₂ , C ₀ = 10 mg/L, initial pH _{natural} = ~ 9.87 where applicable	167
Figure 83. Proposed photocatalytic degradation process mechanism for the removal of IBF by Mo-W/SynTiO ₂	171
Figure 84. a) Preliminary test for the photocatalytic degradation of caffeine (C ₀ = 5 mg/L, initial pH _{natural} (unmodified)) under 365 nm irradiation with SynTiO ₂ and Mo/SynTiO ₂ decorated form, and b) corresponding photocatalytic degradation rate constant (k)	172
Figure 85. pH point of zero charge (pH _{pzc}) plot of 2 wt. % Mo/SynTiO ₂ photocatalyst material.....	173
Figure 86. a) pH effect on the photocatalytic degradation efficiency of Mo/SynTiO ₂ over CAF (C ₀ = 5 mg/L), and b) corresponding photocatalytic degradation rate constant (k).....	174

Figure 87. a) Catalyst effect on the photocatalytic degradation efficiency of Mo/SynTiO ₂ over CAF (C ₀ = 5 mg/L, initial pH _{natural} = ~ 6.5), and b) corresponding photocatalytic degradation constant (k).....	176
Figure 88.a) Catalyst dosage effect on the photocatalytic degradation efficiency of Mo/SynTiO ₂ over CAF (C ₀ = 5 mg/L, initial pH _{natural} = ~ 6.5), and b) corresponding photocatalytic degradation rate constant (k).....	177
Figure 89. a) Initial CAF concentration effect on the photocatalytic degradation efficiency of 1 g/L Mo/SynTiO ₂ (initial pH _{natural} = ~ 6.5), and b) corresponding photocatalytic degradation rate constant (k).....	178
Figure 90. a) Cation effect on the photocatalytic degradation efficiency of 1 g/L Mo/SynTiO ₂ over CAF (C ₀ = 5 mg/L, initial pH _{natural} = ~ 6.5), and b) corresponding photocatalytic degradation rate constant (k).....	180
Figure 91. a) Anion effect on the photocatalytic degradation efficiency of 1 g/L Mo/SynTiO over CAF (C ₀ = 5 mg/L, initial pH _{natural} = ~ 6.5), and b) corresponding photocatalytic degradation rate constant (k).....	181
Figure 92. a) Humic acid (HA) effects on the photocatalytic degradation efficiency of 1 g/L Mo/SynTiO ₂ over CAF (C ₀ = 5 mg/L, initial pH _{natural} = ~ 6.5), and b) corresponding photocatalytic degradation rate constant (k).....	182
Figure 93. a) Hydrogen peroxide (H ₂ O ₂) effect on the photocatalytic degradation efficiency of Mo/SynTiO ₂ over CAF (C ₀ = 5 mg/L, initial pH _{natural} = ~ 6.5),and b) corresponding photocatalytic degradation rate constant (k)	183
Figure 94. a) Dark, photolysis, heat effect without catalyst and heat effect with catalyst under test conditions of 1 g/L Mo/SynTiO ₂ , C ₀ = 5 mg/L, and initial pH _{natural} (unmodified) = ~ 6.5 where applicable	184
Figure 95. Proposed photocatalytic degradation process mechanism for the removal of CAF by Mo/SynTiO ₂	188
Figure 96. a) Photocatalytic degradation activity performance of 1 g/L each of Mo and or W decorated SynTiO ₂ under 365 nm against CBZ (C ₀ = 10 mg/L at their respective initial pH _{natural} (unmodified) condition (Table 25), and b) corresponding photocatalytic degradation rate constant (k)	189
Figure 97. a) Photocatalytic degradation activity performance of 1 g/L each of Mo and or W decorated SynTiO ₂ under 450 nm against CBZ (C ₀ = 10 mg/L at their respective initial pH _{natural} (unmodified) condition (Table 25)), and b) corresponding photocatalytic degradation rate constant (k).....	190
Figure 98.a) Photocatalytic degradation activity performance of immobilized 0.005 g W/HRTiO ₂ on ceramic support showing in general 3 cycle test runs and their related degradation rate constant k (inset) for a): IBF, b) CAF, and	

c) CBZ ($C_0 = 5$ mg/L, initial pH_{natural} (unmodified) values (Table 26), and under 365 nm irradiation..... 192

Figure 99. Surface morphological characteristics obtained of a) XRD measurement, and b) FTIR spectra of tested ceramic supported W/HRTiO₂ photocatalysts after 3 cycle photocatalytic test runs 194

Figure 100. Dark effect on the W/HRTiO₂ overlay on ceramic support, and photolysis effect of uncoated ceramic support only over the degradation of a) IBF, b) CAF, and c) CBZ with conditions: ($C_0 = 5$ mg/L each, initial pH_{natural}(unmodified) condition (Table 26)), and under 365 nm irradiation..... 194



TABLE INDEX

	<u>Page No</u>
Table 1. Classified examples of CECs and their uses	4
Table 2. Standard oxidation potential values of some chemical species [69, 70].	9
Table 3. Some list of AOPs technologies and their pathway mechanisms for hydroxyl (OH) radical generation [58].	10
Table 4. Some classified examples of semiconductor oxide systems and their photocatalytic result outcome over CECs removal and mineralization	23
Table 5. Some pros and cons of slurry (suspension) reaction type system and catalyst support (immobilized) on support [235].	44
Table 6. Cross section of applied immobilized support system, loading techniques of the different TiO ₂ -based photocatalyst in their respective dosages and against different CECs compounds at various tested initial concentrations.....	46
Table 7. Types of ceramic membrane, their pore size and application	49
Table 8. Refractive index (RI) and Moh's hardness properties of two different pigment forms of Huntsman tioxide [269].	60
Table 9. Profile of cobalt (ii) phthalocyanine (CoPc)	64
Table 10. HPLC conditions for the photocatalytic degradation process monitoring of the tested CECs: Ibuprofen (IBF), caffeine (CAF), and carbamazepine (CBZ).....	67
Table 11. Ingredient contents of coarse α -Al ₂ O ₃ by % mass.....	70
Table 12. Geometrical characteristics of disk-shaped ceramic substrate	70
Table 13. Granulometric particle size distribution analysis of α -Al ₂ O ₃ substrate	71
Table 14. Particle size distribution dependence on milling time and pH parameters of a 15 wt. % HRTiO ₂ powder suspension with 3.5 wt. % Darvan C	75
Table 15. Particle size distribution of diluted 15 wt. % HRTiO + 3.5 wt. % Darvan C at 24 h ball milling.....	77
Table 16. Material properties of HRTiO ₂ and its decorated and sensitized forms	86
Table 17. Material properties of synthesized TiO ₂ (SynTiO ₂) and its decorated forms	89

Table 18. XPS elemental compositional and deconvoluted spectral binding energy profile for other decorated/sensitized HRTiO ₂ and SynTiO ₂ sample material forms	101
Table 19. Characteristics of Ibuprofen (IBF), Caffeine (CAF), and Carbamazepine (CBZ) as the tested model CECs compounds.....	111
Table 20. Tested photocatalytic parameters for (C ₀ = 50 mg/L initial IBF concentration under 365 nm, C ₀ = 10 mg/L initial IBF concentration under 450 nm) with 1 g/L catalyst and their associated rate constant k (h ⁻¹ or min ⁻¹), correlation coefficient (R ²), half-life t _{1/2} (h or min), and initial and final pH values	128
Table 21. Tested photocatalytic parameters for (C ₀ = 100 mg/L initial CAF concentration under 365 nm, and C ₀ = 10 mg/L initial CAF concentration under 450 nm) with 1 g/L catalyst and their associated rate constant k (h ⁻¹ or min ⁻¹), correlation coefficient (R ²), half-life t _{1/2} (h or min), and initial and final pH values.....	145
Table 22. Tested photocatalytic parameters for (C ₀ = 50 mg/L, and C ₀ = 100 mg/L initial CBZ concentrations under 365 nm, and C ₀ = 10 mg/L initial CBZ concentration under 450 nm) with 1 g/L catalyst and their associated rate constant k (h ⁻¹), correlation coefficient R ² , half-life t _{1/2} (h), and initial and final pH values	154
Table 23. Tested photocatalytic parameters for (C ₀ = 10 mg/L initial IBF concentration under 365 nm) with 1 g/L catalyst and their associated rate constant (min ⁻¹), correlation coefficient (R ²), half-life t _{1/2} (min), and initial and final pH values.....	167
Table 24. Tested photocatalytic parameters at (C ₀ = 5 mg/L CAF concentration under 365 nm at 1 g/L catalyst) with associated rate constant k (min ⁻¹), correlation coefficient (R ²), half-life t _{1/2} (min), and initial and final pH values.....	184
Table 25. Tested photocatalytic parameters for (C ₀ = 10 mg/L initial CBZ concentration under 365 nm and 450 nm with 1 g/L catalyst) and their associated rate constant k (min ⁻¹), correlation coefficient (R ²), half-life t _{1/2} (min), and their initial and final pH values	190
Table 26. Parametric indicators for the photocatalytic activity performance of ceramic supported W/HRTiO ₂ over IBF, CAF, and CBZ and their associated degradation rate constant k (min ⁻¹), correlation coefficient constant (R ²), half-life t _{1/2} (min), and initial and final pH values.....	195

ABBREVIATIONS

α -Al ₂ O ₃	: Alpha alumina oxide
AOPs	: Advanced oxidation processes
CAS	: Catalyst on support
CB	: Conduction band
CECs	: Contaminants of emerging concern
CoPc	: Cobalt (ii) phthalocyanine
e ⁻	: Photogenerated electrons
E _g	: Energy band gap
h ⁺	: Photogenerated holes
HO [•]	: Hydroxyl radical
HOMO-LUMO	: Highest occupied molecular orbital-lowest unoccupied molecular orbital
HPLC	: High performance liquid chromatography
HRTiO ₂	: Huntsman tioxide
O ₂ ⁻	: Superoxide anion
PMR	: Photocatalyst membrane reactor
ROS	: Reactive oxygen species
SynTiO ₂	: Sol-gel synthesized titania
UV-vis irradiation	: Ultraviolet-visible irradiation
VB	: Valence band
WWTP	: Wastewater treatment plant

1. GENERAL INFORMATION

1.1. Introduction

Economic and social welfare advancement of mankind culminated by the rapid industrialization of the last century has left a deleterious impact on the environment. Environmental pollution concern of recent years has increasingly become topical both at the local and international level of governance. Toxic heavy metal disposal and greenhouse gases emission, oil spillages, use of non-biodegradable materials, agricultural practices involving pesticide spreading and usage of chemical fertilizers, sludge, and waste accumulation of other hazardous substances as consequences of the means cushioning the effects of food and energy demand due to global population explosion is a high risk to the environment [1-4]. The water environment is one such environmental compartment that has seen high level inflow of contaminants where on a global scale persistent organic pollutants (POPs) for more than five decades have affected water systems [5]. Chemical pollutants particularly organic and inorganic micropollutants, toxic metals and metalloids of geogenic, mining, and hazardous waste site sources remain relevant for long-term regional and local water pollution cases [6]. Emphasis placed on water quantity and or quality challenges in the twenty-first century has increased the more due to the diverse scope of synthetic and geogenic natural chemicals released into the aquatic environment [5-6]. A new category of synthetic organic chemicals originating from point and diffuse pollution sources have emerged and found present in the aquatic environment [7]. These compounds are referred to as contaminants of emerging concern (CECs) as they are not commonly monitored in the environment until recently due to low level of detection as well as their potential to filtrate into the environment causing known or suspected adverse effects to both humans and the environment [7-12]. Over 100,000 compounds have been classified and documented as contaminants of emerging concern (CECs) by the network of reference laboratories, research centres and related organisations for monitoring of emerging environmental substances (NORMAN) [13]. They comprise of a wide spectrum of synthetic chemical compounds ranging from pharmaceuticals and personal health care products (PPCPs), to pesticides, to flame retardants (FRs), to surfactants, to artificial sweeteners (ASWs), to endocrine disrupting substances (EDSs), veterinary products, engineered nanomaterials, industrial compounds/by-products, food addediver, and a host array of different compounds including

their metabolites and transformation products [13-19]. The indispensability of these synthetic compounds for various applications can only leave one imagining numerous additional routes by which such chemicals can make their way into the aquatic environment as they are ubiquitously present [6, 7, 17]. Septic tanks, hospital effluents, livestock activity waste lagoons and manure, underground storage of household and industrial wastes, surface water sources, artificial aquifer recharge, human and feeding operations, agricultural fields, landfill leachates, urban run-off, etc., have all been established as media carriers for these group of compounds [17, 20-29]. Amongst these various sources, it has been reported that effluents from urban wastewater treatment plants (UWWTPs), are one of the primary sources by which contaminants of emerging concern (CECs) get into the aquatic environment [16]. Pharmaceutical compounds and oestrogens have been reported reaching the UWWTP through sewage network mainly remaining as parent compounds or breakdown products after metabolism and excretion of urine and or faeces [30]. Additionally, many non-regulated industrial compounds in some parts of the world have been found in surface water- receiving end of pipe UWWTP effluents [16]. The occurrence of CECs in the environment within the concentration range of ng/L to µg/L had previously made their detection challenging [31-35]. However, the breakthrough of high technologically advanced analytical instruments with high level of sensitivity has made their analysis much easier and accomplished the assessment of their occurrence in the environment [36].

Various reports indicating the occurrence of contaminants of emerging concern (CECs) in various aquatic domains like effluents, tap water/drinking water, subsurface/surface waters, catchment outlets, freshwaters, rivers and streams, underground waters, etc., has heighten focus on them by governments and public institutions demanding a more precautionary approach in their handling [37]. Public concern about these compounds due to their widespread occurrence as a matter of their unaccountable sources of production, use and disposability has made their accumulation in the aquatic environment more considered and raised even further question of what their potential short and long term (acute and chronic) harmful effects might be on humans and the environment [31-35].

In this perspective, several guidelines, directives, and legislations at both local and international conventions towards the mitigation of the potential harmful effect of these compounds to ensure and realize the availability and sustainable management of water and sanitation for all has since been pursued [6, 38-40]. For instance, there has been since year 2000 some published European Union (EU) guidelines for the identification of certain

substances, monitor them and put forward mitigation measures to contain their potential environmental threat. The EU Water Framework Directive (EU WFD) documented and launched as Directive 2000/60/EC is a community action based waterframe work for water policy aimed at achieving good level of ecological and chemical surface water status [41]. The EU commission is required by the EU WFD to identify what it calls priority substances/group substances (PSs) with high level of risk to or via the aquatic environment and set up the EU Environmental Quality Standard (EQS) defined as the concentration of a particular pollutant or group of pollutants in water, sediment or biota which should not be exceeded for the protection of humans and the environment where its obtained annual average (AA-EQS) value sets the chronic toxicity data value and the maximum allowable concentration (MAC-EQS) value set the acute toxicity data value point [42]. Similarly, other directives like the 2455/2001/EC and 2008/105/EC for the EU WFD 2000/60/EC has listed 33 priority substances and 8 other certain pollutants respectively designating some of them as priority hazardous substances (PHSs) based on the annual average value Environmental Quality Standard (AA-EQS) and maximum allowable concentration of the Environmental Quality Standard (MAC-EQS) that must be monitored, putting measures in place to progressively reduce or phase out their discharges, emissions, and or loses in order to ensure that good chemical status of EU water bodies is met [43]. The 2455/2001/EC Directive and the Stockholm convention on persistent organic pollutants (POPs) ratified in 2004 by 180 member countries to the convention was adopted as EU legislation of EC regulation no. 850/2004 to eliminate and restrict the production and usage of POPs [44]. Recently, Directive 2013/39/EU was adopted with updated list of first EQS pollutants previously documented in Directive 2008/105/EC, highlighting demand for the development of new water treatment solutions with recommendation for the monitoring of 45 priority substances (PSs). In detail, this directive comprises of 41 priority substances (PSs) with 8 other certain pollutants of EQS limit, totalling 49 substances with 4 metals (cadmium, lead, mercury, and nickel) added [45]. In addition, a first watch list for the Union-wide monitoring in the field of water policy built on Directive 2013/39/EU and later published as Directive 2015/495/EU, examined 17 different organic compounds earmarked as 10 substances or group of substances classified as “contaminants of emerging concern” (CECs), defined as unregulated pollutants for which there is the need for Union-wide data monitoring and prioritization. [46]. Though no EQS for CECs yet, a prioritization evaluation system based on frequency of exceedance and the extent of exceedance of predicted no effect concentrations (PNECs)

has been proposed and applied to 500 contaminants of six different categories as identified by the Working Group on Prioritization for the NORMAN network and as a function of quality and quantity of obtainable data [47-48].

On a general note, the aquatic environment has been stretched to a breaking point with various kinds of organic pollutants. The occurrence, transport, and fate of these compounds in the water environment has received wide coverage of research attention. In the same vein, to help preserve, and restore the natural aquatic ecosystem; several regulations in form of policy frameworks and directives have also been established by local/international governments and institutions with the aim of addressing water pollution issues and help protect man and the environment.

However, use of regulatory tools has not been the only instrument aimed at tackling water pollution challenges and restoring good health status for water sources. To get rid of the majority of these compounds still unregulated, indispensable for our everyday comfort living with the potential to bioaccumulate as they evade conventional wastewater treatment plant (WWTP) due to their poor removal nature; research interest and focus over the last years has been on alternative approaches of their removal from the WWTP effluents seen as the main source of CEC compounds release into the environment.

A non-exhaustive list of contaminants of emerging concern (CECs) indicating their major class/sub class with the different CEC compounds and their applications is displayed in Table 1. Figure 1 shows the connection network of synthetic chemical compounds and their various interactive means/mode of release into the environment while Figure 2 displays some of the reported potential health effects of CECs compounds to humans on a chronic level of exposure.

Table 1. Classified examples of CECs and their uses

Examples	Uses
Surfactants: Anionic	
Dioctyl sodium sulfosuccinate (DOSS)	Wetting agent- coatings, toothpaste, etc.
Linear alkylbenzene sulfonates	Laundry detergents, dishwasher ingredients
Sodium lauryl ether sulfate	Shampoos, bath products, etc.
Lignosulfonate	Concrete plasticizer, plasterboard, DMSO
Sodium stearate	Hand soap, different household, industrial and institutional (HI & I) cleaning products

Continuation of Table 1

Surfactants: Cationic	
Benzalkonium chloride (BAC)	Anti-microbial preservative
Cetylpyridinium chloride (CPC)	Mouthwashes, toothpastes, lozenges, breath, and nasal sprays, etc.
Benzethonium chloride (BZT)	Minor cut treatments, scrapes, wounds, cracked skin, etc.
Cetyl trimethylammonium bromide (CTAB)	Mainly used as topical antiseptic
Cetyl trimethylammonium chloride (CTAC)	As a purifier, cleaning agent, etc.
Surfactants: Non-anionic	
Polyoxyethylene glycol octyl phenol ethers	Wetting agent for coating
Polyoxyethylene glycol alkylphenol ethers	Spermicide
Polyoxyethylene glycol sorbitan alkyl esters	Food ingredients
Sorbitan alkyl esters	Polishes, cleaners, fragrance carriers
Block copolymers of polyethylene glycol and polypropylene glycol	Applicable to various surface-active roles
Flame retardants (FRs)	
Brominated bisphenols and phenols	Flame retardants
Elemental red phosphorus and inorganic phosphates	Flame retardants
Melamine cyanurate	Flame retardants
Aluminium hydroxide and magnesium hydroxide	Flame retardants
Sodium borate and boric acid	Flame retardants
Silicon rubber composite	Flame retardants
Halogens with antimony and phosphorus with nitrogen	Flame retardants
Pharmaceuticals and Personal Care Products (PPCPs)	
Acetaminophen and acetylsalicylic acid	Pain reliever
Carbamazepine and primidone	Anti-convulsant
Gemfibrozil, clofibrac acid, and fenofibrac acid	Lipid regulators
Diclofenac, ibuprofen, ketoprofen and naproxen	Anti-inflammatory
Caffeine, amphetamines	Stimulants/enhancers
Oestrogen, testosterone, 17 α -estradiol, 17 α -ethinylestradiol	Hormone

Continuation of Table 1

Sulfamethoxazole, Erythromycin, and tetracycline	Antibiotic
Triclosan, biphenylol, and chlorophene	Antiseptic, fragrances
N, N-diethylmeta-toluamide (DEET)	Insect repellents
Carbendazim, benomyl, and carbaryl	Herbicides, insecticides, and fungicides
metolachlor and alachlor	Preemergent herbicides
Bentazone and triclopyr	Herbicides
DDT, dieldrin, endrin, and endosulfan	Insecticides
Diazinon, malathion, and chlorpyrifos	Insecticides
Biphenthrin, cypermethrin, and esfenvalerate	Insecticides
Atrazine, cyanazine, and simazine	Herbicides
Artificial Sweeteners (ASWs)	
Acesulfame, sucralose, saccharin, cyclama, aspartame, neotame etc	Sugar substitute
Endocrine Disrupting Substances (EDSs)	
17b-estradiol, Estrone	Natural human oestrogen, metabolite
Nonylphenol and octyl phenol	Manufacturing of household and industrial products (HIPs)
Polychlorinated biphenyls and brominated flame retardants	Flame retardants
Phthalates	Plasticizers
BPA	Industrial production of polycarbonates and epoxy resins

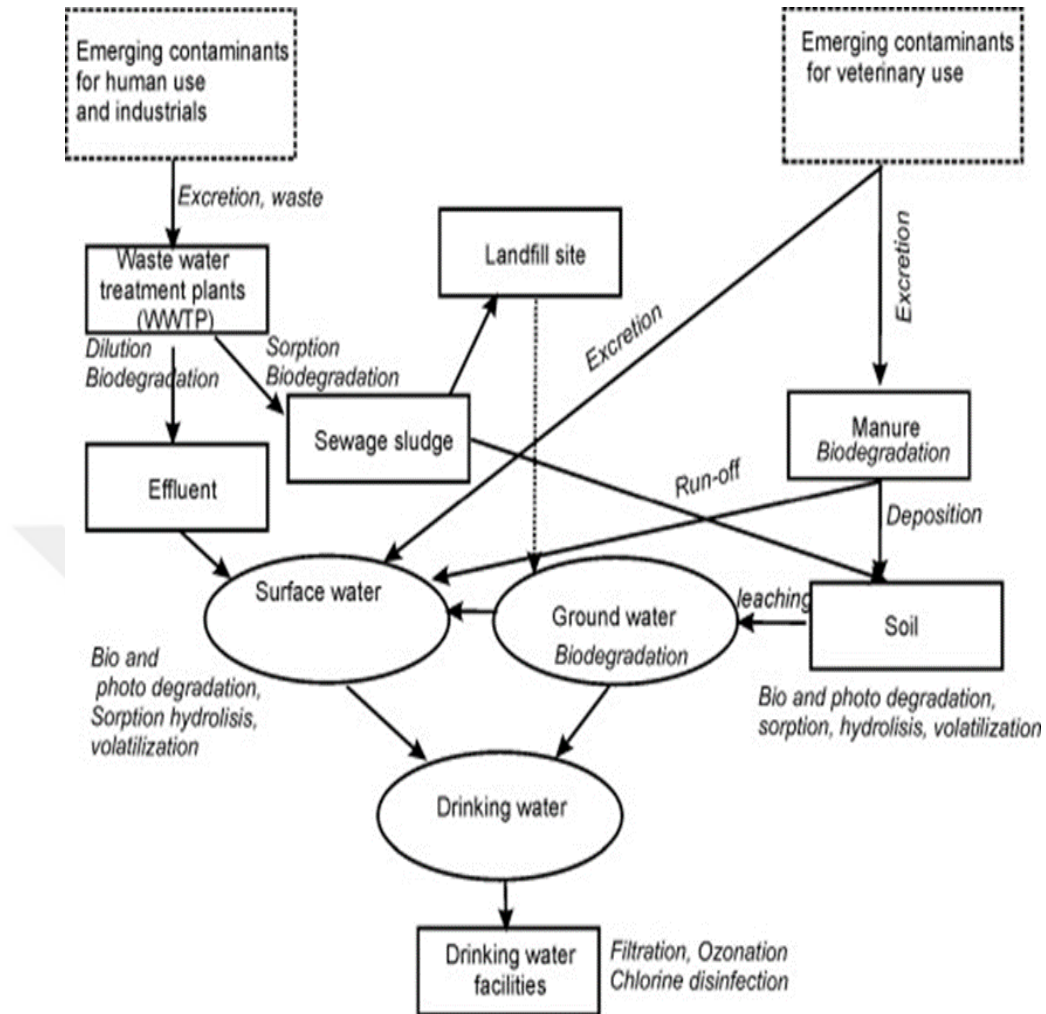


Figure 1. Connection of synthetic chemicals and their interactive ways of transport into the environment [49]

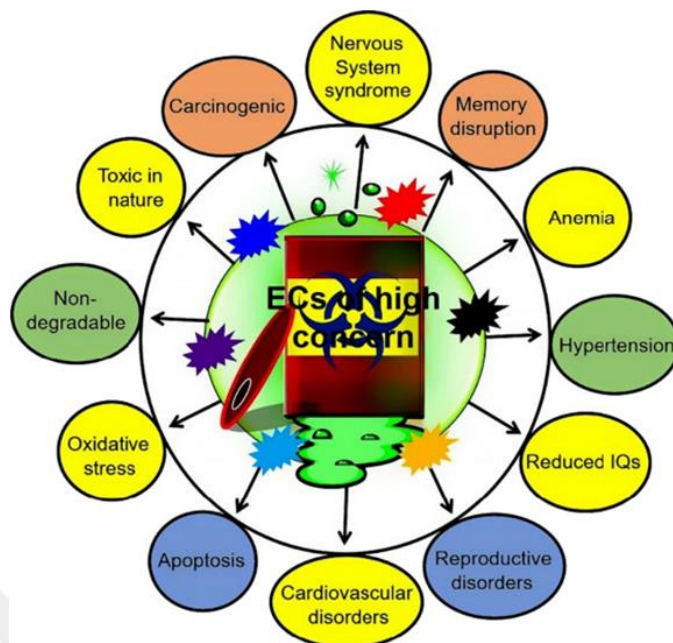


Figure 2. Potential adverse consequential effects of emerging contaminants of high concern to humans [17]

The next section will take a look at some of the approaches that has been focused in the area of CEC compounds removal from wastewaters as part of the remedy to the conventional wastewater treatment plant (WWTP) non-efficient removal of CECs.

1.2. Advanced Treatment Methods

It is now obvious that the WWTP cannot efficiently handle the significant amount of CECs fed into it from the sewer system as they are susceptible to poor removal by this conventional approach. Hence, the widespread occurrence of CECs in the environment triggered by the WWTP inefficiency of their removal has placed enormous research interest in this area. A wide variety of advanced treatment methods for the removal of CECs has been studied for example; advanced oxidation processes (AOPs) that is the new treatment process; activated carbon (AC) adsorption, ozonation, membrane filtration, nanofiltration (NF)/reverse osmosis (RO) that is the consolidated ones etc [50-52].

Treatment processes like ozonation, activated carbon, and pressure driven processes often classified as the consolidated processes for WWTP advanced treatment has long been adopted and even deployed for full scale application for the removal of CECs from specialty

built WWTP in some countries [50]. For instance, following the construction of a drinking water treatment facility based on ozone for disinfection in 1893 at Oudshoorn, Holland; a similar one was also constructed in 1906 at Nice, France adopting ozonation at later stage for CECs removal [53-54].

Though consolidated advanced treatment technologies for CECs removal have been established to a point, other options like advanced oxidation processes (AOPs) have been found effective in the degradation of CECs and therefore, widely investigated.

1.2.1. Advanced Oxidation Processes (AOPs)

Advanced oxidation processes (AOPs) are new advanced treatment technologies that depend on strong radical oxidants (e.g., $\cdot\text{OH}$, SO_4^{2-} , etc.) to drive and facilitate the destruction of majority of organic pollutants in water [50, 55]. AOPs as emergent and attractive treatment technologies offer high efficiency in the degradation of highly stable, toxic, and non-biodegradable organic pollutants [56-57]. Their application has not only found a place in wastewater treatment but also in soil and sediment contaminant remediation, gaseous effluent decontamination, municipal sludge conditioning, water/groundwater polishing, etc., due to the high efficiency of generated hydroxyl ($\cdot\text{OH}$) radical in the elimination of organic product pollutants [58-68].

The high oxidation potential (2.8 V) of hydroxyl ($\cdot\text{OH}$) radical comes only second to fluorine (3.03 V) and gives an advantage over some other traditional oxidants as it exhibits high rate of oxidation reaction [69-70] (Table 2).

Table 2. Standard oxidation potential values of some chemical species [69-70].

Chemical Species	Oxidation Potential (V)
Fluorine	3.03
Hydroxyl radical	2.80
Atomic oxygen	2.42
Ozone	2.07
Hydrogen peroxide	1.77
Potassium permanganate	1.67
Hypobromous acid	1.59

Continuation of Table 2

Chlorine dioxide	1.50
Hypochlorous acid	1.49
Chlorine	1.36
Bromine	1.09
Iodine	0.54

The non-selective reaction character of hydroxyl ($\cdot\text{OH}$) radical, makes it capable of mineralizing almost every organic compound it comes in contact with generating CO_2 and H_2O as the reaction end products [71-73]. Sometimes, the oxidation process might be an incomplete one; however, finally leading to generation of more degradable end product compounds [71-72]. Generally, the oxidation of organic compound, has been reported to occur via 3 steps of addition coupling of the hydroxyl ($\cdot\text{OH}$) radical with a typical organic compound (RH) (Equation 1), electron transfer to the free radical ($\cdot\text{OH}$) (Equation 2), and finally hydrogen abstraction (Equation 3) which leads to the generation of organic radicals and subsequent formation of peroxy radicals (Equation 4) via molecular oxygen addition to the organic radical [61, 70].



Shown in Table 3, are the different reaction mechanisms for the formation of hydroxyl ($\text{HO}\cdot$) radical by various AOPs technologies.

Table 3. Some list of AOPs technologies and their pathway mechanisms for hydroxyl (OH) radical generation [58].

Reaction Pathway mechanisms/AOPs Processes	No of Equation
Photocatalysis	
$\text{TiO}_2 + h\nu \rightarrow e_{\text{CB}}^- + h\nu_{\text{VB}}^+$	5
$h\nu_{\text{VB}}^+ + \text{HO}^- \rightarrow \cdot\text{OH}$	6

Continuation of Table 3

$O_2 + e_{CB}^- + 2H^+ \rightarrow H_2O_2$	7
$2h\nu_B^+ + 2H_2O \rightarrow 2H^+ + H_2O_2$	8
$H_2O_2 + \bullet OH \rightarrow H_2O + HO_2\bullet$	9
$TiO_2 (h^+) + H_2O_{ad} \rightarrow TiO_2 + \bullet OH_{ad} + h^+$	10
$TiO_2 (h^+) + HO_{ad} \rightarrow TiO_2 + \bullet OH_{ad}$	11
$TiO_2 (h^+) + RX_{ad} \rightarrow RX_{ad}^+$	12
UV disinfection and photolysis	
$O_2 + hv (185 \text{ nm}) \rightarrow 2O\bullet$	13
$O\bullet + O_2 \rightarrow O_3$	14
$H_2O_2 + hv \rightarrow 1/2H_2 + \bullet OH$	15
$\bullet OH + RH \rightarrow R\bullet + H_2O$	16
UV/H ₂ O ₂	
$H_2O_2 + hv \rightarrow 2\bullet OH$	17
$H_2O_2 + \bullet OH \rightarrow H_2O + \bullet OOH$	18
$2\bullet OOH \rightarrow H_2O_2 + O_2$	19
O ₃ and UV/O ₃	
$O_3 + H_2O \rightarrow 2\bullet OH + O_2$	20
$O_3 + HO^- \rightarrow O_2^{\bullet -} + HO_2^{\bullet}$	21
$O_3 + hv \rightarrow O_3^* \rightarrow O_2 + O\bullet$	22
H ₂ O ₂ /O ₃	
$O\bullet + H_2O \xrightarrow{hv} H_2O_2 \xrightarrow{hv} 2\bullet OH$	23
$H_2O_2 \rightleftharpoons H^+ + HO_2^-$	24
$HO_2^- + O_3 \rightarrow \bullet OH + O_2 + O_2^{\bullet -}$	25
UV/H ₂ O ₂ /O ₃	
$O_3 + OH^- \rightarrow \bullet OH$	26
$3O_3 + hv \rightarrow 2\bullet OH$	27
$H_2O_2 + hv \rightarrow 2\bullet OH$	28
$H_2O_2 + O_3 \rightarrow 2\bullet OH$	29
$H_2O_2 + O_3 + hv \rightarrow \bullet OH$	30
Sonolysis	
$H_2O \rightarrow H\bullet + \bullet OH$	31

Continuation of Table 3

$O_2 \rightarrow 2O\bullet$	32
$\bullet O + H_2O \rightarrow 2\bullet OH$	33
$H_2O + \cdot\cdot\cdot\cdot) \rightarrow \bullet OH + OH^-$	34
$H_2O + \cdot\cdot\cdot\cdot) \rightarrow 1/2(H_2) + 1/2(H_2O_2)$	35
Fenton	
$Fe^{2+} + H_2O_2 \rightarrow Fe^{3+} + HO^- + HO\bullet$	36
Electrochemical AOPs	
$H_2O \rightarrow \bullet OH + H^+ + e^-$	37
$2\bullet OH \rightarrow H_2O_2$	38
$\bullet OH + H_2O_2 \rightarrow HO_2\bullet + H_2O$	39
Ultrasonic/Fenton	
$Fe^{2+} + H_2O_2 \rightarrow Fe^{3+} + HO^- + HO\bullet$	40
$H_2O_2 + Fe^{3+} \rightarrow Fe^-OOH^{2+} + H^+$	41
$Fe^-OOH^{2+} + \cdot\cdot\cdot\cdot) \rightarrow Fe^{2+} + HOO\bullet$	42
$Fe^{2+} + HOO\bullet \rightarrow Fe^{2+} + H^+ + O_2$	43
Ultrasonic/advanced Fenton	
$Fe^0 + 2H^+ \rightarrow Fe^{2+} + H_2$	44
$Fe^{2+} + H_2O_2 \rightarrow Fe^{3+} + HO^- + HO\bullet$	45
$H_2O_2 + \cdot\cdot\cdot\cdot) \rightarrow 2HO\bullet$	46
$H_2O_2 + HO\bullet \rightarrow H_2O_2 + HOO\bullet$	47
$Fe^{3+} + H_2O_2 \rightarrow Fe(OOH)^{2+} + H^+$	48
$Fe(OOH)^{2+} + \cdot\cdot\cdot\cdot) \rightarrow Fe^{2+} + HOO\bullet$	49
$Fe^0 + 2Fe^{3+} \rightarrow 3Fe^{2+}$	50
$Fe^{3+} + HOO\bullet \rightarrow Fe^{2+} + H^+ + O_2$	51
Sono-Fenton-like	
$Fe^{3+} + H_2O_2 \rightarrow Fe^{2+} + HOO\bullet + H^+$	52
$Fe^{2+} + H_2O_2 \rightarrow Fe^{3+} + HO\bullet + H^-$	53
$H_2O + \cdot\cdot\cdot\cdot) \rightarrow HO\bullet + H\bullet$	54
$\bullet OH + HO\bullet \rightarrow H_2O_2$	55
Radical oxidation process of organic molecules	
$RH + HO\bullet \rightarrow H_2O + R\bullet$	56

Continuation of Table 3

$R\cdot + O_2 \rightarrow ROO\cdot$	57
$ROO\cdot + RH \rightarrow ROOH + R\cdot$	58
$ArH + HO\cdot \rightarrow ArH(OH)\cdot$	59
$ArH(OH)\cdot + O_2\cdot \rightarrow [ArH(OH)OO]\cdot$	60
$[ArH(OH)OO]\cdot \rightarrow ArH(OH) + HOO\cdot$	61
R for Aliphatics, Ar for Aromatics, and))) for ultrasonics	

As an emergent technology, a wide variety of AOPs operate by the generation of hydroxyl ($\cdot OH$) radical. While some AOPs like ozone and or hydrogen peroxide are oxidant systems, others like TiO_2 , ZnO_2 /other metal oxide etc., are semiconductor based, and some other ones are transition metal catalyst or depend on irradiation with UV/visible light to operate or do not even require light (ie., non-irradiation) systems to drive organic compound degradation processes as depicted in Figure 3 [24, 61, 74-75]. Broadly, and depending on the reaction phase; there are the homogeneous AOPs describing systems whereby the reaction media components are all in the same phase and the heterogeneous AOPs describing systems where the reaction media components are in different phases.

Displayed in Figure 3, is the various AOPs technologies widely classified as homogeneous and heterogeneous phases based on the reaction media phase of the contents and sub classified based on light application to irradiate the systems, i.e those operated with light (light driven forms) and those operated without light (non-light driven forms).

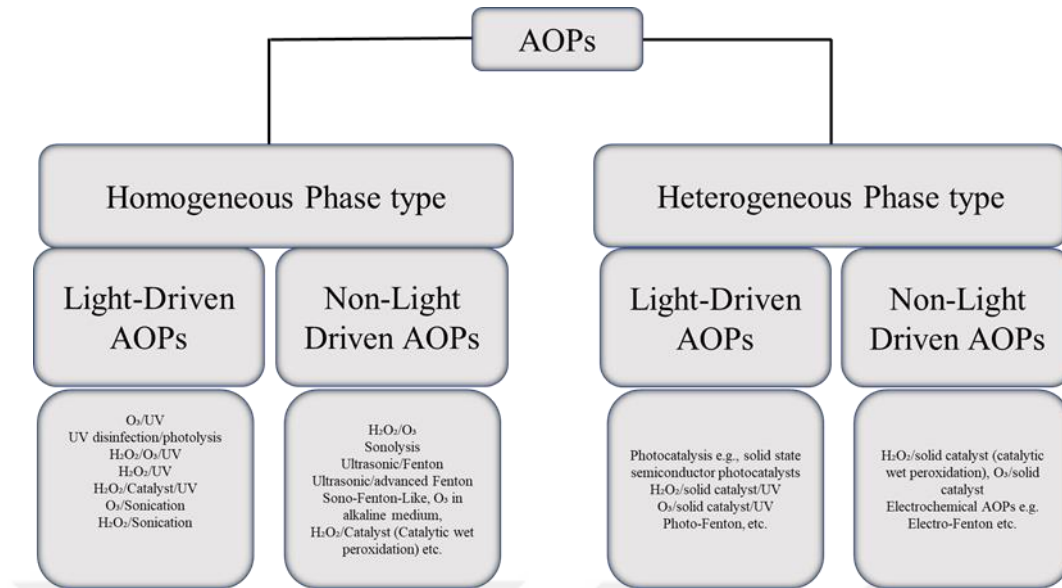


Figure 3. Different form of AOPs classified based on phase types and sub classified based on the light requirement to operate

The great potential of AOPs has no doubt widen advances of scientific knowledge of its application in WWTP both theoretically and experimentally [76-77]. The compatibility of combining AOPs with other treatment methods like biological and adsorption, and the possibility of operating most of the technologies at or near ambient temperature and pressure conditions strategizes them as highly efficient emergent technologies for CEC compounds removal [59, 75]. Despite these advantages, AOPs also present their individual limitations. Requirement for highly advanced installation, high energy, and material demand as well as the need of management and further treatment of residual streams are some of the related drawbacks characteristic of various AOPs technologies [78-80].

However, deploying an effective photocatalyst in a solar driven AOP technology for example UV/TiO₂ photocatalytic process can match expectation for CEC removal from polluted streams and trade off charges for wastewater treatment operations running on high-cost end AOPs [81-83].

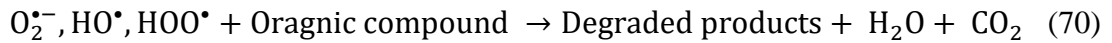
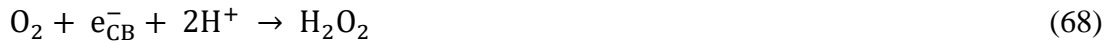
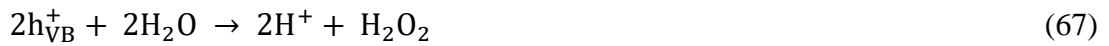
The next section focuses on solar driven TiO₂ based heterogeneous photocatalysis; an AOP that has received wide attention coverage in research efforts recent years as a formidable technology for CECs removal from WWTP.

1.2.1.1. Solar Driven TiO₂ Based Heterogeneous Photocatalysis

Amongst various AOPs technologies, there has been extensive report of studies focused on TiO₂, a typical semiconductor material for the removal from aqueous media CECs compounds [84-90]. This process has received intense research effort on bench and deployed even at pilot scale using mainly solar driven TiO₂ based semiconductor materials as catalysts. This research proliferation beckons on the applicability of solar energy as a green, costless and yet inexhaustible energy source for industry sustainability, pollution reduction and retardation of global warming. Revelation of Aeroxide® TiO₂ P25 has been prominent amongst other commercial titania products and constantly applied as the most active photocatalyst in comparison to various other semiconductor materials investigated; as it boasts of characteristic features of crystalline phases, particle size etc; for enhanced photocatalyst performance [50]. The photocatalytic degradation process of organic compounds by TiO₂ photocatalyst material under solar light irradiation (UV or visible) follows thus process: irradiation of light of photon energy (E) (Equation 62) onto the photocatalyst material able to excite the TiO₂ photocatalyst material (Equation 63) [91]. Emission of electrons (e⁻) and simultaneous induction of generated holes (h⁺) charge carriers from the excited TiO₂ photocatalyst material (Equation 64). Combination of the conduction band electrons (e⁻_{CB}) upon migration with surface oxygen to form superoxide anion (O₂⁻) (Equation 65) [92]. Interaction of the valence band hole (h_{VB}⁺) with hydroxyl ion (HO⁻) electron donor from the surface adsorbed water (H₂O) molecule generating hydroxyl (·OH) radical specie (Equation 66) [92]. Pathways involving the formation of hydrogen peroxide (H₂O₂) radical via valence band (VB) holes (h⁺_{VB}) interaction with surface adsorbed water (H₂O) /conduction band electrons (e⁻_{CB}) interaction with molecular oxygen (O₂) for the subsequent generation of peroxy radicals (HOO₂⁻) via interaction of the generated hydrogen peroxide (H₂O₂) with hydroxyl (·OH) radical respectively during the photo irradiation process is possible (Equations 67-69) [92]. The generated reactive species of superoxide anion (O₂⁻), hydroxyl (·OH) and peroxy (HOO₂⁻) radicals, etc., are involved in the photooxidation and mineralization of organic compounds to yield photodegraded end products, H₂O, and CO₂ (Equation 70).

$$E = hv \quad (62)$$





In Equation 63, h is Planck's constant and ν is the frequency of incident photon.

Shown in Figure 4 is the basic photocatalytic process mechanism involved in a semiconductor photocatalyst material giving a general outlook on how the reactive species are generated and their subsequent attack on the organic compound for their photocatalytic degradation.

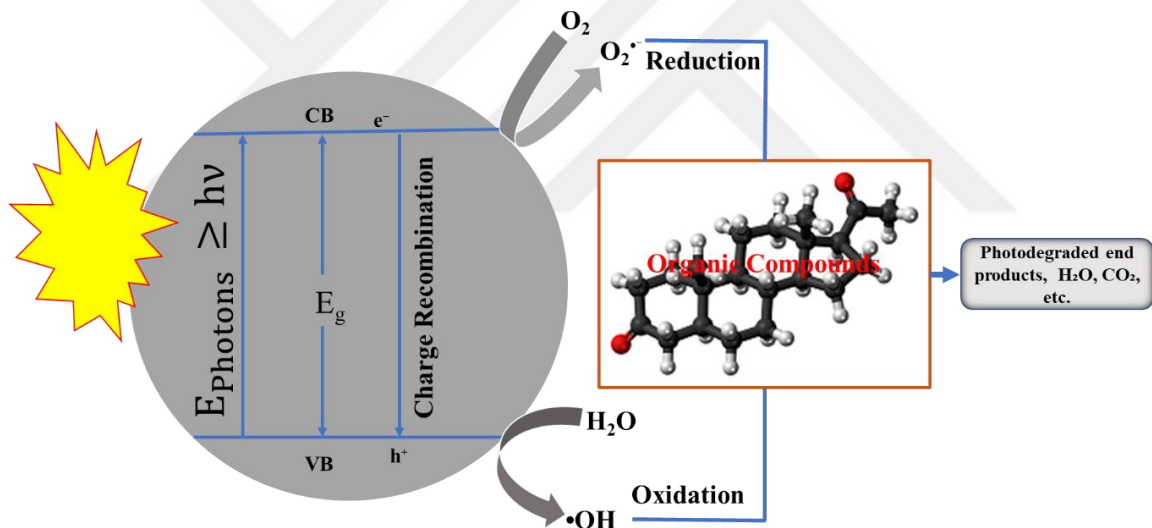


Figure 4. Basic mechanism of reactive species generation involved in semiconductor photocatalyst material

Titania (TiO_2) is the most common used material in heterogeneous photocatalysis due to its several specific advantage characteristics of low cost, non-toxic, good chemical stability, large surface area, etc. as earlier stated [50, 93]. Notwithstanding, limitations of wide energy band gap (3.0-3.2 eV), less energy harnessing of UV-vis spectrum, and non-visible light responsiveness as well as high charge recombination tendency that leads to low

quantum yield hampers its deployment as a standalone photocatalyst material for environmental remediation and other related applications [94-96].

In order to tackle the challenges associated with semiconductor photocatalysts, various strategies aimed at enhancing their performance have been explored. In this perspective, several criteria aimed at meeting specific modification strategy have been employed to help design and develop efficient photocatalyst materials for environmental remediation applications [97]. In the choice for a semiconductor for photocatalyst application, preference is given to materials with lower energy band gap (E_g) to facilitate electron-hole pair excitation and increase the photon absorption capacity [97]. Enhancement of quantum efficiency by the prevention of electron-hole charge recombination, surface area enlargement for reaction site increase as well as tailored photocatalyst chemical and physical structures with high stability and mass transfer promoting are also considered [97]. These features form the basis of criteria requirements channelled through variety of strategies for the realization of enhanced photocatalyst materials performance [97].

Since now, numerous studies have focused design and fabrication of composite semiconductor photocatalysts while engaging various modification strategies. The next section will take a look at modification strategies that have been deployed to better the performance efficiency of photocatalyst materials.

1.3. Modification Strategies

Historically, the early man in his foundry practices was able to join two or more component materials together and achieved a material outcome of superior qualities than each of the individual components he had put together to satisfy their curiosity. The enhanced performance of a composite photocatalyst material has been dedicated to the individual contribution of the constituent elements making up the composite for a synergistic effect, and as such seen appropriate in the design and development of semiconductor photocatalysts materials [98-100]. As shown in Figure 5, heteroatoms doping, metal oxide semiconductor coupling, heterojunctions constructions, surface morphology regulations, dye sensitization, nano-material hybrid fabrications, etc., are among the several techniques reported for the design and fabrication of composite photocatalysts materials with the aim to achieve performance improvement [97, 101-108].

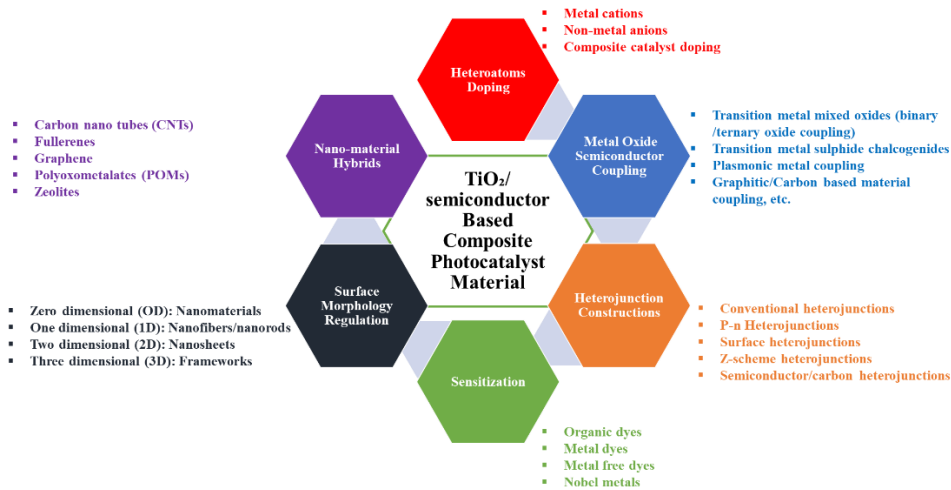


Figure 5. Different modification strategies for the realization of composite photocatalyst material [97, 104, 107]

1.3.1. Heteroatom Doping

The introduction of different atomic elements into the lattice or interstitial sites or even on the surface of TiO₂ and or other semiconductor materials is frequently reported and used to alter the geometric and electronic structure and induce charge density modulation in the base material [97, 101-102, 104, 107]. This tendency of charge density modulation induction leads to energy band gap (E_g) narrowing, increase in energy harvesting, improved charge conductivity and mobility, decrease of bulk charge recombination centres, efficient charge separation and ease of charge transport, active site increment as well as decrease or increase in structural defects [97, 101-102, 104, 107]. These doping effects have been reported resulting to improved photocatalyst performance efficiency for organic compound degradation [97, 101-102, 104, 107].

Semiconductor dopants can mainly be classified as metal cations, non-metal anions, and composite catalysts (Figure 5) [97, 101-102, 104, 107-108]. Each of these classes upon their usage as dopants has produced reported composite photocatalyst material of improved performance efficiency over CECs photocatalytic degradation.

1.3.1.1. Metal Cation Doping

Photocatalytic composites achieved via modification with transition metals have been reported with impressive performance over organic pollutant photocatalytic degradation and in particular CECs compounds. Many studies using metal cations as semiconductor dopants have been reported in the literature. For example, a 0.1 g/L catalyst dose of V-TiO₂ nanoparticles of anatase, brookite, and rutile mixed titania phases obtained via microwave-assisted sol-gel method (MWASG) under UV and within 60 min of irradiation progressed at a very fast reaction rate of 0.0262 min⁻¹ in the photocatalytic degradation of sulfamethazine (SMX) [109]. Tungsten (W) another transition element realized as colloidal W-TiO₂ nanocrystal of anatase phase via hydrothermal method as a 2 % (W)-TiO₂, registered with its 1 g/L catalyst dosage under UV a 80 % removal of 10 mg/L initial phenol concentration at a reaction rate of 0.2694 h⁻¹ within 6 h irradiation; in comparison to 48.9 % reaction rate 0.1092 h⁻¹ for the unmodified TiO₂ within same 6 h [110]. In a similar approach; to enhance the performance of TiO₂ (Degussa P25), 0.125 mol % Mo-TiO₂ of anatase, brookite and rutile phases obtained via micro-wave assisted sol-gel (MWASG) method was employed under UV with a 0.1 g/L catalyst dosage and delivered respective reaction rates of 0.04 and 0.0318 min⁻¹ for the photocatalytic degradation of methylene blue (MB) and sulfamethoxazole (SMX) each 85 mg/L initial concentration within 64 min in comparison to the unmodified TiO₂ at reaction rate of 0.031 min⁻¹ for methylene blue (MB) within same 64 min irradiation exposure time [109]. 0.25 % MoO₃/P25 as the optimum concentration of MoO₃/P25 anatase phase nanoparticles fabricated by impregnation method was employed in a 0.1 g catalyst dosage against 15 mg/L initial concentration of methylene blue (MB); delivering a 38 % MB removal within 150 min under high pressure sodium lamp in comparison to 8 % MB removal recorded for the unmodified P25 TiO₂ [111]. Several other transition metals like nickel (Ni), copper (Cu), manganese (Mn), zirconium (Zr), iron (Fe), chromium (Cr), Co (cobalt), niobium (Nb); noble metals like platinum (Pt), ruthenium (Ru), palladium (Pd), gold (Au), silver (Ag); rare-earth metals like cerium (Ce), erbium (Er), holmium (Ho), gadolinium (Gd), terbium (Tb), neodymium (Nd), yttrium (Y); and other metals like gallium (Ga), indium (In), aluminium (Al), and tin (Sn) are commonly used metallic ions for the enhancement of photocatalytic degradation of organic pollutants [101]. In support, Figure 6, gives an outlook of the most widely, widely and least studied metal dopants for TiO₂ and or other semiconductor photocatalysts materials.

series of graphene oxide modified TiO₂ (GO/TiO₂) fabricated by hydrothermal, solvothermal or mechanical method has been reported as an efficient photocatalyst with the 5% GO/TiO₂ composite obtained via hydrothermal method degrading about 87.1 % dichloroacetic acid (DCA) at 8 h irradiation time under UV-visible light source [118].

On the other hand, C-doped WO₃/TiO₂ obtained by sol-gel method and employed for the photocatalytic degradation of sodium diclofenac (DCF) degraded 82 % of the pollutant in comparison to 65 % degraded by the unmodified TiO₂ under visible light source within an accumulated energy of 400 KJm⁻² [119]. Non-metals like boron (B), and fluorine have equally brought an added performance enhancement to their host material when utilized as dopants to realize composites for the photocatalytic degradation of organic pollutants. While boron doped catalyst has been found effective for photocatalytic activity and more stable than pure TiO₂; fluorine realized composites boasts of increase surface absorptivity of substrate molecules, oxygen vacancy generation as well as site promotion for the extremely reactive hydroxyl (\cdot OH) radical specie [120-121].

In a more recent work, a non-metal co doped B/NaF-TiO₂ photocatalyst composite realized via sol gel method was employed for the degradation of carbamazepine and delivered almost a 100 % degradation of the pollutant at 4 h irradiation under UV light [122]. Reports have also been documented of S atom known for the enhancement of photocatalytic activity via charge separation and absorption band edge shift into the visible region for more light harvesting [123]. In this regard, anatase S-TiO₂ photocatalyst realized via low temperature green approach displayed higher catalytic rate constant for rhodamine B (RhB) dye degradation in comparison to pure TiO₂ under visible light [124]. The inhibition of crystal size growth, surface area increase, resistance of phase transformation and increase of crystallization temperature are some of the reported factor attributes for better photocatalytic activity performances of P incorporated-TiO₂ composites [125].

In the context of modification by doping, composite photocatalysts of two or more constituent metal atom and or non-metal atom as well as other dopant species have also been combined enhancing photocatalytic outcome of the resultant material composite by synergistic influences of their individual makeup contents [97, 101-102, 104, 107-108]. For instance, synergetic effects of lanthanum, nitrogen and phosphorus tri-doping on visible-light photoactivity of TiO₂ fabricated by microwave-hydrothermal process was investigated and found highly efficient for the degradation of 4-chlorophenol (4-CP) under visible-light irradiation with an outstanding superior performance in comparison to commercial P25 TiO₂

[126]. Zr^{4+} , La^{3+} , and C^{3+} doped mesoporous TiO_2 conveniently prepared by sol-gel method in a process involving co-precipitation of TiO_2 and respective metal ion dopant in the presence of triblock copolymer (Pluronic P123) as the structure controlling agent is a doped co-catalyst composite that has been reported and showed high photocatalytic degradation efficiency in comparison to the single (pure) metal doped TiO_2 over alachlor mineralization at UV 365 nm irradiation after 4 h [127].

1.3.1.3. Composite Catalyst Doping

Various other co-catalysts systems involving a mix of metal ions and or non-metal ions as well as carbon or other semiconductor materials have equally been investigated and reported with improved photocatalytic activity when compared to the unmodified base materials [97, 101-102, 104, 107-108].

1.3.2. Metal Oxide Semiconductor Coupling

The drive for the exploitation of advanced multifunctional photocatalyst materials operating under broad spectrum solar light has also brought into focus metal oxide semiconductor coupling as a modification approach [102, 108]. Photocatalysts materials derived from semiconductor metal oxides in lone or in combined forms have found unrivalled applications not only limited to organic pollutant removal but also a range of other applications [102, 108]. Mixed oxide (binary/ternary), metal sulphides, plasmonic metals, graphitic/carbon-based materials, transition metal oxides, transition metal chalcogenides, multiple semiconductor components, are some of the metal oxide system classifications that have been studied and reported with improved competence for environmental and related applications (Figure 5) [102, 107-108]. Their characteristic advantage features of stability, non-toxicity, ease of preparation, suitable band edge positions and readiness in the generation of reactive species in aqueous systems give them edge and make them preferentially considered for host of applications specially in the area of environmental remediation and energy storage [102, 108].

Table 4. Some classified examples of semiconductor oxide systems and their photocatalytic result outcome over CECs removal and mineralization

Catalyst	Target CEC	% Removal/Total organic carbon (TOC) mineralization	Reference
Transition Metal Mixed Oxides Binary/Ternary Oxide coupled Systems			
TiO ₂ -WO ₃ (0.5 g/L)	2,4-dichlorophenoxy acetic acid (2,4-D)	94.6 / (TOC = 88.6)	[128]
TiO ₂ -WO ₃ (0.6 g/L)	Diclofenac	TOC = 91	[129]
TiO ₂ -WO ₃ (0.1 g/L)	Amoxicillin	64.4	[130]
(WO ₃ /TiO ₂ - C) (1.0 g/L)	Diclofenac	100 /TOC = 82.4	[119]
(WO ₃ /TiO ₂ - N) (1.0 g/L)	Diclofenac	100 /TOC = 100	[131]
Cu ₂ O-TiO ₂ supported Palygorskite (1.0 g/L)	Tetracycline Hydrochloride	88.81	[132]
TiO ₂ -Cu ₂ O film	Tetrabromodiphenyl Esthers	90	[133]
0.05CuWO ₄ -TiO ₂ (1 g/L)	Carbamazepine	~100	[134]
Bi ₂ O ₃ -TiO ₂ (50 mg)	Quinalphos	92	[135]
Bi ₂ O ₃ -TiO ₂ (0.5 g/L)	Ofloxacin	92	[136]
N-TiO ₂ /CaFe ₂ O ₄ / diatomite (2 g/L)	Tetracycline	91.7/TOC = ~ 80	[137]
N-TiO ₂ /SrFe ₂ O ₄ / diatomite (2 g/L)	Tetracycline	92/TOC = ~ 80	[138]
Ce/N co-doped TiO ₂ /NiFe ₂ O ₄ diatomite (0.5 g/L)	Tetracycline	98.2/TOC = ~ 95	[139]
ZnFe ₂ O ₄ /TiO ₂ (1 g/L)	Bisphenol A	100	[140]
TiO ₂ /Fe ₂ O ₃ (0.1 g/L)	Diazinon	95.07	[141]
TiO ₂ /Fe ₂ O ₃ (10 mg)	2,4-dichlorophenoxy acetic acid (2,4-D)	100/TOC = 100	[142]
TiO ₂ /Fe ₂ O ₃ (0.5 g/L)	2,4-dichlorophenoxy acetic acid (2,4-D)	96.8/TOC = 90	[128]
TiO ₂ /Fe ₂ O ₃ (70 mg)	Oxytetracycline Hydrochloride	75.6	[143]
TiO ₂ /Fe ₂ O ₃ (1 g/L)	Oxytetracycline	~80	[144]

Continuation of Table 4

TiO ₂ /Fe ₂ O ₃ /CNT (100 mg/L)	Tetracycline	89.41	[145]
TiO ₂ -coated α -Fe ₂ O ₃ core shell (100 mg/L)	Tetracycline Hydrochloride	100	[146]
Transition Metal Oxide Chalcogenide Coupled Systems			
CdS-TiO ₂ (50 mg)	Tetracycline Hydrochloride	87	[147]
Au-CdS/TiO ₂ nanowire (20 mg)	Ciprofloxacin	99	[148]
CdS/TiO ₂ (450 mg)	Ofloxacin	86	[149]
CdS nano-rod/TiO ₂ nano-belt (0.5 g/L)	17 α -ethynylestradiol	92	[150]
CuS/TiO ₂ nanobelts	Enrofloxacin	85.5/TOC = 27.7	[151]
Au-CuS-TiO ₂ nanobelts	Oxytetracycline	96/TOC = 68	[152]
MoS ₂ /TiO ₂ (25 mg/L)	Acetaminophen	40	[153]
N, S co-doped TiO ₂ @ MoS ₂ (0.98 g/L)	Diclofenac	98	[154]
TiO ₂ /SnS ₂ films	17 β -estradiol	51	[155]
TiO ₂ /SnS ₂ films	Diclofenac	76.21	[156]
Plasmonic Metal Oxide Based Coupled Systems			
Ti ³⁺ -doped TiO ₂ nanotubes/Ag ₃ PO ₄ quantum dots (0.5 g/L)	Tetracycline	90	[157]
TiO ₂ nanotube / Ag ₃ PO ₄ nanoparticles (40 mg)	Ciprofloxacin	85.3	[158]
TiO ₂ -x/Ag ₃ PO ₄ (100 mg)	Bisphenol A	95	[159]
Ag ₂ O/TiO ₂ quantum dots (0.25 g/L)	Levofloxacin	81	[160]
Ag ₂ O/TiO ₂ -zeolite (50 mg)	Norfloxacin	98.7	[161]
Ag-ZnSnO ₃ (1 g/L)	Caffeine	~100	[162]
Graphitic Carbon-Based Oxide Material Coupled Systems			
TiO ₂ /WO ₃ /GO (2 mg)	Bisphenol A	93.2	[163]
Graphene-WO ₃ /TiO ₂ nanotube (photoelectrodes)	Dimethyl Phthalate	75.9	[164]

Continuation of Table 4

TiO ₂ /ZnO/GO (0.5 g/L)	Bisphenol A	UV/99.7; Vis/94.9	[165]
TiO ₂ /ZnO/GO (0.5 g/L)	Ibuprofen	UV/98.5; Vis/79.6	[165]
TiO ₂ /ZnO/GO (0.5 g/L)	Flurbiprofen	UV/98.1; Vis/82.2	[165]
ZnFe ₂ O ₄ /Rgo/TiO ₂ (0.1 g)	Fulvic acid	95.4	[166]
0.5 g TiO ₂ /MoS ₂ /Rgo	Bisphenol A	62.4	[167]
TiO ₂ /BiVO ₄ /rGO	Tetracycline	96.2	[168]
TiO ₂ /BiVO ₄ /rGO	Chlorotetracycline	97.5	[168]
TiO ₂ /BiVO ₄ /rGO	Oxytetracycline	98.7	[168]
TiO ₂ /BiVO ₄ /rGO	Doxycycline	99.6	[168]
g-C ₃ N ₄ /TiO ₂ (30 mg)	Ciprofloxacin	88.1	[169]
g-C ₃ N ₄ /TiO ₂ (30 mg)	Acyclovir	100	[170]
mpg-C ₃ N ₄ /TiO ₂ (membrane)	Sulfamethoxazole	69	[171]
TiO ₂ @g-C ₃ N ₄ core shell (100 mg)	Tetracycline	2.2 mg/min	[172]
g-C ₃ N ₄ -shielding polyester/TiO ₂ (130 mg)	Sulfaquinoxaline	97	[173]
g-C ₃ N ₄ -shielding polyester/TiO ₂ (130 mg)	Thiamethoxam	~95	[173]
g-C ₃ N ₄ /TiO ₂ /kaolinite (200 mg)	Ciprofloxacin	92	[174]
S-Ag/TiO ₂ @g-C ₃ N ₄ (0.20 g/L)	Triclosan	92.3 (64.3±3.9 detoxification efficiency)	[175]
Co-TiO ₂ @g-C ₃ N ₄ (5 mg; 2x2 cm ² membranes)	Tetracycline Hydrochloride	90.8	[176]
D35-TiO ₂ /g-C ₃ N ₄ (0.5 g/L)	Bisphenol A	100/TOC = 50	[177]
C dots decorated g-C ₃ N ₄ /TiO ₂ (1.0 g/L)	Enrofloxacin	91.6	[178]
graphene quantum dots/Mn-N-TiO ₂ /g-C ₃ N ₄ (45 mg)	Ciprofloxacin	89	[179]
graphene quantum dots/Mn-N-TiO ₂ /g-C ₃ N ₄ (45 mg)	Dimethyl Phthalate	70.4	[179]

Continuation of Table 4

MoS ₂ supported TiO ₂ / g-C ₃ N ₄ (30 mg)	Atrazine	86.5	[180]
WO ₃ -TiO ₂ @g-C ₃ N ₄	Acetylsalicylate	98	[181]
WO ₃ -TiO ₂ @g-C ₃ N ₄	Methyl-theobromine	97	[181]

Methods like solid-state, incipient wet impregnation, coprecipitation, sol-gel, combustion, ultrasonic spray pyrolysis, electrochemical synthesis and relevant characterization techniques have been used to fabricate and realize doped oxide systems investigated for various other applications [182]. Outside photocatalytic degradation of organic pollutants including CECs, in a related development and for other environmental remediation applications, doped apatite type lanthanum silicate of Fe and 5 % wt. NiO compositions fabricated via different synthesis routes of solid state, wet impregnation, mechanical mixing and sol-gel methods were reported catalytically active for carbon monoxide (CO) oxidation [183]. Al₂O₃ and CeO₂-Al₂O₃ has been utilized as supports to facilitate the activity and selectivity of on the support noble metal catalyst (Ir, Pd, Pt) applicable in glycerol energetic valorisation via steam reforming for hydrogen production [184]. Different methods of preparation effect of oxide system support employed for variety of applications (e.g., dry reforming methane reaction on Ni/CeO₂) on its carbon deposition contribution and removal route has been studied and reported [185]. Reported efficient catalytic activity of Mn-based mixed oxide for deep oxidation of methane and lean-NO_x reduction has been attributed to the high surface area of the mesoporous material [186]. Evaluation of mixed oxidic materials for potential catalytic/photocatalytic applications has also been explored by the investigation of pore structure-chemical composition interactions of a new high surface area manganese based porous mixed oxide (MANPOs) [187].

1.3.3. Heterojunction Constructions

The coupling of TiO₂ and or semiconductors with other semiconductor materials has resulted in increase in photocatalytic efficiency of the obtained composites due to differences in redox energy levels that leads to heightened charge carrier lifetime by virtue of enhanced charge separation processes [188]. In coupling, with the aim of separating the charges to

avoid their rebinding, proper selection of the semiconductors to be coupled is important in order to activate the heterojunction system and induce efficient interfacial charge transfer to adsorbed substrates [189-190]. A heterojunction is the interface configuration of two sector layers of two different semiconductor materials with different band gaps [97, 102, 104, 188]. In contrast, there is the homojunction. In heterocouplings, the epitaxial growth of one semiconductor over the other leads to epitaxial bonding interfaces which in elaborate configurations suppress charge recombination tendencies and improve radiative lifetime [102].

In tuning engineered TiO₂/semiconductor-based materials for photocatalytic applications, the seamless operability of modification strategy tools makes them convenient to design and develop materials that exist as heterocoupled systems; display alternate configurations of crystal structure and optical band edge dissimilarity which favours among other features easy charge separation in such systems as a key design outcome of heterojunctions. For instance, several fabricated transition metal oxides composite coupled systems take advantage of minimal interface defect density during formation, and also the new functionalities existing at the interfacial structure not present in their individual component phases [102] (Table 4).

Basically, there are two forms of heterojunctions viz- conventional and new generational heterostructures [97].

1.3.3.1. Conventional Heterojunctions

The conventional heterojunctions can be classified in three forms and depends on the different band gaps of the constituent semiconductors making up the composite [191-192]. The three different conventional heterojunctions are- type I heterojunction with a straddling gap, type II with a staggered gap, and type III with a broken gap (Figure 7) [191].

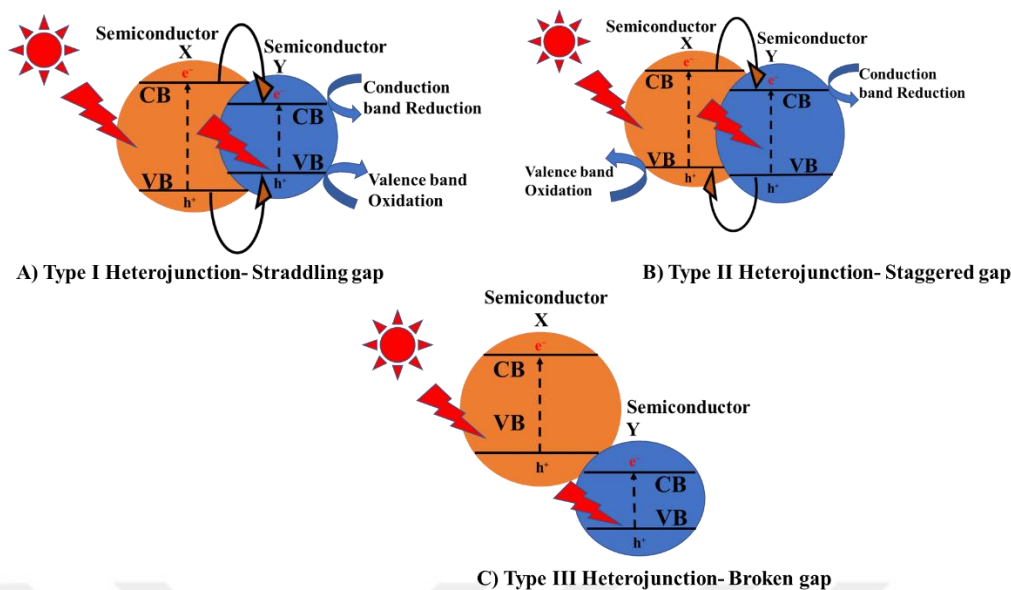


Figure 7. Schematic pattern of illustration displaying photocatalysis mechanism of the three different heterojunction semiconductor photocatalyst: a) Type I, b) Type II, and c) Type III [191]

Type I heterojunction is formed in a configured orientation where the valence band (VB) and conduction band (CB) of semiconductor X is lower and higher than the corresponding VB and CB energy levels of semiconductor Y (Figure 6A). This configuration result to the transfer of the photogenerated electrons (e^-) and induced holes (h^+) of respective CB and VB energy levels of semiconductor X into the corresponding energy levels of CB and VB of semiconductor Y favouring charge separation. In a type I heterojunction photocatalyst, the redox reaction usually conducts on the semiconductor Y with lower redox potential compared to semiconductor X and as such the overall semiconductor photocatalyst composite redox ability maybe hampered. In contrast, with type II heterojunction composites, the VB and CB energy levels of semiconductor X are both higher than the corresponding VB and CB of semiconductor Y (Figure 6B). In this case, the photogenerated electron (e^-) of semiconductor X will migrate and escape into the CB of semiconductor Y with a lower reduction potential, while the induced holes (h^+) from the VB energy level of semiconductor Y will migrate and escape into the VB energy level of semiconductor X; as such in this way, this configuration favours a more spatial charge separation. There is no band gap coincidence in the type III configuration and this orientation do not favour charge transfer nor separation (Figure 6C). Based on this and as the semiconductor configuration with effective charge transmission and separation, type II heterojunction has received a more focused attention from the research community than types I and III. For example, a

mesoporous SnO₂-ZnO type II band aligned heterojunction photocatalyst was successfully fabricated via two-step synthesis strategy and showed a high photocatalytic activity in comparison to the individual SnO₂ and ZnO nanocatalyst for the degradation of methyl blue in water [193]. Highly efficient TiO₂-coated α -Fe₂O₃ core-shell heterojunction of 15 nm TiO₂ shell dimension exhibited a 100 % tetracycline hydrochloride removal in 90 min with such efficiency attributed to added H₂O₂ for the generation of more reactive hydroxyl (HO·) radical specie aided by the photocatalyst suppression of electron (e⁻)/hole (h⁺) charge carriers recombination [146].

In another study, CdS-TiO₂ heterojunction composite have been employed for visible light degradation of tetracycline and delivered a commendable activity attributed to the combination of the separated electron (e⁻) charge carrier with surface adsorbed oxygen to form superoxide anion (O₂⁻), a reactive specie responsible for driving photocatalytic degradation processes [147].

Several other heterojunction structured semiconductor composites of type II configuration have been developed and reported for effective photocatalytic degradation of CEC compounds and bacteria inactivation building the more efficient transmission and separation of the composites [135-138, 140, 151, 154, 165, 168, 172, 176].

Beside inorganic semiconductor heterojunction composites, organic semiconductor components have also been used to realize type II heterojunction organic semiconductor-based composites and deployed for photocatalytic applications. Polyaniline (PANI) combined with ZnSe nanoparticles via simple and cost-effective co-precipitation method under ambient conditions has been reported for enhanced photocatalytic performance in comparison to pristine ZnSe nanoparticles [194].

Conventional type II heterojunctions have showed promising results in their capability of spatially separating photo-generated electron-hole pairs (e⁻/h⁺); however, limitations of weak redox ability and charge carriers migration suppression remains [191].

1.3.3.2. New Generation Heterojunctions

Addressing the limitations of conventional heterojunctions as already stated, a new generation of heterojunctions have been developed, namely p-n heterojunctions, the surface heterojunctions, Z- scheme heterojunctions and semiconductor/carbon heterojunctions (Figure 5).

1.3.3.2.1. p-n Heterojunctions

The incorporation of a p-type semiconductor with an n-type semiconductor has generated p-n heterojunction semiconductors that has shown highly efficient photocatalyst character and therefore, making it a widely considered choice as a photocatalyst composite for the degradation of organic pollutants [195-196]. As part of its working mechanism, the p-n heterojunctions has the intrinsic capability of establishing internal electric field in the close by p-n interface region in the absence of irradiated light due to the electron-hole diffusion phenomenon of the semiconductor composite constituent systems unequal fermi levels [191, 197].

Contrastingly, upon irradiation with a photon energy state larger than the gaps of both p and n type semiconductors (Figure 8), electron-hole charge pairs (e^-/h^+) are generated and by the dominance of the internal electric field, the photo-generated electrons, and holes (e^-/h^+) respectively migrate to the CB of the n-type semiconductor and VB of the p-type semiconductor. The combination of the intrinsic electric field current and band gap alignment of p-n heterojunction semiconductors is a synergy in effect not present in type II conventional heterojunction which adequately orients the spatial separation of photo-generated charges. This synergistic tendency makes p-n heterojunction considered as a better choice of composite semiconductor fabrication in photocatalytic applications. In this view, various research groups have developed and reported p-n heterojunction photocatalyst semiconductor materials with outstanding photocatalytic capabilities. For instance, SnS₂/MoO₃ hollow nanotube fabricated via facile hydrothermal method has been reported to exhibit a typical p-n heterojunction structure with a synergistic effect of its MoO₃ and SnS₂ constituents confirmed to have been responsible for the composite optimal yield of hydrogen peroxide, a proof for photocatalytic performance efficiency [198]. BiOI/CeO₂ p-n heterojunction fabricated via in situ chemical bath method has been reported with a

(001) and (101) has been worked and reported with a demonstrated significant photocatalytic activity [202]. Report has also been documented of a surface heterojunction TiO_2 that can be self-adjusted with a high photocatalytic performance when combined with a Schottky junction [203].

Other than TiO_2 -based surface heterojunction materials, bismuth-based semiconductor materials have also been used to design and develop surface heterojunction composite. By regulating the water quantity in the hydrolysis step for the synthesis of BiOI photocatalyst at room temperature, a tetragonal shaped material was derived which displayed a surface heterojunction structure between crystal facets (001) and (110) and showed in return a high photocatalytic performance capability under visible light for the degradation of organic contaminants in water [204].

1.3.3.2.3. Z-scheme/Direct Z-scheme Heterojunctions

Z-scheme heterojunctions was fabricated to address the challenge of lower redox potential of the heterojunction composites [191, 205]. The basics of the working mechanism principle of Z-scheme heterojunction is such that involves two different semiconductor materials where one acts as the electron donor and the other as the electron acceptor. Photo-generated electron (e^-)/hole (h^+) pairs during photocatalysis reaction is transmitted from the base semiconductor grid to the coupled semiconductor either through the electron acceptor/donor pair pathway or via an electron mediator channel. By this way, electron (e^-)/hole (h^+) charge carriers will mount and accumulate over the semiconductor with a higher redox potential consequently establishing an effective spatial electron/hole (e^-/h^+) charge carrier separation. This suppression tendency of charge recombination in Z-scheme heterojunction structures has widen studies on its application for improved photocatalytic degradation of organic pollutants [205]. For example, a nano composite comprising of Ti^{3+} doped TiO_2 nanotube (TNTs) and Ag_3PO_4 quantum dots fabricated by a two-step method involving reductive introduction of Ti^{3+} into TiO_2 the TNTs with NaBH_4 as the reducing agent and deposition of the Ag_3PO_4 quantum dots on the TNTs via precipitation was reported of a high photocatalytic performance under visible light with 90 % of tetracycline removed in 8 min. The high-performance activity of the nanocomposite photocatalyst material was attributed partly to the reductive titania ion (Ti^{3+}) introduction into the TNT and the efficient electron-hole charges separation by the nanocomposite as a Z-scheme photocatalyst [157].

In a related study, $\text{Ag}_2\text{CO}_3/\text{Ag}/\text{AgNCO}$ composite photocatalyst fabricated via a facile in situ ion exchange method, have been reported to be Z-scheme acquainted heterojunction with a demonstrated photocatalytic degradation efficiency over rhodamine B (RhB) dye and Cr (VI) reduction under visible light [206]. Due to the rarity and high cost of noble metals which most often serve as electron mediators in Z-scheme heterojunctions, special efforts have been directed towards the construction of noble free Z-scheme heterojunction nanocomposites. This drive has given birth to a new generation of Z-scheme heterojunctions referred to as direct Z-scheme systems [191]. Typically, $\text{CuInS}_2/\text{Bi}_2\text{WO}_6$ is a direct Z-scheme heterojunction system fabricated via in situ hydrothermal growth of Bi_2WO_6 on the surface of CuInS_2 network matrix reported to have demonstrated superior visible light photocatalytic degradation of tetracycline hydrochloride (THC) in comparison to those of its building blocks of CuInS_2 and Bi_2WO_6 [207]. The superior performance of this direct Z-scheme heterojunction has been down well established by the intimate interfacial contact between the composite make-up contents which in turn aided an unhindered charge mobility across the structure matrix interface [207].

1.3.3.2.4. Semiconductor-based Carbonaceous Materials Heterojunction

Photocatalyst surface modification has also been performed with carbonaceous materials like graphene, graphene quantum dots (GQDs), carbon nano dots (CNDs), carbon nano tubes (CNTs), fullerenes (C_{60}), etc. [104]. High surface area, good conductivity and excellent chemical stability are the various advantage features of carbonaceous materials [97]. Most used carbonaceous materials for semiconductor combination are carbon dots (CDs), carbon nanotubes (CNTs) and graphene [208].

Carbon dots (CDs) is an example of a nanocarbon material and possess outstanding optical and electronic characteristics, low chemical toxicity, tuneable photoluminescence, and specific quantum effect [209]. These special features make it a focal point of interest in semiconductor photocatalysis process applications. For example, carbon quantum dots (CQDs) / TiO_2 nanotubes (TNTs) composite fabricated via an improved hydrothermal method with the CQDs incorporated on the surface of the TNTs has been reported a highly visible-light responsive photocatalyst with demonstrated advantages of photo-generated electron (e^-) trapping by the CQDs from the surface of the TNTs and its subsequent suppression of charge recombination, up-conversion of the photoluminescence property

enhancing the visible light harvesting capabilities of the CQDs, and lifetime prolongment of the photogenerated charges by the formed hetero-structure between CQDs and the TNTs [210]. In another study, carbon dots (CDs) coupled BiOI composite with sufficiently exposed (001) crystal facet delivered an impressive photocatalytic activity for the degradation of organic dyes in water; an outcome attributed to the available numerous constructed surface electron trap sites on the CDs/BiOI heterojunction that aided charge separation and supported the visible light responsiveness of the composite [211].

CNTs are well organized sp^2 -ordered structures with high metallic conductivity and ability to form Schottky barrier junction with semiconductors; therefore, prolong photo-generated charges recombination time [208, 212]. Apart from this, the electron accepting capability of CNTs in combined semiconductor composite systems due to their large electron-storage capacity facilitates their impedance of photo-generated charge recombination as charge separation is enabled. Based on these photoactivity enhancing attributes, plethora of semiconductor-based CNT photocatalysts systems have been developed. For instance, facile hydrothermal method prepared TiO_2 /CNT composite has been reported for an impressive photocatalytic degradation of Sudan (I) under UV-vis irradiation at a 0.3 wt % loading amount of the CNT constituent in the composite [213]. Other semiconductor-based CNT composites instead of the TiO_2 based ones have also been reported while demonstrating commendable photocatalyst activity efficiency. For example, by hydrothermal method, a novel CNT/ $LaVO_4$ nanocomposite was prepared and showed excellent photocatalytic activity about 2 times faster than the pristine $LaVO_4$ in the degradation of tetracycline under visible light and maintained a remarkable stability [214]. Graphene is an SP^2 hybridized 2D monolayer material with a zero-band gap and sheet-like structure [215]. Its distinct properties of excellent electron mobility ($200,000\text{ cm}^2/\text{V}$), substantial specific surface area ($2630\text{ m}^2/\text{g}$), superior electrical and thermal conductivity, remarkable chemical and physical stability, and high optical transmittance amongst other features including handy achievability from graphite bulk through mechanical, chemical, and thermal routes has distinguished it as a material of high interest within the research community for wanton applications [104, 208, 215-217]. The easiness with which graphene materials attain reverse saturation density (approx. 10^{13} cm^{-2}) of hot electrons above the fermi level makes it a powerful agent for redox processes [218]. Hence, the combination of graphene-based materials either in form of graphene oxide (GO) or as reduced graphene oxide (rGO) with TiO_2 was credited for possible suppression of photo-generated electron-

hole (e^-/h^+) charge recombination. Hence, a plethora of studies have investigated and reported graphene coupled TiO_2 / other semiconductor materials for enhanced photocatalytic performance over organic pollutant degradation. Foundation work of fabricated TiO_2 (P25)-graphene composite with chemically bonding-structure via one-step hydrothermal method exerted a superior photocatalytic performance over the degradation of methylene blue in comparison to the unmodified P25 titania. The high-performance outcome was dedicated to the enhancement of pollutant adsorption, extension of light absorption spectrum, and improved charge separation mechanism all to the credit of the introduced graphene material onto the titania P25 [219]. Following this breakthrough, lots of investigations has gone into the development of various TiO_2 /graphene-based composites applied and reported for the photocatalytic degradation of CECs (Table 4). Recent progress has been directed to the area of poor homogeneous dispersion of graphene. In this context, fabricated ternary Fe-doped TiO_2 /rGO via simple sol-gel route has been reported as an effective photocatalyst in the removal of rhodamine B (Rh B) out of water and in a well dispersed and homogeneous suspension system [220].

Generally, the concept of Schottky junctions, heterojunction (type II) systems, p-n junctions and direct Z-scheme heterojunction has been approached with the central focus of improving and as much as possible the separation of photogenerated electron-hole (e^-/h^+) charge carriers, facilitate charge migration processes and among many other issues retard charge recombination tendencies in semiconductor-based photocatalysts in order to enhance their activity performance for and not limited to photocatalytic degradation of organic pollutants.

Displayed in Figure 9 is the scheme showing basic charge separation mechanism involved in Schottky junctions, heterojunction type II, p-n heterojunctions, and direct Z-scheme junctions for semiconductor-based photocatalyst composites.

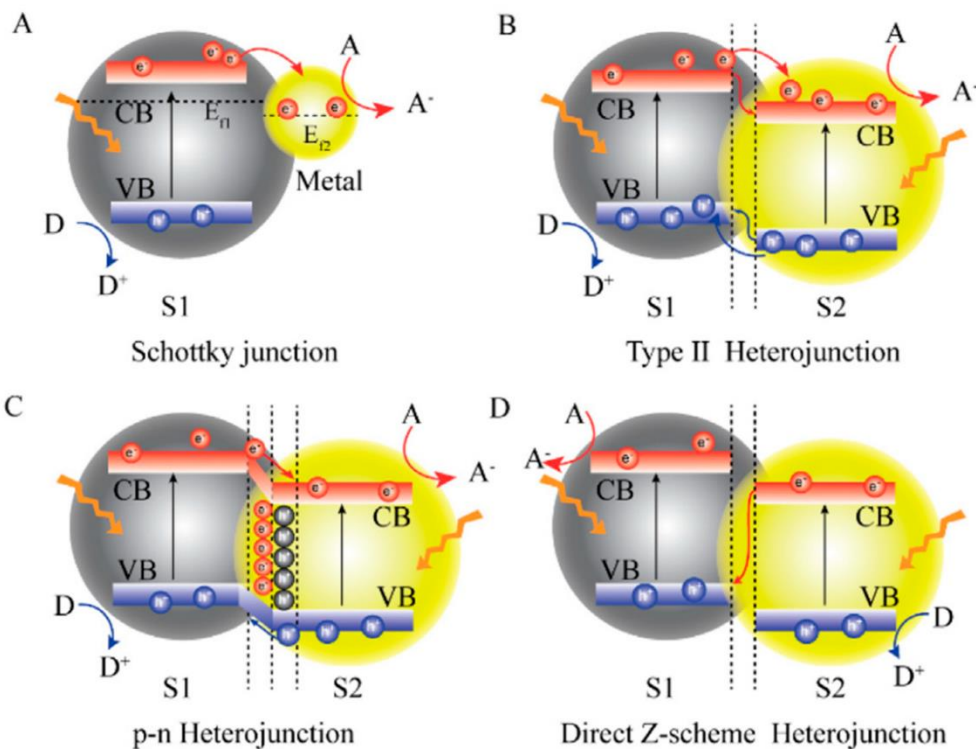


Figure 9. Schematic display of charge separation mechanisms involved in modified semiconductor-based photocatalyst composites operating as: a) Schottky junction, b) Type II Heterojunction, c) p-n Heterojunction, or d) Direct-Z scheme Heterojunction [221]

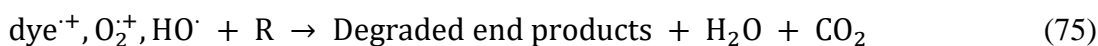
1.3.4. Sensitization

Sensitization as a modification strategy has also been employed to help increase the UV-visible light spectrum range harvesting of semiconductor-based photocatalyst materials [104, 107, 122, 134, 162, 222-223]. In this approach, dye anchoring using metal-complex dyes, metal-free dyes, organic dyes, etc., and sensitization with noble metals have all been used to realize photocatalysts materials with demonstrated high level activity performance in the degradation of organic pollutants [104, 107, 122, 134, 162, 222-223].

1.3.4.1. Inorganic/Organic Metal/Metal-Free Dye Anchoring

Sensitization of TiO₂ with in (organic) dye materials have gained huge attention as a modification approach for solar light driven TiO₂-based heterogeneous photocatalytic process degradation of organic pollutants in water. The photochemical process involved in the sensitization of TiO₂/semiconductor-based photocatalysts is one that is initiated by the photoexcitation of Highest Occupied Molecular Orbital (HOMO)-Lowest Unoccupied Molecular Orbital (LUMO) energy level of the dye molecule (Equation 71). Following this step is the transfer of electron from the photoexcited dye molecule, specifically (HOMO-LUMO) to the conduction band (CB) of any potential semiconductor photocatalyst designate- MO e.g., TiO₂, ZnO, etc., (Equation 72) where it combines with surface adsorbed oxygen (O₂) to generate superoxide anion (O₂^{·-}) (Equation 73) and subsequent regeneration of the oxidized dye molecule in the presence of suitable electron donors, e.g., water which is usually preferred for potential water purification photocatalyst materials (Equation 74) [107, 224].

During the photochemical processes of the dye molecules, reactive species in the form of oxidized state dye molecule (dye^{·+}), superoxide anion (O₂^{·-}) are readily available for the breaking down of the organic pollutants to entities like degraded organic products, water, and carbon dioxide (Equation 75). Shown in (Equations 71-75) below are the photochemical processes involved during irradiation of dye sensitized semiconductor photocatalyst material.



Where, h is Planck's constant, and ν is the frequency of incident radiation in Equation 71, and R represents any organic compound pollutant in Equation 75.

Up till now, several kinds of dyes have been evaluated for the sensitization of TiO₂, namely ruthenium bipyridyl derivatives, coumarins, porphyrins, phthalocyanines, and humic acids etc. [104, 107, 222-223].

For example, a dye sensitization incorporated system of Pt(dcbpy)Cl₂ where dcbpy is 4,4'-

dicarboxy-2,2'-bipyridine) on titania (TiO_2) for the visible light degradation of 4-chlorophenol in the presence of dioxygen in water has been reported with a better demonstrated enhanced photocatalytic performance of the sensitized material in comparison to the bare TiO_2 [224]. We employed B/NaF co-doped TiO_2 sensitized with methoxy substituted silicon phthalocyanine (- OCH_3SiPc) and achieved an impressive removal of carbamazepine in comparison to unmodified TiO_2 under UV irradiation at 4 h exposure window [122].

In other related studies, with a copper sensitized TiO_2/ZnO heterostructured photocatalyst, and manganese (III) phthalocyanine sensitized ZnWO_4 (ZnWO_4MnPc), we reported high photocatalytic degradation rates of the modified photocatalyst materials in comparison to their unmodified counterparts by sensitization over their respective removal of ibuprofen and bisphenol-A (BPA) under UV-visible light illumination [222-223].

Though the deployment of dye sensitized TiO_2 /semiconductor-based photocatalyst materials continue to garner attention as a modification strategy for better material performance either for energy or environmental applications; challenges of photostability and solubility, rarity, purification, environmental toxicity, and low molar extinction coefficient (MEC) especially as regards metal containing in(organic) dyes remains a challenge [225].

Metal-free organic sensitizers have recently drawn huge interest from researchers over their metal counterparts thanks to their low toxicity, advanced structural flexibility, environmental friendliness, easy method of synthesis as well as high molar extinction coefficient [107, 226]. Recently, for example, by phenolic condensation approach, carbon dots organic dye molecule procyanidins and 4-methoxybenzaldehyde were formulated into a metal free photocatalyst and deployed as an efficient catalyst for the photosynthetic production of hydrogen peroxide (H_2O_2) from real seawater [227].

Efforts in increasing the water solubility of dye compounds by the introduction of more polarizable functional groups into their side structure macrocyclic rings for sensitization modification purposes and activity enhancement performance of TiO_2/ZnO and other semiconductor-based photocatalyst materials have also been made and reported [122, 223, 228].

1.3.4.2. Nobel Metal Loading

Sensitization has not only been approached using in(organic) dyes to make semiconductor-based photocatalysts perform better but also metals especially noble metal sensitization strategy has equally been employed. Nobel or precious metals like Pt, Pd, Au, Ni, Rh, Cu and Ag have been reported to improve TiO₂ photocatalytic activity [104]. As part of their mechanism of operation when combined with semiconductor material; photogenerated electron charge carriers (e⁻) due to their lower fermi level position migrates easily into the conduction band of the noble metallic particle with the restriction of the hole charge carrier (h⁺) into the valence band (VB) of the base semiconductor material. This phenomenon results to better charge separation tendency and therefore, improved photocatalyst activity performance [104].

Depending on this, various works have reported improved noble metal loaded TiO₂/other semiconductor-based material photocatalytic activity improvement for the degradation of organic pollutants. For example, efficient degradation of acid green 16 has been reported of moderately loaded TiO₂ photocatalyst with Pt, Au, and Pd in comparison to the bare and unsensitized TiO₂ material [229]. In this approach, the famous surface plasmon resonance (SPR) which sometimes can operate in a localized manner that is localized surface plasmon resonance (LSPR) effect has been put forward as one of the effective charge transfer mechanisms associated with loaded noble metal particles on semiconductors by which charge recombination is suppressed and photocatalytic activity efficiency improved due to the high work function energy value of the noble materials [162].

1.3.5. Surface Morphology and Regulation

Another modification strategy tool that has been applied in the engineering of semiconductor-based photocatalyst materials for enhanced photocatalytic activity performance is surface morphological regulation or tuning.

Various surface morphology modification techniques have been made to bring changes to photocatalysis process mechanisms and accelerate the kinetics.

Whether a semiconductor-based material modification strategy method for photocatalytic activity improvement has been approached via heteroatom doping, semiconductor metal oxide coupling, combination of semiconductors to achieve

heterojunctions, or even surface sensitization by anchoring different dyes or loading noble metals; resultant outcome effects has always hinged on different size, shape, surface area, crystallinity or even surface charge properties induced by variety of surface impurity defect-dependent reactive species.

On this basis and of course applied synthesis method/route for composite material fabrication, physico-chemical and optical properties of modified materials for semiconductor photocatalysis together with the integrated support of the other already highlighted modification strategies can well be considered as parameters interwoven with structural/surface morphology regulation as a modification technique [102, 104, 107,187,122, 134, 162, 222-223]. Thus, the next section will briefly look on 0D, 1D, 2D and 3D materials as structural dimensional outcome of morphology regulation as modification approach.

1.3.5.1. Zero-Dimensional Nanoparticles (0D)

These are characteristically spherical shaped and nano-scaled dimension materials. Among pro features of large surface area, easy handling/preparation method, and functionalization, nanoparticles have been widely applied in whole lot of sectors including photocatalytic process of water purification where methods like sol-gel, hydrothermal, solvothermal, precipitation etc., have been employed for their fabrication [97]. Plethora of nanoparticle composites have been produced and employed as photocatalysts for the abatement of CECs in water (Table 4).

1.3.5.2. One-Dimensional Nanofibres/Nanorods (1D)

Typical 1D nanomaterials like nanofibers or rods have received wide study coverage thanks to their distinct aspect ratio, large surface, and ease of functionalization. Employing most frequently used fabrication techniques, namely- hydrothermal and electrospinning methods, they have been realized of various shapes as rings, wires, rods, belts etc [97]. Different fabricated 1D nanofibrous/rod-like materials have also been deployed for the abatement of CECs in water (Table 4).

1.3.5.3. Two-Dimensional Nanosheets (2D)

Great attention has been diverted to semiconductor nanosheets as typical 2D materials and applied in several areas like energy storage and environmental applications. Distinct features of large surface area and amenable structures for suit of purpose have raised its choice of application in photocatalysis. Hydrothermal method is the most widely considered fabrication technique for the synthesis of 2D nanosheet materials as photocatalysts for wastewater purification applications [97].

Other methods like photo-reduction, and solvothermal processes have also been reported in the realization of 2D nanosheet material composites [230]. For example, $\text{Bi}_{12}\text{O}_{15}\text{Cl}_{16}$ nanosheet fabricated via solvothermal method displayed a commendable photocatalytic activity over the degradation of bisphenol-A (BPA) under visible light irradiation at respective rates of 13.6 times and 8.7 times faster than the pristine base BiOCl and TiO_2 materials while maintaining a good stability and recyclability during the photocatalytic process [230]. Many other composite materials of 2D nanosheet morphology have also been fabricated and reported as photocatalysts for CEC degradation [97].

1.3.5.4. Three-Dimensional Frameworks (3D)

Majority of new generation materials have been worked and reported as 3D frameworks. Large surface area, good structure stability, high adsorptive capacity, effective mass transfer ability, large amount of active surface area credits them as one of most sought photocatalyst materials for wastewater treatment applications [231]. There are two routes of realizing 3D framework materials, namely- direct photocatalyst fabrication with 3D morphology construct referred to as type-I, and or blending a fabricated photocatalyst with a 3D material framework template referred to as type II [232].

Most used fabrication techniques for the realization of 3D composite materials are sol-gel process, in situ assembly as well as template methods. Amongst these methods, sol-gel process has been scaled-up and even commercialized for aerogel production [233]. The simplicity of sol-gel synthesis route also for the 3D frameworks materials made it attractable for the synthesis of 3D aerogel-based frameworks for photocatalytic applications. However, the limitation of some precursor metal oxide or metal chalcogenide not able to be formulated into aerogels and develops low crystallinity has led to the development of a new strategy for

aerogel synthesis. The new aerogel development strategy involves building block fabrication, preparation of the building block dispersion and solidification of the building block suspension to form a 3D monolith structure. With a re-engineered sol-gel route for the synthesis of 3D frameworks, variety of 3D aerogel based photocatalyst have been realized. For example, based on the re-engineered sol-gel synthesis route for aerogels, a 3D framework Au-TiO₂ photocatalyst as building block unit without added template has been reported [234]. Others like C₃N₄/SiO₂ composite aerogel, Fe₃O₄@TiO₂/SiO₂ core shell microspheres 3D aerogel material has equally been realized via the re-engineered sol-gel route/subsequent removal of SiO₂ from composite with 4 M NH₄HF₂ and combined re-engineered sol-gel route with hydrothermal method respectively: showing remarkable efficiency as photocatalysts over the degradation organic pollutants [97].

1.3.6. Nanomaterial Hybrids

The modification of semiconductor-based materials with strategies like semiconductor metal oxide couplings, morphology regulations and then blending the composite outcome with carbon materials like CNTs, Fullerenes (C₆₀), graphene, POMs and zeolites has birthed advanced set of material composites referred to as nanomaterial hybrids (Figure 5). These carbon-based nanomaterial hybrid composites leverage sole TiO₂/other semiconductor based photocatalysis limitations by various enhancement effects upon their application as modifiers in composite materials. Increase visible light absorption, increase in surface area, charge recombination suppression, pollutant dependent synergy effect, improved dispersion, enhanced water solubility of composite via surface complexation with free hydroxyl (OH) functional group, electron charge (e⁻) scavenging and subsequent increase of hydroxyl (HO·) radical generation, electron mobility rate increase etc., are the various modifier advantage effects obtained of the introduction of these carbon materials in their nanomaterial hybrid composite structures [107]. Based on this, several carbon materials modified TiO₂/other semiconductor-based hybrid composites have been reported of their efficient photocatalytic activity performance for the degradation of organic pollutants (CECs inclusive) in comparison to their bare (unmodified) base materials (Table 4) [107].

Part of the highlights made from the previous section focused on continued research studies made towards addressing the limiting factors for sole TiO₂/other semiconductor-based photocatalysts applicability for CECs/organic compound pollutants with the aim of

achieving robust high performing photocatalyst materials yet less energy intensive and more environmentally friendly. However, other challenges remain in that, semiconductor based heterogeneous AOPs treatment of contaminated water still operate on two main configurations; that is: the catalyst can either be in suspension (slurry design) or anchored on a support (immobilized design).

The next section will take a general look on the catalyst anchored on a support (CAS) configuration or the immobilized design with focus on why suspension or slurry design became a challenge and how investigations channelled towards CAS configuration continue to advance, the different types of support materials already investigated as well as various techniques employed for anchoring active photocatalyst material on support.

1.4. Core Configuration of TiO₂/Semiconductor Based Photocatalyst Reaction System

Two key configurations underpin TiO₂/semiconductor based light irradiation photocatalysis reaction system. Namely, the slurry or suspension reaction system, a case where the photocatalyst material is added and mixed with the pollutant in aqueous suspension media and the held on a supporting material or immobilized design, another case where the active photocatalyst material is anchored on a supporting material during the reaction process [50]. Majority of studied photocatalysis reaction system till date runs on the slurry system. However, the recovery and reuse of such nanoparticles from large volume effluents of industrial scale is challenging. Apart from this, little or no knowledge of the human and ecotoxicological effects at least in the short term of spent TiO₂, ZnO, and several other semiconductors nanoparticles after their application in the photocatalytic degradation of CECs may be a potential source of risk concern as their unregulated accompanied treated effluent matrix discharges accumulate in the aquatic environment [235]. As such, techniques capable of anchoring active photocatalyst materials and make it possible for their recovery and reused in photochemical processes for CECs removal from water offers a huge possibility in overcoming this challenge and upgrade the eco friendliness of photocatalysis process [235].

Table 5 gives a summarized outlook on some of the pros and cons of the slurry or suspension reaction system type and that of catalyst on support or immobilized system type.

Table 5. Some pros and cons of slurry (suspension) reaction type system and catalyst on support (immobilized) type [235].

Slurry or suspension reaction type system
Pros
Homogeneous distribution of catalyst particles in suspension
Higher ratio of illuminated photocatalytic surface area to reactor volume
Minimal catalyst fouling effect
Adequate mixing and uniform distribution of suspension particles
Less reactor system pressure drop
Facilitated mass transfer
Cons
Difficult and expensive due to post treatment filtration processes for catalyst recovery from treated downstream effluents
High loading catalyst amount can cause screening effect affecting full light penetration into reaction system and as such reduced photocatalysts degradation efficiency
Tendency of catalyst particle aggregation mostly at higher dosage
On-support or immobilized type system
Pros
Continuous operation
Enhancement of organic compound removal if immobilization substrate boasts adsorptive features
Easy catalyst separation from reaction media, possibility of reusability and recycability
Cons
Potential catalyst deactivation and washout
Limited catalyst accessibility to irradiation photons
Significant external mass transfer reduction at low flow rates of

Continuation of Table 5

of the to-be treated pollutant due to the reactant diffusion path length increase which impedes its transfer from bulk to catalyst surface
Catalyst thin film thickness increase can lead to dominating internal mass transfer that limits supported photocatalyst usage

In the accomplishment of this, a few of the non-exhaustive list of support materials like glass, activated carbon, polymers, alumina and minerals like pumice, quartz, zeolites, cellulose, plant material-based fibres, fly ash, vycor glass, optical fibres, polyethylene sheets, ceramic membranes, monoliths, glass wool, glass slides, anodized iron, Raschig rings, etc., has been employed in the construction of immobilized photocatalyst materials [235].

Wide range of techniques like dip coating, cold plasma discharge, polymer assisted hydrothermal decomposition (PAHD), radio frequency (RF) magnetron sputtering, photoetching, solvent casting, electrophoretic deposition, spray pyrolysis, sol-gel process, etc., have equally been employed as part of the immobilization protocols in the development of supported photocatalyst materials [235].

In the context of the elimination of post-treatment polishing step of treated wastewater effluents and additional operational costs saving, several studies have been performed and reported on the feasibility of using immobilized photocatalysts in the degradation of organic pollutants. Some of the examples of the commonly used material supports together with deposition techniques for the development of supported photocatalysts materials and corresponding CECs compounds they have been applied to can be seen listed in (Table 6)

Table 6. Cross section of applied immobilized support system, loading techniques of the different TiO₂-based photocatalyst in their respective dosages and against different tested CECs compound pollutants

Pollutant	Catalyst	Reaction mode	Synthesis Method	Ref.
Acetaminophen, Antipyrine, Atrazine, Caffeine, Carbamazepine, Diclofenac, Flumequine, Hydroxy biphenyl, Ibuprofen, Isoproturon, Ketorolac, Ofloxacin, Progesterone, Sulfamethoxazole, and Triclosan (100 µg/L) each	* 0.5mgTiO ₂ / Sphere	Glass-spheres & Slurry	Sol-gel	[236]
Methyl orange	87 wt. % TiO ₂	CNTs	Sol-gel	[237]
Methyl Blue, Methyl Orange, Reactive Blue 4, Sulfamethoxazole, and Microcystin -LR (10 µm each)	* TiO ₂ (1 mg/mL)	Poly (vinylidene difluoride) coated steel mesh	Dip-coating, Electro spraying and Thermal fixation	[238]
Acid Orange 95, Acid Red 18, and Direct Red 81 (0.1 mM)	* Precrystallised TiO ₂ (Aeroxide P25 & VLP 700 titania) (20 g/L)	Al ₂ O ₃ based ceramic paper	Direct spraying of titania on immobilizer agent	[239]
2,4-Dichlorophenoxyacetic acid (20 mg/L)	* C coated N doped TiO ₂ (0.21 g (±0.005))	Polyenes over glass support	Photoetching	[240]
Carbamazepine, Ibuprofen, Sulfamethoxazole (5 mg/L) each	* TiO ₂ -rGO (30 bundle) of 2.7 wt.% rGO in TiO ₂)	Optical fibres	Polymer assisted hydrothermal	[241]
Phenol (40 mg/L)	TiO ₂ nanofibre (0.5 g/L)	Chemically treated metal support	sol-gel electro-spinning	[242]

Continuation of Table 6

Fenamiphos (10 ppm)	* TiO ₂ (1mg/m ² each commercial powder: P25 Degussa and Millennium PC500	Borosilicate glass	spray coating	[243]
Acid red 14 (50 mg/L)	* TiO ₂ (0.08 g/L)	GO electrode	Electroche mical deposition	[244]
Reactive Orange 16 (60 mg/L)	^x TiO ₂ : ZnO	Spacer fabrics	Cold plasma discharge	[245]
Reactive Red 4 (30 mg/L)	* TiO ₂ - Polyaniline Nanocomposite Using ENR, PVC as adhesive	Glass plate	Dip-coating	[246]
1,2-Dichlorobenzene (100 ppm)	TiO ₂ /SnO ₂ /WO ₃ (0.1 g)	PVC, Chitosan	Chemical methods	[247]
Phenol (60 mg/L)	* TiO ₂ (20 mg/L anatase TiO ₂ content of composite film)	Cellulose	Sol-gel process	[248]
Amoxicillin (2000 mg/L COD)	* TiO ₂ (0.279 g)	Quartz tubes	Dip-coating	[249]
Methylene Blue (17.6 μM)	* TiO ₂ /ZnO (15 wt. %)	Poly (vinylidene difluoride) - co-trifluoro ethylene	Solvent casting	[250]
Orange G (10 ⁻⁵ M)	* TiO ₂ (0.8 g/dm ³)	Na ⁺ - Beidellite	Chemical methods	[251]
* Powder material is of commercial content either in part or whole, ^x other material component making up the composite				

Amongst the listed components in Table 6 for the realization of immobilized TiO₂ photocatalysts, various support materials and the means of anchoring the active TiO₂ topcoat have been explored. However, much attention has been focused lately on simple support materials and non-complex deposition techniques for accomplishing immobilized semiconductor photocatalyst materials. In the light of this ceramic as a support material and

dip coating as a deposition technique has received huge attention and therefore intensely studied.

1.4.1. Ceramics

Ceramic materials became important and widely used in a variety of applications. More so, as membrane separation technologies attract more interest in issues of environmental regulations and need for more eco-friendly water depuration systems, demand for membranes continue to surge [252]. Waste disposal costs, material recovery and reuse in the 21st century circular economy has seen membrane application in a whole range of sectors gain momentum for economic reasons [253]. Their suitability for filtration application purposes made them deployed either in micro-filtration, ultra-filtration, or nano-filtration especially for water purification [254]. Notwithstanding, they have also been applied for component separations, and even as support for anchoring photoactive materials employed in heterogeneous photocatalytic process of organic compound removal [255-256].

Ceramic membranes despite the complexity involved in polymer membranes fabrication are more expensive due to the precursor materials for their development. However, distinct features of long-term stability, high mechanical strength, chemical resistance, and thermal stability etc., is a trade-off in terms of cost for their wider application [257].

1.4.1.1. Types of Ceramic Membranes

Categorically, ceramic membranes based on their structure can be either porous or dense membranes.

1.4.1.1.1. Porous Ceramic Membranes

The pore size of membranes is the main factor used primarily to determine which use a membrane can be subjected to. Porous membranes are primarily characterized based on pore size, surface porosity and thickness.

Basically, porous membranes are used in solid-liquid and or solid-gas phase separations.

Structurally, ceramic membranes can be symmetric or asymmetric. While majority of

the pores are equally distributed by size across the ceramic structure in symmetric orientation, the pore size progressively reduces towards the edge of ceramic surface where the separation usually takes place in asymmetric ceramic membranes. Separation mechanism in porous ceramics has been attributed to molecular sieving [258].

1.4.1.1.2. Dense Ceramic Membranes

This category of ceramic membranes exhibits complex permeation mechanism and separation protocol. Normally applied for gas separation, for instance, the transportation of oxygen in ZrO_2 at elevated temperatures. In their difference from the porous ceramic membranes, the separation technique is such that occurs through a solution-diffusion mechanism whereby the permeating molecules dissolve firstly into the membrane matrix, diffuse and desorbs finally out of the membrane [258].

Depicted in Table 7 is the different types of ceramic membranes and their applications based on pore size range.

Table 7. Types of ceramic membrane, their pore size and application

Type	Pore size (nm)	Application
Macro-porous	> 50	Ultra-filtration, Micro filtration
Meso-porous	2-50	Ultra-filtration, Micro filtration, Gas separation
Micro-porous	< 2	Gas separation
Dense	-	Gas separation, support for other reactions

1.4.1.2. Geometrical Configuration of Ceramic Membranes

Ceramic membranes have been fabricated and developed in various shapes, namely: disks or tablets, plate and frame, tubular/straw, hollow fibre, and capillary membranes etc., [259]. The designed geometric configuration outcome of the final products depends on the use of application particularly in wastewater treatment and the associated treatment process based on the porous structure; for example, drain flow, nano-filtration, reverse osmosis

(RO), etc., [259-260]. Shown in Figure 10 are the different geometrical shape configurations of ceramic membranes.

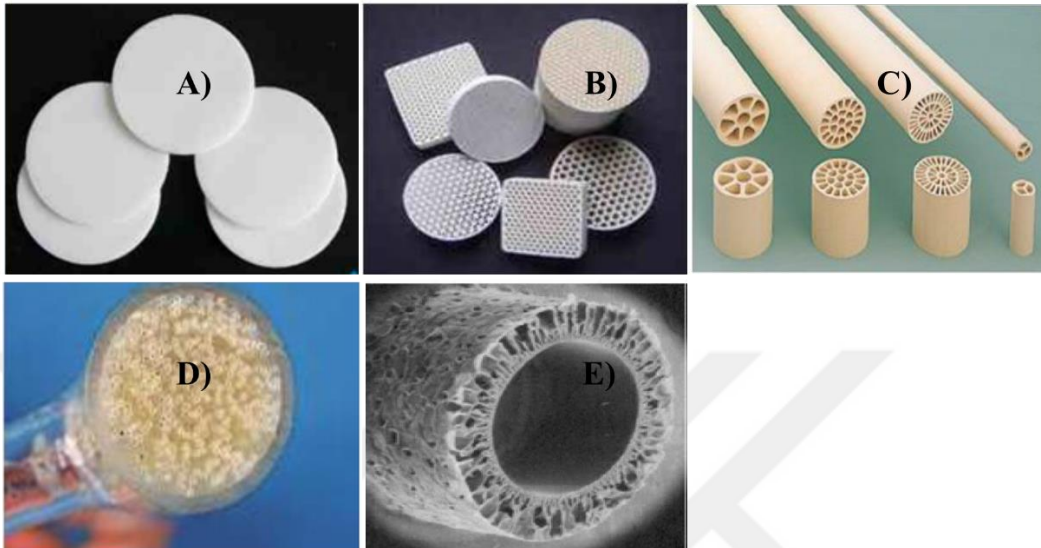


Figure 10. Different geometric configurations of ceramic membrane: a) Disk or tablet shaped, b) Plate and frame shaped, c) Tubular or straw shaped , d) Hollow shaped fibre, and e) Capillary shaped membranes [261]

1.4.1.3. Development and Fabrication of Ceramic Membranes

Various methods have been employed for the development and fabrication of ceramic membranes, namely, extrusion, slip casting, tape casting, pressing, solid state method, sol-gel method, dip coating method, anodic oxidation method, free-casting method, and chemical vapour disposition, etc., [260]. In summary, to manufacture ceramic membranes, mixing of the starting powders with appropriate binding liquid in what is the suspension preparation, shaping of the prepared suspension based on pre-set conditions in what is referred to as the forming stage, and binding of the membrane particles at elevated temperatures in what is the heat treatment stage are the series of protocol steps involved [261].

Displayed in Figure 11 are some of the primary steps involved in the fabrication and development of ceramic membranes. The fabrication protocols: 1a (powder formation), and 1b (slurry or paste) is administered to the fabrication techniques of extrusion, slip casting, tape casting and pressing for the precursor formation (1c) (Figure 11). Following this, is the sintering protocol which is the most important step of all the fabrication protocols in ceramic membrane development. A route not preferred of protocols 1a, 1b, and 1c can proceed via sol-gel process (2) (Figure 11) to arrive at the final ceramic membrane product for support and other applications.

Dip coating technique can be employed to coat the ceramic membrane support with powder or particle suspension or in sol formulation and then sintered to arrive at desired surface coat layer depending on preference of thickness and application (Figure 11). Otherwise, employing chemical vapour deposition (CVD) or electro vapour deposition (EVD), etc., materials like multi-layers membrane can be achieved before the sintering step to achieve required on surface coat layer product (Figure 11).

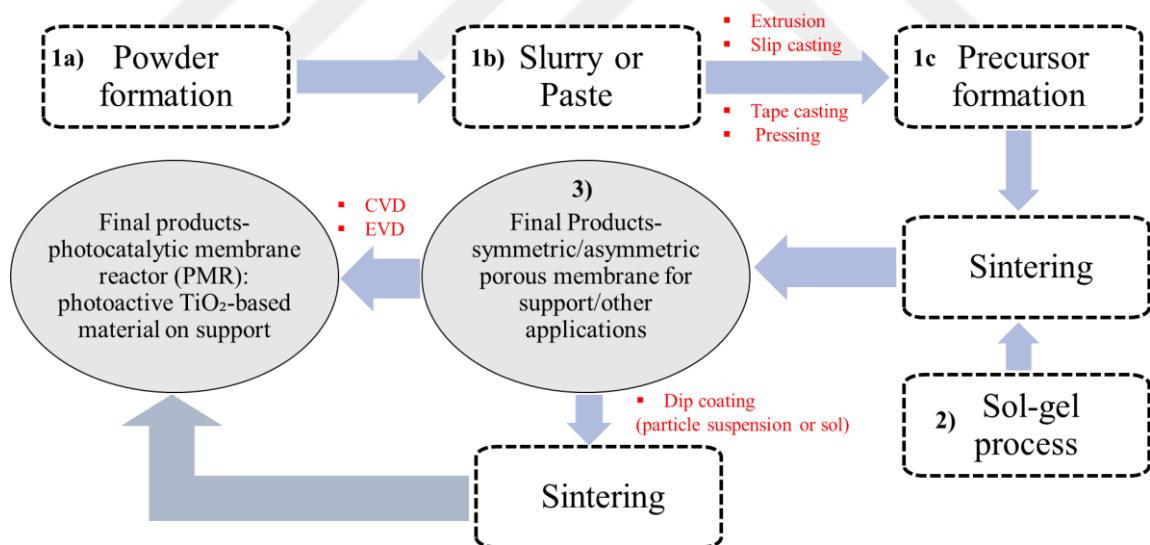


Figure 11. Basic protocol steps involved in ceramic membrane fabrication and development [261]

1.4.1.4. Commonly Used Immobilized Technique

Immobilization technique for photocatalyst materials on support, play vital role to the extent that they control the photocatalytic activity of the photocatalyst [235, 261]. Choice of support for photocatalyst gives preference to the type of catalyst and the organic pollutant to be degraded [235, 261]. Applied technique for the anchoring of the photoactive material on the support must be one that ensures minimal interference with the activity of the photocatalyst. In line with this, several methods have been reported to the achieve the target of developing a supported photocatalyst material with high performance efficiency for the degradation of organic pollutants. Sol-gel accompanied dip coating method, chemical vapour disposition (CVD) and its subsidiaries like atmospheric pressure chemical vapour deposition (APCVD), plasma enhanced chemical vapour deposition (PECVD), metal-organic chemical vapour deposition (MOCVD), as well as hybrid physical chemical vapour deposition (HPCVD) and several others previously mentioned have been used [262-266]. Factors like elevated thermal treatment by calcination, intricate and complex operational conditions, as well as sophisticated instrumentation have made majority of these techniques not so widely applicable [235]. Choice selection of deposition technique of low temperature criterion requisite has placed sol-gel and sputtering techniques as the best options because they can be executed at lower operating temperature conditions [235].

However, sol-gel based immobilization technique advances amorphous TiO₂ phase formation during sol-gel synthesis [235]. Therefore, to ensure recovery and smooth phase transition to anatase phase whose role is fundamental for enabled photo-generated charge (e⁻/h⁺) separation, there is the need for elevated temperature thermal treatment after sol-gel deposition of TiO₂ layer on support. Hence, a support material of high thermal resistivity is cherished despite the easy workability of some versatile deposition techniques like sol-gel, dip coating methods when compared to the other deposition techniques.

1.4.1.4.1. Sol-gel and Dip Coating as Versatile Applied Immobilization Technique

Sol-gel is an important, yet simple technique used in the development and fabrication of ceramic membranes where for example metal oxide on support are fabricated from the corresponding chemical solution as the precursor containing the targeted metal ion [235,

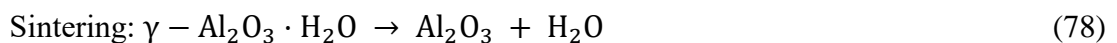
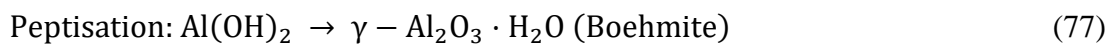
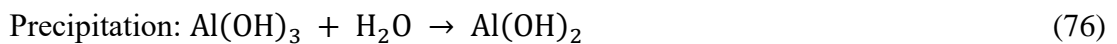
261]. These chemical precursors play vital role as they control pore size, pore size distribution and the morphology of the deposited photocatalyst material [235, 261].

Basically, the sol-gel fabrication technique comprises of two main routes: namely the colloidal route and the polymer route [261].

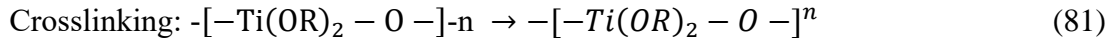
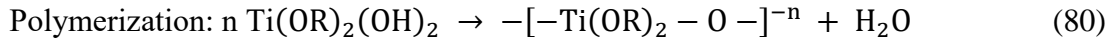
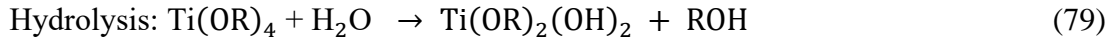
The colloidal route involves the dissolution by hydrolysis of the metal alkoxides and metal chlorides as the precursor materials in alcohol with addition of excess acid or water [235, 261]. During this time, a stable colloidal solution of dense oxide particle is formed by staying the resultant precipitate over a certain time as a hot solution. While the temperature of the formed colloidal solution is lowered, a variety of reaction processes like hydrolysis and condensation take place leading to the interconnectivity of metal centres (M) with oxo (-O) species in O-M or metal (M) – hydroxy (-OH) linkage networks [235].

Drying process to remove excess hang on solvents is completed with possible effect of volume shrinkage and densification of photocatalyst film. Resulted metal oxide coat layer on support is then thermally treated between temperature range of 500-800 °C at which time further ploy-condensation takes place and improves the mechanical property of the film accompanied by structural stability effects of sintering, densification, and grain size growth [235, 261].

For example, the Equations (76-78) generally show the chemical reaction processes involved in the fabrication and development of γ -alumina membrane which happens to be a pioneer work and to date most investigated mesoporous membrane realized via sol-gel process [261].



On the other hand, the polymer route proceeds with the metal alkoxide precursors incompletely hydrolyzed upon the addition of small amount of water. Formation of the inorganic polymer molecule then deposited on the membrane support surface [235, 261]. Post drying thermal treatment is then performed by sintering for the development of metal oxide film. For example, (Equations 79-81) show the involved chemical reaction processes for the formation of a typical TiO_2 film on membrane support [261].



Dip coating technique is usually accomplished with sol-gel method and can also be singly deployed for membrane surface coatings. Dip coating is executed with the help of a dip coating apparatus fitted to an adjustable motor used to control the pull rate of the material when immersed into a sol and retrieved at a pre-set speed [235]. Dip coating can be employed for the realization of either a thin film or thick film layer [262]. By calculated immersion and withdrawal rate, dip coating can be manually executed, however, with compromised uniform distribution of nanoparticle on substrate especially at high wt. % powder suspension concentrations. Depicted in Figure 12 and Figure 13 is the schematic illustration of sol-gel fabrication and development of membranes involving the colloidal route and the polymeric route and dip coating of a photocatalyst material in suspension on a typical membrane support (e.g., ceramic) respectively.

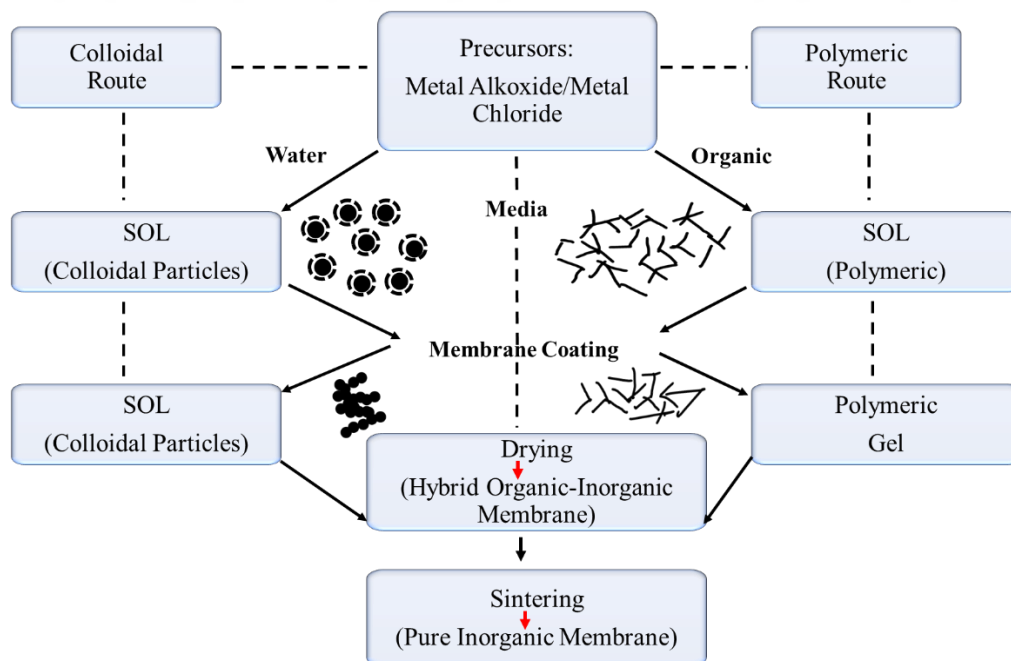


Figure 12. Schematic illustration of sol-gel method for the fabrication and development of ceramic membrane [261]

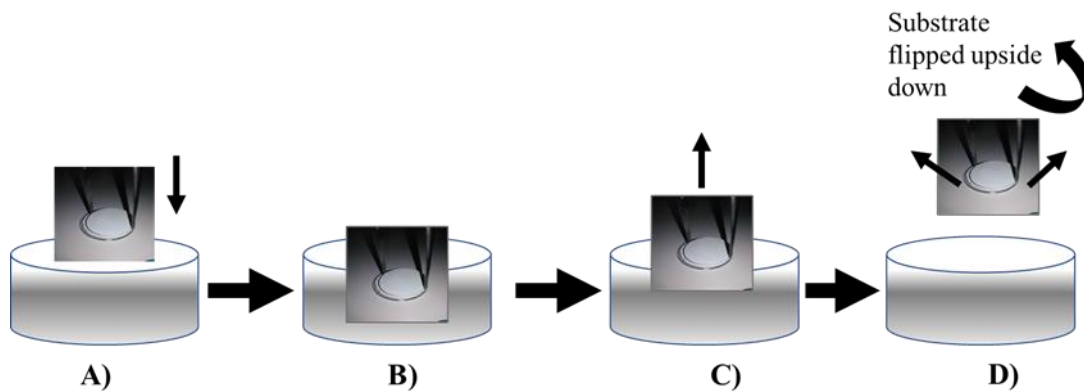


Figure 13. Illustration of a manually controlled dip coating of a typical photocatalyst material on α - Al_2O_3 ceramic substrate

The stages of the process involved in Figure 13 can be explained thus: a) Support is being lowered to be immersed into a prepared suspension containing photocatalyst material, b) The support is completely immersed, c) Just about the elapse of a pre-set time of immersion (few seconds), support is withdrawn out of suspension, and d) Support is flipped upside down to allow deposition of active photocatalyst material on top while unwanted contents like water, water moisture is drained off the support surface by gravity.

1.4.1.4.2. Characterization of Membranes Support

Following a successful immobilization of TiO_2 active surface layer membrane supports, the fabricated composite structure needs to be controlled for structural morphological features before and after photocatalytic test deployment. This is vital as the performance of immobilized membrane support materials rely to a large extent on their structural morphology which accounts for physical properties like pores size and its distribution, shape, density, particle packing as well as membrane surface used for the assessment and evaluation of membrane quality for its designated performance in either photocatalysis or component separation [261].

Variety of morphology test related techniques for worked membrane characterization have been used; namely, scanning electron microscope (SEM) for surface morphology, the associated energy dispersive x-ray spectroscopy (EDS) for elemental composition determination. Others are transmission electron microscope (TEM) for the determination of crystal/particle size structure of the sample, x-ray diffraction (XRD) analysis for the

crystallographic phase properties of sample structure and x-ray photoelectron spectroscopy (XPS) for the determination of sample structure chemical environment composition. Information pertaining the permeability of fabricated membrane relies on its pore size which is a key parameter for the assessment of stream to be separated [261]. Permporometry and Gas absorption/desorption are two main techniques amongst other ones employed for the membrane permeability tests.

For the case of practical applicability of immobilized TiO_2 -based photocatalyst material on support for the photocatalytic degradation of contaminants of emerging concerns, various support active surface TiO_2 materials immobilized with sol-gel and or dip coating including other immobilization techniques have been employed for the degradation of CEC compounds, while demonstrating enhanced photocatalytic activity performance (Table 6).

In other classic examples for validation of these techniques, TiO_2 was immobilized onto glass plates in a rotating disc reactor (RDR) employing a reported sol-gel method and deployed in the study of the degradation of antipyrine [267]. In a related development, immobilized goethite ($\alpha\text{-FeOOH}$) particles in glass tube via dip coating technique have been reported with the as prepared photocatalyst completely able to mineralize organic pollutants like nicotine, ranitidine etc. [268].

Building on the fabrication and development of $\alpha\text{-Al}_2\text{O}_3$ ceramic support, modification strategy of metal oxide semiconductor coupling; this thesis contributed to the study of W and or Mo modified TiO_2 referred to as HRTiO_2 henceforth and its sol-gel synthesized counterpart referred to as SynTiO_2 henceforth for the photocatalytic degradation of ibuprofen (IBF), caffeine (CAF), and carbamazepine (CBZ) as the target CECs compounds. While the photocatalytic process reaction involving the two different modified photocatalyst materials (i.e., HRTiO_2 and SynTiO_2) proceeded in suspension mode, the W modified version of HRTiO_2 (W/ HRTiO_2) was employed as on the support photocatalyst material for the photocatalytic degradation evaluation tests of the immobilized photocatalyst towards the target CECs compounds.

Therefore, the upcoming sections of this thesis will be divided according to the scheme below in Figure 14 and focused.

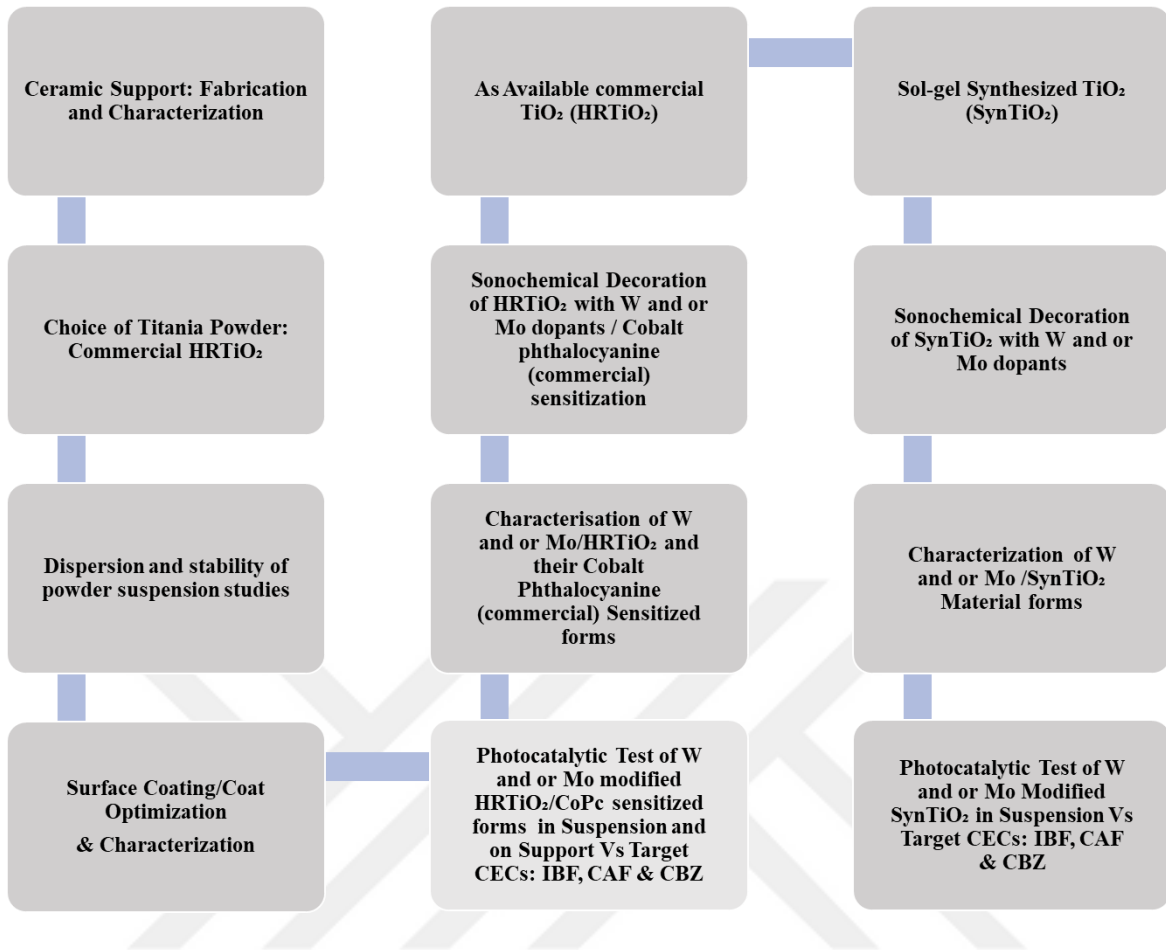


Figure 14. Schematic of thesis work outline

2. MATERIALS AND METHODS

2.1. Chemical Reagents

All the reagents, chemicals and materials used in this study were of analytical grade and used as purchased without further purification or treatment except for the α -Al₂O₃ ceramic substrate that was processed, fabricated, and developed at Materials Industrial Research and Technology Centre (MIRTEC) SA, Chalkida, Greece and with the industry protocol which involved some drying, and thermal treatment by sintering before the final product was obtained.

Chemical reagent materials used were α -Al₂O₃ powder (VAW Aluminium AG, Schwandorf, Germany), culminal methyl cellulose derivative MHPC 2000 P (Ashland Specialty ingredients, Switzerland), sodium stearate ($\geq 99\%$, Sigma Aldrich), ammonium polymethacrylate (Darvan C) (Vanderbilt, Germany), titania (AH-R: Huntsman tioxide) (Scarlino, Italy) as the coating powder. Other used chemicals are titanium isopropyl oxide (TiP) [Ti(O₄C₁₂H₂₈)] (97 %), ammonium metatungstate [(NH₄)₆H₂W₁₂O₄₀.xH₂O] (≥ 66.5 % W), ammonium molybdate tetrahydrate [(NH₄)₆Mo₇O₂₄.4H₂O] (99.98 %) respectively employed as metal source precursors for Ti, W and Mo. Cobalt (II) phthalocyanine [C₃₂H₁₆CoN₈] (dye content 97 %) was used for catalyst dye sensitization). Ethanol (C₂H₅OH, 99.5 %), nitric acid (HNO₃, 70 %) were used as solvent for sol-gel synthesized titania (SynTiO₂), and ibuprofen sodium salt (α -Methyl-4-(isobutyl) phenyl acetic acid) [C₁₃H₁₇O₂Na] (≥ 98 %), caffeine (1,3,7-Trimethylxanthine) [C₈H₁₀N₄O₂] (99 %), and carbamazepine (5H-Dibenz[b,f]azepine-5-carboxamide) [C₁₅H₁₂N₂O] (> 99 %) were investigated as the model CECs for photocatalytic degradation. Sodium hydroxide [NaOH] (≥ 98 %), hydrochloric acid [HCl] (37 % wt./v) were employed for aqueous media pH controls. p-benzoquinone- BQ (2,5-Dimethyl-1,4-benzoquinone) [C₆H₄O₂] (≥ 98 %), isopropyl alcohol-IPA [(CH₃)₂CHOH] (≥ 99 %), ammonium oxalate (AO) monohydrate [(NH₄)₂C₂O₄.H₂O] (≥ 99 %) were used as chemicals for reactive oxygen (ROS) probe. Sodium chloride [NaCl], sodium sulphate [Na₂SO₄], sodium carbonate [Na₂CO₃], sodium hydrogen carbonate [NaHCO₃], sodium hydrogen phosphate [NaHPO₄], and ammonium chloride [NH₄Cl], iron (iii) chloride [FeCl₃], magnesium chloride [MgCl₂], aluminium chloride [AlCl₃], calcium chloride [CaCl₂] (all inorganic salts ≥ 99 % purity) as well as

hydrogen peroxide [H_2O_2] (30 wt./v) and sodium humic acid salt ($\geq 99\%$) were employed for their investigative influences on the photocatalytic tests.

Except for the fabrication of the ceramic support where distilled water was used, milli-Q water was employed throughout the entire photocatalytic studies.

2.2. Methods and Instrumentation

2.2.1. Chemical Reagents

The disk/tablet shaped $\alpha\text{-Al}_2\text{O}_3$ ceramic membrane was fabricated via extrusion method with INSTON L 1477 -1003 extrusion device from the coarse particle size substrate. α -alumina coarse particle size determination was carried out through granulometric analysis of large particle (coarse) with D90 value of $14.1\mu\text{m}$ while with same granulometric approach, particle size distribution (PSD) of worked powder topcoat suspensions was obtained with Laser Diffraction Particle Size Analyzer MASTER Sizer 3000G by Malvern Instruments, United Kingdom. The porosity and density properties of the alumina substrate were determined using Archimedes method while the mechanical strength evaluation through change in flexion resistance of 4-point bending test of the coarse α alumina ($\alpha\text{-Al}_2\text{O}_3$) as a function of the sintering temperature was measured with the INSTON L 1477 - 1003 and final sintering temperature of $1500\text{ }^\circ\text{C}$ adopted. XRD measurements of material were obtained with XRD model DIFFRAKTOMETER by SIEMENS- DACO-MP of 30 mA, 40 kV, angle range of $5 - 70^\circ\text{C}$ and scan speed of $3^\circ\text{C}/\text{min}$.

Surface morphological analysis of HRTiO_2 topcoats on the ceramic substrate has been obtained using scanning electron microscopy measurement by (SEM JEOL JSM 6300) with discrete capacity of 3.5 nm and Polaron SC515 SEM coating system used to drop films of gold or carbon through sputtering to improve the conductivity of the samples before measurement. Cross sectional thickness of deposited active layer HRTiO_2 topcoat for preliminary test purpose prior to the suspension working and deposition of the final choice decorated HRTiO_2 (either W and Mo) based on slurry or suspension mode photocatalytic reaction process was obtained by scanning electron microscopy-energy dispersive x-ray spectroscopy (SEM-EDS) technique measuring part of SEM JEOL JSM 6300 scanning microscope device.

2.2.2. Titania Powder Materials

Two different titania powder forms were employed; namely a technical grade commercially available titania manufactured by Huntsman and sold under the trademark name Huntsman tioxide- HRTiO_2 . The other form is sol-gel synthesized TiO_2 (SynTiO_2). These two titania powder forms were then by sonochemical method decorated with W and or Mo as dopant generating either singly doped or co-doped series for each of these two powder forms with/without cobalt phthalocyanine compound incorporated as a sensitizer with best performing materials deployed for further photocatalytic tests following preliminary investigations.

2.2.2.1. Anatase Commercial TiO_2 (HRTiO_2)

The commercial TiO_2 powder employed in this study is a high performance anatase pigment manufactured by Huntsman Tioxide (Scarlino, Italy) [269]. Hence, the name HRTitania (HRTiO_2) as the grade name given to the powder by the manufacture was used as a means of referencing it in this thesis. The anatase form exhibits outstanding optical properties with ease of dispersion in aqueous media as well as high purity level as reported the manufacturer [269]. In addition, other properties like low toxicity, controlled chalking, high temperature stability have equally been reported for the material and therefore, made it applicable in a wide range of products from paper to ceramics [269].

In this view, this material amongst other commercial titania was preferred for the delivery of the active topcoat on the ceramic support. As can be seen from Table 8, and Figure 15, both of its anatase and rutile phases, have moderate Moh's hardness which make them less abrasive with greater UV reflectance an indication of their high refractive index values (Table 8, Figure 15) [269].

Table 8. Refractive index (RI) and Moh's hardness properties of two different pigment forms of Huntsman tioxide [269].

Pigment	Refractive Index (RI)	Moh's Hardness
TiO_2 Anatase	2.55	5.50
TiO_2 Rutile	2.70	6.50

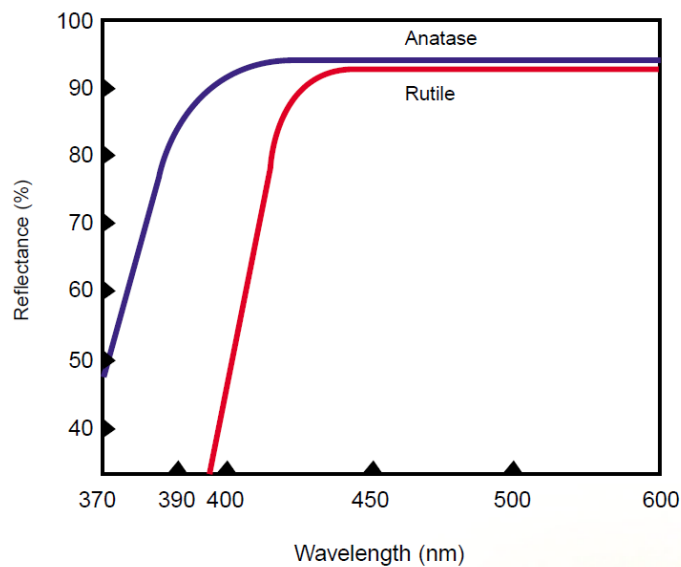


Figure 15. Optical property of the anatase and rutile phases of Huntsman tioxide (HRTiO_2) pigment [269]

2.2.2.2. Sol-gel Synthesized TiO_2 (SynTiO_2)

The sol-gel method of synthesis for the preparation of the second form of titania powder material employed in this thesis and referred to as (SynTiO_2) followed the protocol as reported in a previous work for pristine titania preparation [122, 134, 222].

Briefly, Figure 16 show the stepwise protocol approach involved in the preparation of the pristine titania powder (SynTiO_2).

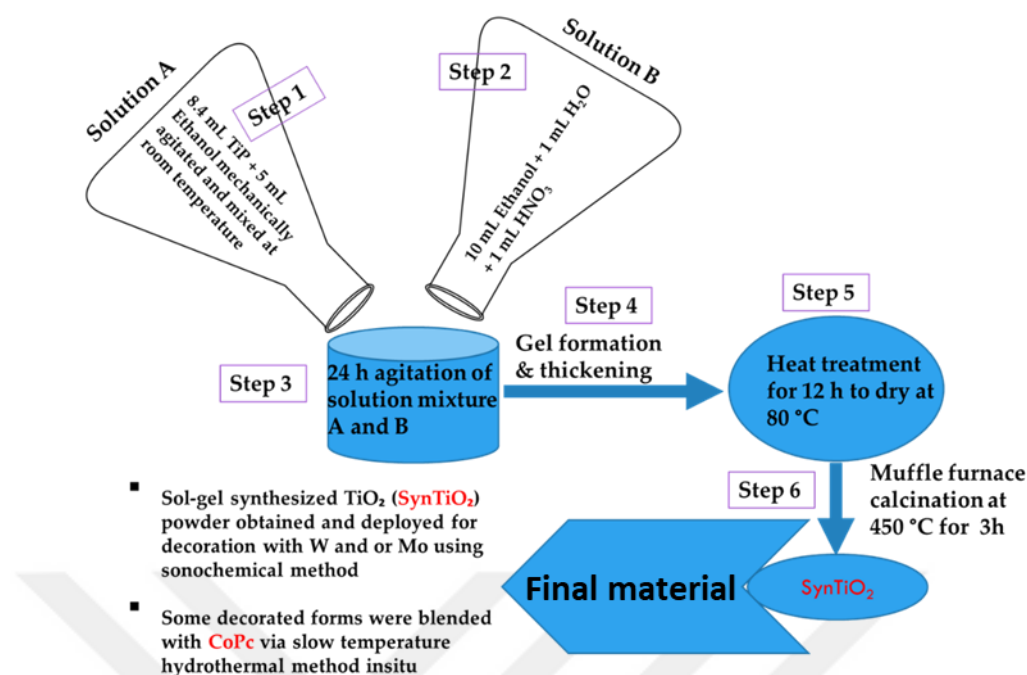


Figure 16. Stepwise approach for sol-gel preparation of titania (SynTiO₂)

The commercially available technical grade HRTiO₂ and obtained sol-gel TiO₂ (SynTiO₂), were then by sonochemical method decorated with W and or Mo dopants from their chemical precursors.

2.2.2.3. Sonochemical Decoration of HRTiO₂ and SynTiO₂

The decoration of HRTiO₂ with W and or Mo dopants was achieved by sonochemical procedures. More specifically two different precursors: ammonium metatungstate [(NH₄)₆H₂W₁₂O₄₀.xH₂O], and ammonium molybdate tetrahydrate [(NH₄)₆Mo₇O₂₄.4H₂O] as precursor sources of W and Mo.

These precursors were diluted in aqueous solutions of 200 mg of the pristine titania powder (HRTiO₂) calculating each 2 wt. % W, 2 wt. % Mo for singly doped forms and 1 wt. % W and 1 wt. % Mo in the co-doped form of the HRTiO₂ in final solution before sonication. Sonication was performed by a UIP 500hd transducer (Heilscher) as the ultrasound generator.

Performed sonication used a continuous U/S generation of 100 W/cm² lasting 3h. After the sonochemical experiments the solutions were centrifuged and the substrates were

collected, left overnight at 80 °C to dry. The following sample series: 2 wt. % W/HRTiO₂, 2 wt. % Mo/HRTiO₂, and 1 wt. % W-1 wt. % Mo/HRTiO₂ were obtained as the modified HRTiO₂ powder materials to be evaluated for photocatalytic activity.

Thus, and henceforth the decorated materials from the HRTiO₂ sample series will be referred to as: HRTiO₂ for HRTiO₂, W/HRTiO₂ for 2 wt. % W/HRTiO₂, Mo/HRTiO₂ for 2 wt. % Mo/HRTiO₂ and W-Mo/HRTiO₂ for 1 wt. % W- 1 wt. % Mo/HRTiO₂.

In the same vein, the same sonochemical procedure as already outlined for the preparation of HRTiO₂ series was also extended to the sol-gel obtained titania (SynTiO₂). In outcome, the following series were obtained as the modified SynTiO₂ sample series: 2 wt. % W/SynTiO₂, 2 wt. % Mo/SynTiO₂ and 1 wt. % W-1 wt. % Mo/SynTiO₂ for photocatalytic test evaluation.

These material samples henceforth and in the rest part of the thesis will now be referred to as SynTiO₂ for sol-gel synthesized TiO₂, W/SynTiO₂ for 2 wt. % W/SynTiO₂, Mo/SynTiO₂ for 2 wt. % Mo/SynTiO₂ and W-Mo/SynTiO₂ for 1 wt. % W- 1 wt. % Mo/SynTiO₂.

After Preliminary photocatalytic test evaluation of both TiO₂ forms in slurry or suspension mode; best performing photocatalyst of the series was employed for further photocatalytic test evaluations.

Sensitization of the best performing HRTiO₂ photocatalyst series following preliminary test was performed via low temperature insitu hydrothermal method with a commercial cobalt (ii) phthalocyanine dye.

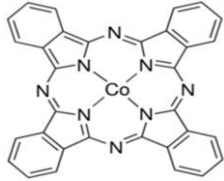
The best performing SynTiO₂ photocatalysts series samples after preliminary tests were not considered for the immobilized reaction type mode nor for sensitization for the reason of employing a more suitable technical grade titania and that is HRTiO₂.

2.2.2.4. Sensitization: Cobalt (II) Phthalocyanine (CoPc)

Sensitization of the materials was only carried out on the best performing photocatalysts samples of the HRTiO₂ series for reason already stated. The employed CoPc dye is a commercial type and incorporated on the modified HRTiO₂ via low temperature insitu hydrothermal method in order to prevent the decomposition of the Pc molecular materials known for not surviving high temperatures.

Below in Table 9, are the physicochemical properties of CoPc.

Table 9. Chemical profile of cobalt (ii) phthalocyanine (CoPc)

Chemical Property/Name	Cobalt (ii) phthalocyanine (CoPc)
Chemical Structure	
Molecular formula	$C_{32}H_{16}CoN_8$
CAS	3317-67-7
Molecular weight	571.46 g/mol
Application	Used as a hole injection layer (HIL) in organic dye sensitizer solar cells

2.2.5. Material Characterization

Following the choice of technical grade $HRTiO_2$ and the synthesis of $SynTiO_2$, their decoration with either W and or Mo, and sensitization of the $HRTiO_2$ powder material sample series, the following techniques were adopted for photocatalysts material characterization: simultaneous thermal analysis (STA) technique involving thermal gravimetric analysis-differential scanning calorimetry (TGA-DSC) was performed on the decorated samples to elucidate the extent of mass change of samples in connection with their enthalpy of heat change under ambient measurement conditions. X-ray diffraction (XRD) measurement was carried out using a Rigaku D/Max-IIIc diffractometer (RIGAKU, Corp., Tokyo, Japan) with operational functions of $CuK\alpha$ radiation ($\lambda = 0.1541 \text{ nm}$) over the range $2\theta = 20-70^\circ$ at ambient temperature and 35 kV at 25 mA at the rate of $3^\circ/\text{min}$ scan speed for the crystallographic phase analysis of the materials [122, 134, 162, 222-223]. Fourier transform infrared (FTIR) spectroscopy measurement was carried out with a Perkin-Elmer Spectrum one FT-IR spectrometer (Thermo-Fischer Scientific, Leicestershire, UK) employing the attenuated total reflection (ATR) method to understand the chemical functional groups present in the synthesized photocatalyst materials. Transmission electron microscopy (TEM) measurement was performed with FEITecnaIG2 Spirit (FEI, Hillsboro, OR, USA) for the particle size analysis of material samples while scanning electron microscopy (SEM) measurement for the surface morphological analysis was done with Zeiss

EVO LS10 (Carl Zeiss Microscopy, Hamburg, Germany), of 0.2-30 kV acceleration voltage and 0.5 pA-5 μ A probe current, attached with energy dispersive x-ray spectroscopy (EDS) detector (Carl Zeiss SmartEDX, Hamburg, Germany), with samples attached to sample holder and prepared with Au using sputter-coating (SEM coating System Machine). The surface area of materials and other related parameters of particle size distribution was measured by the Brunauer-Emmett-Teller (BET) technique recorded on the nitrogen adsorption-desorption isotherm at 76 K employing a Micromeritics 3 Flex version 5.00 (Micromeritics, Norcross, GA, USA) after degassing while the particle size distribution (PSD) was obtained by Barret Joyner Halenda (BJH) application method [122, 134, 162, 223]. X-ray photoelectron spectroscopy (XPS) measurement was performed with a PHI 5000 VersaProbe spectrometer (ULVAC PHI, Inc., Kanagawa, Japan) with an AlK α radiation source for the elucidation of the elemental compositions within chemical environment of the synthesized materials [122, 134, 162, 223]. The optical properties of the synthesized materials were measured with UV-Vis diffuse reflectance spectroscopy (UV-Vis/DRS) in absolute measurement employing BaSO₄ as the reference plate on a Shimadzu UV-2550 (Scintek Instruments LLC., Manassas, VA, USA) [134, 162].

2.2.6. Determination of pH Point of Zero Charge (pHpzc) of Catalyst Materials

In order to determine the pH point of zero charge (pHpzc) of the catalyst materials, the reported drift method was employed [162, 223]. Sequentially, 50 mL of 0.01 M NaCl solution was measured out in conical flasks. The initial pH of these solutions were adjusted and maintained at room temperature between 2 and 12 using 1 M each of either HCl or NaOH. Upon the stability of the initial pH values, 0.05 g of the catalyst powder was added to each of the measured flask solutions, stirred for 48 h and final pH value of each flask solution and for each investigated catalyst measured employing HANNA, edge pH meter (Woonsocket, RI, USA).

2.2.7. TiO₂ Photocatalytic Measurements

Photocatalytic measurement of the sample materials was performed in evaluation of their activity under 365 nm and extended visible light source of 450 nm wavelength for the best performing photocatalyst material and their CoPc sensitized forms following

preliminary runs. A homemade 200-degree internal reflector for optimal efficiency (99.9 %), UV-A and visible blue wavelength of range 300-475 nm spectral power distribution with 5 Philips Mercury (Hg) lamps-TL-K 40W/10R ACTINIC BL REFLECTOR, (Germany) was employed as irradiation light source for the photocatalytic tests of the synthesized materials [122, 134, 162, 222-223]. The irradiation light source intensity was measured with Lafayette SPM-7, (Italy) at 1.2 mW/cm², and 2.3 mW/cm² for the UV-A 365 nm and extended 450 nm cut off filter irradiation light sources respectively.

For the slurry/photocatalyst powder in suspension experiments and with the modified HRTiO₂ photocatalyst materials, sixty millilitres of working powder suspension containing 1 g/L catalyst and 50 mg/L, 100 mg/L initial concentrations of ibuprofen (IBF), and caffeine (CAF) respectively, and a one-off photocatalytic test for carbamazepine (CBZ) with 1 g/L catalyst dose at both initial concentrations of 50 mg/L and 100 mg/L; under 365 nm irradiation and at initial natural (unmodified) pH condition was executed.

An extended 450 nm irradiation light source experiment was conducted with the best performing photocatalysts under UV irradiation at 1g/L catalyst dose and 10 mg/L initial IBF and CAF concentration at initial natural (unmodified) pH condition while with carbamazepine (CBZ) under 450 nm visible light irradiation, the tested photocatalyst material amount of 1 g/L with 10 mg/L initial CBZ concentration was carried out under two other pH conditions instead of only the initial natural (unmodified) pH condition.

On the other hand, with the sol-gel synthesized photocatalysts materials (SynTiO₂) series, employing the same slurry reaction mode system, 1 g/L catalyst, 10 mg/L initial IBF concentration, and 1g/L catalyst and 5 mg/L CAF under 365 nm UV irradiation and natural (unmodified) pH condition were evaluated for photocatalytic activity.

A one-off photocatalytic evaluation of the employed photocatalysts was also performed with 10 mg/L initial CBZ concentration as per 1 g/L catalyst dose under initial natural (unmodified) pH conditions and under both 365 nm and 450 nm irradiation light sources.

In a procedure of the photocatalytic tests evaluation, the working suspension media, containing the relevant at 1 g/L dosage and the investigated initial pollutant concentration of the tested CECs were first of all introduced into a 50 mL cylindrically shaped quartz glass sleeve reactor cells and kept under mechanical agitation for 30 min to establish adsorption-desorption equilibrium state of the media prior to irradiation. Afterwards, aqueous media content is maintained under continuous mechanical agitation during light irradiation with a

30 cm distance between sample and light source maintained throughout as sample aliquots are withdrawn at pre-set time interval of irradiation. At such pre-set time intervals, about 1 mL sample aliquots each of the tested IBF, CAF and CBZ CECs compounds under their various reaction test conditions, is drawn from the reactor cells, cooled, and filtered through 0.45 μm CA filter for high performance liquid chromatography (HPLC) analysis monitoring of the photocatalytic process degradation of the CECs compounds.

Specifically, for each of the tested CECs compounds, the HPLC monitoring condition of the photocatalytic degradation process is detailed in Table 10.

Table 10. HPLC conditions for the photocatalytic degradation process monitoring of the tested CECs: Ibuprofen (IBF), caffeine (CAF), and carbamazepine (CBZ)

Column Description and producer	Phase Composition (%)	Wavelength (nm)	Flow rate (mL/min)	Runtime (min)	Monitored CEC
Kinetex 5 μm EVO C 18, column 150 mm \times 4.6 mm, Phenomenex (USA)	Acetonitrile [A]:70 and Acetic acid [B]: 30	223	0.4	15	IBF
Kinetex 5 μm EVO C 18, column 150 mm \times 4.6 mm, Phenomenex (USA)	Methanol [A]:(60) and Milli Q Water [B]: 40	272	0.4	10	CAF

Continuation of Table 10

Inertsil 5 μ m EVO C 18, column 4.6 mm \times 1.5 mm, GL Sciences Inc. (Japan)	Acetonitrile [A]:(65) and acid Milli Q Water (H ₃ PO ₄ , pH ~3) [B]: 35	285	0.8	6	CBZ
--	---	-----	-----	---	-----

The photocatalytic degradation process of the tested CECs compounds is assumed to have followed the pseudo first order reaction kinetics and was estimated as a linear regression slope expressed according to Equation (82).

$$-\ln \frac{C}{C_0} = k_{app}t \quad (82)$$

where, k_{app} , C_0 , and C are apparent degradation constant, initial pollutant concentration, and pollutant concentration after a time t , respectively. All the photocatalytic experimental data were average of triplicate measurements.

Beside the initial pH conditions of tested photocatalysts in slurry aqueous media system, a range of other pH values were investigated and the accompanied changes in pH condition during the reaction were also followed by measuring the final pH values after photocatalytic degradation test. A HANNA edge pH meter (Woonsocket, RI, USA) was used for the measurement of the initial and final pH values.

2.2.8. Immobilized Photocatalyst Material

By dip coating technique (Fig 13), ~ 0.005 g active topcoat of the best performing modified HRTiO₂ was deposited on the disk-shaped ceramic support. The dip coating process involved a two-time coating cycle of the surface to arrive at the 0.005 g active modified HRTiO₂ amount on the surface. After coating, the deposited samples were left to dry and heal naturally over 24 h under ambient conditions. Then, coated samples were subjected to 1 h heating at 60 °C in an electric oven and a further 2 h calcination at 600 °C with a ramp rate of 1°C/min in an electric furnace. Finally, samples were allowed to cool and then deployed in quartz cells containing 60 mL of initial 5 mg/L concentrations each of IBF, CAF, and CBZ for the photocatalytic test evaluation. To ascertain the photostability and reusability of the coated samples, a 3-cycle photocatalytic evaluation test was performed for each of the 3 studied CECs. To follow up on the photocatalytic degradation process monitoring of the tested CECs compounds with the coated samples, the HPLC analysis procedures already stated for the powder suspension photocatalytic tests experiments was implemented.

XRD and FTIR techniques were used to control coated ceramic support surface before and after usage.

3. RESULTS

3.1. α -Al₂O₃ Ceramic Support Development

In order to obtain high porosity and permeability, large particle or coarse grained α -Al₂O₃ substrate was chosen for the ceramic support fabrication as developed by Materials Industrial Research and Technology Centre (MIRTEC) via extrusion method with INSTON L 1477-1003 extrusion device. Combined properties of α -Al₂O₃ coarse particle size (D90, ~14 μ m) together with the 1500 °C sintering temperature, 43 % porosity and 30 mPa strength of the ceramic support material was preferred to compensate for the dispersion of particle phase size range of (1-10 μ m) of topcoat layer suspension (Tables 11-13). Shown in Table 11 is the percentage of the different ingredients present in 100 g mass of the α -Al₂O₃ substrate employed for the fabrication of the ceramic support material. Table 12 depicts the geometric characteristics of the developed disk-shaped ceramic support material based on α -Al₂O₃.

Table 11. Ingredient contents of coarse α -Al₂O₃ by % mass

Coarse grain α -Al ₂ O ₃	
Ingredients	Mass/% wt
Al ₂ O ₃	100 g
Cellulose MHPC 20000	4
Sodium stearate	2
Water	20-23

Table 12. Geometrical characteristics of disk-shaped ceramic substrate

Shape	Imposed load (kN)		Geometric characteristics (mm)	
	Coarse	Fine Grain		
Disk	7	7.5	Diameter d	Thickness W
			40	2

3.2. α -Al₂O₃ Coarse Particle Size Determination (PSD)

From Table 13, the granulometric analysis of the employed large particle (coarse) α -Al₂O₃ showed D90 value of 14.1 μ m with the rest substrate particle size distribution for d50, d10, as well as specific surface area indicated.

Table 13. Granulometric particle size distribution analysis of α -Al₂O₃ substrate

D ₉₀ (μ m)	D ₅₀ (μ m)	D ₁₀ (μ m)	Specific surface area (m ² /g)
14.1	4.7	2.6	1.38

3.3. Determination of Porosity

The porosity and density properties of the alumina substrate were determined using Archimedes method. Porosity value was 43 % at a sintering temperature of 1500 °C while density was 2.4 g/cm³. Since the increase in sintering temperature results in shrinkage of pores, a 43 % porosity achieved at 1500 °C was seen as ideal and convenient for the developed ceramic support offering the pore size and thickness for facilitated mass transfer of the net photocatalytic phase flow hence the ceramic substrate can function appropriately as support for catalyst and as a photocatalytic membrane reactor (PMR).

3.4. Process Development of α -Al₂O₃ Substrate Ceramic Support

The fabrication of the α -Al₂O₃ ceramic substrate support is such that followed these development processes, namely: the processing proceeded via mixing of mass organic and inorganic components and addition of water, plugging (paste generation), aging, extrusion, drying and roasting. As already indicated, Table 11 show the ingredient content of the coarse α -Al₂O₃ ceramic material by % mass while the Scheme in Figure 17 portrays the development process flow diagram.

On these bases, tablet/disk shaped ceramic materials produced contained 74 wt. % α -Al₂O₃ (porous) + 4 wt. % Cellulose MHPC + 2 wt.% Sodium stearate + 20 wt. % H₂O.

Specifically, for easy paste mass formulation, cellulose as a plasticizer was added while sodium stearate aided the lubrication of the paste mass with the added water aiding that process.

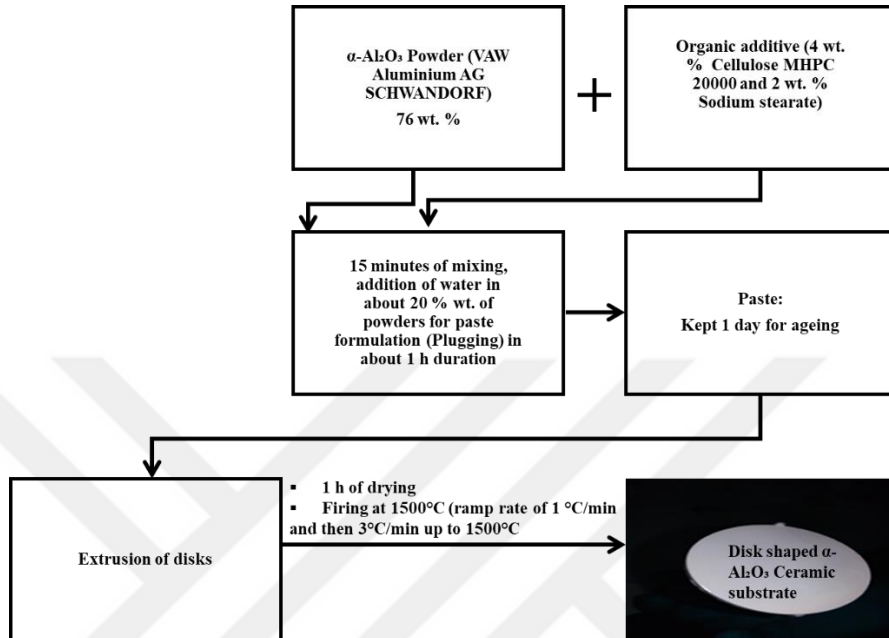


Figure 17. α - Al_2O_3 ceramic substrate development process

3.5. TiO_2 Base Powder Selection for Support Surface Coating: HRTiO_2

As already stated, the choice of commercial powder for support surface coat was based on the criteria outlined in section 2.2.2.1 with the HRTiO_2 powder having outstanding aqueous media dispersibility and therefore, a well distributed particle size. Moreover, as already stated in Table 6, various commercial TiO_2 powders have been deployed for support surface coating in immobilized photocatalytic system; nevertheless and based on the knowledge available as at the time of this work, Huntsman titania (HRTiO_2) has not been deployed for any photocatalytic process involved in the degradation of organic pollutants and in particular CECs compounds. Most common investigated and reported commercial TiO_2 powders include Degussa P25, STS01(Ishihara), Sachtleben Homikat UV100, Millenium TiONA PC50, Ishihara Sangyo A100 etc., [107].

3.6. Dispersion and Stability of Powder Suspension

Powder suspensions of HRTiO_2 and comparison with that of titania P25 (Degussa) the most common utilized titania powder for photocatalytic organic compound degradation investigations were controlled in order to ascertain the best powder choice for support surface topcoat. Comparatively, powder suspension of HRTiO_2 and P25 Degussa TiO_2 powder without any added additive were prepared, administered with the same volume in the cylindrical tube to ascertain the dispersibility of the particles in suspension as an indication of their stability. Upon macroscopic inspection, and over 24 h period maintaining the two powder suspensions, P25 Degussa TiO_2 as can be seen from Figure 18, showed a phase layer separation; an indication that over such a period, the powder particles in suspension did not remain totally distributed, separated, hence a mark of their instability for the coating.

On the contrary, HRTiO_2 particles in suspension over this period were still well dispersed with no visible separated phase. Hence, the choice of HRTiO_2 as the preferred powder suspension for surface coat in this study.

Notwithstanding, it must be pointed out that the observed outcome in the powder suspension dispersion and stability under the investigated condition of additive absence is not generic and therefore, a change in outcome is possible should there be any added additive for improved powder dispersion in aqueous media. In such a case, P25 may be a better dispersed and stable powder in suspension than HRTiO_2 under different powder in suspension and added additive concentrations.



Figure 18. Dispersion and stability control by visual inspection at 24 h of a) HRTiO_2 , and b) P25 Degussa TiO_2 powder suspensions without dispersant additive

3.7. Particle Size Distribution of HRTiO₂ Powder Suspension

In order to understand and have more insight into the particle size distribution at (D90) of the HRTiO₂ powder and ascertain the most suitable coating powder suspension conditions, further studies were performed on the effect of different ball milling time, different pH values at different Darvan C dispersant concentrations will have on the particle size distribution of a 15 wt.% HRTiO₂ powder suspension. As can be seen from Table 14, the evaluated ball milling times of 0 h, 2 h, 4 h, and 24 h at Darvan C dispersant concentration of 3.5 wt. % showed such an effect where at pH 6, pH 7, and pH 9; the D90, particle sizes and the specific surface areas remained more or less the same at 2 h, 4 h, and 24 h ball milling time.

The observed effect of D90 particle size value of 1.16 μm and its associated specific surface of 18.3 g/m^2 at 2 h ball milling time for a pH 9 (Table 14) which at 4 h displayed a further particle size increase and reduced specific surface area with subsequent reduction in value for these two parameters at 24 h ball milling might be attributed to induced surface charge phenomenon displayed at pH 9 of the powder suspension creating variations in particle size and specific surface area [270].

In general, ball milling effect at the investigated ball milling time and pH values and at the 3.5 wt. % Darvan C for a 15 wt. % powder suspension concentration can be seen as one with no significant influence with respect to 0 h at the tested powder suspension conditions (Table 14). The exceptional case of D90 of 8.507 μm at pH 6 for no ball milling in comparison to the other D90 distributions at this pH is due to surface energy effects.

Table 14. Particle size distribution dependence on milling time and pH parameters of a 15 wt. % HRTiO₂ powder suspension with 3.5 wt. % Darvan C

pH 6	Particle size distribution functions			
milling time (h)	D ₉₀ (μm)	D ₅₀ (μm)	D ₁₀ (μm)	Spec. Surface area (m ² /g)
0	8.507	0.673	0.329	9.65
2	1.885	0.675	0.312	10.2
4	1.539	0.648	0.306	10.6
24	1.165	0.667	0.377	9.89
pH 7	Particle size distribution functions			
milling time (h)	D ₉₀ (μm)	D ₅₀ (μm)	D ₁₀ (μm)	Spec. Surface area(m ² /g)
0	1.133	0.593	0.341	10.82
2	2.718	0.790	0.362	8.66
4	2.189	0.773	0.362	8.83
24	1.529	0.781	0.399	8.71
pH 9	Particle size distribution functions			
milling time (h)	D ₉₀ (μm)	D ₅₀ (μm)	D ₁₀ (μm)	Spec. Surface area(m ² /g)
0	0.987	0.362	0.107	25.1
2	1.162	0.460	0.160	18.3
4	2.463	0.561	0.247	12.50
24	1.131	0.548	0.279	12.3

Further studies on the particle size distribution with respect to the specific surface area was conducted on the 15 wt. % of the powder suspension at varying Darvan C dispersant concentration of 1 wt. %, 2 wt. % and 3.5 wt % subjected to 0 h and 24 h ball milling under unmodified pH condition. As can be seen from the Figure 19, addition of a 1 wt. % Darvan C to 15 wt. % HRTiO₂ powder suspension at 0 h ball milling resulted to a D₉₀ value of 8.005 μm and a 10.72 m²/g specific surface area in comparison to a D₉₀ value of 1.02 μm and 19.6 m²/g specific surface area for same powder condition but at 24 h milling (Figures 19 a, and b). On the contrary, at 24 h ball milling of a 15 wt. % powder suspension of 2 wt. % Darvan C content, D₉₀ value of 1.27 μm , and specific surface area of 9.14 m²/g was registered

(Figure 19c) while at same powder suspension 15 wt. % but with 3.5 wt. % Darvan C content at 24 h milling, a D90 of 0.99 μm and specific surface area of 20.6 m^2/g was registered (Figure 19d). It can be inferred from the observations made of the powder suspension particle size distribution pattern, that effects of ball milling based on pH variation with respect to a constant dispersant concentration like Darvan C is overly influential as compared to the case where the particle suspension is ball milled at different dispersant concentrations while keeping the pH at unmodified state (Table 14, Figures 19 a, b, c, and d).

Further confirmation of this observation can be collaborated with already reported scenario, where some aqueous microsuspension materials did not establish an isoelectric point (IEP) of charge with respect to its zeta potential measurement at different pH values indicating the high dispersibility of such materials in aqueous media just like the case of HRTiO_2 [271].

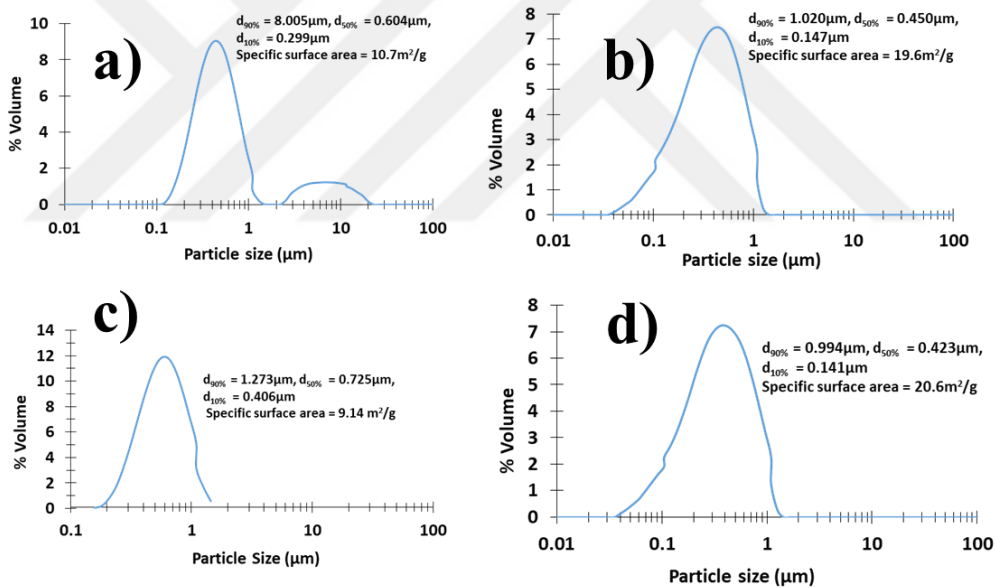


Figure 19. Particle size distribution pattern of 15 wt. % HRTiO_2 powder suspension formulated with: a) 1 wt. % Darvan C at 0 h milling, b) 1 wt. % Darvan C at 24 h milling, c) 2 wt. % Darvan C at 24 h milling, and d) 3.5 wt. % Darvan C at 24 h milling

On this basis therefore, dilutions were made of the 15 wt. % HRTiO₂ powder suspension of 3.5 wt. % Darvan C content at 24 h ball milling and employed to develop the surface topcoat of the α -Al₂O₃ ceramic support substrates.

3.8. Surface Topcoat Development with HRTiO₂ Powder Suspension

Three (3) different suspensions of 2 wt. %, 5 wt. % and 10 wt. % for substrate coating was made from the dilution of 15 wt. % HRTiO₂ powder suspension plus a 3.5 wt. % Darvan C dispersant and granulometric analysis was carried out at 24 h ball milling as can be seen from Table 15.

Table 15. Particle size distribution of diluted 15 wt. % HRTiO + 3.5 wt. % Darvan C at 24 h ball milling

Particle size distribution parameter	10 wt. % HRTiO ₂ + 3.5 wt. % Darvan C	5 wt. % HRTiO ₂ + 3.5 wt. % Darvan C	2 wt. % HRTiO ₂ + 3.5 wt. % Darvan C	1 wt. % HRTiO ₂ + 3.5 wt. % Darvan C
D ₉₀ (μm)	0.87	0.94	0.94	10.5
Specific surface area (g/m ²)	27.4	22.7	23	12.9

These further dilutions of the 15 wt. % HRTiO₂ powder suspension even after controlling its stability and particle dispersibility in phase as previously stated was to ensure the best possible quality of deposits on the support substrate in order to avoid risk of titania layer detachment during application. Mono layer and bilayer coatings have been performed on the supports over a respective 1-cycle and 2- cycle coating process with these diluted concentrations and surface morphology of the coats controlled by SEM.

At most, 2-layer coating has been considered on the substrate as going up to 3 layers would eventually lead to the collapse of the surface coats. From Table 15, the D₉₀ particle sizes and the specific surface areas of the diluted suspensions of 10 wt. %, 5 wt. %, and 2 wt. % HRTiO₂ did not differ significantly, however, a different outcome in D₉₀ value of 1

wt. % and its specific surface area from the rest dilutions can be attributed to surface energy phenomenon at this diluted concentration due to high ball milling energy that led to the coalescing of the suspended particles a consequent decrease of their surface area [271].

Going forward, these diluted suspensions of 10 wt.%, 5 wt. % and 2 wt. % HRTiO₂ were employed for coating by manual dip coating on a ceramic support of approx. mass weight 5 g. A respective 1 and 2-cycle process of deposition was performed to achieve mono and bilayer surface coats. Surface deposits were allowed a natural healing for 24 h under ambient conditions, dried in an electric oven for 1 h at 60 °C and further calcined in an electric furnace at 600 °C (at a ramp rate of 1°C) for 2 h; to ensure better surface coat adherence, improved mechanical property as well as counter any titania phase transformation change that might have occurred during coat suspension preparation and restore the anatase phase [235].

As detailed in Figure 20, different load charges of these diluted suspensions connected to deposition layer level were obtained in percentages and showed however, surface morphology of cracks, fissures, and sink holes despite a smooth, good, and uniform surface coat at D90 particle size of < 1µm for the employed diluted suspensions. Deposition outcomes were independent on immersion time (t_{dip}) and may have varied from one diluted suspension to the other as the process coating method was manual.

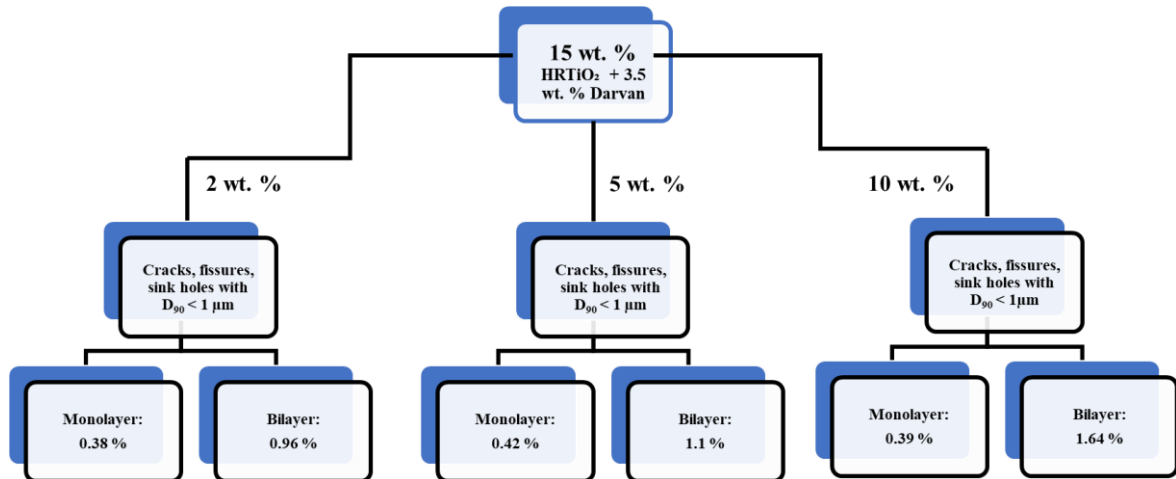


Figure 20. Support coat deposition outcome of α -Al₂O₃ ceramic support with diluted HRTiO₂ powder suspension

Depicted in Figure 21 are some of the SEM micrograph representatives of the deposition outcome displayed in Figure 20.

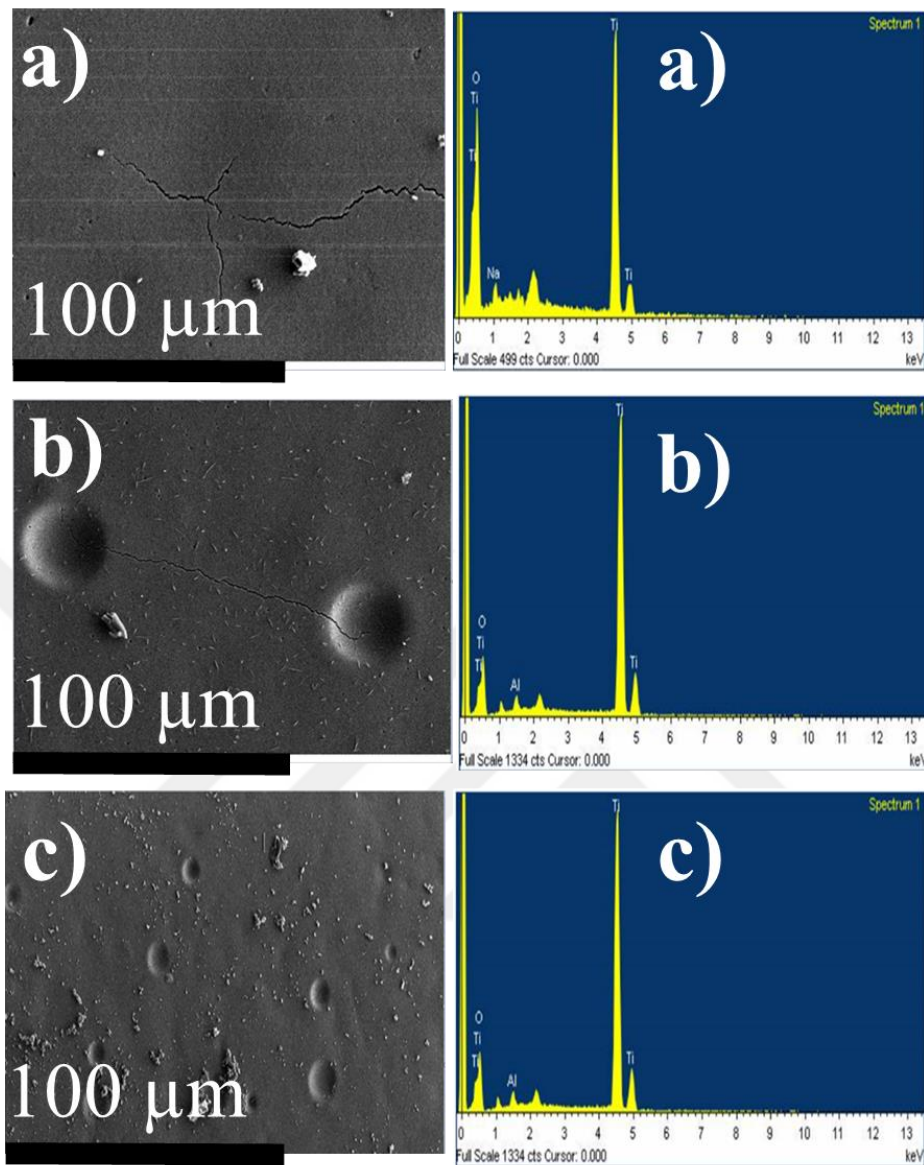


Figure 21. SEM-EDS micrographs coated support surfaces with HRTiO₂ diluted powder suspensions: a) 2 wt. %, b) 5 wt. %, and c) 10 wt. % concentrations

Displayed images of Figure 21 depicted surface morphology anomalies with associated EDS graphs relating as expected elemental contents from powder suspensions. Presence of Na in SEM-EDS (Figure 21a) can be attributed to transfection of the α -Al₂O₃ content of the ceramic support during heat treatment. Otherwise, all other identified elements from the EDS map originated as expected from the TiO₂ powder suspension with the Al coming from the α -Al₂O₃ substrate content of the ceramic support.

In order to attain a smooth, good, and uniformly homogeneous coated support surface, the 1 wt. % diluted suspension with particle size distribution (PSD) characteristics (Table 15) was employed. An ~ 0.005 g surface topcoat delivered over a 2-cycle surface coating process at bilayer deposition was obtained. The same surface coating procedure and surface coat treatment already outlined was implemented.

SEM-EDS analysis of the surface topcoat delivered a uniform, homogeneous and crack free outcome as can be seen from (Figure 22a and b). The EDS map relayed as expected elemental composition content of powder suspension with Na and Al elements presence down to reason already stated. Film thickness was obtained with cross sectional measurement of surface topcoat in the micro scale range (Figure 22c).

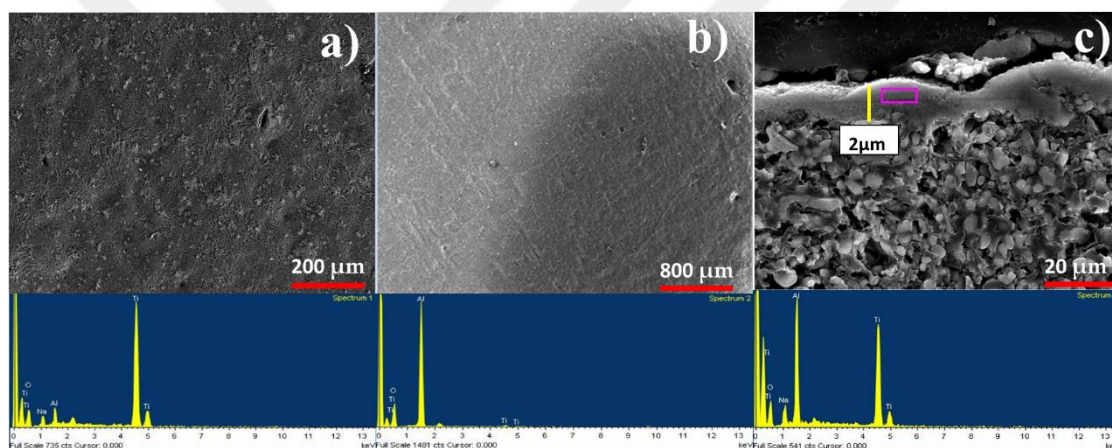


Figure 22. a), and b): SEM-EDS micrographs of coated support surfaces with HRTiO_2 diluted at 1 wt. % suspension concentration, and c) topcoat cross-sectional image

With the surface topcoat outcome of Figure 22, a replicated coating process was performed with best performing decorated HRTiO_2 material sample series following preliminary photocatalytic evaluation tests in powder suspension towards ibuprofen (IBF), caffeine (CAF), and carbamazepine (CBZ) and characterized for structural crystallographic plane identification control before and after photocatalytic test.

3.9. Powder Material Characterizations: HRTiO₂ and SynTiO₂ Sample Series

3.9.1. Thermogravimetric Analysis-Differential Scanning Calorimetry (TGA-DSC) Measurement

The W and/or Mo decorated HRTiO₂ samples were analyzed using thermogravimetric analysis-differential scanning calorimetry (TGA-DSC) in order to evaluate mass changes due to evaporation, decomposition and interaction with atmospheric conditions while linking the thermal effects outcome of the samples from physical and chemical processes involving phase transitions, specific heat etc. As can be observed from (Figure 23a), a pronounced thermal decomposition with a sharp endothermic phenomenon of the control HRTiO₂ sample around 25 °C to 100° C triggered a total mass loss of about 0.8 % and has been reported and attributed to dehydration of the physisorbed water molecule from the external surface [272-274]. The associated endothermic peak with a slightly overlapping exothermic peak observed within this temperature range and at ~ 100 °C has also been reported and attributed to the surface water physisorption phenomenon (Figure 23a) [273-274]. A further observed 1 % mass loss from 360 °C upwards can be attributed to decarboxylation process [272-274]. During this stage, there was the completion of exothermic process as the material stabilized at around 800 °C (Figure 23a). Comparatively, the addition of W and or Mo dopants in the obtained HRTiO₂ decorated forms resulted to better stabilized materials as has been previously reported (Figure 23b, c, and d) [275]. Based on these results, thermal treatment of HRTiO₂ can be administered at temperatures around 800 °C without uncompromising mass alterations as well as phase transition outcome as per specific heat due to thermal effects.

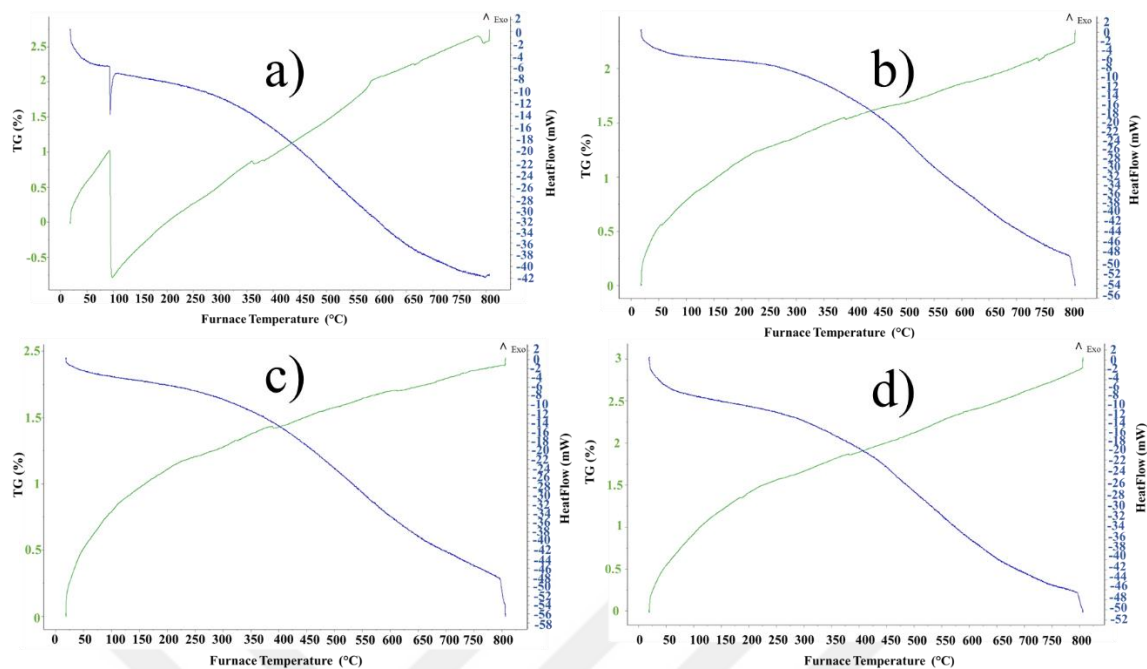


Figure 23. TGA-DSC measurements of a) HRTiO₂, b) W/HRTiO₂, c) Mo/HRTiO₂, and d) W-Mo/HRTiO₂ samples

In contrast to the TGA-DSC measurement analysis of W and Mo decorated HRTiO₂ samples (Figures 23a, b, c, and d) the SynTiO₂ analogues showed different TGA-DSC curves (Figure 24a, b, and c). From Figure (24a, b and c), the thermal decomposition of the samples occurred in 3 successive not well-defined steps. The first step of samples decomposition occurred within the range of room temperature to about 200 °C (Figure 24a, b, and c). A mass loss of about 0.8 % for W/SynTiO₂ (Figure 24a), 0.38 % for Mo/SynTiO₂ (Figure 24b), and 0.39 % for W-Mo/SynTiO₂ (Figure 24c), can be observed and has been attributed to desorption of water molecule [276]. The second decomposition phase of the samples between 200°C to around 400°C and with mass losses of 0.2 % for W/SynTiO₂ (Figure 24a), 0.2 % for Mo/SynTiO₂ (Figure 24b), and 0.4 % for W-Mo/SynTiO₂ (Figure 24c) has been attributed to the elimination of contents from the organic compound precursor used for synthesis [272]. The final decomposition phase at temperatures > 400 °C is attributed to the decarboxylation stage with the advanced temperatures ensuring complete elimination of the organic compounds in the samples as well as better thermal stability [272, 275]. The shallow endothermic peaks at 80°C and alternated exothermic peak at around 400°C and the shallow broad peak that completed the exothermic process at the final decomposition stage of the sample materials corroborated with the reported mass losses for the water molecule

desorption, organic compound content elimination and the final decarboxylation stages in the formation of the material composites at favourable thermal treatment temperatures (Figure 24a, b, and c) [272-276].

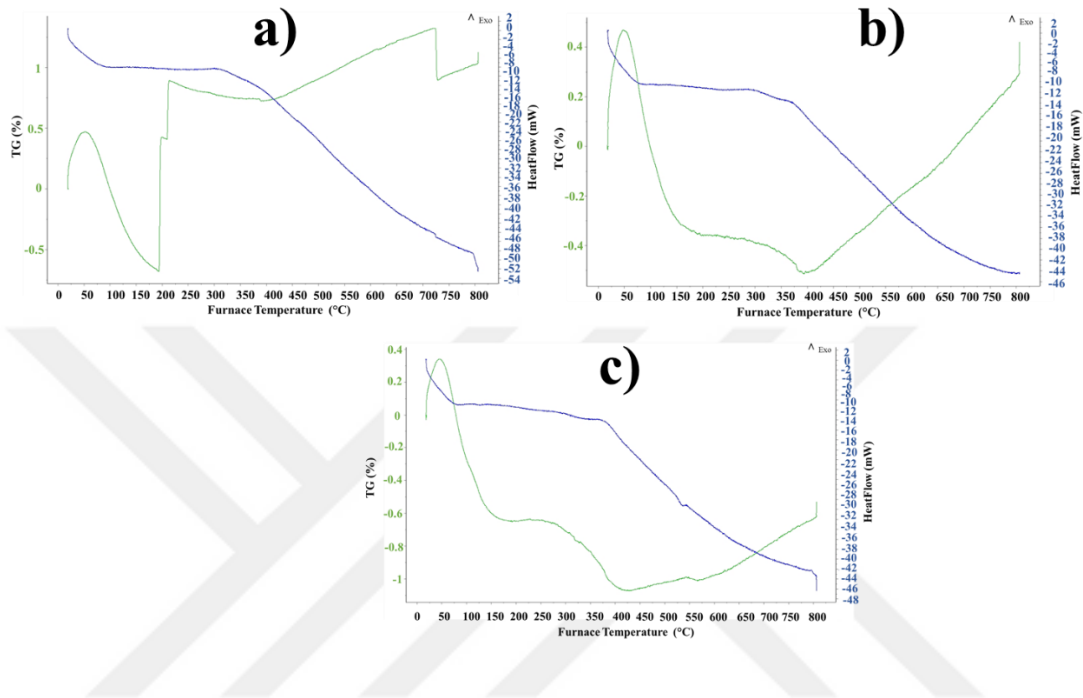


Figure 24. TGA-DSC measurements of a) W/SynTiO₂, b) Mo/SynTiO₂, and c) W-Mo/SynTiO₂ samples

3.9.2. X-ray Diffraction (XRD) and Fourier Transform Infrared (FTIR) Measurements

XRD measurement patterns for the W and or Mo decorated HRTiO₂ samples as can be seen from Figure 25a, manifested clearly anatase phases of the reference HRTiO₂ sample material. The prominent {101} crystallographic phase at $2\theta = 25.39^\circ$ suggested a high-ordered crystalline structure of the decorated material samples.

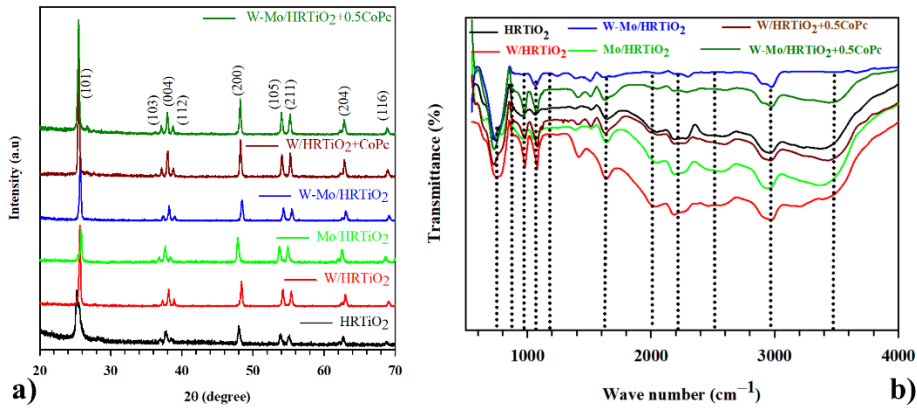


Figure 25. a) XRD, and b) FTIR measurement of HRTiO₂ and its decorated and sensitized forms

Crystallite sizes estimated with Debye-Scherrer function according to Equation (83) showed crystallite size improvement of decorated HRTiO₂ sample materials over the undecorated HRTiO₂ (Table 16).

$$D_{hkl} = \frac{K\lambda}{\beta_{hkl}\cos\theta} \quad (83)$$

where, $\lambda = 1.54059 \text{ \AA}$ is the wavelength of the CuK α source, β is the integral breadth of the XRD peaks depending on the width of the particular hkl plane obtained at full width at half height maximum (FWHM) in degrees, θ is the diffraction angle obtained from XRD data of the most intense reflection and K is the shape factor constant take for a value of 0.9. Apart from the registered {101} peak, other anatase TiO₂ peaks in HRTiO₂ sample found and indexed with (JCPDS card # 01-071-1168) corresponded to the registered crystallographic plane peaks of the decorated HRTiO₂ samples in the order: {103}, {004}, {112}, {200}, {105}, {211}, {204}, and {116} at respective $2\theta = 36.95^\circ, 37.79^\circ, 38.57^\circ, 48.07^\circ, 53.89^\circ, 55.07^\circ, 62.69^\circ, \text{ and } 68.76^\circ$ (Figure 21a). The intensities of these peaks and their positions agreed with reported literature values [272, 277-282]. The uncompromised identified anatase TiO₂ peak phases in the HRTiO₂ modified samples is an indication of the non-alteration of the crystalline phase of the control HRTiO₂ sample following the decoration of same by the W and or Mo dopants as well its sensitization with CoPc in some of the decorated composite samples [134, 222, 282].

Table 16. Material properties of HRTiO₂ and its decorated and sensitized forms

Measured characterization data							Band edge potential (E) eV	
Materials	d _{XRD} nm	d _{TEM} nm	S _{BET} m ² /g	V _p cm ³ /g	d _p nm	E _g eV	E _{VB}	E _{CB}
HRTiO ₂	16.47	27.52	9.78	0.02	7.06	3.23	2.92	- 0.31
W/HRTiO ₂	37.79	47.82	7.12	0.02	9.52	3.26	2.53	- 0.73
Mo/HRTiO ₂	29.99	58.66	8.4	0.02	9.11	3.24	2.39	- 0.85
W- Mo/ HRTiO ₂	33.31	43.44	7.31	0.02	9.96	3.24	2.19	- 1.05
W/ HRTiO ₂ + 0.5CoPc	36.92	39.99	7.91	0.02	9.33	3.23	3.63	0.40
W-Mo/ HRTiO ₂ + 0.5CoPc	35.17	137.6 9	9.78	0.02	8.11	3.23	3.58	0.35
* d _{XRD} , average crystallite size estimated by XRD, # d _{TEM} average particle size estimated by TEM, S _{BET} , surface area, V _p , total pore volume, d _p , average pore size, E _g , energy band gap, E _{VB} is valence band edge potential, and E _{CB} is conduction band edge potential								

With respect to the chemical functional group identification; FTIR measurement was carried out on the HRTiO₂ and forms (Figure 25b). As can be seen, the acquired FTIR spectra of the sample materials in the range 400-4000 cm⁻¹ displayed key functional groups identified with pristine TiO₂ material. Characteristic absorption band peaks around 751.06 cm⁻¹, 802.73 cm⁻¹ is attributed to Ti-O stretching and Ti-O-Ti network linkages in the titania and modified sample materials [122, 134, 222]. The 958.75 cm⁻¹, 1062.59 cm⁻¹, and 1173.54 cm⁻¹ absorption bands are attribute of Ti-OH vibrations and have been reported to possibly arise due to carbonates or carboxylic acid (C=O) stretching mode and or C=C stretching originating from unsaturated precursor materials employed in material components of the composites [122, 222, 272]. Observed peaks at around 1400 cm⁻¹, and 1625.18 cm⁻¹ are

characteristic attributes of surface hydroxyl groups (-OH) and the bending and stretching of the hydrogen bond in the surface absorbed physical water (H-O-H) respectively [122, 134, 222-223]. Peak vibrations at 2003.56 cm^{-1} , 2210.53 cm^{-1} , and 2507.11 cm^{-1} have been reported to be associated with the -CH₂ functional group [223]. The signal at around 2958.75 cm^{-1} is an attribute of the -CH vibrational bond while band at 3470.13 cm^{-1} identifies the broader stretching signal affiliate for the -OH functional group of surface adsorbed water molecule [122, 134, 222-223, 272].

Apart from the confirmation of the unchanged pristine profile of the unmodified HRTiO₂ base by the presence of these key signal attributes in all the decorated samples (Figure 25b), signals at around 958.74 cm^{-1} and 2958.75 cm^{-1} coincide with reported signal values of stretching vibration of WO₃ and W-OH.....H₂O for W intercalated water molecule respectively; thus confirms the presence of W in the related W decorated HRTiO₂ sample (Figure 25b) [283]. In the case of Mo, absorption bands around 802.73 cm^{-1} , and 958.75 cm^{-1} gave additional evidence of the presence of Mo in the related Mo decorated HRTiO₂ reported as a characteristic signal of symmetric and asymmetric stretching vibrations of cis MoO₂ (Figure 25b) [284]. The band signatures at 1062.18 cm^{-1} , 1173.54 cm^{-1} , and 1625.18 cm^{-1} are all within the band signals reported for the presence of cobalt phthalocyanine (CoPc) and therefore, confirms the presence of same in the related decorated CoPc sensitized HRTiO₂ samples (Figure 25b) [285].

In another development, the XRD measurement analysis of the sol-gel synthesized TiO₂ (SynTiO₂) and its W and or Mo decorated forms displayed similar trend of crystallographic patterns as previously stated (Figure 26a).

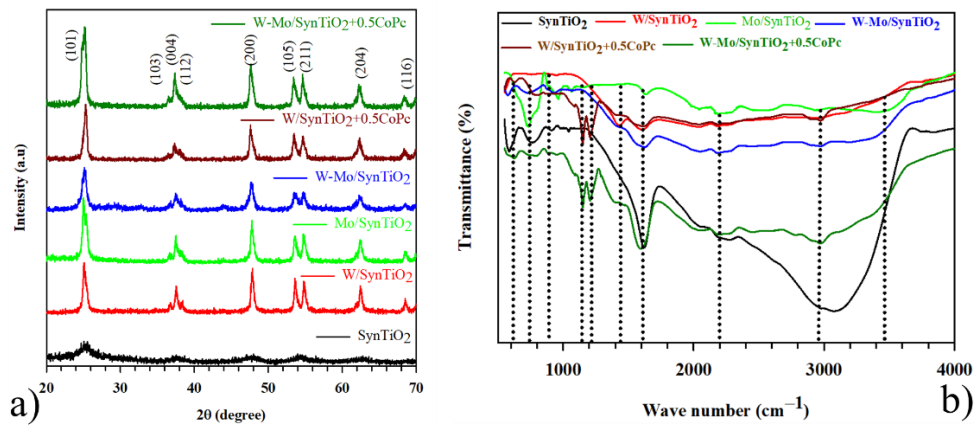


Figure 26. a) XRD, and b) FTIR measurement of SynTiO₂ and decorated and sensitized forms

In the same way as was for the case of HRTiO₂ and decorated forms, the planes and the angle position profile of W and Mo decorated SynTiO₂ forms as indexed with the (JCPDS card # 01-071-1168) matched and coincided with the control SynTiO₂ sample (Figure 26a). Obtained data results agreed with already reported literature data [272, 277-282]. This outcome suggests that the modification strategy by decoration did not alter to a significant point the pristine state of the unmodified SynTiO₂ control sample material. The crystallite sizes as estimated by the Debye-Scherrer function of Equation (83) revealed an increase in crystallite size of decorated sample materials in comparison to the undecorated SynTiO₂ sample (Table 17). While all other crystallite sizes of the decorated SynTiO₂ appreciated with respect to the control undecorated SynTiO₂, an exception occurred in the case of the W and Mo co-decorated SynTiO₂ with a little difference in the crystallite size value of 13.83 nm in comparison to that of the control sample at 14.24 nm (Table 17). The reason for this outcome can be attributed to the crystallite size suppression phenomenon of both W and Mo when they exist in co-decorated form on SynTiO₂ [272].

Though there were no comparison drawn between the two different TiO₂ powder forms employed in this study (i.e. HRTiO₂ and SynTiO₂), the outright improvement in crystallite size of the decorated sample materials in HRTiO₂ series with respect to their control which was not the case with the SynTiO₂ can be attributed to differences in powder nature where one is a technical grade titania and the other is sol-gel synthesized titania (Table 16, and Table 17).

In all, the crystalline phases of the pristine SynTiO₂ were all identified in the modified samples despite W and and or Mo addition and CoPc sensitization [134, 222, 282].

Table 17. Material properties of synthesized TiO₂ (SynTiO₂) and its decorated forms

Measured characterization data							Band edge potential (E) eV	
Materials	d _{XRD} nm	d _{TEM} nm	S _{BET} m ² /g	V _p cm ³ /g	d _p nm	E _g eV	E _{VB}	E _{CB}
SynTiO ₂	14.24	16.02	133.87	0.08	2.32	3.30	2.96	- 0.34
W/SynTiO ₂	19.4	29.99	30.44	0.04	5.73	3.05	2.43	- 0.63
Mo/SynTiO ₂	16.10	24.55	43.30	0.07	6.23	3.05	2.29	- 0.76
W-Mo/SynTiO ₂	13.83	26.15	12.73	0.03	8.25	3.02	2.10	- 0.94
* d _{XRD} , average crystallite size estimated by XRD, # d _{TEM} average particle size estimated by TEM, S _{BET} , surface area, V _p , total pore volume, d _p , average pore size, E _g , energy band gap, E _{VB} is valence band edge potential, and E _{CB} is conduction band edge potential								

With respect to the identified functional group signatures in the SynTiO₂ sample and its decorated forms (Figure 26b), obtained band signals of the FTIR spectra were similar as was the case with the HRTiO₂ and forms (Figure 25b). Thus, identified key band signals for the different functional groups already outlined did not make a significant shift in values, The little differences shown was down to the powder forms being of different grade and synthesis protocol. While HRTiO₂ was a technical titania and employed as purchased, SynTiO₂ was synthesized by sol-gel. As such, band signals at 729.02 cm⁻¹, 839.97 cm⁻¹ are representatives of Ti-O stretching and Ti-O-Ti network linkages [122, 134, 222] while 958.75 cm⁻¹, 1062.59 cm⁻¹, are reported absorption band signals for Ti-OH vibrations and possibly carbonates or carboxylic acid (C=O) stretching mode and or C=C stretching due to the presence of unsaturated compounds [122, 222, 272]. 1388.34 cm⁻¹, and 1618.07 cm⁻¹ signal bands are attributes of surface hydroxyl groups (-OH) and the bending and stretching of the hydrogen bond in the surface adsorbed water (H-O-H) respectively [122, 134, 222-223]. Vibrations at 2032.72 cm⁻¹, 2173.54 cm⁻¹, and 2529.16 cm⁻¹ band signals originate

from the $-CH_2$ functional group [223]. The signal at around 2958.75 cm^{-1} belongs to the $-CH$ vibrational bond while 3485.06 cm^{-1} is identified with the broader stretching signal for the $-OH$ functional group of surface adsorbed water molecule [122, 134, 222-223, 272]. For W and Mo confirmation in the samples, 958.75 cm^{-1} and 2958.75 cm^{-1} are for respective stretching vibration of WO_3 and $W-OH\dots\dots H_2O$ for W intercalated water molecule (Figure 26b) [283] and for symmetric and asymmetric stretching vibrations of *cis* MoO_2 (Figure 26b) [284], thereby confirming the presence of these dopants in the samples. Band signals at 1062.59 cm^{-1} , and 1618.17 cm^{-1} confirmed the presence of cobalt phthalocyanine (CoPc) in the related decorated CoPc sensitized $SynTiO_2$ samples (Figure 26b) [285].

Decorated and sensitized samples: $W/SynTiO_2 + 0.5CoPc$ and $W-Mo/SynTiO_2 + 0.5CoPc$ were not included in Table 17 as they did not show strong photocatalytic activity over the CECs compounds degradation following preliminary photocatalytic test evaluation after material characterization.

3.9.3. Surface Topcoat Development of W/HRTiO₂ Powder Suspension

By the same coating procedure as previously outlined in section (3.8), surface topcoat was replicated. With a 2 wt.% W/HRTiO₂ (the best performing photocatalytic material in the HRTiO₂ sample series) suspension, 0.005 g of W/HRTiO₂ topcoat on ceramic support surface was obtained and structurally characterized by XRD and FTIR measurement techniques and evaluated as a photocatalytic membrane reactor (PMR) for the photocatalytic degradation of the selected 3 CECs compounds as will be discussed in later section.

3.9.3.1. XRD and FTIR Measurements of W/HRTiO₂ Topcoated $\alpha-Al_2O_3$ Ceramic Support

Just like in the case of the powder material samples, XRD graph (Figure 27a) of the on ceramic support coated W/HRTiO₂ showed prominent crystallographic planes of the content materials in the composite.

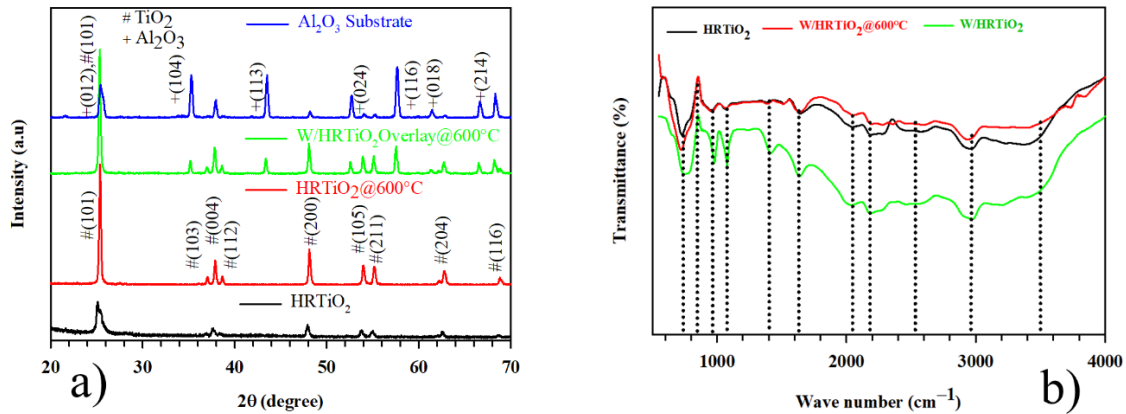


Figure 27. a) XRD, and b) FTIR measurements of W/HRTiO₂ topcoat on α -Al₂O₃ ceramic support annealed at 600 °C and in comparison with its base control components before photocatalytic test

As can be seen from the Figure 26a, crystallographic planes of {101}, {103}, {004}, {112}, {200}, {105}, {211}, {204}, and {116} at respective 2 θ values of 25.39°, 36.95°, 37.79°, 38.57°, 48.07°, 53.89°, 55.07°, 62.69°, and 68.76° as indexed with the (JCPDS card #01-071-1168) for anatase TiO₂ is confirmed of the base HRTiO₂ and its decorated W/HRTiO₂ form treated at 600 °C which was the final annealing temperature of the topcoat for improved mechanical adherence. The identified peak phases of HRTiO₂ and W/HRTiO₂ samples each annealed at 600 °C in comparison to HRTiO₂ sample not annealed and kept at normal room temperature condition (as available) were more intense and stronger (Figure 27a). This outcome means that the annealing treatment at 600 °C which was aimed for improved mechanical adherence of the topcoat also increased the crystalline structure and phase reflection prominence of involved samples [286]. Peak phase reflections of the α -Al₂O₃ content of the ceramic support bearing the W/HRTiO₂ overlay were indexed at {012}, {104}, {113}, {024}, {116}, {018}, and {214} with a JCPDS card #01-071-1683 and agreed with already reported data [287]. The peak phases of the W/HRTiO₂ overlay corresponded with that of the anatase TiO₂ crystal phases and showed an existence of sharper and narrower peaks indicating good crystallinity of topcoat (Figure 27a). Moreover, similarity in peak phase pattern of W/HRTiO₂ overlay with that of the α -Al₂O₃ show that overlay and support had phase co-existence as an indication of the uniform and homogeneous distribution of the topcoat over the support surface [Figure 27a].

On the other hand, the FTIR measurement of the HRTiO₂, W/HRTiO₂ overlay with annealing treatment at 600 °C, and W decorated HRTiO₂ (W/HRTiO₂) untreated showed similarity in their spectral patterns (Figure 27b). As already, stated the key band signals at around 1000 cm⁻¹, 1400 cm⁻¹, 1600 cm⁻¹, 2000-2200 cm⁻¹, 2580 cm⁻¹, 2880 cm⁻¹, and 3500 cm⁻¹ were identified and characteristic of the expected functional groups of the HRTiO₂ and W/HRTiO₂ sample material contents and matched those identified in Figure 25b. The sharper and narrower crystalline peaks of the W/HRTiO₂ treated at 600 °C which was the annealing temperature of the after-topcoat deposition on support can be observed in comparison to W/HRTiO₂ (decorated) (Figure 25a).

This observation corroborated with the outcome seen of the same W/HRTiO₂ overlay sample material in the XRD graph with improved crystallinity at 600 °C annealing temperature (Figure 27a).

3.9.4. Transmission Electron Microscopy (TEM) Measurement and Scanning Electron Microscopy-Energy Dispersive X-ray Spectroscopy (SEM-EDS) Measurement Analysis

From the TEM image in Figure 28a, it can be seen spherically shaped nanoparticles of the HRTiO₂ sample with some large spherical components in a disjointed form of connection within the base TiO₂ matrix network. In comparison with the decorated forms, the W and Mo dopants in the respective singly decorated W/HRTiO₂ and Mo/HRTiO₂ samples can be seen deposited on the surface of the HRTiO₂ base material revealing core shell ring like structures (Figure 28b, and c) [122, 272, 288-289]. The connection networks in these decorated forms can also be seen narrowed in comparison to the HRTiO₂ control sample making them appear in denser and larger aggregated forms. The co-decorated W-Mo/HRTiO₂ sample revealed a structural pattern with an extended interconnected network and the co-existence of both W and Mo dopants abiding on the surface of the HRTiO₂ base matrix as core shell ring like structures [122, 272, 288-289] (Figure 28d). Again, there was a revelation of a polyhedral elongated microstructured material form exhibited by the W-Mo/HRTiO₂ sample.

Particle size estimate of the HRTiO₂ and decorated sample forms were obtained by ImageJ Software Version 8 and showed improvement with respect to the unmodified sample which agreed with the obtained average crystallite sizes of the samples as estimated from the XRD measurement (Table 16). The disparity seen in the decorated and sensitized

samples of $W/HRTiO_2 + 0.5CoPc$ and $W-Mo/HRTiO_2 + 0.5CoPc$ can be attributed to the already reductive effect of $W/HRTiO_2$ as can be seen from (Table 16) which did not improve even with addition of the $0.5CoPc$ molecule at 39.99 nm. However, the $W-Mo/HRTiO_2$ co-decorated sample showed a higher particle size value of 137.69 nm, an indication that the co-dopants in the presence of the $CoPc$ exhibited increased particle size effect [122] (Table 18) due to the large size of Pc molecules which even though in the presence of only W in $W/HRTiO_2$ was not significantly contributing but exerted a particle size growth effect in the presence of W and Mo as co-dopants. Figure 28e, show the TEM image of the $W-Mo/HRTiO_2 + 0.5CoPc$ with a polydisperse form outlook combining rounded shaped particles with some rod-like transformations [122]. The TEM image of $W/HRTiO_2 + 0.5CoPc$ has not been included as its estimated particle size in comparison with the other decorated samples did not show a wider variation like that of $W-Mo/HRTiO_2 + 0.5CoPc$.

On a general note, the microstructural outlook of the decorated samples in comparison to the $HRTiO_2$ control sample did not alter to a significant extent and retained the pristine state of the base $HRTiO_2$ material after modification by decoration.

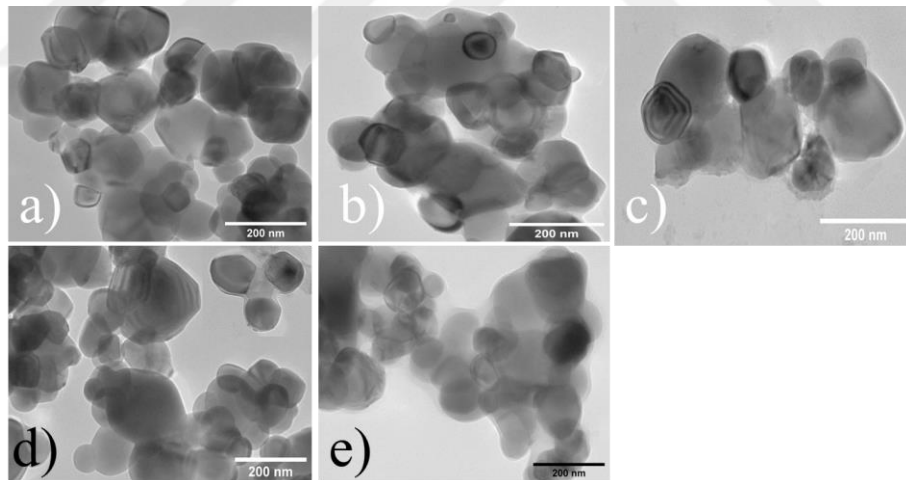


Figure 28. TEM images of a) $HRTiO_2$, b) $W/HRTiO_2$, c) $Mo/HRTiO_2$, d) $W-Mo/HRTiO_2$, and e) $W-Mo/HRTiO_2 + 0.5CoPc$

The morphology of the $HRTiO_2$ and decorated forms obtained from SEM and the associated EDS map reveal such an outlook whereby the samples appear in aggregated and dense form [134, 280, 283] (Fig 29a, b, c, d, and e). Amongst the decorated and sensitized samples, morphological outlook did not vary widely. As can be seen from the SEM image,

samples existed in tiny agglomerated spherical nanoparticles [134, 280, 283]. However, the seemed loosely nanoparticle agglomerates appeared in a more reinforced and compact form in the co-decorated sample (W-Mo/HRTiO₂) [134, 280, 283] (Figure 29d). Correspondingly, the EDS map revelations of the HRTiO₂ and its decorated and sensitized forms showed as expected the elemental sample contents (Figure 29a, b, c, d, and e). Exceptionally, the meagre detection of Co at 0.1 wt. % marking the presence of CoPc sensitizer and the outright non-detection of N in W/HRTiO₂ + 0.5CoPc as well the total absence of both Co and N as CoPc markers in the EDS map of W-Mo/HRTiO₂ + 0.5CoPc sample is an indication of not only the small added CoPc amount of 0.5 wt. % but also confirmation that the CoPc sensitizer was localized on the material surfaces, hence, SEM-EDS is a bulk material analytical technique (Figure 29d and e). Key core elements in the respective samples were identified in the associated EDS maps and C is attribute to adventitious carbon [134].

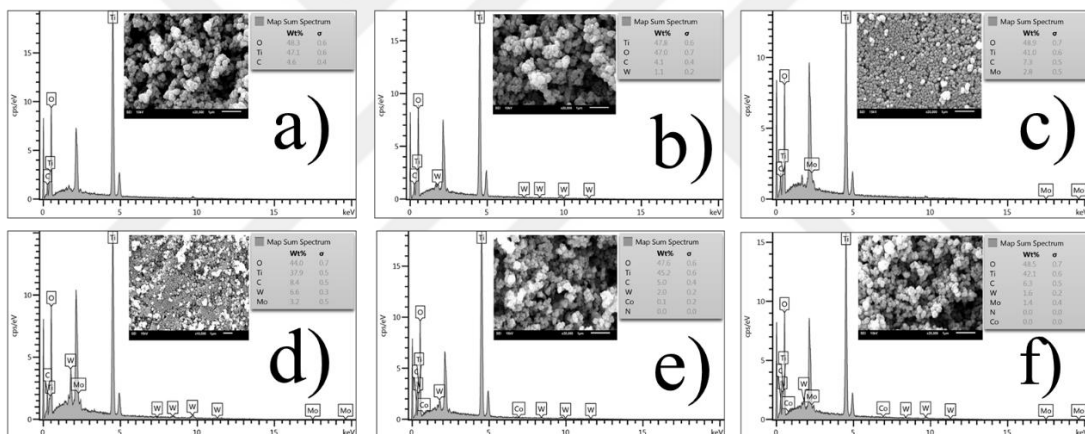


Figure 29. SEM-EDS measurement of a) HRTiO₂, b) W/HRTiO₂, c) Mo/HRTiO₂, d) W-Mo/HRTiO₂, e) W/HRTiO₂ + 0.5CoPc, and f) W-Mo/HRTiO₂ + 0.5CoPc

On the other hand, the TEM images of SynTiO₂ and decorated forms as shown below reveals the unmodified SynTiO₂ as finely divided and sparsely distributed nanoparticles (Figure 30a). The W/SynTiO₂ sample showed a largely grown, compactly connected bulkier and agglomerated particles upon the decoration of SynTiO₂ with W (Figure 30b) [122, 272, 288-289]. Likewise, Mo/HRTiO₂ resulted to aggregated clustered particle lumps with more large size in comparison to the unmodified SynTiO₂ (Figure 30c) [122, 272, 288-289]. The co-decoration of SynTiO₂ with W and Mo delivered in like manner aggregated clustered particles seen in the singly decorated of W and Mo; however, particles assumed more

randomized, distributed, and distinct nanopolyhedral pattern (Figure 30d) [122, 272, 288-289]. The estimated particle sizes of the decorated SynTiO₂ samples in comparison to the unmodified sample appreciated and agreed with obtained average crystalline size from the XRD measurement (Table 17). In a similar development like with the average crystallite size of W-Mo/SynTiO₂ (Table 17), the particle size depreciated in comparison to that of W/SynTiO₂ (Table 17). The reason for this is due to the suppressive effect of the Mo dopant in the W-Mo/SynTiO₂ co-decorated sample [272].

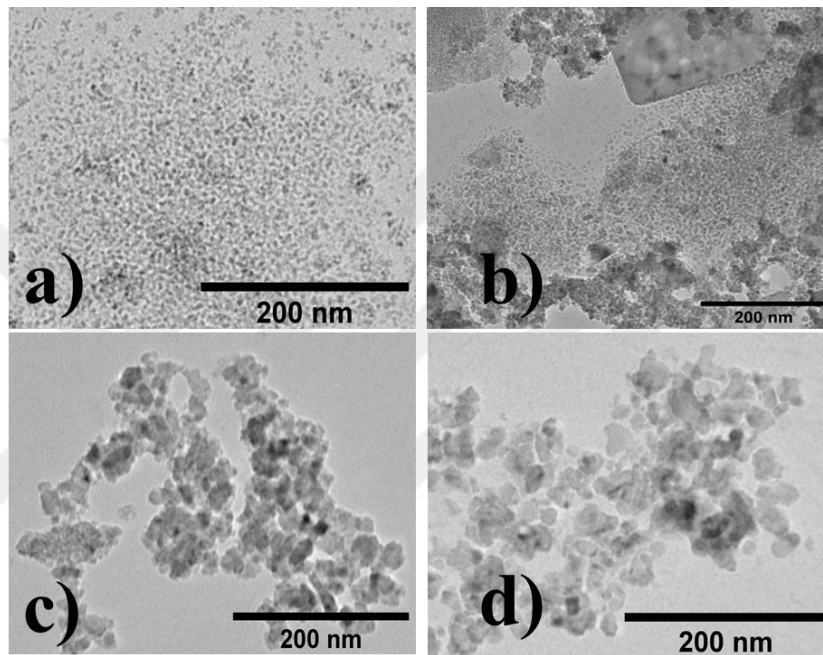


Figure 30. TEM images of a) SynTiO₂, b) W/SynTiO₂, c) Mo/SynTiO₂, and d) W-Mo/SynTiO₂

In another development the structural morphology of the SynTiO₂ and decorated forms were investigated. From the SEM images, SynTiO₂ showed morphological outlook of small densely populated spherical particles (Figure 31a). Upon the decoration of SynTiO₂ with W, it can be seen that the distinct spherical particle of SynTiO₂ aggregate and form lumps (Figure 31b) [134, 283]. The Mo/SynTiO₂, displayed a more aggregated lump structure with some prominence of rough surface edges (Figure 31c) [280, 283]. The W-Mo/SynTiO₂ displayed dissected rough edged irregular shaped forms of various particle sizes isolated upon the decoration of SynTiO₂ with W and Mo as co-dopants (Figure 31d) [272]. As expected, the accompanied EDS maps revealed the elemental content in the as prepared

samples (Figure 31a, b, c, and d). Presence of C in the samples is of adventitious origin (Figure 31a, b, c, and d) [134].

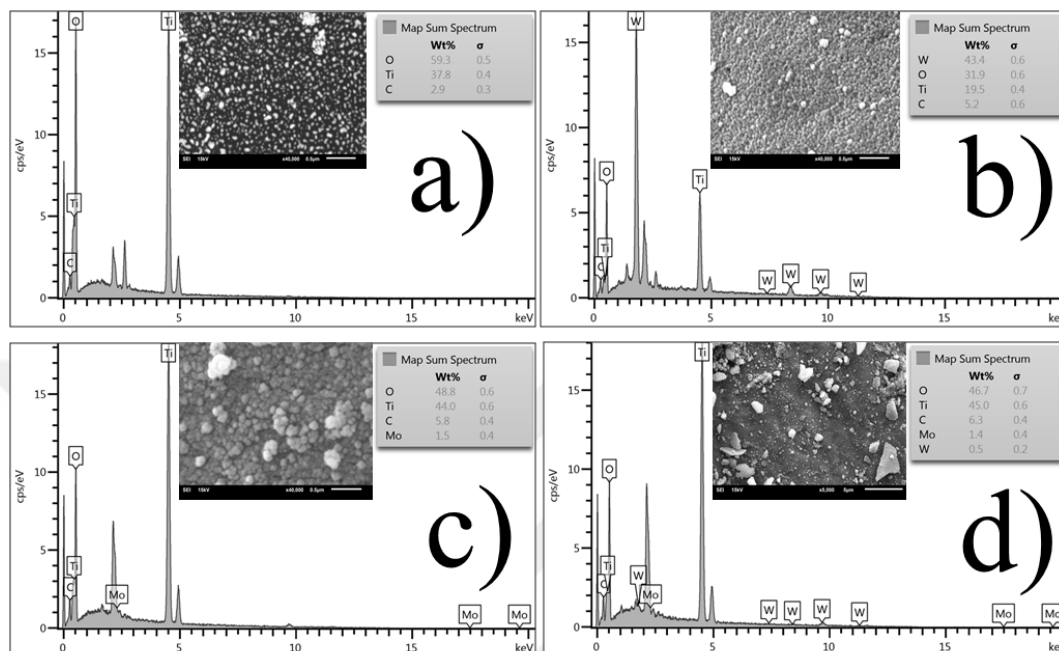


Figure 31. SEM-EDS measurement of a) SynTiO₂, b) W/SynTiO₂, c) Mo/SynTiO₂, and d) W-Mo/SynTiO₂

3.9.5. Brunauer Emmet Teller (BET) and X-ray Photoelectron Spectroscopy (XPS) Analysis Measurement

The surface area and the pore size distribution of the HRTiO₂ and decorated forms were respectively investigated using the nitrogen adsorption-desorption isotherm and BJH application method as shown in Figures 32 and 33. As can be seen all the samples exhibited type II isotherm as classified by the international union of Pure and Applied Chemistry (IUPAC) [272]. The absence of adsorption at low pressure is an indication of the disappearance of micropores in the HRTiO₂ control and as decorated samples [290] (Figure 32a-f). The well overlapping of the adsorption and desorption isotherm branches led to almost no hysteresis loop and indicates significant loss of mesopores and rather more presence of larger pores with respect to the higher relative pressure (P/P_0) adsorption ratio [290].

Correspondingly, the non-uniformity in the porous structural network of the HRTiO₂ sample materials with near absence of mesopores and predominant larger pores in display led to a pore size distribution with mixed mode pattern (Figure 33a-f) [272]. In comparison to the control HRTiO₂ sample, the decorated and sensitized samples strikingly exhibited more mix of modal pattern as a shift is experienced upon the addition of the W and or Mo dopants as well as the CoPc sensitizer (Figure 33a-f).

From the particle size distribution measurement obtained by the Barrett Joyner Halenda (BJH) application method, majority of the overall pores of the decorated samples lie between 2.5 nm to 100 nm with their peak maxima around 4.5 nm-7.5 nm (Figure 33a-f). This implies that though, the materials lack outright mesoporous network pattern; they however possess relatively regular channels within the mesoporous region [292].

As detailed in Table 16, while estimated total pore volume of samples were the same at 0.02 cm³/g; the surface areas of the samples, and average pore size showed some disparity in estimated value however not to a significant level. For instance, the surface area of HRTiO₂ at 9.78 cm²/g is relatively higher in comparison to the modified forms. This could be attributed to the core shell ring-like structures of the W and or Mo transition metal dopants anchored onto the HRTiO₂ sample surface with a proportional increase in surface population density and consequent reduction in surface area. The exceptional case where the estimated surface area of the W-Mo/HRTiO₂ + 0.5CoPc sample was the same value of 9.78 m²/g as the control is attributed to the presence of the large CoPc molecule in a co-doped environment of W and Mo. The estimated total pore volume though not changed amongst samples is an indication of not too a variation change and loss of surface area of samples with consequent blockage of pores [278]. However, slight reduction in pore sizes of HRTiO₂ control and that of co-decorated sensitized W-Mo/HRTiO₂ + 0.5CoPc was observed relative to the other samples due to a slight appreciation in their surface areas in comparison to the other samples (Table 16).

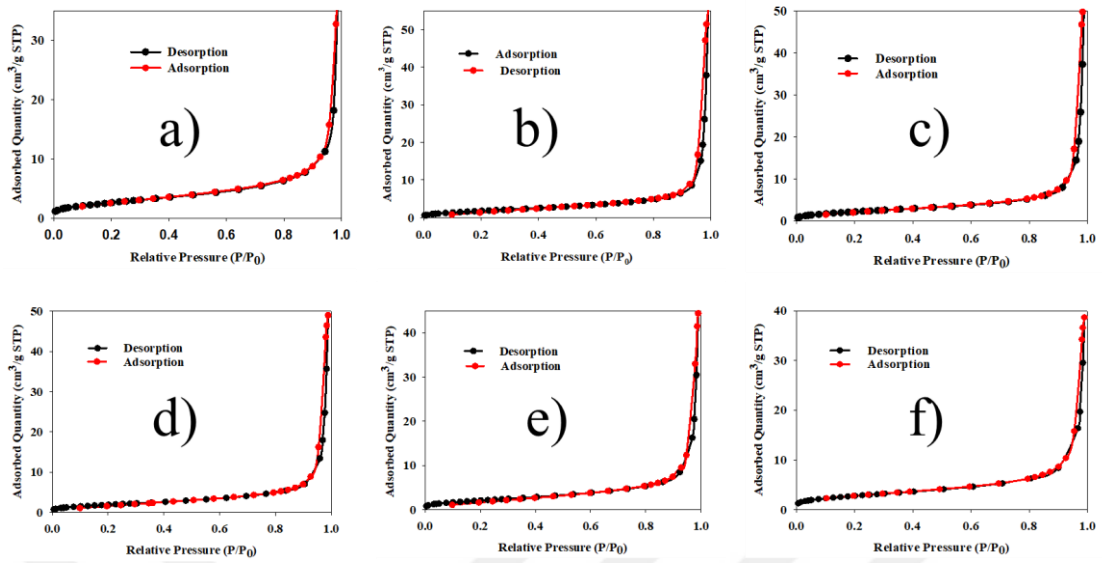


Figure 32. N₂ adsorption -desorption isotherm measurements of a) HRTiO₂, b) W/HRTiO₂, c) Mo/HRTiO₂, d) W-Mo/HRTiO₂, e) W/HRTiO₂ + 0.5CoPc, and f) W-Mo/HRTiO₂ + 0.5CoPc

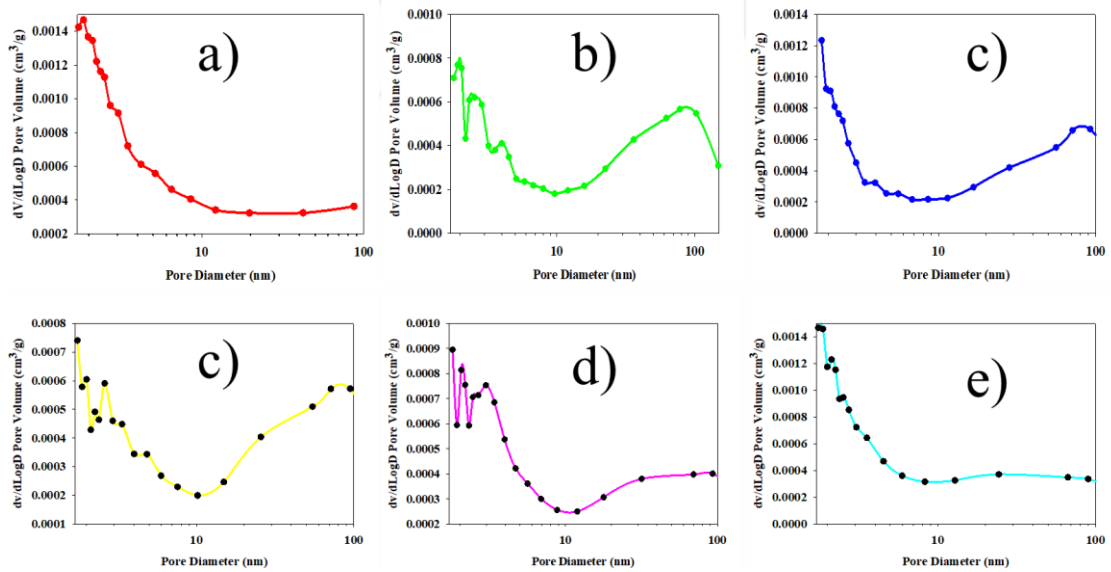


Figure 33. Pore size distribution obtained by BJH application method of a) HRTiO₂, b) W/HRTiO₂, c) Mo/HRTiO₂, d) W-Mo/HRTiO₂, e) W/HRTiO₂ + 0.5CoPc, and f) W-Mo/HRTiO₂ + 0.5CoPc

The chemical environment of the HRTiO_2 and decorated samples was elucidated with XPS analysis. Depicted in (Figure 34a-e) is the respective XPS survey of the HRTiO_2 sample and its decorated and sensitized forms. It can be seen as expected from the survey, the constituent elemental compositions in the as prepared samples relative to the added W and or Mo dopants in comparison to the control sample. N and Co elemental markers of the CoPc sensitized samples have not been identified due to the small amount of the employed CoPc and as well as limitations of XPS measurement tool as a surface analytical technique.

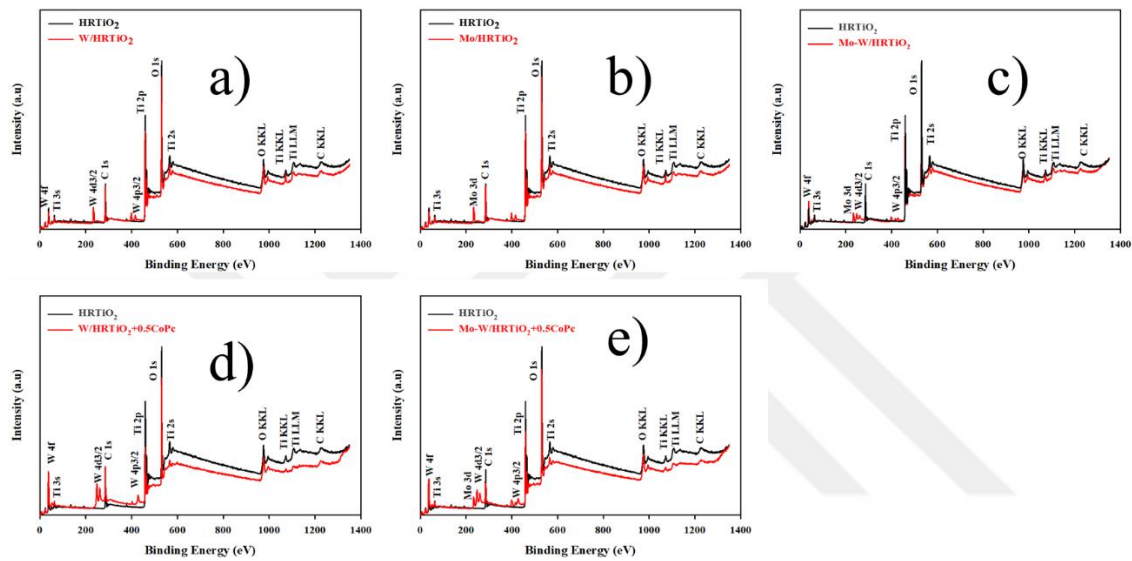


Figure 34. XPS survey spectrum of a) W/HRTiO_2 , b) Mo/HRTiO_2 , c) $\text{W-Mo}/\text{HRTiO}_2$, d) $\text{W}/\text{HRTiO}_2 + 0.5\text{CoPc}$, and e) $\text{W-Mo}/\text{HRTiO}_2 + 0.5\text{CoPc}$ in comparison to HRTiO_2 control sample

Correspondingly, resolved and deconvoluted spectra of the decorated samples indicated as expected the elemental compositions of the as prepared sample materials (Figure 35a-c). As shown, the XPS spectra of Ti 2p in W/HRTiO_2 sample showed two peaks assigned to Ti 2p_{3/2} and Ti 2p_{1/2} located at respective binding energies of 459.1 eV and 464.8 eV reported to be associated with Ti^{4+} ions in TiO_2 lattice structure (Fig 35a) [122, 134, 272, 278, 280, 282]. The O 1s spectra at displayed peaks with respective binding energies of 530.6 eV and 532.2 eV can be attributed to the Ti-O bond in TiO_2 and hydroxyl (-OH) functional groups (Figure 35b) [122, 134, 162, 223, 272, 280, 282, 286, 290-291]. Resolved XPS spectra of W 4f peaks can be seen in (Figure 35c) with W 4f_{7/2} at binding energy 35.9 eV and W 4f_{5/2} at binding energy 38.0 eV and agrees with already reported literature data

attributing the peak shift of 2.1 eV as part of the W^{+6}/W^{+5} valence pair states ($W 4f_{7/2} - W 4f_{5/2}$) spin doublets [122, 223, 272, 282].

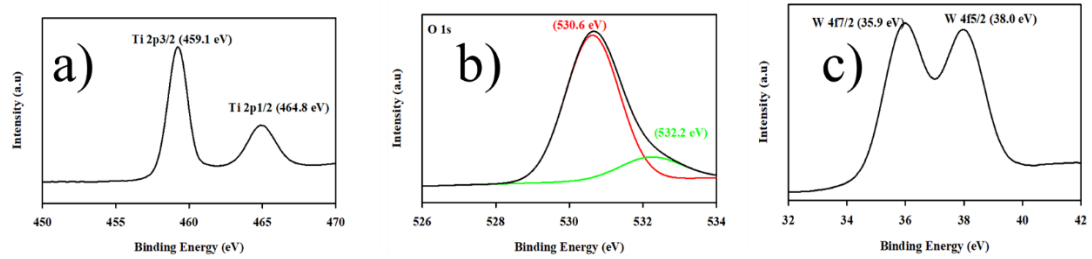


Figure 35. XPS spectra of W/HRTiO₂ showing chemical elemental compositional peaks for a) Ti 2p, b) O 1s, and c) W 4f

Other resolved XPS spectral peaks of the decorated and sensitized HRTiO₂ forms can be seen listed in Table 18 displaying the respective binding energies of sample individual elemental compositions as well as that of their deconvoluted spectra. While it was more realistic to mark the CoPc sensitized material samples by the present N 1s (Table 18) with a surface analytical tool like XPS, the non-identification of the CoPc markers in bulk with the SEM technique was not facilitated as the CoPc is assumed to have been anchored onto the material surface (Figure 29e and f). Presence of core level C 1s at binding energies of about 285 eV and 289 eV (Table 18) is attributed to adventitious carbon and or associated with other bond functionalities like C-H and or C-C, C=C, C-O-H, C=O [122, 162, 280, 290]. It is worthy of note to say that observed shift in binding energy instances of decorated samples with respect to the HRTiO₂ as well as little observable discrepancy in literature data values can be attributed to physico-chemical changes in the bonding environments of obtained materials following the applied modification strategies (doping by decoration and Pc sensitization) [122, 134, 162, 223, 272].

Table 18. XPS elemental compositional and deconvoluted spectral binding energy profile for other decorated/sensitized HRTiO₂ and SynTiO₂ sample material forms

Element	Binding energy (eV)
W/HRTiO ₂ + 0.5CoPc	
Ti 2p _{1/2}	465.28
Ti 2p _{3/2}	459.48
O1s	530.98
W 4f _{5/2}	38.48
W 4f _{7/2}	36.58
C1s	285.08, 288.88
N1s	402.58, 398.98
Mo/HRTiO ₂	
Ti 2p _{1/2}	464.54
Ti 2p _{3/2}	458.78
O1s	530.08
Mo 3d _{3/2}	235.68
Mo 3d _{5/2}	232.58
C1s	284.88, 288.78
Mo-W/HRTiO ₂	
Ti 2p _{1/2}	464.48
Ti 2p _{3/2}	459.08
O1s	530.28
W 4f _{5/2}	37.58
W 4f _{7/2}	36.18
Mo 3d _{3/2}	235.68
Mo 3d _{5/2}	232.58
C1s	285.18, 289.68
Mo-W/HRTiO ₂ + 0.5CoPc	
Ti 2p _{1/2}	464.98
Ti 2p _{3/2}	458.98
O1s	530.28

Continuation of Table 18

W 4f _{5/2}	37.88
W 4f _{7/2}	35.8
Mo 3d _{3/2}	235.98
Mo 3d _{5/2}	232.88
C1s	284.98, 288.98
N1s	402.38, 398.68
W/SynTiO ₂	
Element	Binding energy (eV)
Ti 2p _{1/2}	464.98
Ti 2p _{3/2}	459.18
O1s	530.68
W 4f _{5/2}	37.98
W 4f _{7/2}	36.08
C1s	285.08, 288.88

On the other hand, and with the same measurement technique and protocol for HRTiO₂ and forms, the surface area, and the pore size distribution (PSD) of synthesized TiO₂ (SynTiO₂) was analysed. As shown in Figure 36a, observed isotherm of the SynTiO₂ control sample exhibited Type-Ib kind of isotherm with a continuous N₂ adsorption uptake with pressure increment and establishing a very narrow hysteresis loop at high end relative pressure (P/P₀) ratio [292].

In comparison to the associated pore size distribution (PSD) (Figure 37a), it can be seen a pattern of extended PSD towards a wider micropore range with narrower or even total absence of mesopores [272].

Upon the modification of the control SynTiO₂ with W and or Mo, there was a transformation of the exhibited Type-Ib isotherm of the control sample into Type-IV isotherm in the decorated samples with a defined H3 hysteresis loop due to the coincidence of the adsorption and desorption isotherm branches at about 0.4 relative pressure value (Figure 36b-d) [272, 292]. This indicates that with the introduction of the W and Mo dopants into the SynTiO₂ sample, obtained materials exhibited characteristic mesoporous structural network with more than one PSD modal pattern (Figure 37b, and d) [272]. The exceptional

case seen in the PSD pattern of Mo/SynTiO₂ can be attributed to the reported compact surface accompanied with surface area fluctuation resultant effect of Mo doping leading to a more widely spread and extended pore channel without modal confinements in pattern (Figure 31c, Figure 37c) [280].

The textural properties of the SynTiO₂ and decorated forms are given in Table 17. As can be seen the surface area of the control sample has a higher surface area of 133.87 m²/g than the obtained decorated materials. The surface areas of W/SynTiO₂ and Mo/SynTiO₂ did not differ significantly between them (Table 17). The W-Mo/SynTiO₂ sample showed a lower surface area of 12.73 m²/g in comparison to both the control and the mono decorated samples due to the combining dopant effect on the structural morphology of the SynTiO₂ base material (Figure 30d, Figure 31d, Table 17). While pore volume for SynTiO₂, and Mo/SynTiO₂ did not differ significantly at 0.08 cm³/g and 0.07 cm³/g (Table 17); that of W/SynTiO₂ and W-Mo/SynTiO₂ were almost the same at 0.04 cm³/g and 0.03 cm³/g respectively (Table 17). The pore volume reduction in the co-decorated form can be attributed as the carryover pore volume reduction effect of W/SynTiO₂ as a mono dopant which it further exerted when combined with Mo/SynTiO₂.

Though, sample surface area and total pore volume of materials were of a mixed outcome in data values; pore sizes were all appreciative with respect to the SynTiO₂ sample material upon modification (Table 17). In all, textural data agreed with already reported literature values [272, 280].

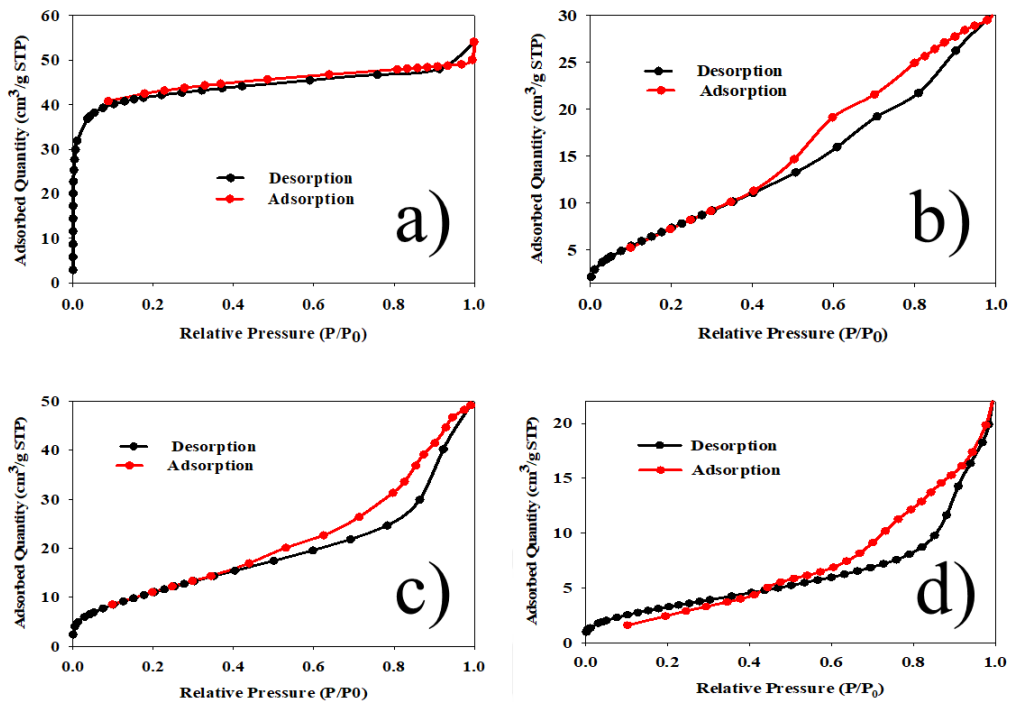


Figure 36. N_2 adsorption-desorption isotherm measurement of a) SynTiO₂, b) W/SynTiO₂, c) Mo/SynTiO₂, and d) W-Mo/SynTiO₂

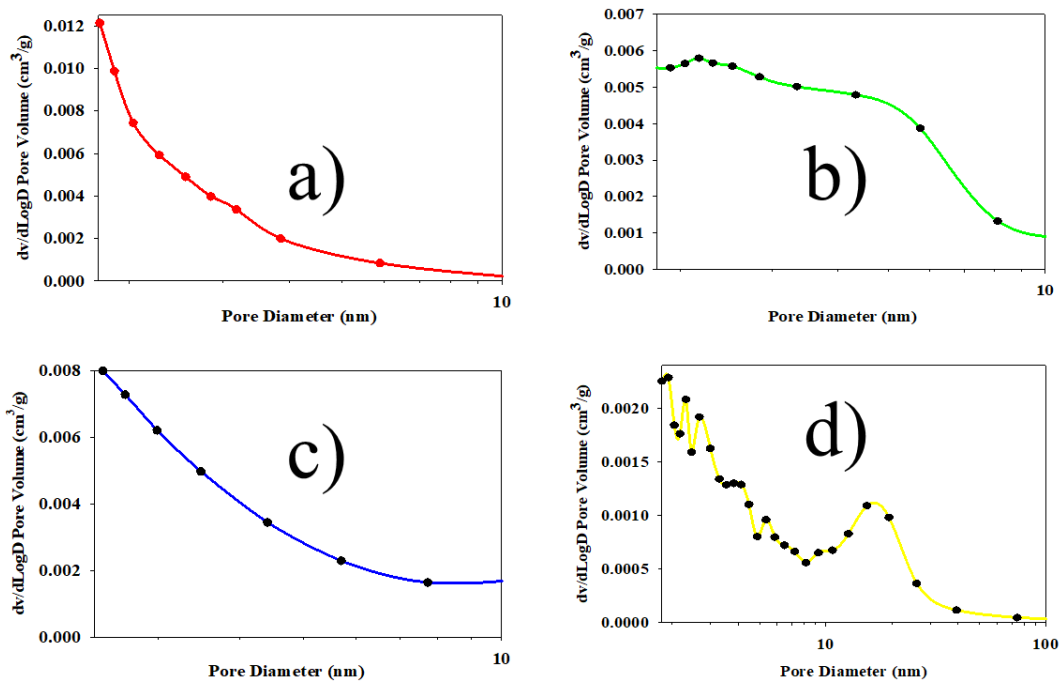


Figure 37. Pore size distribution obtained by BJH application method of a) SynTiO₂, b) W/SynTiO₂, c) Mo/SynTiO₂, and d) W-Mo/SynTiO₂

To analyse the chemical states of the decorated SynTiO₂ and forms, XPS analysis measurement was carried out. Shown in Figure 38a-c is the XPS survey spectrum of W/SynTiO₂, Mo/SynTiO₂ and W-Mo/SynTiO₂ in relation to the SynTiO₂ control sample. As expected, each of the sample survey marked and displayed the individual elemental compositional content in their makeup as a confirmation of successful modification of the control material with W and or Mo dopants. Presence of C 1s is attributed to same reason as earlier stated in the case of HRTiO₂ and forms.

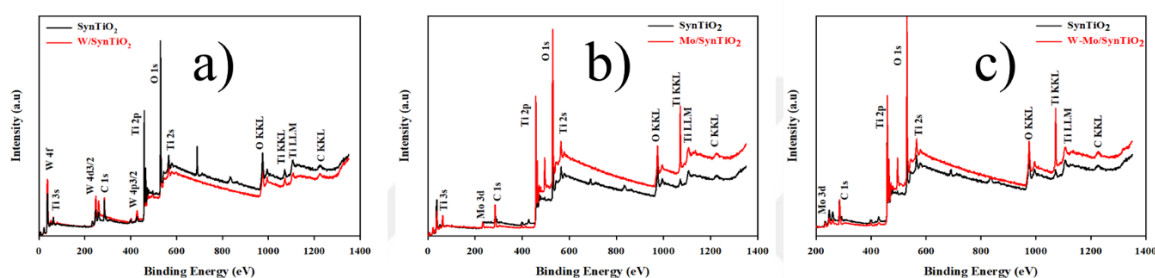


Figure 38. XPS survey spectrum of a) W/SynTiO₂, b) Mo/SynTiO₂, c) W-Mo/SynTiO₂ in relation to SynTiO₂ control sample

Displayed in Figure 39a-c are the XPS spectra images depicting the elemental compositional signatures of Mo/SynTiO₂. The Ti 2p energy level distinguished as expected the Ti 2p_{3/2} and Ti 2p_{1/2} at respective binding energies of 458 eV and 464.1 eV (Figure 39a). These binding energies agreed with already reported literature data of Ti⁴⁺ state and did not show a significant shift towards higher BE values of the two peaks in connection with already reported unmodified Ti 2p binding energies [122, 134, 272, 278, 280, 282]. This is a further confirmation of the non-alteration of the pristine state of the base TiO₂ material. The O 1s spectra resolved at binding energies of 529.5 eV and 530.9 eV is assigned to Ti-O bond in TiO₂ and hydroxyl (-OH) functionalities and has been reported (Figure 39b) [122, 134, 162, 223, 272, 280, 282, 286, 290-291]. The Mo 3d spectra for the Mo dopant at 235 eV and 231.9 eV binding energies were assigned for Mo 3d_{3/2} and Mo 3d_{5/2} respectively (Figure 39c). These values were in the range of already reported data for the respective Mo⁶⁺ and Mo⁵⁺ excited spin states contributions of Mo 3d_{3/2} and Mo 3d_{5/2} [272, 278, 280, 284].

In the same vein, the W and Mo co-decorated form of SynTiO₂ depicted also as expected the elemental compositions in the sample. From Figure 40a, Ti 2p spectra of Ti 2p_{3/2} and Ti 2p_{1/2} were obtained at 459 eV and 464.5 eV respectively and as attribute of Ti⁴⁺ ion state reported for TiO₂ material [122, 134, 272, 278, 280, 282]. O 1s spectral peaks were at 530.3 eV and 532.8 eV and attributed to Ti-O bond and Ti-OH functional groups linked to TiO₂ materials (Figure 40b) [122, 134, 162, 223, 272, 280, 282, 286, 290-291]. The Mo 3d spectral assignments were at 235.4 eV and 232.3 eV binding energies for the respective Mo 3d_{3/2}, and Mo 3d_{5/2} states while the W 4f spectra were assigned at respective binding energies of 35.9 eV and 37.9 eV for W 4f_{7/2}, and W 4f_{5/2} energy levels (Figure 40c, and d).

Again, these values were in line with already reported literature data for both Mo⁶⁺ and Mo⁵⁺ excited spin states contributions of Mo 3d_{5/2} and Mo 3d_{3/2} states as well those of W⁶⁺ and W⁵⁺ respective contributions of W 4f_{7/2}, and W 4f_{5/2} energy level states [272, 278, 280-282, 284].

The other case of W/SnyTiO₂ elemental atom composition spectral peak binding energies can be seen detailed in Table 18 with data values in line as already stated [122, 134, 162, 223, 272, 278, 280-282, 284, 286, 290-291].

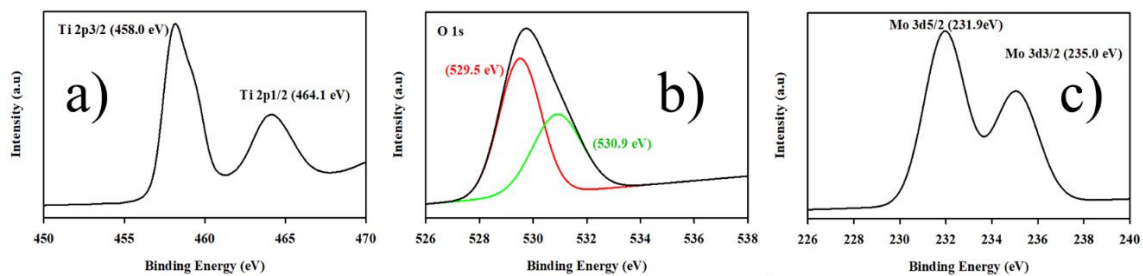


Figure 39. XPS spectra of Mo/SynTiO₂ showing elemental compositional peaks for: a) Ti 2p, b) O 1s, and c) Mo 3d

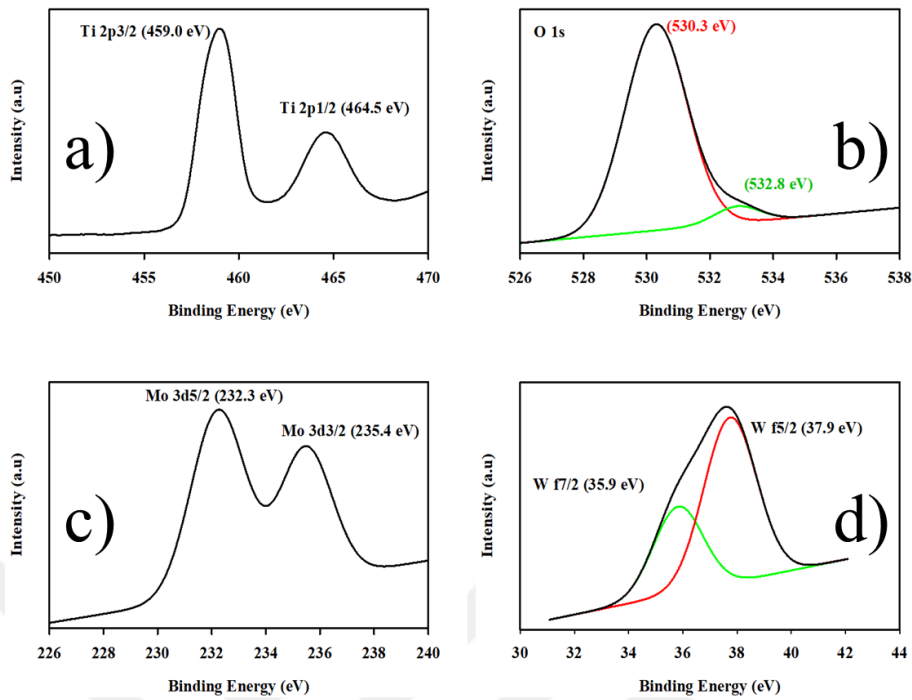


Figure 40. XPS spectra of W-Mo/SynTiO₂ showing elemental compositional peaks for: a) Ti 2p, b) O 1s, c) Mo 3d, and d) W 4f

3.9.6. UV-Visible Diffuse Reflectance Spectroscopy (UV-vis/DRS) Mode Measurement Analysis

Sample materials were analyzed by UV-vis diffuse reflectance spectroscopy (UV-vis/DRS) technique for the estimation of the energy band gap (E_g) values. Figure 41a-c show energy band gap estimates of HRTiO₂ and forms.

Kubelka-Munk function (Equation 84) has been used to obtain the Tauc's plot for the energy band gap (E_g) derivation, transforming the reflectance spectra into absorption spectra [293]. As can be seen from Figure 41a-c, band gap energies of the materials have been obtained from the Tauc's plot of $h\nu$ against $[F(R)h\nu]^{1/2}$ and extrapolating the linear part to the point where the $[F(R)h\nu]^{1/2}$ axis is equal to zero. Obtained E_g data values of the decorated materials did not show any significant shift in value relative to the unmodified HRTiO₂ sample material, hence the E_g values of both the modified and unmodified material samples were more or less the same and of range between 3.23 -3.26 eV (Table 16, Figure 41a-c).

Minute disparity of about 0.01-0.03 eV of measured E_g values amongst sample materials can be attributed to surface modification effects in the cases where they had occurred [134, 223].

$$F(R) = \frac{S(1-R)^n}{2R} \quad (84)$$

where $F(R)$, R and S are absorbance, reflectivity, and scattering factor respectively while we have assumed S to be a unit value as powder and $n = \frac{1}{2}$ as energy transition for indirect band gap semiconductor materials

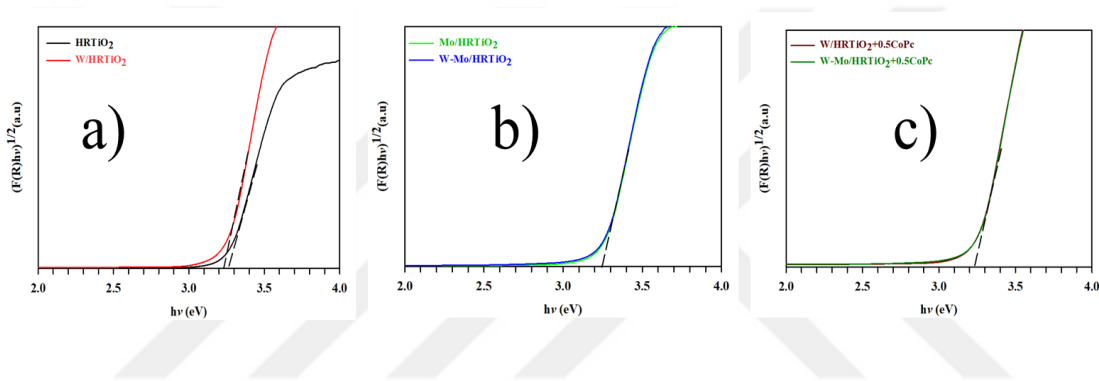


Figure 41. Energy band gap (E_g) estimates for: a) HRTiO_2 (black line), and W/HRTiO_2 (red line), b): Mo/HRTiO_2 (light green line), and $\text{W-Mo}/\text{HRTiO}_2$ (blue line), and c): $\text{W-Mo}/\text{HRTiO}_2 + 0.5\text{CoPc}$ (dark red line), and $\text{W-Mo}/\text{HRTiO}_2 + 1\text{CoPc}$ (dark green line)

Band edge potential as a related optical parameter was also estimated for HRTiO_2 and decorated forms with respect to their energy band gaps (E_g). This was in order to have some insight into the optical and electronic conditions favouring the transfer mechanism of photogenerated charges and their involvement in the subsequent formation of related reactive species needed for the photocatalytic degradation of the CECs compounds.

From the obtained energy band gaps (E_g), and employing Mulliken function according to Equations 85, and 86, conduction band (CB) and valence band (VB) edge potentials of the semiconductor photocatalyst materials were obtained as listed in (Table 16).

$$E_{cb} = \chi - E_e - 0.5E_g \quad (85)$$

$$E_{vb} = E_{cb} + E_g \quad (86)$$

where, from Equation 85, E_{cb} is the conduction band (CB) edge potential in (eV), χ is the absolute electronegativity value of the semiconductor photocatalyst material obtained from the geometric mean of the individual element electronegativity present in the photocatalyst material in (eV). E_e is the energy of the free electron on the standard normal hydrogen electrode (SHE) taken as a value of 4.5 eV [294]. E_g is the energy band gap of the considered photocatalyst material in (eV). Relating obtained conduction band edge potential (E_{cb}) in (eV) from Equation 85 with the energy band gap (E_g) of the semiconductor photocatalyst material, the valence band edge potential (E_{vb}) can be obtained and according to Equation 86.

Further explanation concerning this aspect will be given in the coming discussion section of the thesis.

In a similar development and using the same measurement technique and protocol, the energy band gaps of SynTiO₂ and decorated forms were also obtained.

As can be seen from (Figure 42a, and b), the estimated energy band gaps were considerably lower than that of the unmodified SynTiO₂. Energy band gap (E_g) value of 3.30 eV was obtained for SynTiO₂ in comparison to 3.05 eV for each of W/SynTiO₂ and Mo/SynTiO₂ and 3.02 eV for the co-decorated W-Mo/SynTiO₂ form (Table 17, Figure 42a, and b).

The modification strategy of doping by decoration of the base TiO₂ (SynTiO₂) in this case is suggested to have shifted the E_g to some extent other than that of HRTiO₂ material forms due to not only already suggested surface modification effect but also variation in synthesis protocol [223, 294].

Accordingly, the band edge potentials of the materials were also estimated and by Mullikan Equations 85-86 as already stated and listed in Table 17.

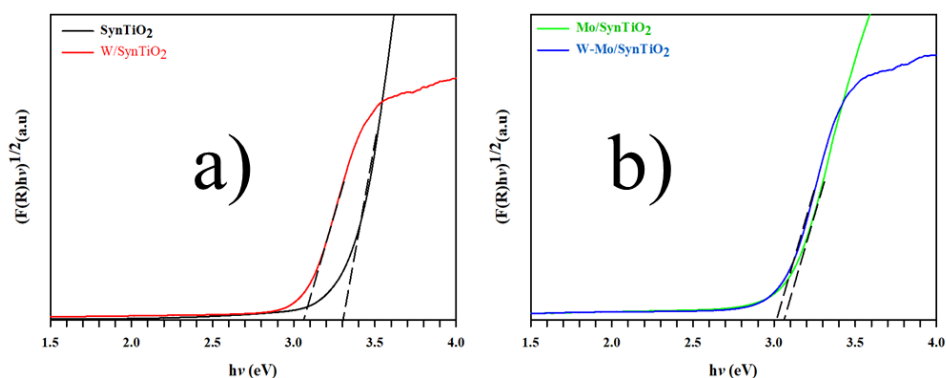


Figure 42. Energy band gap (E_g) estimates for a): SynTiO₂ (black line) and W/SynTiO₂ (red line), b): Mo/SynTiO₂ (green line), and W-Mo/SynTiO₂ (blue line)

3.10. Photocatalytic Test Measurement

The photocatalytic tests of the modified TiO₂ forms was conducted following their successful preparation and characterization towards ibuprofen (IBF), caffeine (CAF), and carbamazepine (CBZ) as the selected CECs compounds in order to ascertain their activity performance and under various experimental test conditions as will be discussed in the next sections.

3.10.1. Target CECs Compounds

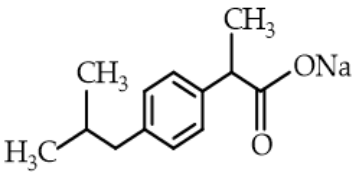
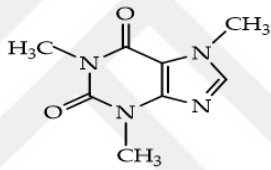
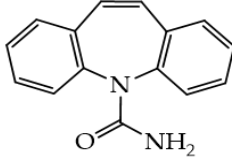
The target CECs compounds for the photocatalytic activity performance evaluation were ibuprofen, caffeine, and carbamazepine.

Ibuprofen is an anti-inflammatory substance and consumed as a pain relief for body pains, aches, and inflammations [222]. Caffeine on the other hand is a stimulant and widely consumed in a range of food and drink products helping the body overcome fatigue and get more actively engaged while carbamazepine is an anticonvulsant for epileptic remedies [122, 134, 162].

These compounds are regarded as contaminants of emerging concerns (CECs) and have been classified as pharmaceuticals and personal care products (PPCPs) (Table 1).

Table 19 below show some basic information on their physico-chemical properties

Table 19. Characteristics of Ibuprofen (IBF), Caffeine (CAF), and Carbamazepine (CBZ) as the tested model CECs compounds

Chemical property/Name	Ibuprofen sodium salt
Chemical structure	
Molecular formula	C ₁₃ H ₁₇ O ₂ Na
CAS No.	31121-93-4
Molecular weight, g/mol	228.26
Solubility in water, g/L	100
pK _a	4.52-4.9
Chemical property/Name	Caffeine
Chemical structure	
Molecular formula	C ₈ H ₁₀ N ₄ O ₂
CAS No.	58-08-2
Molecular weight, g/mol	194.19
Solubility in water, g/L	18.7
pK _a	10.4
Chemical property/Name	Carbamazepine
Chemical structure	
Molecular formula	C ₁₅ H ₁₂ N ₂ O
CAS No.	298-46-4
Molecular weight, g/mol	236.27
Solubility in ethanol, g/L	50
pK _a	13.9

4. DISCUSSION

4.1. General Outlook on Material Sample Characterizations

Following the characterization of the as available HRTiO₂ as well as the sol-gel synthesized TiO₂ (SynTiO₂) and decorated forms and on the α -Al₂O₃ ceramic support immobilized active TiO₂, there were no outright alteration in the structural/textural, morphological, and optical properties of the modified material samples suggesting that the pristine profile of the base TiO₂ materials was maintained. Some observed differences in material sample characterization result output, however, were because of the adopted surface modification strategy (decoration and sensitization) and to some other point the sol-gel adopted synthesis protocol for the preparation of SynTiO₂ and its forms.

4.2. Photocatalytic Activity Evaluation of the HRTiO₂ and Decorated Material Forms

Firstly, and for a preliminary test, HRTiO₂ and the decorated forms were tested towards each of model CECs compounds and the best performing photocatalyst material deployed for further photocatalytic test investigations.

4.2.1. Photocatalyst Material Test Evaluation Over Ibuprofen (IBF)

Seen in Figure 43 is the display of the preliminary test result of the photocatalytic degradation of the decorated HRTiO₂ forms towards ibuprofen.

At initial natural (unmodified) pH condition and under 365 nm irradiation for 1 h, W/HRTiO₂ removed almost completely the initial 50 mg/L IBF concentration. Comparatively, the anatase HRTiO₂ control material as well as the Mo/HRTiO₂ also showed impressive performance but from the photocatalytic degradation rate constant (Figure 43b), W/HRTiO₂ edged out the rest in its activity performance with a k value of about 3.15 h⁻¹.

Based on this outcome, W/HRTiO₂ was investigated further for the photocatalytic degradation of ibuprofen and under series of other test conditions with sampling performed (per min basis rather than (per h) as was the case with the preliminary test for the photocatalyst selection in order to have more understanding over the trend of degradation rate (k) constant.

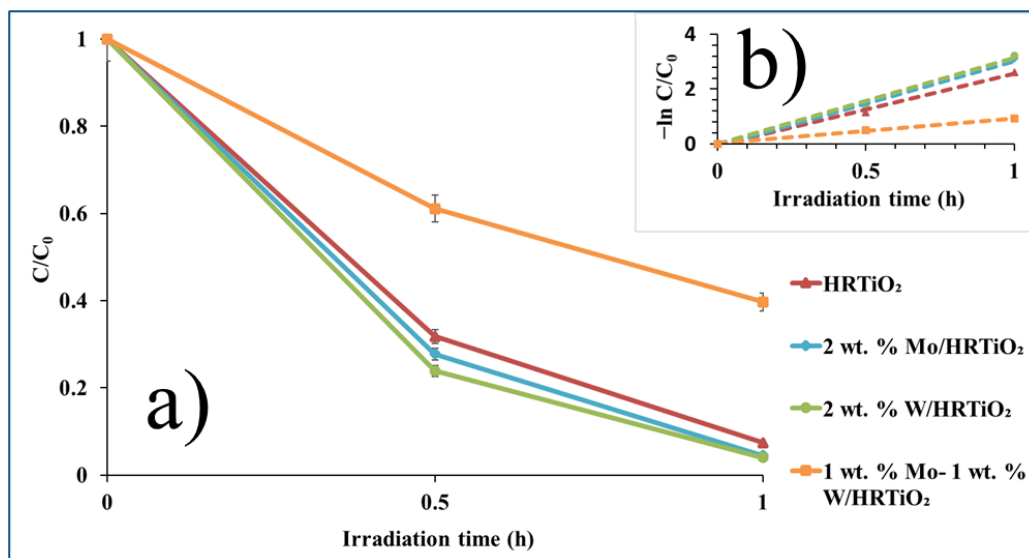


Figure 43. a) Preliminary test for the photocatalytic degradation of ibuprofen ($C_0 = 50$ mg/L, initial pH_{natural} (unmodified) condition under 365 nm irradiation with HRTiO₂ and decorated forms, b) corresponding photocatalytic degradation rate constant (k)

4.2.1.1. Effect of pH

4.2.1.1.1. pH Point of Zero Charge (pH_{pzc})

pH being an important parameter in the degradation of organic chemical compounds was investigated. For this reason, the pH_{pzc} of the W/HRTiO₂ was estimated and found to be around 4.4 (Figure 44). The acidic nature of the transition W metal oxide might have shifted the pH_{pzc} of the photocatalyst material to a lower point despite being in combination with base TiO₂ material of reported pH_{pzc} of range 5.5-6.5 [134].

Firstly, an unmodified initial pH value of 5.13 was tested in aqueous suspension of W/HRTiO₂ for the photocatalytic degradation of IBF (Figure 45). A 1 g/L catalyst under this unmodified pH condition after 140 min of 365 nm UV irradiation, removed almost 100 % of initial 50 mg/L IBF concentration. Other initial pH values of 4.5 and 6.5 were also tested (Figure 45).

The order of photocatalytic activity performance with respect to the tested initial pH values (Figure 45) is $\text{pH} = 4.5 \geq \text{pH} = 5.13 > \text{pH} = 6.5$. The pK_a value of IBF has been reported in the range of 4.52-4.9 (Table 19) [222]. This result can be explained by the pH point of zero charge (pH_{pzc}) of the W/HRTiO₂ photocatalyst material (Figure 44). It is well

known that the photocatalytic degradation efficiency of the photocatalyst over IBF can be related to the speciation and distribution of the IBF species in aqueous medium and the charge state of the W/HRTiO₂ photocatalyst material surface. At the initial natural (unmodified) pH condition of 5.13, the IBF molecules become ionically speciated with anion predominance and partial protonation as the aqueous pH condition at this point lies within the IBF pK_a value range of 4.9-5.2.

Associatively, the photocatalyst surface with pHPzc of 4.4 at this pH condition induces a negatively charged photocatalyst surface thereby exerting a force of attraction on the protonated IBF species to surface of the photocatalyst for subsequent degradation. At the pH = 4.5 condition, the more fully protonated IBF ions are attracted to the negatively charged photocatalyst material surface for subsequent degradation. The pH = 6.5 condition showed a lesser photocatalytic degradation activity in comparison to pH = 5.13 (unmodified) and pH = 4.5 as large number of anionic species dominated under this condition. As such with the dominance of more anionic species and negatively charged photocatalyst surface, induced electrostatic force of repulsion tend to inhibit the photocatalytic degradation of IBF molecule as they maintain a rather not close contact with the catalyst surface where the degradation takes place.

Though the pH condition of 4.5 showed a more concerted photocatalytic activity performance with a little edge than the natural (unmodified) pH = 5.13 condition (Figure 45a), further photocatalytic tests evaluations were carried out under the natural (unmodified) pH = 5.13 in order to keep test pH condition as less varied as possible.

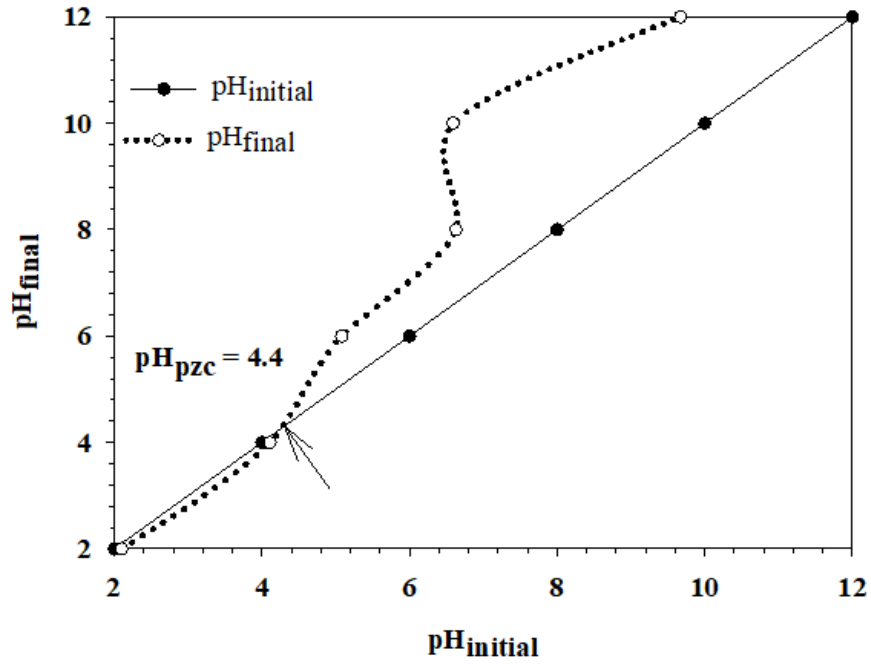


Figure 44. pH point of zero charge (pH_{pzc}) plot of 2 wt. % W/HRTiO₂ photocatalyst material

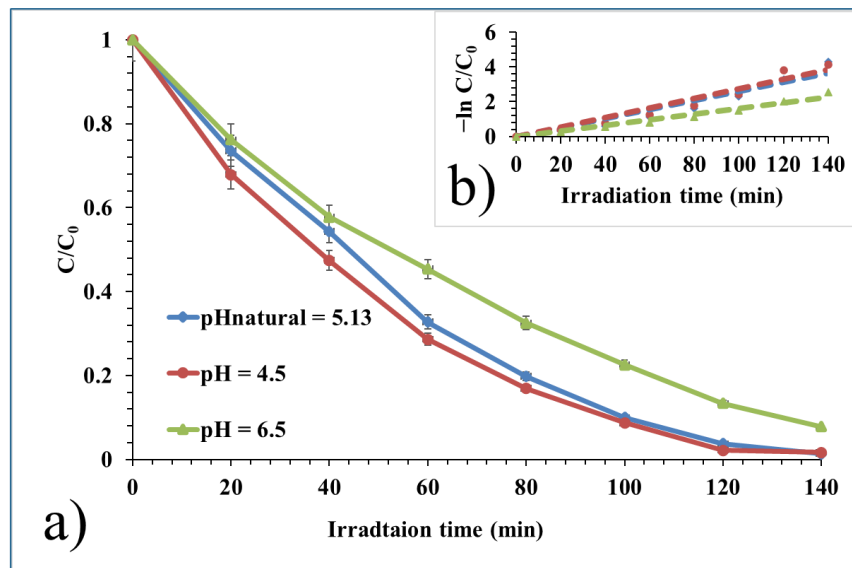


Figure 45. a) pH effect on the photocatalytic degradation efficiency of W/HRTiO₂ over IBF ($C_0 = 50$ mg/L), and b) corresponding photocatalytic degradation rate constant (k)

4.2.1.2. Effect of Catalyst Dosage and Initial IBF Concentration

The effect of catalyst dosage was investigated employing different amount of the W/HRTiO₂ photocatalyst. In addition to the 1 g/L catalyst dose, 0.5 g/L, 1.5 g/L and 2 g/L W/HRTiO₂ catalyst doses were tested of their photocatalytic activity efficiency over the degradation of 50 mg/L initial IBF concentration and at natural (unmodified) pH condition of 5.13. As can be seen from the Figure 46a, with the increase in catalyst load, photocatalytic degradation rate increased. This is because with certain amount increase in catalyst load, more active sites are available on the photocatalyst surface for the degradation of the organic pollutant. However, 1 g/L catalyst load was more efficient in the removal of almost completely the initial 50 mg/L IBF concentration while at 2 times that amount and that is 2 g/L the photocatalytic degradation rate of removal of IBF was a bit inhibited (Figure 46a). This is because at higher catalyst load amount, shielding effect is encountered whereby proper photo illumination of the aqueous suspension reaction media is suppressed [162, 223].

While the photocatalytic degradation rate constant at 1 g/L and 2 g/L catalyst doses were more or less the same, 1.5 g/L catalyst dosage delivered a degradation effect more like 0.5 g/L at rate constants of $\sim 0.01 \text{ min}^{-1}$ each (Fig 46b). The light penetration hindering due to shielding effect at some elevated catalyst dose concentration may suggest the reason for the low photocatalytic degradation rate constant of 1.5 g/L compared to 1 g/L and 2 g/L (Figure 46a, and b).

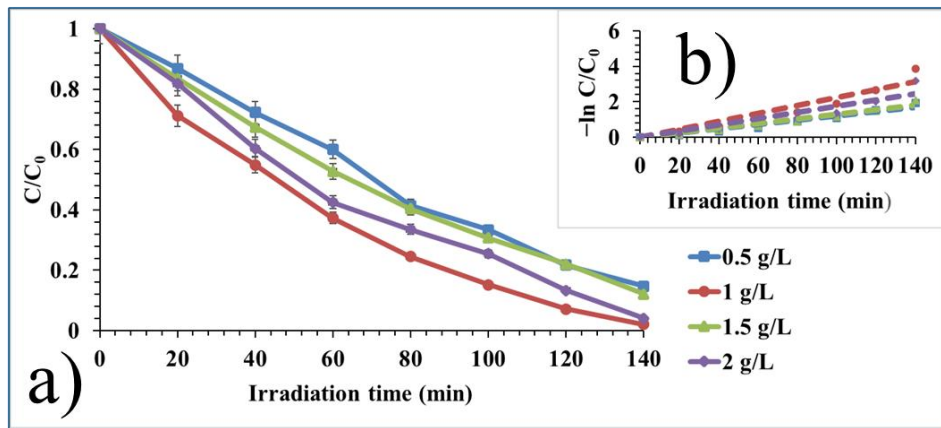


Figure 46. a) Catalyst dosage effect on the photocatalytic degradation efficiency of W/HRTiO₂ over IBF ($C_0 = 50$ mg/L, initial pH_{natural} (unmodified) = ~ 5.13), and b) corresponding photocatalytic degradation rate constant (k)

On the other hand, initial pollutant effect of IBF on the photocatalyst activity degradation efficiency as can be seen from Figure 47a and b is such that photocatalyst efficiency reduced with increase in initial pollutant concentration. This has been attributed to the blockage of active photocatalyst sites at higher pollutant concentration thereby resulting to inefficient mass transfer of the substrates across the surface of the photocatalyst material for subsequent degradation (Figure 47) [162, 223].

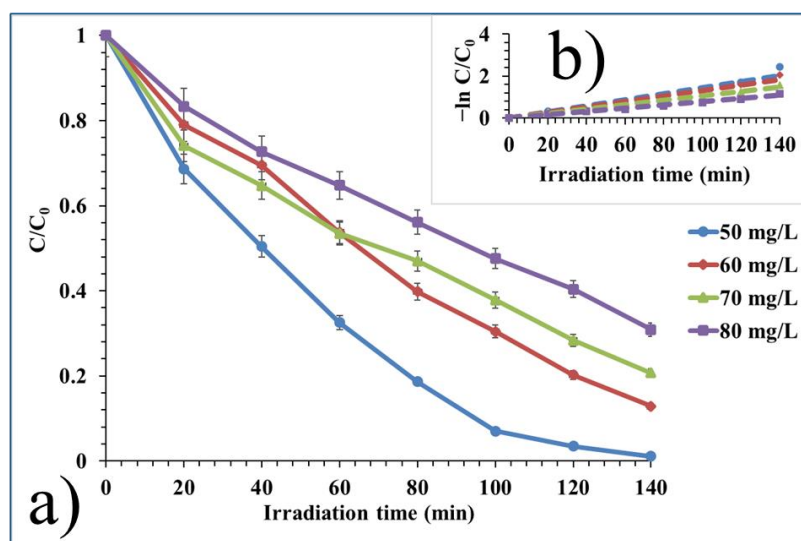


Figure 47. a) Initial IBF concentration effect on the photocatalytic degradation efficiency of 1 g/L W/HRTiO₂ at initial pH_{natural} (unmodified) = ~ 5.13, and b) corresponding photocatalytic degradation rate constant (k)

With the investigated catalyst dosage and initial IBF pollutant effects at pH_{natural} (unmodified) value = 5.13 showing best photocatalytic activity outcome, further photocatalytic test evaluations were carried out with 1g/L catalyst dosage, 50 mg/L initial IBF concentration and pH_{natural} (unmodified) condition of 5.13.

4.2.1.3. Effect of Chemical Scavengers

The effect chemical scavengers will have on the photocatalytic degradation rate was investigated and subsequently used to decipher the reactive species responsible for driving the photooxidation reaction. Benzoquinone (BQ), isopropyl alcohol (IPA), and ammonium oxalate (AO) were employed as the chemical scavengers for the respective probe of superoxide anion (O₂^{•-}), hydroxyl radical (HO[•]), and hole charge carrier (h⁺) at 1 mM concentration each [134, 162, 222-223]. As can be seen from the Figure 48, isopropyl alcohol (IPA) showed a stronger suppression effect on the photocatalytic degradation of IBF. Similarly, the introduction of ammonium oxalate (AO) probing for hole charge carrier (h⁺), though with no show of suppression upon its addition up to the 60 min irradiation time, exerted at 140 min irradiation suppression effect as witnessed with IPA addition. In contrast to the no added scavenger, while IPA and AO suppressed the photocatalytic degradation of

ibuprofen at 140 min irradiation with $\sim 0.02 \text{ min}^{-1}$ rate constant for each in comparison to $\sim 0.03 \text{ min}^{-1}$ for no added scavenger (Figure 48b), benzoquinone (BQ) for ($\text{O}_2^{\cdot-}$) probe instead exerted an enhanced effect on the photocatalytic degradation rate of IBF with a rate constant of $\sim 0.04 \text{ min}^{-1}$ (Figure 48b).

This observation has been reported of reactive species instead of impeding reaction rate on addition, accelerate it due to favoured prevailing experimental conditions upon their addition that can bring about the destruction of the organic compound substrates easily and make it possible for these reactive species to interact with them to a positive resultant effect of promoting the degradation process [295-296]. Therefore, the added chemical scavengers have exerted their suppressive effects on the photocatalytic degradation of IBF in the order: $\text{BQ} \ll \text{AO} \leq \text{IPA}$.

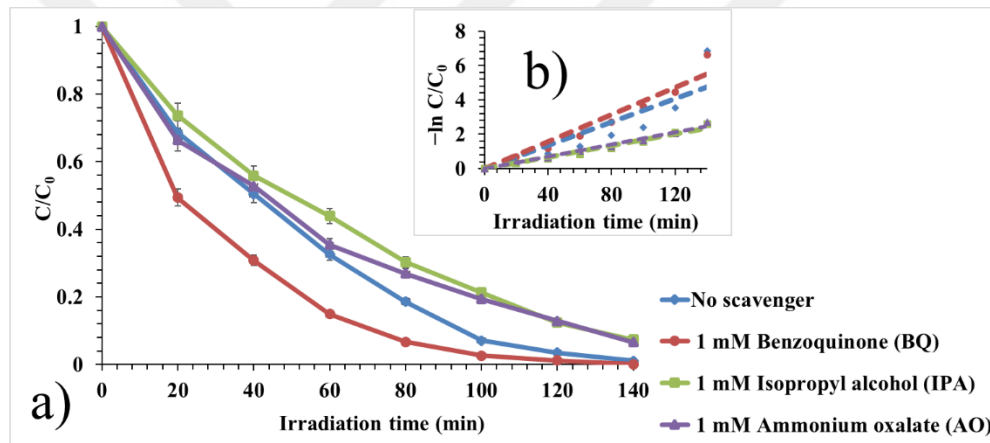


Figure 48. a) Chemical scavenger effect on the photocatalytic degradation efficiency of 1 g/L W/HRTiO₂ over IBF ($C_0 = 50 \text{ mg/L}$, initial $\text{pH}_{\text{natural}}$ (unmodified) = ~ 5.13), and b) photocatalytic degradation rate constant (k)

4.2.1.4. Effect of Contaminant Ions (Cations and Anions), and Humic Acid (HA)

The effects of some contaminant ions as well as humic acid in form of surrogate dissolved organic matter (DOM) was investigated on the photocatalytic degradation process of IBF. As can be seen from Figure 49, the influence of these selected cations: Mg^{2+} , Ca^{2+} , Al^{3+} , and NH_4^+ and at 1 M concentration each on a general basis increased the removal rate of IBF in comparison to no added cation. At 140 min of irradiation and in the presence of the added inorganic cations, there was approximately complete removal of IBF (Figure 49).

The photocatalytic degradation removal rate for Mg^{2+} , Ca^{2+} , and NH_4^+ was $\sim 0.05 \text{ min}^{-1}$ in comparison to no added cation at 0.03 min^{-1} . On the other hand, photocatalytic activity performance in the presence of Al^{3+} ion was more impressive with almost a complete IBF removal at 60 min irradiation time and an $\sim 0.06 \text{ min}^{-1}$ degradation rate in comparison to the other tested and no added cations (Figure 49). Though the non-influence of Mg^{2+} , and Ca^{2+} ions as well the inhibitory effect of NH_4^+ and Al^{3+} ions on the photocatalytic degradation process of some organic compounds have been reported [162, 223, 297-298].

The observed facilitated effect on the oxidation/reduction of IBF taking place during the photochemical process can be attributed to the stimulating IBF photocatalytic effect by the chloride ion (Cl^-) counterpart of these cations [297]. Moreover, the shift from some kind of a moderate acidic initial pH values before the addition of these cations to much a lower moderate final pH values in comparison to the no added cation condition and in particular with the case of NH_4^+ and Al^{3+} ions addition; indicate a favoured hydroxyl radical ($\text{HO}\cdot$) generation condition and thus the more increased photocatalytic degradation rate witnessed in the presence of these ions (Figure 49).

Based on the photocatalytic degradation rate kinetics, the enhancing effect of the tested cations over IBF degradation can be seen to have followed the order: $\text{Al}^{3+} > \text{Mg}^{2+} \sim \text{Ca}^{2+} \sim \text{NH}_4^+$ (Figure 49a, and b). Result outcome might also differ based on different photocatalyst material usage and other accompanied experimental test conditions.

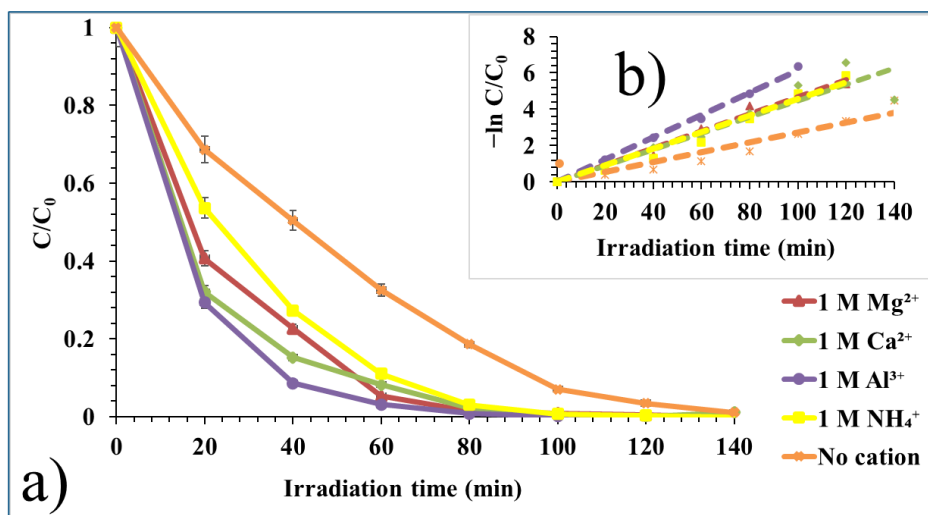


Figure 49. a) Cations effect on the photocatalytic degradation of 1 g/L W/HRTiO₂ over IBF ($C_0 = 50$ mg/L, initial pH_{natural} (unmodified) = ~ 5.13), b) corresponding photocatalytic degradation rate constant (k)

Similarly, tested anions at 1 M concentration; showed CO₃²⁻ ion at 20 min irradiation time removed over 95 % initial 50 mg/L IBF concentration (Figure 50). By 100 min. irradiation time, Cl⁻, HCO₃⁻, HPO₄²⁻ together with CO₃²⁻ with an already impressive activity at 60 min irradiation, removed almost completely the initial 50 mg/L IBF concentration showing a better photocatalytic degradation rate kinetics than SO₄²⁻ which showed kind of equal activity performance at 140 min irradiation time with no added anion (Figure 50). As can be seen, a gradually improved photocatalytic degradation kinetics in the presence of the anions categorically was drastic in the first 20 min irradiation for CO₃²⁻ and stabilizes up to 100 min irradiation while for Cl⁻, and HCO₃⁻ it was a bit slow yet steady up to 100 min irradiation. HPO₄²⁻ and SO₄²⁻ were the most impeding of the photocatalytic degradation reaction rate but more enhancing than the no added anion condition with the three conditions reaching equal rate of reaction at 80 min (Figure 50). Data analysis from the photocatalytic degradation rate of the reaction of the photocatalyst material towards IBF show that in the presence of CO₃²⁻, Cl⁻, HCO₃⁻, HPO₄²⁻ anions, photocatalyst activity performance increased but with a retarding effect in the presence of SO₄²⁻ in comparison to no added anion (Figure 50a, and b). While the enhancing effect seen from the added CO₃²⁻ anion is attributed to its possible co-existence with HCO₃⁻ as a buffer at the final suspension medium of pH condition of ~ 11 (Table 20), Cl⁻ promoted generation of chlorinated

oxidants that supported the generation of free hydroxyl radical ($\text{HO}\cdot$) needed for the decomposition of IBF [298]. The scavenging ability of HPO_4^{2-} , and SO_4^{2-} including CO_3^{2-} and HCO_3^- is also a positive effect as it creates additional radicals that synergistically improved the photocatalytic degradation of IBF as an organic compound with a carboxylic functional group [134, 298]. However, the less significant inhibition shown by SO_4^{2-} at 140 min irradiation is attributed to its ability as a doubly charged ion to displace surface hydroxyl (OH^-) ion on the photocatalyst via ligand transfer mechanism aided by its van der Waals forces and hydrogen bond affiliation power [134, 162, 223, 298]. This interference is possible with CO_3^{2-} , and HPO_4^{2-} anions as doubly charged ions as well but showed little or no inhibition effect by the presence of these ions based on this phenomenon in the sense that it was offset by the buffer co-existence of CO_3^{2-} and HCO_3^- as an enhancing factor and the presence of displaceable hydrogen ion (H^+) in HPO_4^{2-} anion which can be readily available to generate other oxidant species enabling photocatalytic degradation process as a counter compensation effect [162].

Notwithstanding, a shift of initial pH values to higher ones in the presence of these ions except for the case of Cl^- which inherently is an oxidant is an attribute to their presence for an enhanced photocatalytic activity performance. The initial pH condition of no added anion to that of its final pH condition by a unit decreased but made no difference as there was no externally added effects (Table 20).

Thus, for the anions, order of their enhancing effect on the photocatalytic degradation process follows: $\text{CO}_3^{2-} > \text{Cl}^- > \text{HCO}_3^- > \text{HPO}_4^{2-} > \text{SO}_4^{2-}$ (Figure 50a, and b).

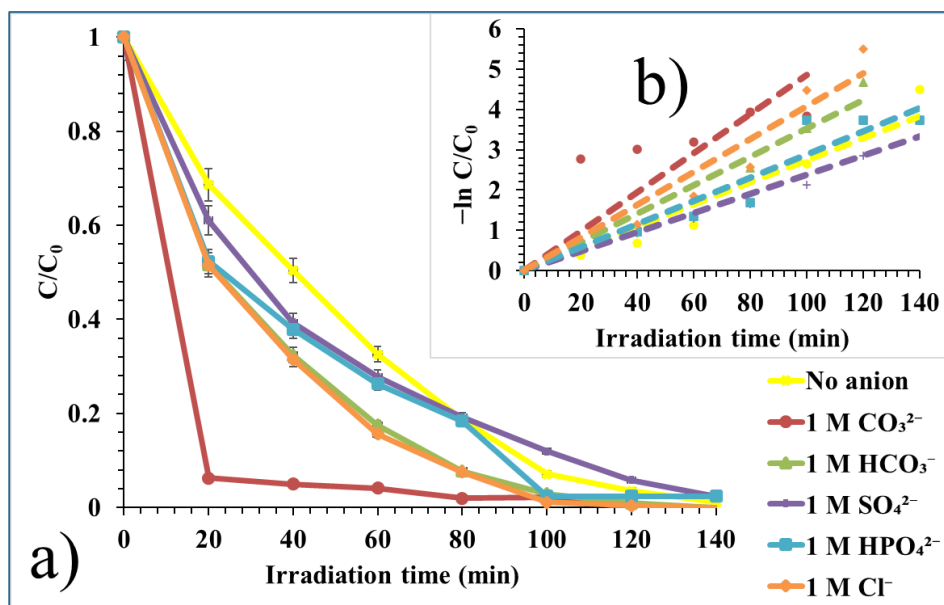


Figure 50. a) Anions effect on the photocatalytic degradation efficiency of 1 g/L W/HRTiO₂ over IBF ($C_0 = 50$ mg/L, initial pH_{natural} (unmodified) = ~ 5.13), and b) corresponding photocatalytic degradation rate constant (k)

Effect of organic matter on the photocatalytic degradation process was investigated with the addition of synthetic Na humic acid (HA) each of concentration 1 mg/L – 4 mg/L. As can be seen from Figure 51, almost total removal of the initial 50 mg/L IBF concentration occurred at 140 min irradiation time in the presence of 1 mg/L and 2 mg/L HA as was the case also with no HA addition. The photocatalytic degradation rate kinetics at 1 mg/L HA and 2 mg/L, progressed at a gradual rate until the 140 min irradiation time window and showed no significant difference in comparison to no HA addition as each test condition displayed an $\sim 0.03 \text{ min}^{-1}$ degradation rate constant (Figure 51a, and b). This indicates that addition of 1 mg/L HA and 2 mg/L HA produced little or no effect on the photocatalytic degradation process when compared to no HA addition.

Though addition of HA acids has been reported to show hampering effect on the photocatalytic degradation of organic pollutants due to competitive coverage of catalyst surface active sites as well as blockage of light penetration into suspension media meant for generation of reactive species which drive the reaction process [134, 162, 223].

However, and in some other cases, they have been able to induce indirect alternative reactive species generation with their inner filtering capacity as they scavenge radicals and, in the process, produce reactive radicals themselves for the enhancement of photocatalytic degradation process [223]. The slight but not significant positive effect of the photocatalytic

degradation process witnessed in the presence of 1 mg/L and 2 mg/L HA seen between 60-120 min irradiation time (Figure 51a) in comparison to no HA addition can be attributed to one of such its positive impact while the inhibitory effect of HA at 3 mg/L and 4 mg/L to the photocatalytic degradation process is an attribute of its retardation effect as already pointed out especially at higher concentration (Figure 51a, and b) [134, 162, 223]. While the initial pH condition of the suspension media changed to a little lower final pH point values (Table 20) and maintained these values at the final point; felt influence on the photocatalytic degradation process in the presence of these HA concentration can be ruled out to a point and rather not exclude some possible interactions from the Na content of the HA in ionic form. Thus, the inhibition effect of HA on the photocatalytic degradation process of IBF is such of the order: 1 mg/L HA = 2 mg/L HA < 3 mg/L HA ≤ 4 mg/L HA.

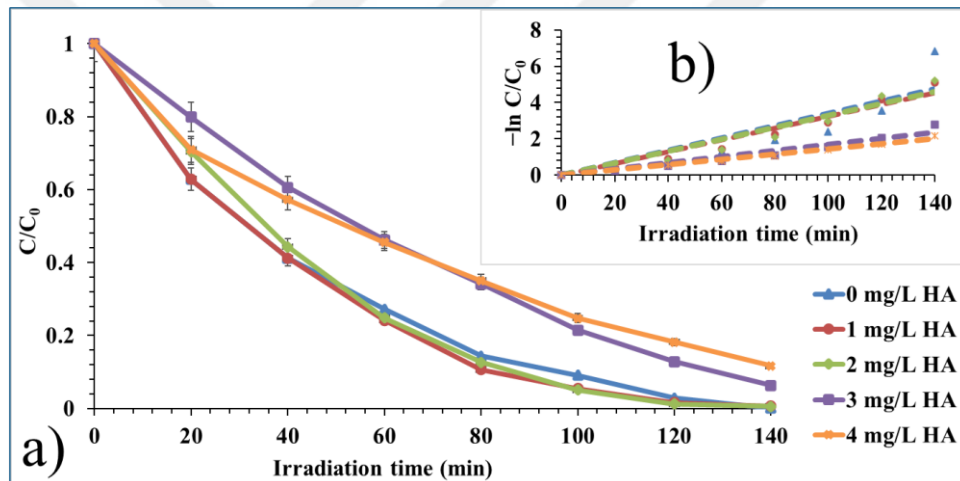


Figure 51. a) Humic acid (HA) effect on the photocatalytic degradation efficiency of 1 g/L W/HRTiO₂ over IBF ($C_0 = 50$ mg/L, initial pH_{natural} (unmodified) = ~ 5.13), and b) corresponding photocatalytic degradation rate constant (k)

4.2.1.5. Effect of Hydrogen Peroxide (H₂O₂)

In the presence of H₂O₂ of different concentrations, 1 mM – 4 mM, no significant effect on the photocatalytic degradation process was exerted as almost complete IBF removal at 140 min irradiation occurred (Figure 52).

Retrospectively, during the early irradiation time window, there were mixed outcome, where in the presence of 2 mM H₂O₂, photocatalytic degradation rate kinetics was the most favoured at $\sim 0.05 \text{ min}^{-1}$ than 1 mM H₂O₂ at $\sim 0.04 \text{ min}^{-1}$ and with 4 mM H₂O₂ at $\sim 0.03 \text{ min}^{-1}$ than 3 mM H₂O₂ at $\sim 0.02 \text{ min}^{-1}$ (Figure 52). This observation can be attributed to different possible electron (e⁻) scavenging attitude by the different added H₂O₂ doses [223]. While this electron scavenging attitude of the added H₂O₂ at those tested concentrations remained within limit where it was not excessive, there was overall improvement of the photocatalytic degradation process in comparison to no H₂O₂ addition (Figure 52a, and b).

Thus, the added H₂O₂ as an external oxidant exerted enhancing effect on the photocatalytic degradation process over no H₂O₂ addition in the order: 2 mM H₂O₂ > 1 mM H₂O₂ > 4 mM H₂O₂ > 3 mM H₂O₂. Again, changes in the final pH condition were maintained and remained stable during the photocatalytic degradation process reaction (Table 20).

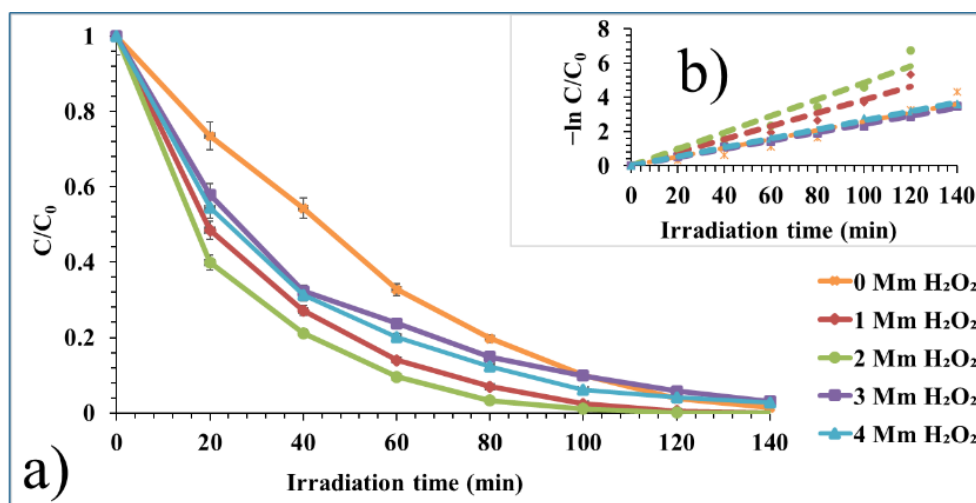


Figure 52. Hydrogen peroxide (H₂O₂) effect on the photocatalytic degradation efficiency of 1 g/L W/HRTiO₂ over IBF ($C_0 = 50 \text{ mg/L}$, initial pH_{natural} (unmodified) = ~ 5.13 , and b) corresponding photocatalytic degradation rate constant (k)

Dark reaction condition effect, 365 nm UV light (photolysis) effect, heat effect without the presence of catalyst in the reaction media whereby the photo reactor cells were wrapped with aluminium foils to prevent light irradiation into cells as well heat effect with the presence of catalyst with again reactor cells wrapped with aluminium foils to ward off light penetration were all investigated and found of no significant contribution towards the photocatalytic/photodegradation of IBF. Figure 53 shows the plotted effect of these investigated test conditions.

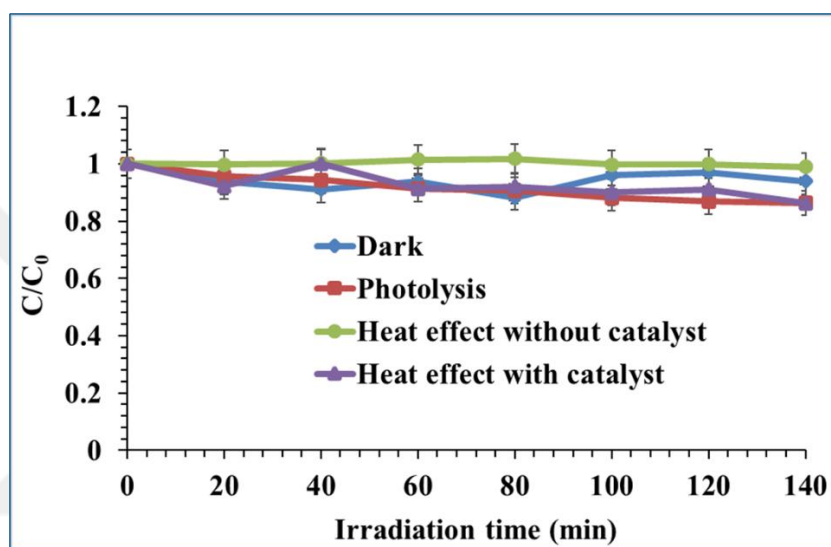


Figure 53. Dark, photolysis, heat effect without catalyst and heat effect with catalyst test conditions at 1 g/L W/HRTiO₂, [IBF]₀ = 50 mg/L, initial pH_{natural} (unmodified) = ~ 5.13 as applicable

4.2.1.6. Evaluation of Visible Light Photocatalytic Activity

Under 450 nm visible light irradiation, the cobalt phthalocyanine sensitized W/HRTiO₂ of 0.5 and 1 (wt. % CoPc) each were investigated. As can be seen from Figure 54, 0.5 wt. % CoPc sensitized W/HRTiO₂ (2 wt. % W/HRTiO₂ + 0.5CoPC) at 240 min irradiation achieved over 60 % IBF removal at initial natural (unmodified pH) condition. For the first 120 min irradiation and in terms of the degradation kinetics, the 2 wt. % W/HRTiO₂ + 0.5CoPC was more appreciative than the unsensitized form of 2 wt. % W/HRTiO₂ but equalled at 160 min irradiation maintaining that till the complete irradiation time window at 240 min (Figure 54). Approximately at the 240 min irradiation time, the degradation rate constant was ~ 0.005 min⁻¹ for both the 0.5 wt. % CoPc sensitized

W/HRTiO₂ and the unsensitized W/HRTiO₂. This suggest that both the unsensitized and the 0.5CoPc sensitized material were visible light photoactive for the degradation of IBF, however, the excitation of the sensitized form was faster as can be seen in the Figure 54 during the first 160 min of irradiation with the unsensitized form lagging at this time. The 1 wt. % sensitized CoPc material (2 wt. % W/HRTiO₂ + 1CoPC) did not show a better performance than the unsensitized and 0.5 wt. % CoPc sensitized. With only just about 20 % IBF removal after 140 min irradiation and $\sim 0.002 \text{ min}^{-1}$ degradation rate constant; a conclusion that at a higher load of 1 wt. % CoPc as a sensitizer; photocatalytic activity performance is impeded hence the steric interfering feature of Pc molecules due to their large size especially at advanced weight loads is confirmed [122, 222-223]. The final pH condition of reaction media was steady and maintained almost the same value throughout the entire irradiation process (Table 20).

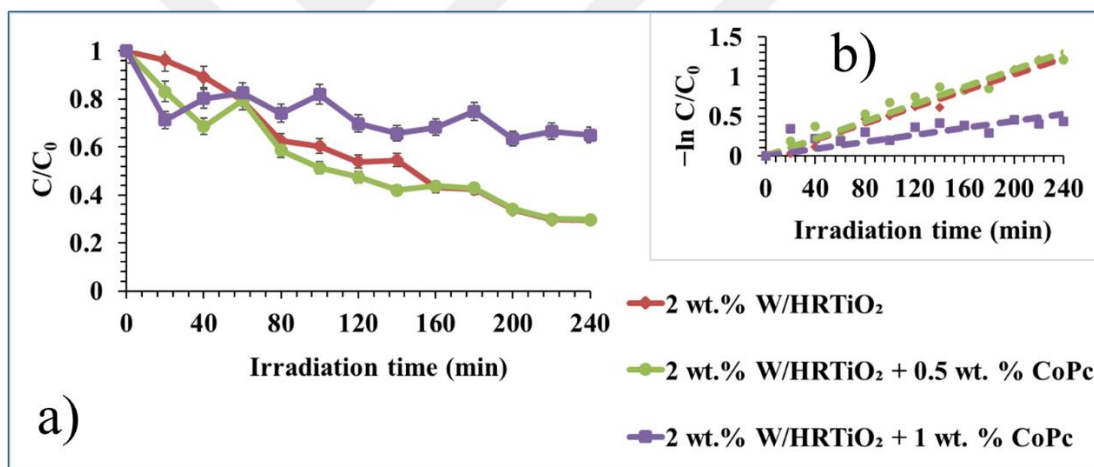


Figure 54. a) Visible light photocatalytic evaluation of W/HRTiO₂, W/HRTiO₂ + 0.5CoPc, and W/HRTiO₂ + 1CoPc at 1 g/L each for IBF degradation ($C_0 = 10 \text{ mg/L}$, initial $\text{pH}_{\text{natural}}$ (unmodified) = ~ 5.13), and b) corresponding photocatalytic degradation rate constant (k)

Shown in Table 20 is the different investigated photocatalytic test parameters with data results as per their degradation rate constant k (h^{-1} or min^{-1}), correlation coefficient constant (R^2), half-life ($t_{1/2}$) (h or min) as well as variation between the initial and final pH values of the different test conditions of the photocatalyst material.

Table 20. Tested photocatalytic parameters for ($C_0 = 50$ mg/L initial IBF concentration under 365 nm, $C_0 = 10$ mg/L initial IBF concentration under 450 nm) with 1 g/L catalyst and their associated rate constant k (h^{-1} or min^{-1}), correlation coefficient (R^2), half-life $t_{1/2}$ (h or min), and initial and final pH values

Test	Degradation rate constant k (h^{-1} or min^{-1})	R^2	Half-life ($t_{1/2}$) (h or min)	pH _{initial}	pH _{final}
Preliminary test for photocatalyst material selection ^{#, *}					
HRTiO ₂	2.5411	0.99	0.27	6.42	6.19
W/HRTiO ₂	3.1458	0.99	0.22	5.13	4.25
Mo/HRTiO ₂	0.29978	0.99	2.31	4.31	3.78
W-Mo/HRTiO ₂	0.9364	0.99	0.74	4.72	4.19
Selected photocatalyst material: W/HRTiO ₂					
pH effect ^{#, □}					
pH _{natural} = 5.13	0.026	0.97	26.65	5.14	4.30
pH = 4.5	0.0274	0.98	25.29	4.50	3.97
pH = 6.5	0.0163	0.99	42.52	6.50	4.95
Catalyst dosage effect ^{#, □}					
0.5 g/L	0.0121	0.98	57.27	5.13	4.31
1 g/L	0.0223	0.96	31.08	5.13	4.30
1.5 g/L	0.0129	0.98	53.72	5.13	4.31
2 g/L	0.0176	0.95	39.38	5.11	4.31
Initial pollutant (IBF) concentration effect ^{#, □}					
50 mg/L	0.0244	0.97	28.40	5.13	4.31

Continuation of Table 20

60 mg/L	0.013	0.99	53.31	5.20	4.28
70 mg/L	0.0105	0.99	66.00	5.22	4.30
80 mg/L	0.0078	0.99	88.85	5.20	4.22
Chemical scavengers ^{#, □}					
No scavenger	0.0277	0.90	25.02	5.13	4.28
1mM BQ	0.0395	0.98	17.54	5.17	3.96
1mM IPA	0.0169	0.99	41.01	5.07	4.41
1 mM AO	0.0177	0.99	39.15	5.09	4.45
Contaminant ion effect: Cation ^{#, □}					
No Cation	0.0274	0.97	25.29	5.11	4.22
1 M Mg ²⁺	0.0468	0.99	14.81	4.99	4.06
1 M Ca ²⁺	0.0447	0.96	15.50	5.21	4.14
1 M Al ³⁺	0.0614	0.99	11.29	5.24	3.69
1 M NH ₄ ⁺	0.0457	0.99	15.16	5.24	3.98
Contaminant ion effect: Anion ^{#, □}					
No Anion	0.0274	0.97	25.29	5.12	4.24
1 M CO ₃ ²⁻	0.0485	0.90	14.29	5.20	11.03
1 M HCO ₃ ⁻	0.0352	0.99	19.69	5.10	9.18
1 M SO ₄ ²⁻	0.0238	0.99	29.12	5.13	4.17
1 M HPO ₄ ²⁻	0.0223	0.99	31.08	5.22	8.67
1 M Cl ⁻	0.0408	0.97	16.99	5.07	4.18
Humic acid (HA) effect ^{#, □}					
0 mg/L HA	0.0264	0.98	26.25	5.15	4.25
1 mg/L HA	0.0339	0.90	20.44	5.05	4.11
2 mg/L HA	0.0329	0.97	21.06	5.04	4.02
3 mg/L HA	0.0169	0.98	41.01	5.08	4.25
4 mg/L HA	0.0144	0.99	48.13	5.01	4.29
Hydrogen peroxide (H ₂ O ₂) effect ^{#, □}					
0 mM H ₂ O ₂	0.0260	0.97	26.65	5.10	4.28
1 mM H ₂ O ₂	0.0387	0.96	17.91	5.00	4.02

--	--	--	--	--	--

Continuation of Table 20

2 mM H ₂ O ₂	0.0483	0.98	14.35	5.02	3.98
3 mM H ₂ O ₂	0.0242	0.99	28.64	5.01	4.23
4 mM H ₂ O ₂	0.0266	0.99	26.05	5.01	4.17
450 nm Visible range Test [□]					
W/HRTiO ₂	0.0054	0.96	128.33	5.14	4.42
W/HRTiO ₂ + 0.5CoPc	0.0051	0.99	135.88	4.67	4.17
W/HRTiO ₂ + 1CoPc	0.0022	0.88	315.00	5.02	4.41
^{#, *} Tests performed under 365 nm near UV-vis irradiation/preliminary test at initial pH _{natural} (unmodified) condition, HRTiO ₂ is a commercial TiO ₂ sold under portfolio name Huntsman tioxide, CoPc is cobalt phthalocyanine, photocatalytic degradation constant (k) and half-life (t _{1/2}) estimated respectively as per time unit of sampling in h ⁻¹ and h, and min ⁻¹ and min, [□] other test conditions performed at initial pH _{natural} (unmodified) condition/450 nm visible range test [□] other test conditions performed at initial pH _{natural} (unmodified) condition/ 450 nm visible range test					

4.2.1.7. Possible Photocatalytic Degradation Process Mechanism

Based on the chemical scavenger effect test for the probe of the reactive species responsible in the photocatalytic degradation of IBF (Section 4.2.1.3), an outcome where hydroxyl radical (HO·) probed with IPA, hole charge carrier (h⁺) probed with AO is seen as the primary contributing reactive species involved in the degradation of IBF is envisaged (Figure 48, Figure 55). Notwithstanding the non-selectivity of BQ for superoxide anion (O₂⁻) detection due to likely reported reasons already stated (Section 4.2.1.3), its probable involvement due to alternative favorable pathway generation in the photocatalytic degradation process is not ruled out.

From Figure 54, upon the irradiation of the photocatalyst material with adequate photon energy, electron charge carriers (e^-) are ejected, and migrate to the conduction band (CB) energy level with the simultaneously generated hole charge carriers (h^+) by induction remaining at the valence band (VB) energy level of the semiconductor photocatalyst material.

At the VB, generation of hydrogen ion (H^+) is favoured based on the final pH of 3.96 (Table 20) for the formation of superoxide anion ($O_2^{\cdot-}$) via surface adsorbed oxygen -hydrogen ion pathway ($O_2 + H^+ / O_2^{\cdot-}$) even though that it was not selectively and directly intercepted as a reactive specie probed by BQ. The non-direct involvement of superoxide anion ($O_2^{\cdot-}$) via some of the migrated CB electrons (e^-) reduction makes only available same electron charges (e^-) abstracted at this level by the surface decorated W^{+6}/W^{+5} couple system for the reduction-oxidation (redox) process mechanism of charge transfer and separation and drive the photooxidation process more efficiently (Figure 55).

Therefore, the case for the indirect involvement of the superoxide anion ($O_2^{\cdot-}$) reactive specie in the photocatalytic degradation process of IBF through some other mediated charge transfer mechanism like the surface adsorbed oxygen -hydrogen ion pathway is plausible. Furthermore, the VB energy level edge potential value (2.53 eV) guarantee the generation of superoxide anion ($O_2^{\cdot-}$) via surface adsorbed oxygen -hydrogen ion pathway ($O_2 + H^+ / O_2^{\cdot-}$). This is possible as the VB edge potential value of 2.53 eV for the W/HRTiO₂ semiconductor photocatalyst material (Table 16, Figure 55) is positive enough to offset the minimum the E°_{ox} (0.682 eV) required on the normal standard hydrogen electrode (SHE) for the formation superoxide anion ($O_2^{\cdot-}$) via surface adsorbed oxygen -hydrogen ion pathway ($O_2 + H^+ / O_2^{\cdot-}$).

With the justification of the feasibly indirect involvement of superoxide anion ($O_2^{\cdot-}$) though not selectively probed by the employed BQ chemical scavenger for the conventional migrated CB level e^- charge reduction, the case of a more direct involvement of hydroxyl radical (HO^{\cdot}) and the indirect participation of its associated hole charge carrier (h^+) is also supported (Figure 55).

In line, the VB edge potential of the photocatalyst with value 2.53 eV (Figure 55) in comparison with the E°_{ox} values (2.38 eV) and (1.99 eV) on the normal standard hydrogen electrode (SHE) for the respective formation of (H_2O/HO^{\cdot}) and ($^{\cdot}OH/HO^{\cdot}$) guarantees the generation of hydroxyl radical (HO^{\cdot}) and hydroxyl ion ($^{\cdot}OH$) species via those pathways. Based on this insight, such a mechanism where hydroxyl radical (HO^{\cdot}) species played a

prominent role together with the indirect involvement of hole charge carrier (h^+) and superoxide anion ($O_2^{\cdot-}$) is suggested.

Figure 55 displays the scheme which details possibly involved processes of the proposed mechanism.

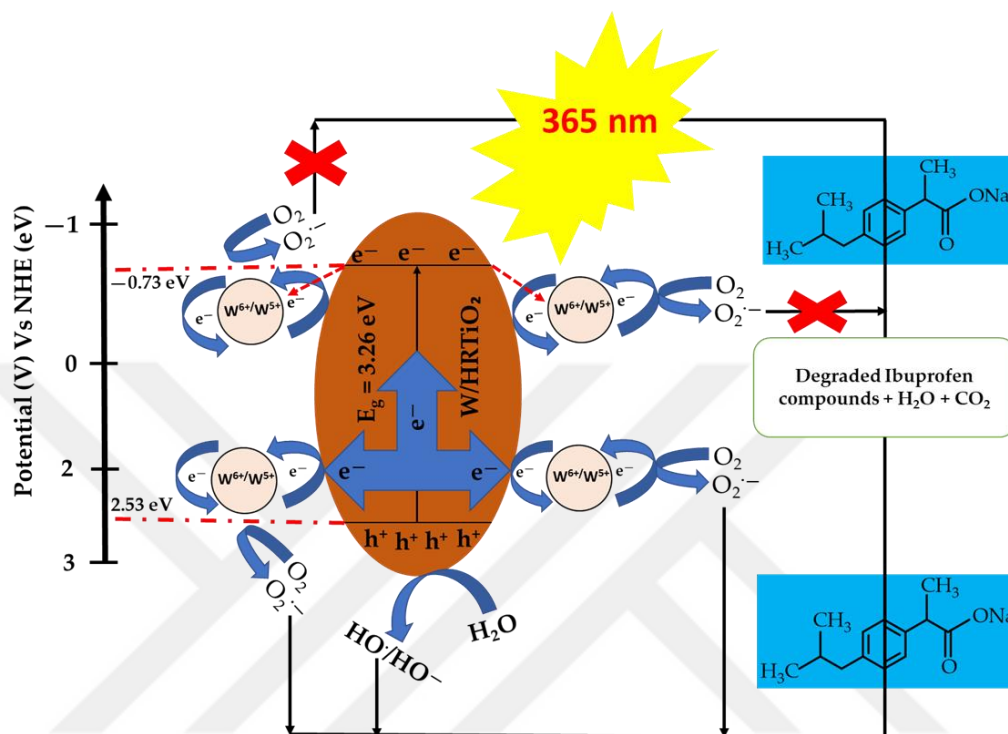


Figure 55. Proposed photocatalytic degradation process mechanism for the removal of IBF by W/HRTiO₂

4.2.2. Photocatalyst Material Test Evaluation Over Caffeine (CAF)

As already stated, preliminary test was again carried out with the photocatalysts materials of HRTiO₂ decorated forms over the degradation of initial 100 mg/L caffeine to ascertain their efficiency and select the best performing catalyst at first instance. As can be seen from the Figure 56, amongst the tested photocatalyst materials, W/HRTiO₂ removed about 80 % initial 100 mg/L CAF concentration under 1 h irradiation time of 365 nm UV light exposure and at natural (unmodified) pH = ~ 5.48 (Table 21). The natural (unmodified) pH values of the other tested photocatalyst materials are also stated in (Table 21).

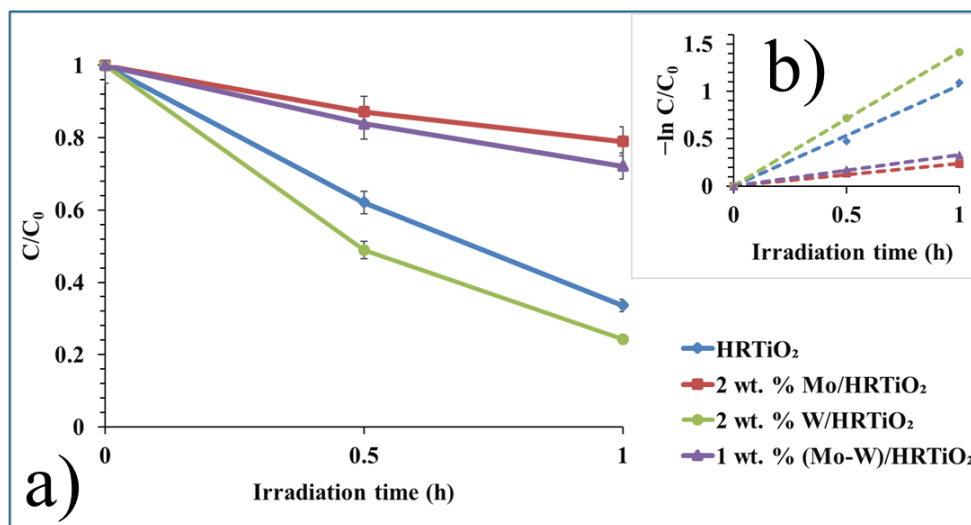


Figure 56. a) Preliminary test for the photocatalytic degradation of caffeine ($C_0 = 100$ mg/L, initial pH_{natural} (unmodified)) condition under 365 nm irradiation with HRTiO₂ and decorated forms, and b) corresponding photocatalytic degradation rate (k)

Following the preliminary test; W/HRTiO₂ as the best performing photocatalyst material in comparison to the HRTiO₂ control sample and the other decorated material forms, and with a rate constant of ~ 1.42 h⁻¹ and half-life of ~ 0.49 h (Figure 56, Table 21) was selected and employed for further photocatalyst test investigations. In order to have a better insight into the photocatalytic degradation reaction kinetics, other investigated test conditions were sampled per min during irradiation.

4.2.2.1. Effect of pH

The pH_{pzc} charge of W/HRTiO₂ photocatalyst has already being determined and given as 4.4 (Figure 44, Section 4.2.1.1). Apart from the natural unmodified initial pH = ~ 5.48 of the W/HRTiO₂ catalyst suspension, other initial pH values of 4 and 9 were tested of their effects towards the photocatalytic degradation of CAF (Figure 57).

As can be seen from the Figure 57, the initial natural (unmodified) pH = 5.48 exhibited a better performance activity up to the 120 min irradiation time in comparison to the initial pH values of 4 and 9. At this time, over 90 % initial 100 mg/L CAF concentration was removed as compared to the about 80 % removal at initial pH = 4 and pH = 9.

The photocatalyst performances witnessed at these initial pH points can be linked to the pH point of zero charge (pHpzc). At the initial natural pH = 5.48, the catalyst surface will be negatively charged with respect to its pHpzc of 4.4 while the caffeine molecules (pKa = 10.4) (Table 19) [162] are protonated with a positive charge. The initial natural pH shift to 5.86 as the final pH value maintained the electrostatic force of attraction condition as the CAF molecules were almost completely removed by the photocatalyst at 240 min irradiation time (Table 21, Figure 57). In the case of initial pH = 4, the catalysts surface will possess a net charge of zero due to its pHpzc of 4.4 while the CAF molecules will be protonated due to its pKa 10.4 value. At such an instance, the CAF substrate molecules will remain farther away at a distance from the surface of the catalyst as there are no compelling forces to draw them closer for degradation. However, the witnessed degradation at pH = 4, can be attributed to the hydrogen ion (H⁺) formation acidic enabling condition that promoted the seen photocatalytic activity performance (Figure 57) [134, 222].

This promoting condition could be seen facilitated as the initial 100 mg/L CAF concentration is further removed to almost 100 % at 240 min irradiation where now the final pH condition shifted to 5.31 (Table 21) and established a force of attraction between the CAF organic compound molecules and the catalyst surface for degradation. The prevailing pH condition with respect to the catalyst pHpzc 4.4 and caffeine pKa 10.4 is now more favourably activated. Photocatalytic degradation rate at initial pH = 9 is also favoured as the pH point lie between catalyst pHpzc (4.4) and caffeine pKa (10.4) values. Hence, the negatively charged catalyst surface and the protonated CAF substrate molecules are electrostatically favoured by pulling forces towards the surface of the catalyst for degradation (Figure 57). Initial pH = 9, however, seem to be a bit retarding, though, not significantly at the early irradiation stages of the suspension irradiation (Figure 57).

This display can be attributed to the low ionic charge strength of the aqueous media dissociated caffeine molecules which at somehow advanced pH values (e.g., 9) are closer to the pKa 10.4 value. The photocatalytic degradation kinetics could be seen accelerate towards the 240 min irradiation time where almost 100 % of the initial 100 mg/L CAF pollutant was removed (Figure 57). At this point, the final pH value was 7.39 (Table 21) and can confirm a more facilitated electrostatic force of attraction between the negatively charged catalyst surface and the stronger protonated caffeine molecule with respect to the catalyst pHpzc and caffeine pKa value.

Thus, in order of initial pH photocatalytic activity performance enhancement, a trend effect of such: pH_{natural} (unmodified) = 5.48 > pH = 4 > pH 9 is confirmed.

For this reason, other investigated photocatalyst tests were carried out under initial natural (unmodified) pH = ~ 5.48.

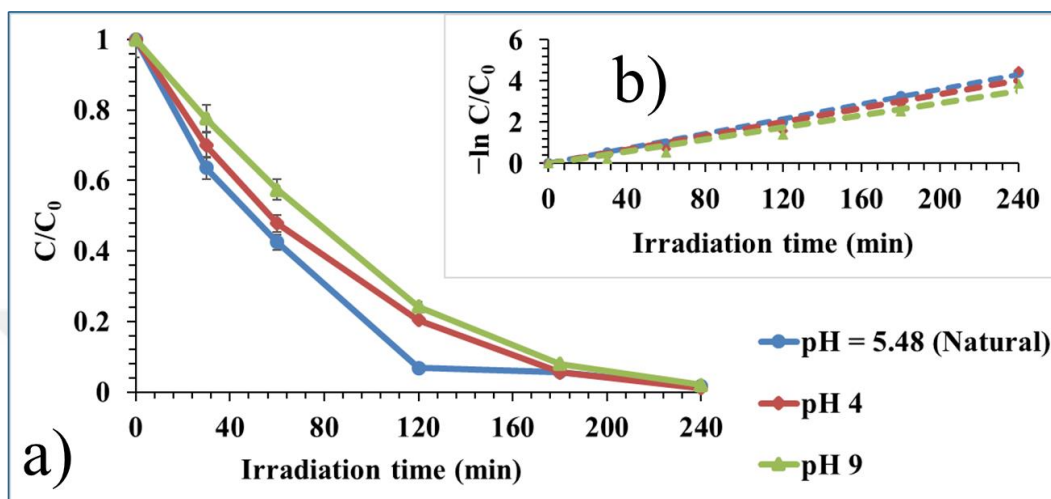


Figure 57. a) pH effect on the photocatalytic degradation efficiency of W/HRTiO₂ over CAF ($C_0 = 100$ mg/L), and b) corresponding photocatalytic constant (k)

4.2.2.2. Effect of Catalyst Dosage and Initial CAF Concentration

Different catalyst amounts of W/HRTiO₂ were employed to investigate the effect of catalyst dose on the photocatalytic degradation of CAF. Other doses of 0.5 g/L, 0.75 g/L, and 1.25 g/L in addition to 1 g/L were investigated at initial pH = 5.48 towards the photocatalytic degradation of CAF. As can be seen from Figure 58, a photocatalytic degradation rate kinetic pattern of such that with increase in catalyst dosage the photodegradation process proceeds faster exist. This trend though with no wider significant difference continued amongst the tested catalyst dosage until 240 min irradiation where almost the initial 100 mg/L CAF was removed (Figure 58). A distinct outcome however does exist as from 0 min to 120 min irradiation; the higher dose photocatalyst was more active and facilitated a faster removal rate of CAF (Figure 58). This outcome can be attributed to the creation of more active sites of the photocatalyst at higher catalyst amount for the degradation of CAF [162, 223]. With a uniform rate constant at approximate value of 0.02 min^{-1} for all the tested dosages at 240 min irradiation, changes between initial and final pH conditions were stable (Table 21).

Considering there was no clear-cut difference in the activity performance of the tested catalyst dosages at 240 min irradiation, a moderate 1 g/L dose continued to be employed for the rest of the photocatalytic tests.

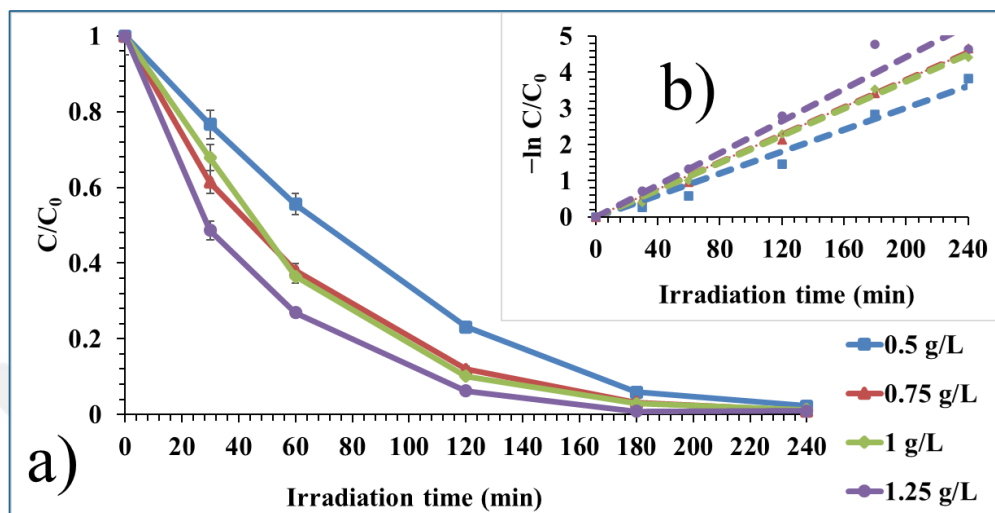


Figure 58. a) Catalyst dosage effect on the photocatalytic degradation efficiency of W/HRTiO₂ over CAF ($C_0 = 100$ mg/L, initial pH_{natural} (unmodified) = ~ 5.48), and b) corresponding photocatalytic degradation constant (k)

On the other hand, a similar pattern in photocatalytic degradation process was also witnessed of the investigated initial caffeine concentrations at 120 mg/L, 130 mg/L, and 140 mg/L in addition to the already tested 100 mg/L. As can be seen from the Figure 59, photocatalytic degradation activity performance reduced with increase in initial CAF concentration. This is because at higher initial pollutant concentrations, catalyst surface tends to be saturated irreversibly thereby reducing the catalyst efficiency at such high pollutant concentrations [162, 223]. Though, at 240 min irradiation the photocatalytic activity performance over 100 mg/L and that of 120 mg/L did not show a significant difference in their reaction rate; with almost complete removal by the catalyst of both initial CAF concentration, the already employed 100 mg/L initial CAF concentration continued to be used for further photocatalytic tests. While the photocatalyst displayed at higher initial CAF concentrations of 140 mg/L and 130 mg/L approximate reaction rates of 0.01 min^{-1} each in comparison to $\sim 0.02 \text{ min}^{-1}$ for 120 mg/L and 100 mg/L each; variation among initial pH and final pH suspension conditions was negligible (Table 21).

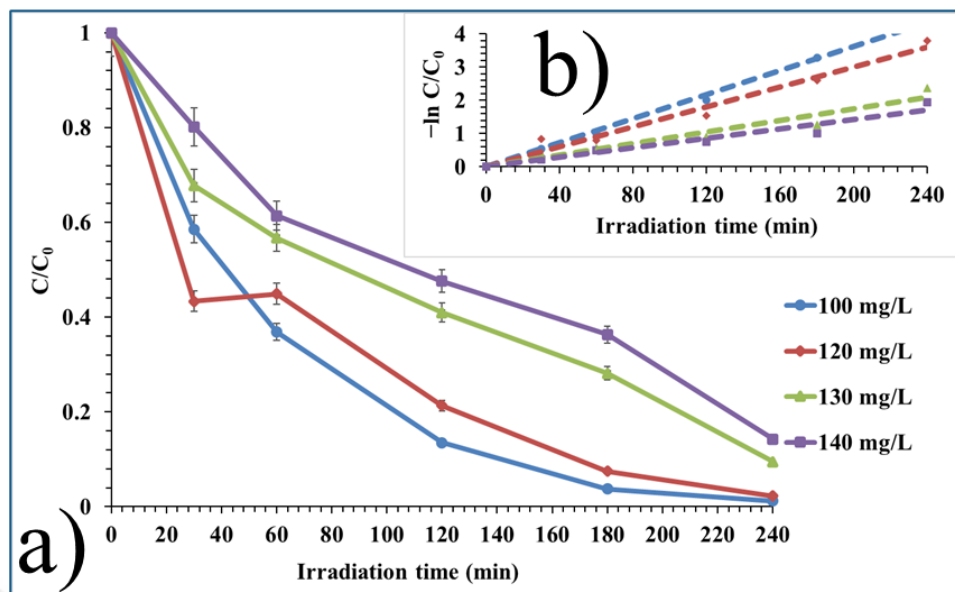


Figure 59. a) Initial CAF concentration effect on the photocatalytic degradation efficiency of 1 g/L W/HRTiO₂ (initial pH_{natural} (unmodified) = ~ 5.48), and b) corresponding photocatalytic degradation rate constant (k)

4.2.2.3. Effect of Chemical Scavengers

To investigate the responsible reactive species for driving the photocatalytic degradation process, quenching effects of chemical scavengers was employed. Similarly, and just like in the case of IBF, 1 mM each of ammonium oxalate (AO), isopropyl alcohol (IPA), and benzoquinone (BQ) were employed as the chemical scavengers for the respective probe of hole charge carriers (h^+), hydroxyl (HO^\bullet) radical and superoxide anion ($O_2^{\bullet-}$) reactive species [134, 162, 222-223]. As can be seen from the Figure 60, the suppression effect of the tested chemical scavengers on the photocatalytic degradation rate of caffeine did not produce a significant difference as reaction rate remained approximately equal at 0.02 min^{-1} with almost complete IBF removal at 240 min irradiation amongst them (Table 21). However, between 60 min-180 min irradiation time, the effect of both IPA and BQ for the respective probe of hydroxyl (HO^\bullet) radical and superoxide anion ($O_2^{\bullet-}$) can be seen more prominently in comparison to the non-selectivity effect of the AO probing for the presence of hole charge carrier (h^+) with respect to the no added scavenger condition (Figure 60).

The non-selectivity of the tested AO scavenger towards the hole charge carrier (h^+) can be attributed to some interfering species evoked upon the addition of the AO scavenger that rather tend to mask its direct detection and do not represent its total and verified absence

as a reactive specie in the suspension media; thus, may have been possibly generated through other pathways [295-296].

However, based on the scavenger test outcome, a particular trend of inhibitory effect of the tested chemical scavenger on the photocatalytic degradation of CAF follows such an order: BQ > IPA > AO = ~ No scavenger. While the presented half-life values of the chemical scavengers confirm this outcome, the initial pH and final pH condition values remained stable (Table 21).

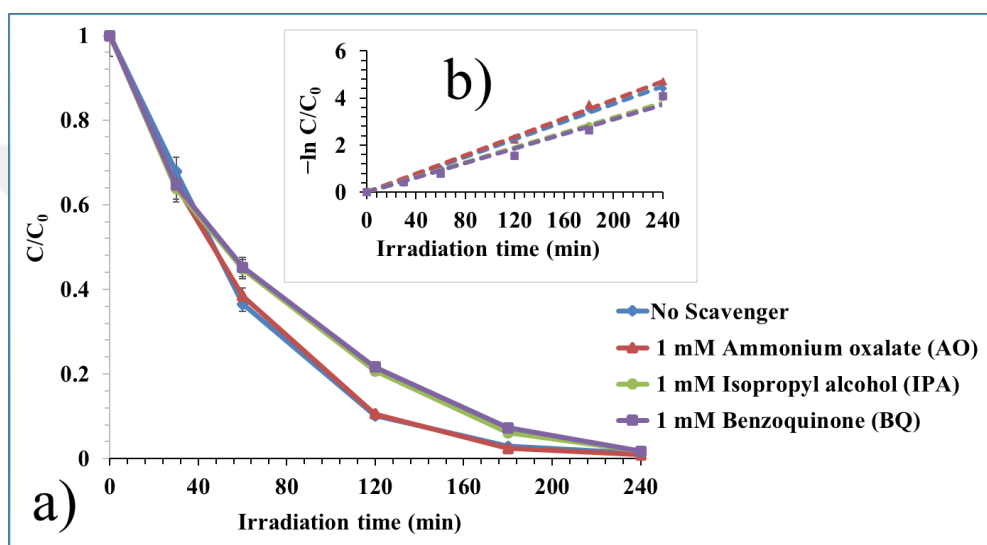


Figure 60. a) Chemical scavenger effect on the photocatalytic degradation efficiency of 1 g/L W/HRTiO₂ over CAF ($C_0 = 100$ mg/L, initial pH_{natural} (unmodified) = ~ 5.48), and b) corresponding photocatalytic degradation rate constant (k)

4.2.2.4. Effect of Contaminants Ion (Cations and Anions), and Humic Acid (HA)

The effect of chloride inorganic cations: Al³⁺, Mg²⁺, and NH₄⁺ of 1 M equivalent each was investigated towards the photocatalytic degradation of 100 mg/L initial CAF concentration (Figure 61). As can be seen, the tested cations had a mixed behaviour of effect as their photocatalytic degradation kinetics for the first 60 min equalled except for the case of Al³⁺ which lagged in the previous 20 min from the rest as the suspension system readjust. The difference in rate of reaction outcome within the 60 min irradiation of Al³⁺ presence though not significant diminished along the irradiation time with almost 100 % removal of CAF achieved at the 240 min in the presence of the cations (Figure 61). This establishes the negligible and non-significant impact of the added cations on the photocatalytic degradation

process. Moreover, facilitated photodegradation process of organic pollutants in the presence of Al^{3+} , Mg^{2+} , and NH_4^+ ions, with non-exertion of their influence in some cases as well exhibition of inhibitory effect especially for the case of Al^{3+} to some extent as seen in this case has been reported [162, 223, 297-298].

In all, however not with a big margin, the added cations exerted a facilitating effect on the photocatalytic process with an approximate rate constant of 0.02 min^{-1} for each of the cations in comparison to 0.018 min^{-1} for no cation addition (Figure 61, Table 21).

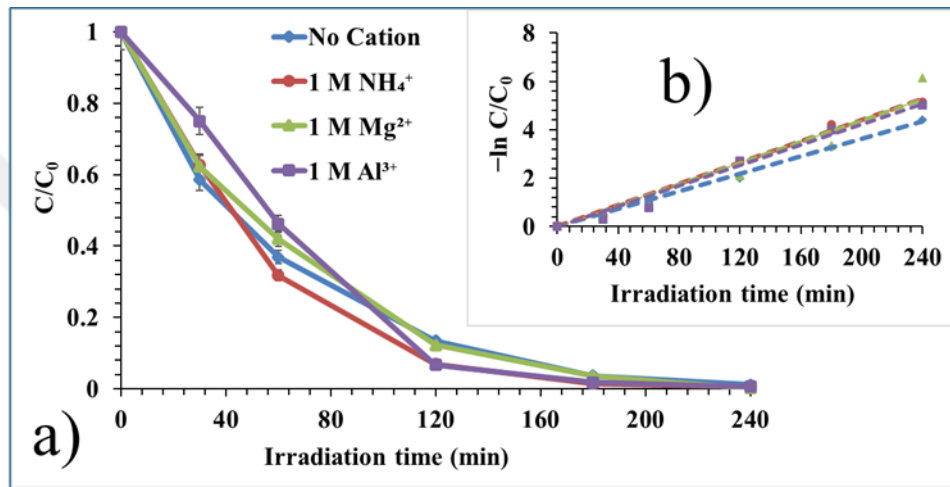


Figure 61. a) Cation effects on the photocatalytic degradation efficiency of 1 g/L W/HRTiO_2 over CAF ($C_0 = 100 \text{ mg/L}$, initial $\text{pH}_{\text{natural}}$ (unmodified) = ~ 5.48), and b) corresponding photocatalytic degradation constant

On the other hand, and as seen from Figure 62, anion effect of the tested 1 M equivalent of Cl^- , HCO_3^- , SO_4^{2-} , and HPO_4^{2-} showed such effect where the impact of Cl^- and SO_4^{2-} ions were not influential in comparison to no added anion except for the later showing a mixed behaviour of retardation though not significant at 240 min. In general, while addition of Cl^- and SO_4^{2-} ions interfered with an enhancing impact on the photooxidation process due to their abilities in generating more reactive species [298], the inhibitory effect of HCO_3^- and HPO_4^{2-} can be attributed to their strong scavenging character of hydroxyl ($\text{HO}\cdot$) radicals thereby lowering the activity performance of the photocatalytic process [298]. This can be confirmed as the final pH values of the HCO_3^- and HPO_4^{2-} anion conditions shifted to a more advanced point different from the rest (Table 21).

As such, exerted enhancing effect of added anions can be seen to have followed an order: $\text{Cl}^- \geq \text{SO}_4^{2-} > \text{HCO}_3^- > \text{HPO}_4^{2-}$.

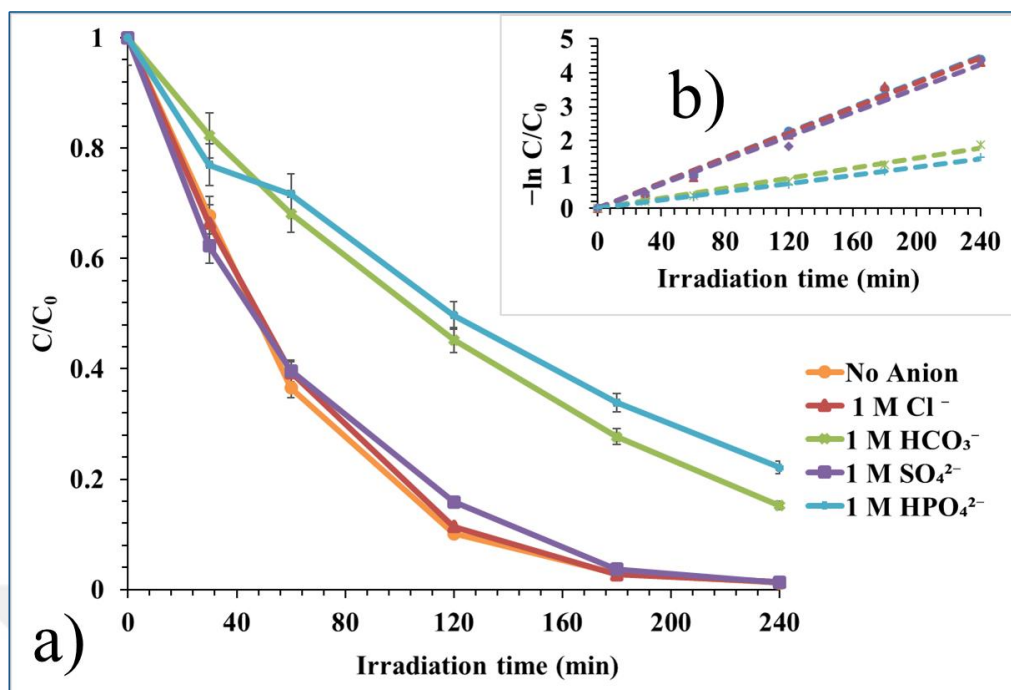


Figure 62. a) Anion effect on the photocatalytic degradation efficiency of 1 g/L W/HRTiO₂ over CAF ($C_0 = 100$ mg/L, initial pH_{natural} (unmodified) = ~ 5.48), and b) corresponding photocatalytic degradation rate constant

Dissolved organic matter (DOM) effect was tested using sodium humic acid (HA) of concentration range of 1 mg/L – 4 mg/L (Figure 63). As can be seen a mixed effect behaviour was displayed. During the 60 min irradiation time, the 1 mg/L HA, 2 mg/L HA, and 4 mg/L HA though by not a significant difference were more facilitative in the photocatalytic degradation process than the 3 mg/L HA and no added HA condition (Figure 63). This outcome agrees with the reported attribute of humic acid (HA) able to hinder light penetration due to its shielding effect reducing photooxidation activity as well as its ability to alternatively generate radicals for photooxidation enhancement [134, 162, 223]. In all, at 240 min irradiation the added humic acid effect was not influential in the range of the tested concentrations as almost 100 % CAF removal was achieved. The slight difference in performance retardation in the presence of 3 mg/L HA equal with no HA addition with respect to the other tested concentrations was however not significant (Figure 63, Table 21).

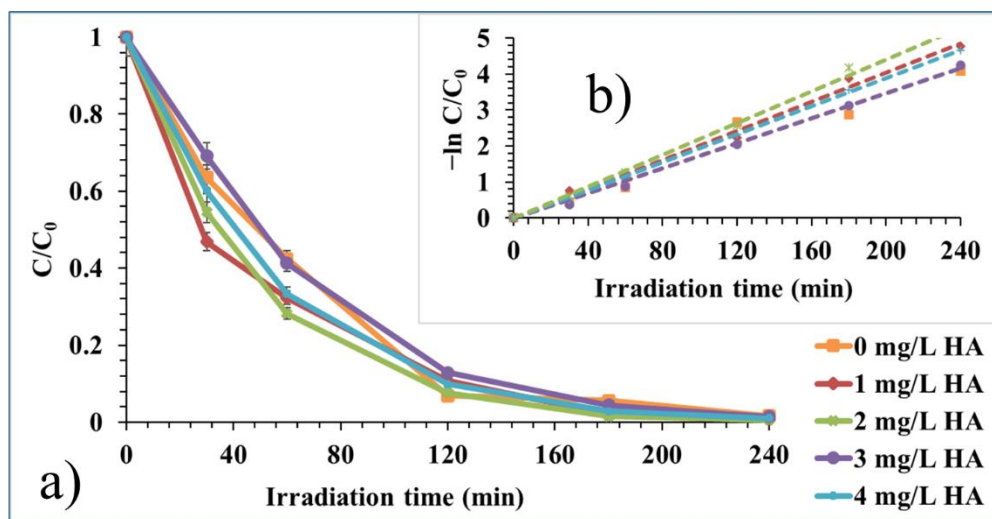


Figure 63. a) Humic acid (HA) effects on the photocatalytic degradation efficiency of 1 g/L WHRTiO over CAF ($C_0 = 100$ mg/L, initial pH_{natural} (unmodified) = ~ 5.48), and b) corresponding photocatalytic degradation rate constant (k)

4.2.2.5. Effect of Hydrogen Peroxide (H_2O_2)

Hydrogen peroxide (H_2O_2) effect on the photocatalytic degradation process was also investigated employing 1 mM - 4 mM range of concentration. As can be seen from the Figure 64, the 4 mM H_2O_2 , 2 mM H_2O_2 , 1 mM H_2O_2 and, 3 mM H_2O_2 exerted a short-lived impeding effect in the presented order on the photocatalytic degradation process between 60 min- 120 min irradiation time with respect to 0 mM H_2O_2 condition. This occurrence can be attributed to the interfering scavenging effect of the added H_2O_2 as external oxidant into the suspension media that within those irradiation time intercepted the hydroxyl (HO^\bullet) species at those concentrations [223]. However, by the 240 min irradiation, the non-significant impeding effect of the H_2O_2 oxidant disappeared with now a non-negatively impacted photodegradation process restored and almost complete removal of the initial 100 mg/L CAF recorded (Figure 64). Rate constant and half-life of the photocatalytic degradation process remained approximately the same at 0.02 min^{-1} and ~ 40 min respectively (Table 21). pH variation was also minimal as there was approximate stability of initial and final values.

In all, the photocatalytic degradation process retardation effect of added H_2O_2 followed such an order: 3 mM $H_2O_2 > 1 \text{ mM } H_2O_2 > 2 \text{ mM } H_2O_2 > 4 \text{ mM } H_2O_2$.

This mixed behaviour is an attribute of the different scavenging effects exhibited by the different tested H_2O_2 concentrations (Figure 64).

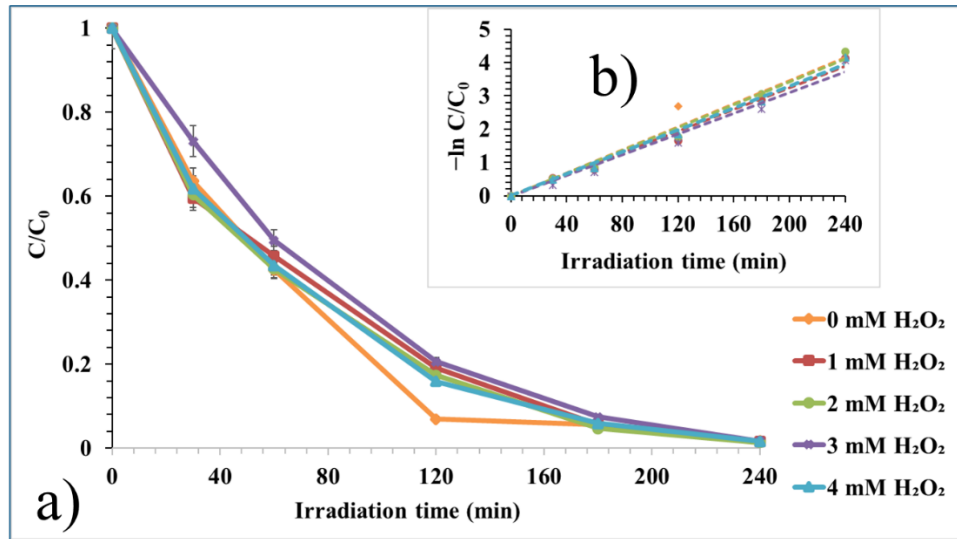


Figure 64. a) Hydrogen peroxide (H_2O_2) effect on the photocatalytic degradation efficiency of 1 g/L W/HRTiO₂ over IBF ($C_0 = 100$ mg/L, initial pH_{natural} (unmodified) = ~ 5.48), and b) corresponding photocatalytic degradation rate constant (k)

As part of the photocatalytic parametric activity evaluation, dark: (suspension content of 1 g/L catalyst + 100 mg/L caffeine), heat effect with catalyst: (suspension content of 1 g/L catalyst + 100 mg/L caffeine in a reactor cell kept under light illumination but wrapped with aluminium foil to prevent light penetration), heat effect without catalyst: 100 mg/L caffeine only in a reactor cell kept under light illumination but wrapped with aluminium foil to prevent light penetration) and photolysis: (100 mg/L caffeine only in a reactor cell fully irradiated) tests conditions were investigated of their impact on the photocatalytic degradation of caffeine. As can be seen from the Figure 65, these outlined conditions were investigated under 365 nm irradiation and under initial pH_{natural} (unmodified) value of ~ 5.48 with no significant impact on the photocatalytic degradation of CAF and therefore neglected.

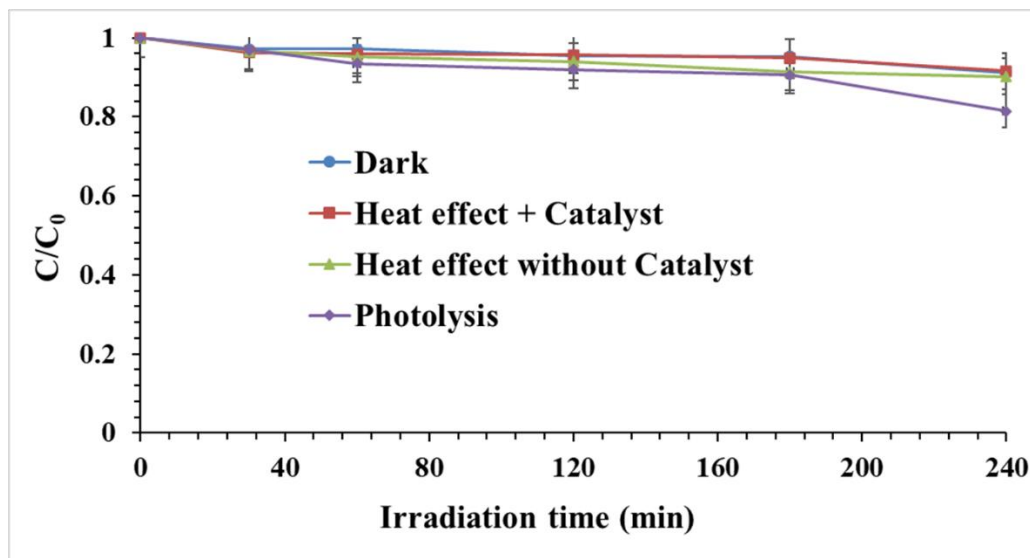


Figure 65. Dark, photolysis, heat effect without catalyst and heat effect with catalyst test at conditions of 1 g/L W/HRTiO₂, C₀ = 100 mg/L, initial pH_{natural} (unmodified) = ~ 5.48 where applicable

4.2.2.6. Evaluation of Visible Light Photocatalytic Activity

An extension of the photocatalyst visible light activity was carried out with W/HRTiO₂ and sensitized forms of 0.5 wt.% and 1 wt. % CoPc concentrations together with their control material samples under 450 nm irradiation and different natural initial pH values as stated in Table 21 for each of the tested photocatalyst material. It can be observed from the Figure 66, the increase in photocatalytic degradation kinetic effect of the 0.5CoPc sensitized W/HRTiO₂ which at 6 h irradiation time achieved over 60 % CAF removal with a 0.23 h⁻¹ degradation rate constant and half-life of 2.96 h (Figure 66, Table 21). The CoPc modification strategy by sensitization of the W/HRTiO₂ improved its visible light range photoactivity response in comparison to the bare HRTiO₂, and unsensitized W/HRTiO₂ with respective degradation rate constants and half-life values of ~ 0.07 h⁻¹, and 10.25 h, and ~ 0.15 h⁻¹, and 4.67 h (Table 21). The least performance ability of the 1 wt. % CoPc sensitized W/HRTiO₂ where less than 20 % CAF removal was achieved at 6 h irradiation can be attributed to the interfering influential effect of the large Pc molecules which at this load % hindered effective excitation of the photocatalyst material upon irradiation [122, 222-223]. Variation between initial and final pH values of the investigated photocatalyst materials maintained a balance and did not shift significantly (Table 21).

It is worth noting that the light source intensity for photocatalyst tests performed under these two different light sources (365 nm and 450 nm) influenced the irradiation time length in achieving some level of desirable and expected pollutant degradation outcome. While photocatalytic degradation rate kinetics is much faster within the UV light exposure and can be sampled within minutes, that of visible light range take a bit of time to get materials excited; hence the need for much longer time sampling (e.g., in h).

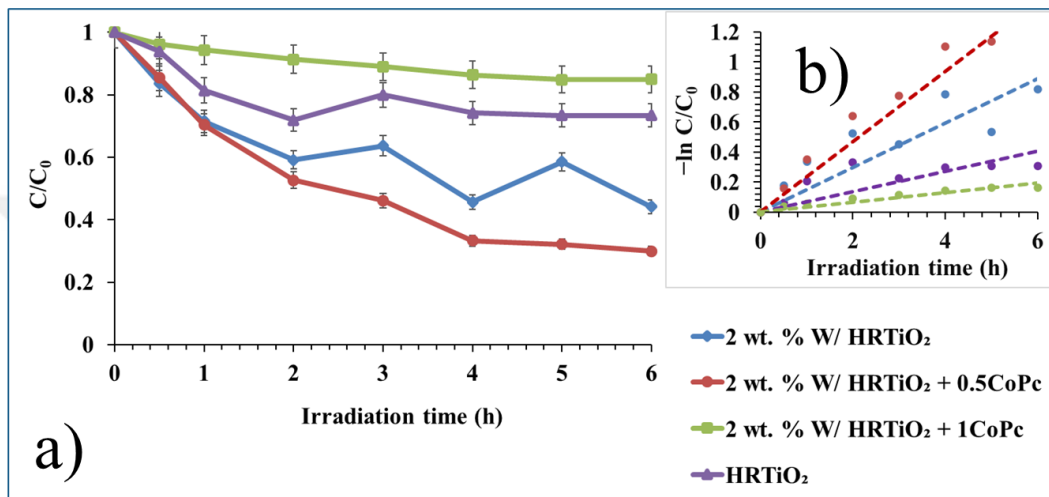


Figure 66. Visible light photocatalytic evaluation of W/HRTiO₂, W/HRTiO₂ + 0.5CoPc, and W/HRTiO₂ + 1CoPc at 1 g/L each for CAF degradation ($C_0 = 10$ mg/L) at initial pH_{natural} values (Table 21)

Table 21 show the different investigated photocatalytic test parameters with data results as per their degradation rate constant k (h^{-1} or min^{-1}), correlation coefficient constant (R^2), half-life ($t_{1/2}$) (h or min) as well as variation between the initial and final pH values of the different test conditions of the photocatalyst material.

Table 21. Tested photocatalytic parameters for ($C_0 = 100$ mg/L initial CAF concentration under 365 nm, and $C_0 = 10$ mg/L initial CAF concentration under 450 nm) with 1 g/L catalyst and their associated rate constant k (h^{-1} or min^{-1}), correlation coefficient (R^2), half-life $t_{1/2}$ (h or min), and initial and final pH values

Test	Degradation rate constant k (h^{-1} or min^{-1})	R^2	Half-life ($t_{1/2}$) (h or min)	pH _{initial}	pH _{final}
Preliminary test for photocatalyst material selection ^{#, *}					
HRTiO ₂	1.063	0.99	0.65	7.61	6.20
W/HRTiO ₂	1.419	1	0.49	5.48	6.2
Mo/HRTiO ₂	0.243	0.99	2.85	9.84	8.85
W-Mo/HRTiO ₂	0.332	0.99	2.09	4.73	4.19
Selected photocatalyst material: W/HRTiO ₂					
pH effect ^{#, □}					
pH _{natural} = 5.48	0.018	0.99	38.29	5.48	5.86
pH = 4	0.002	0.98	410.06	3.69	5.31
pH = 9	0.015	0.98	47.14	8.65	7.39
Catalyst dosage effect ^{#, □}					
0.5 g/L	0.015	0.99	45.89	5.48	6.54
0.75 g/L	0.019	0.99	45.89	5.47	6.65
1 g/L	0.019	0.99	45.89	5.45	5.88
1.25 g/L	0.022	0.98	45.89	5.48	5.77
Pollutant concentration effect ^{#, □}					
100 mg/L	0.018	0.99	38.29	5.48	6.19
120 mg/L	0.015	0.99	46.20	5.45	6.44
130 mg/L	0.009	0.98	79.66	5.46	5.50
140 mg/L	0.007	0.97	97.61	5.44	5.56
Chemical scavengers ^{#, □}					
No scavenger	0.019	0.99	37.06	5.46	5.85
1mM IPA	0.016	0.99	43.58	5.48	6.38
1mM BQ	0.016	0.98	44.71	5.47	6.08

--	--	--	--	--	--

Continuation of Table 21

1mM AO	0.019	0.99	35.18	5.45	5.95
Contaminant ion effect: Cation ^{#, □}					
No cation	0.018	0.99	38.29	5.48	5.88
1 M NH ₄ ⁺	0.022	0.99	31.50	5.46	6.43
1 M Al ³⁺	0.021	0.99	32.69	5.45	4.10
1 M Mg ²⁺	0.022	0.97	31.50	5.47	6.51
Contaminant ion effect: Anion ^{#, □}					
No anion	0.019	0.99	37.06	5.47	5.86
1 M Cl ⁻	0.019	0.99	37.46	5.48	6.27
1 M SO ₄ ²⁻	0.018	0.99	39.15	5.45	6.47
1 M HCO ₃ ⁻	0.007	0.99	93.65	5.48	8.24
1 M HPO ₄ ⁻	0.006	0.99	113.61	5.46	7.55
Humic acid (HA) effect ^{#, □}					
0 mg/L HA	0.017	0.99	40.06	5.45	5.87
1 mg/L HA	0.020	0.99	34.31	5.47	6.27
2 mg/L HA	0.022	0.99	31.50	5.48	6.23
3 mg/L HA	0.017	0.99	39.83	5.45	6.10
4 mg/L HA	0.019	0.99	35.65	5.47	6.22
Hydrogen peroxide (H ₂ O ₂) effect ^{#, □}					
0 mM H ₂ O ₂	0.017	0.99	40.06	5.48	5.87
1 mM H ₂ O ₂	0.016	0.99	42.52	5.46	5.94
2 mM H ₂ O ₂	0.017	0.99	40.53	5.45	5.99
3 mM H ₂ O ₂	0.016	0.99	44.71	5.47	5.84
4 mM H ₂ O ₂	0.016	0.99	42.26	5.48	5.99
450 nm Visible range Test [□]					
HRTiO ₂	0.068	0.86	10.25	6.93	6.50
W/HRTiO ₂	0.149	0.92	4.67	6.3	5.85
W/HRTiO ₂ + 0.5CoPc	0.234	0.98	2.96	6.85	5.88
W/HRTiO ₂ + 1CoPc	0.033	0.97	21.12	6.88	5.92

Continuation of Table 21

#, * Tests performed under 365 nm near UV-vis irradiation/preliminary test at initial pH_{natural} (unmodified) condition, HRTiO₂ is a commercial TiO₂ sold under portfolio name Huntsman tioxide, CoPc is cobalt phthalocyanine, photocatalytic degradation constant (k) and half-life (t_{1/2}) estimated respectively as per time unit of sampling in h⁻¹ and h, and min⁻¹ and min, □ other test conditions performed at initial pH_{natural} (unmodified) condition/450 nm visible range test

4.2.2.7. Possible Photocatalytic Degradation Process Mechanism

Based on the outcome of the chemical scavenger test discussed in Section 4.2.2.3, it can be suggested that superoxide anion ($O_2^{\cdot-}$) and hydroxyl (HO^{\cdot}) radical were the most effective reactive species involved in the photocatalytic degradation of caffeine by the W/HRTiO₂ photocatalyst (Figure 60). Though the probe of hole charge carrier (h^+) revealed almost a negligible suppression effect on the photocatalytic degradation process; its involvement might have been an indirect one through interaction with surface adsorbed water molecule to generate hydroxyl (HO^{\cdot}) radical as it was not selectively detected by the employed AO chemical scavenger. Thus, a classical type of photocatalytic degradation process mechanism where all the reactive species played part was envisaged and a surface reaction mechanism proposed accordingly.

From the Figure 67, upon the photoirradiation of the catalyst, electrons are ejected from the valence band (VB) energy level while leaving the holes (h^+) behind. As the electrons migrate to the conduction band (CB) level, some of the spill over electron charges are trapped by the surface attached W^{+6}/W^{+5} redox system at the VB energy level thereby facilitating the generation of the superoxide anion ($O_2^{\cdot-}$) while the induced hole (h^+) charge carrier interacts with surface adsorbed water molecules leading to the generation of hydroxyl (HO^{\cdot}) radical. Meanwhile, the drifted photogenerated electrons (e^-) to the conduction band (CB) energy level cascade again into the surface attached W^{+6}/W^{+5} redox system with a subsequent generation of superoxide anion ($O_2^{\cdot-}$) (Figure 67).

The involvement of hydroxyl (HO^{\cdot}) radical, superoxide anion ($O_2^{\cdot-}$), hydroxide ion (HO^-), and other active species like (H_2O_2) in the photocatalytic degradation caffeine can further be

supported via favoured energetics of charge transfer/active species generation based on the evaluated band edge potentials (Table 16, Equation 85, and Equation 86). Redox reaction pairs $O_2/O_2^{\cdot-}$, H_2O/HO^{\cdot} , HO^-/HO^{\cdot} and even the possible generation of $O_2 + H^+/O_2^{\cdot-}$ as part of the radical species pathways involved in the photocatalytic degradation of caffeine can all be supported by the proposed reaction mechanism of the scheme in Figure 67.

As can be seen, the CB edge potential of the photocatalyst (- 0.73 eV) (Table 16) is more negative in value compared to the (- 0.046 eV) required for the generation of $E^{\circ}_{ox} (O_2/O_2^{\cdot-})$ Vs the standard normal hydrogen electrode (SHE) scale and therefore, favours the interaction of the conduction band (CB) electrons for the formation of superoxide anion ($O_2^{\cdot-}$) at this level [162]. In the same vein, the valence band (VB) edge potential of the photocatalyst with a value of 2.53 eV (Figure 67) against the standard normal hydrogen electrode (SHE) is of a higher potential energy than those required for the formation of H_2O/HO^{\cdot} , HO^-/HO^{\cdot} reactive pair species at respective values of 2.38 eV and 1.99 eV; hence favours their formation at this level [162].

Again, the W^{6+}/W^{5+} with the reported potential of - 0.03 eV is higher than that reported for TiO_2 conduction band (CB) and also higher than that obtained in this study (- 0.31 eV) (Table 16) and as such favours the capture of electron charge species by the W^{6+}/W^{5+} redox system (Figure 67) [107]. This implies that the possibility of photogenerated charge recombination is effectively suppressed as the charges are more free now to undergo VB hydrogen ion (h^+) oxidation with surface adsorbed water molecules and CB electron (e^-) reduction with molecular surface oxygen to generate hydroxyl (HO^{\cdot}) radical, superoxide anion ($O_2^{\cdot-}$) respectively as well as other reactive species like (H_2O_2) via H_2O/HO^{\cdot} , HO^-/HO^{\cdot} and $O_2 + H^+/O_2^{\cdot-}$ as they have possibly favoured pathways for the photocatalytic degradation of caffeine. Thus, with all the drawn analogies, the scheme depicted below exhibits the mechanism suggested to have been involved in the photocatalytic degradation process of caffeine.

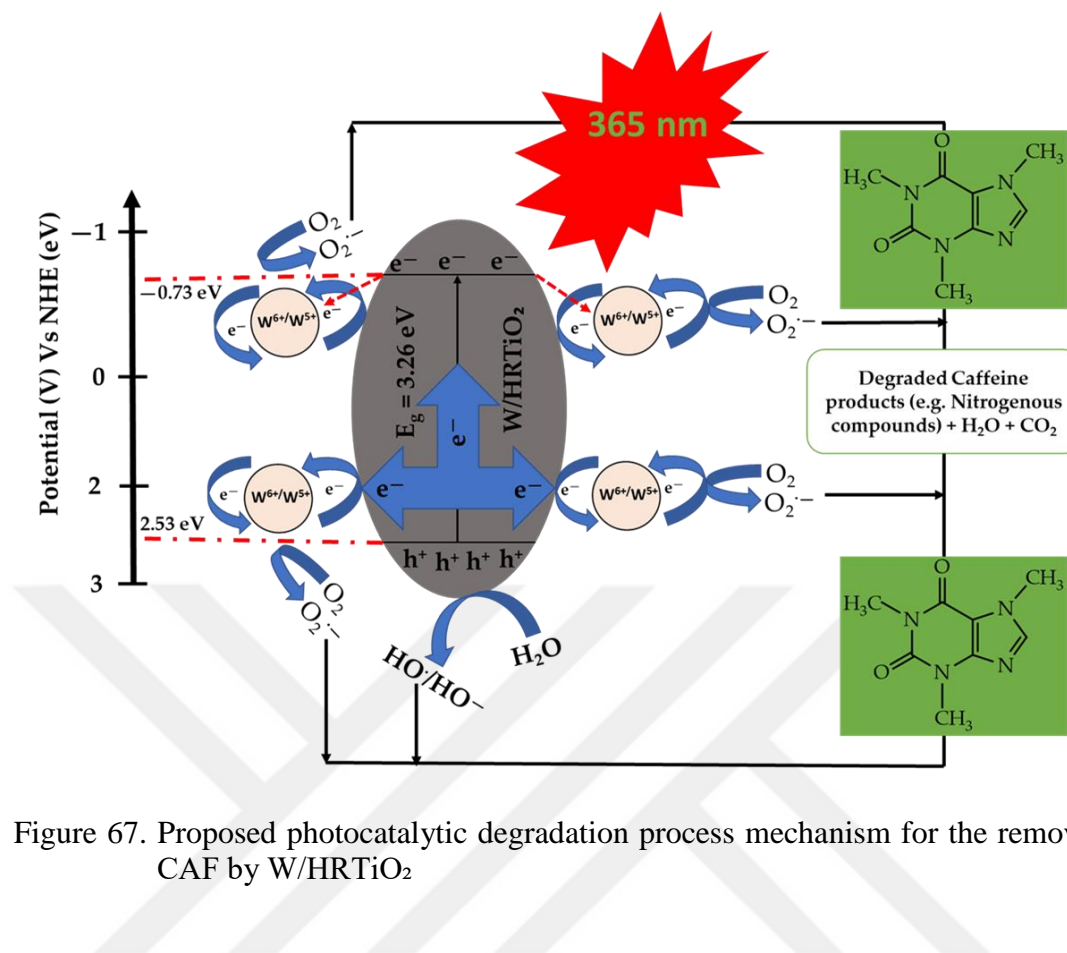


Figure 67. Proposed photocatalytic degradation process mechanism for the removal of CAF by W/HRTiO₂

4.2.3. Photocatalyst Material Test Evaluation Over Carbamazepine (CBZ)

A One-off preliminary test was conducted with the W decorated HRTiO₂ and the other forms of W/and or Mo decorated CoPc sensitized HRTiO₂ analogues under 365 nm UV and 450 nm visible light irradiation respectively. As can be seen from Figure 68, the W/HRTiO₂ photocatalyst under 365 nm irradiation at a 1 g/L catalyst dose against 50 mg/L initial CBZ concentration removed almost completely the CBZ in comparison to a little above 90 % removal achieved with the unmodified anatase HRTiO₂. In a similar outcome, at 100 mg/L initial CBZ concentration the W/HRTiO₂ photocatalyst removed over 90 % initial CBZ concentration in comparison to about 70 % removal achieved with the anatase pure HRTiO₂ (Figure 68). These results indicates that the W/HRTiO₂ photocatalyst were more photocatalytically active in the degradation of CBZ at those initial concentrations and under natural (unmodified) pH condition [122, 134, 164, 222-223].

The outcome also confirms that with increase in initial pollutant concentration, the photocatalyst activity performance diminish as more pollutant substrates occupy available

active photocatalyst material sites at higher pollutant concentration thereby retarding the overall photocatalyst activity performance [162, 223].

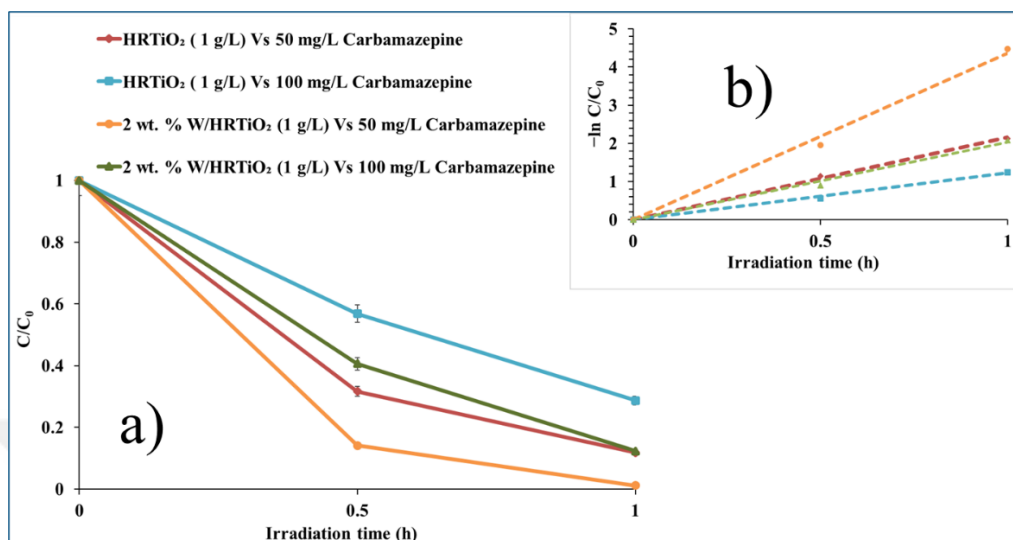


Figure 68. Photocatalytic evaluation of 1 g/L W/HRTiO₂ for CBZ degradation ($C_0 = 50$ mg/L, and $C_0 = 100$ mg/L) in comparison to unmodified pure anatase HRTiO₂ under 365 nm irradiation and at initial pH_{natural} conditions (Table 22), and b) corresponding photocatalytic degradation rate constant (k)

On the other hand, and under 450 nm visible light irradiation, the CoPc sensitized co-decorated Mo and W HRTiO₂ (Mo-W/HRTiO₂ + 0.5CoPC) showed photoactivity by the removal of about 60 % initial 10 mg/L CBZ at 6 h irradiation (Figure 69). The unsensitized co-decorated Mo-W/HRTiO₂ equally showed photoactivity performance matched by unmodified pure anatase HRTiO₂ with a little above 40 % of initial 10 mg/L CBZ removal under natural (unmodified) initial pH condition and 6 h irradiation time (Figure 69). Comparatively, the addition of 0.5CoPc sensitizer onto the Mo-W/HRTiO₂ can be confirmed to make the difference in the photoactivity response of the materials as unsensitized and sensitized forms towards the photocatalytic degradation of CBZ, hence sensitization is seen as one of the modification strategies for improved photocatalyst performance [122, 222-223].

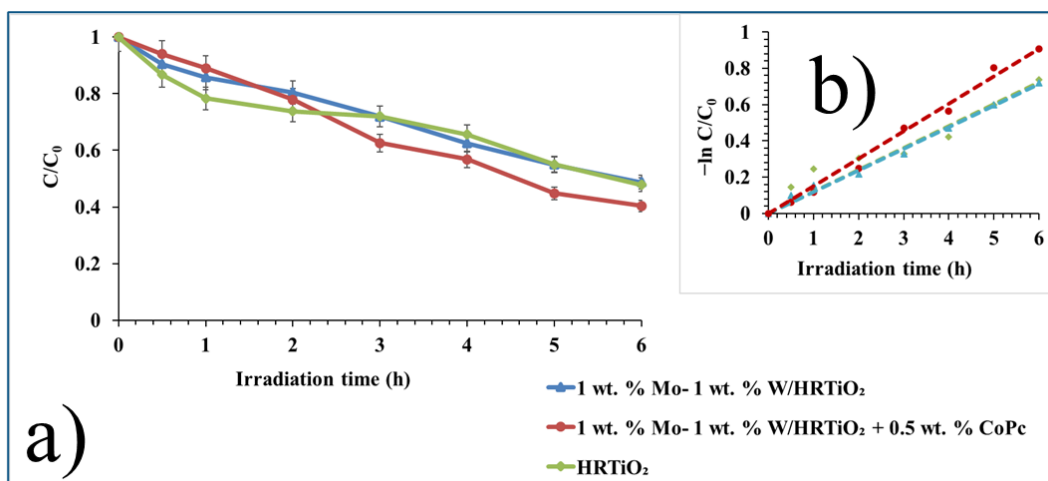


Figure 69. Photocatalytic evaluation of 1 g/L Mo-W/HRTiO₂ and 1 g/L Mo-W/HRTiO₂ + 0.5CoPc for CBZ degradation ($C_0 = 10$ mg/L) in comparison to unmodified pure anatase HRTiO₂ under 450 nm irradiation and at initial pH_{natural} (unmodified) conditions (Table 22), and b) corresponding photocatalytic degradation rate constant (k)

The photocatalytic degradation process of CBZ haven occurred at natural (unmodified) pH condition under the 365 nm and 450 nm irradiation sources (Table 22), pH effect was further examined towards the photocatalytic performance of the Mo-W/HRTiO₂ + 0.5CoPc in the degradation of CBZ. Other pH values of 4, 9, and 11 were investigated. Relatively, the pH_{pzc} of Mo-W/HRTiO₂ + 0.5CoPc as 4 (Figure 70) and the pK_a value of CBZ as 13.9 (Table 19) can be used to explain the outcome of the photocatalyst activity performance at those investigated pH conditions.

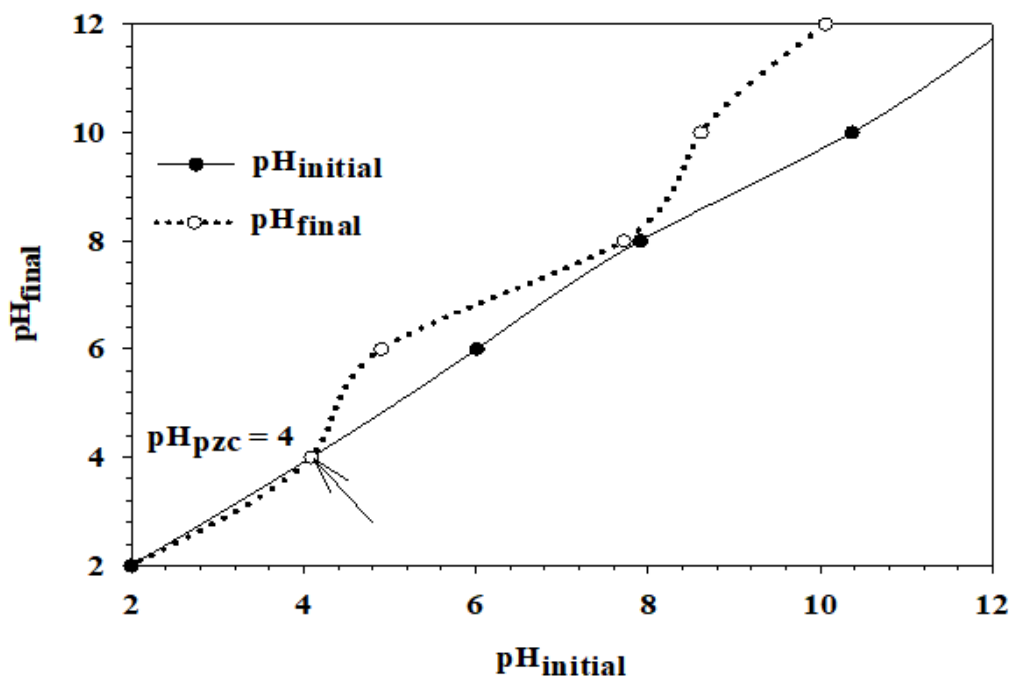


Figure 70. pH point of zero charge (pHpzc) plot of 1wt. % W-1 wt. % Mo/HRTiO₂ + 0.5CoPc photocatalysts material

As can be seen from (Figure 71), pH = 4 showed the best performance activity with about 70 % 10 mg/L initial CBZ concentration removed at 6 h irradiation. While pH = 11 achieved about 42 % removal of 10 mg/L initial CBZ concentration, pH = 9 did not show significant activity performance over CBZ degradation at 6 h irradiation (Figure 71). The best photocatalyst activity performance of pH = 4 can be attributed to the enabling acidic proton (H⁺) promoting environment for the photocatalytic of organic pollutants obtainable at this pH point [134, 222]. The pH = 4 condition with respect to photocatalyst pH_{pzc} = 4, and CBZ pK_a = 13.9, will strongly protonate the CBZ molecules in the aqueous media and as such transmit a harsh aqueous media environment that will facilitate reactive species like hydroxyl (HO[•]) radicals to drive the photocatalytic process degradation of CBZ. The shift of the pH value to a final point of 5.84 (Table 22) as the reaction proceeded guaranteed the needed force of attraction required to keep the protonated CBZ substrate molecules closer to the negatively charged photocatalyst surface for the sustained photocatalytic CBZ removal by the photocatalyst and under this final pH condition. In the case of pH = 9, the initial as well as the final pH values (Table 22) though stabilized and lie within the pH_{pzc} of catalyst (4, Figure 70) and the pK_a of CBZ (13.9, Table 22) will induce a force attraction

between the negatively charged catalyst surface and the protonated CBZ substrate molecules.

However, this did not result to meaningful activity performance by the photocatalyst probably due to degradants of the parent CBZ molecule that built up at this pH condition [134].

On the other hand, the moderate photocatalyst activity performance shown by pH = 11 condition can be attributed to the attractive force established between negatively charged photocatalyst surface and the protonated CBZ molecules at this pH condition where perhaps being more an advanced pH point than pH = 9 did not witness degraded product build up effect (Figure 71) [134, 222].

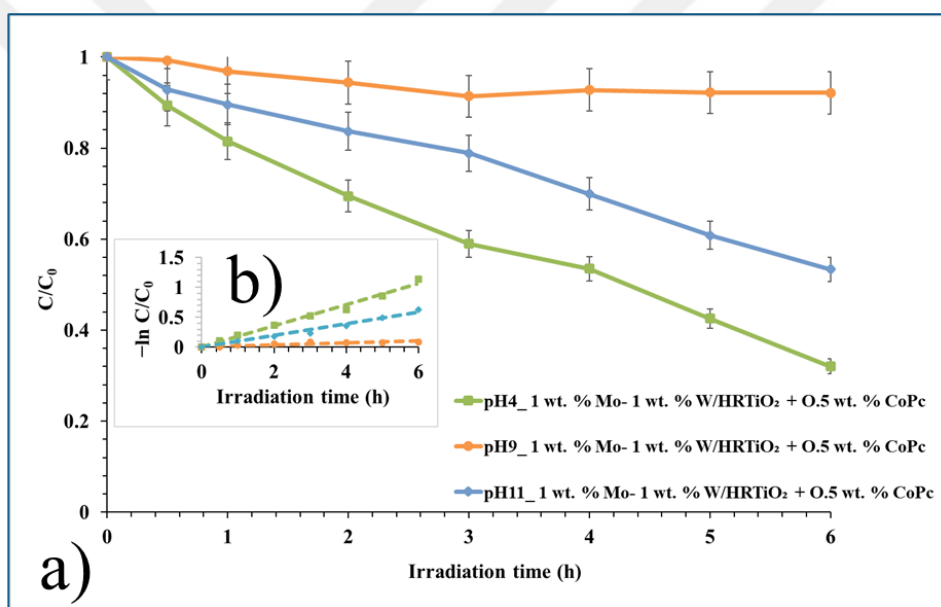


Figure 71. Photocatalytic evaluation of 1 g/L Mo-W/HRTiO₂ + 0.5CoPc for CBZ degradation ($C_0 = 10$ mg/L) under 450 nm irradiation at (initial pH_{natural} (unmodified) = 4, 9, and 11, Table 22), and b) corresponding photocatalytic degradation rate constant (k)

Table 22, show the tested photocatalytic parameters and the degradation outcome in terms of rate constant, correlation factor, half-life, and variation between initial and final pH condition.

Table 22. Tested photocatalytic parameters for ($C_0 = 50$ mg/L, and $C_0 = 100$ mg/L initial CBZ concentrations under 365 nm, and $C_0 = 10$ mg/L initial CBZ concentration under 450 nm) with 1 g/L catalyst and their associated rate constant k (h^{-1}), correlation coefficient R^2 , half-life $t_{1/2}$ (h), and initial and final pH values

Test	Degradation rate constant k (h^{-1})	R^2	Half-life ($t_{1/2}$) (h)	pH _{initial}	pH _{final}
# Decorated photocatalyst material test Vs $[CBZ]_0 = 50$ mg/L and $[CBZ]_0 = 100$ mg/L					
HRTiO ₂ Vs initial 50 mg/L CBZ	2.166	0.99	0.32	7.60	6.84
HRTiO ₂ Vs initial 100 mg/L CBZ	1.224	0.99	0.57	7.64	6.78
W/HRTiO ₂ Vs initial 50 mg/L CBZ	4.359	0.99	0.16	5.50	6.20
W/HRTiO ₂ Vs initial 100 mg/L CBZ	2.032	0.99	0.34	5.62	6.34
*Decorated photocatalyst material test Vs $[CBZ]_0 = 10$ mg/L					
HRTiO ₂	0.121	0.98	5.74	7.64	6.74
W-Mo/HRTiO ₂	0.119	0.99	5.84	4.74	5.36
W-Mo/HRTiO ₂ + 0.5CoPc	0.151	0.99	4.59	4.89	5.63
* pH effect on W- Mo/HRTiO ₂ + 0.5 CoPc Vs $[CBZ]_0 = 10$ mg/L					
pH 4	0.177	0.99	3.91	4.05	5.84

Continuation of Table 22

pH 9	0.018	0.91	39.15	8.89	9.42
pH 11	0.098	0.99	7.11	10.88	11.35
[#] Tests performed under 365 nm near UV-vis irradiation, and initial pH _{natural} (unmodified) condition, [*] Tests performed under 450 nm visible light irradiation, and initial pH _{natural} (unmodified) condition					

4.3. Photocatalyst Activity Evaluation of SynTiO₂ and Decorated Material Forms

Preliminary tests were performed of all the W and or Mo decorated sol-gel synthesized TiO₂ sample materials towards the model CECs compounds. Afterwards, the best performing photocatalyst material for each of CEC compound is selected and employed for further photocatalytic tests evaluation.

4.3.1. Photocatalyst Material Test Evaluation Over Ibuprofen (IBF)

The SynTiO₂ and decorated forms were deployed for a preliminary test towards ibuprofen (IBF). As can be seen from the Figure 72, after 240 min irradiation exposure under 365 nm, Mo-W/SynTiO₂ showed the better photocatalytic activity performance outcome over the rest of Mo/SynTiO₂, and W/SynTiO₂ and in comparison, to the unmodified SynTiO₂. Haven achieved almost 90 % initial 10 mg/L IBF concentration removal at a rate constant of $\sim 0.007 \text{ min}^{-1}$, half-life of 100.4 min (Table 23) at 240 min irradiation time in comparison to about 60 % and ~ 56 % removals for Mo/SynTiO₂ and W/SynTiO₂ respectively, Mo-W/SynTiO₂ was chosen as the best performing photocatalyst and deployed for IBF degradation under various other tested conditions. The pH value at this stage for all the catalyst tested preliminarily remained natural hence unmodified (Table 23).

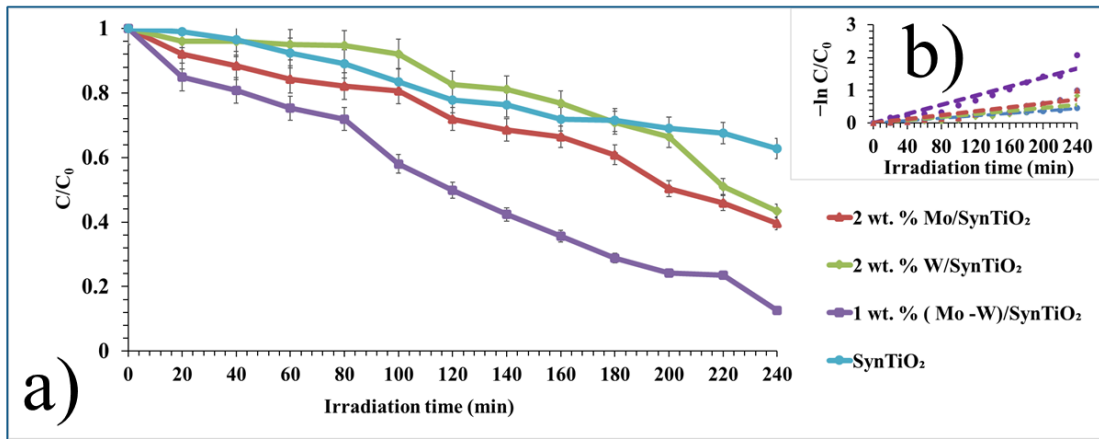


Figure 72. a) Preliminary test for the photocatalytic degradation of ibuprofen ($C_0 = 10$ mg/L, initial pH_{natural} (unmodified) conditions, Table 23) under 365 nm irradiation with SynTiO₂ and decorated forms, and b) corresponding photocatalytic degradation rate constant (k)

4.3.1.1. Effect of pH

4.3.1.1.1. pH Point of Zero Charge (pHpzc) Value

Other than the natural (unmodified) initial $pH = 9.87$ for the preliminary test of Mo-W/SynTiO₂, initial $pH = 5.5$, and initial $pH = 6.5$ were investigated of their effect on the photocatalytic degradation of IBF. pH is a crucial parameter in the heterogeneous photocatalytic degradation process of organic pollutants and can therefore exert significant influence on the photocatalyst activity performance.

To understand better the pH effect on the photocatalyst activity performance, pH point of zero charge (pHpzc) of MO-W/SynTiO₂ was determined at 8.5 and Figure 73 show the pHpzc plot of the Mo-W/SynTiO₂ photocatalyst.

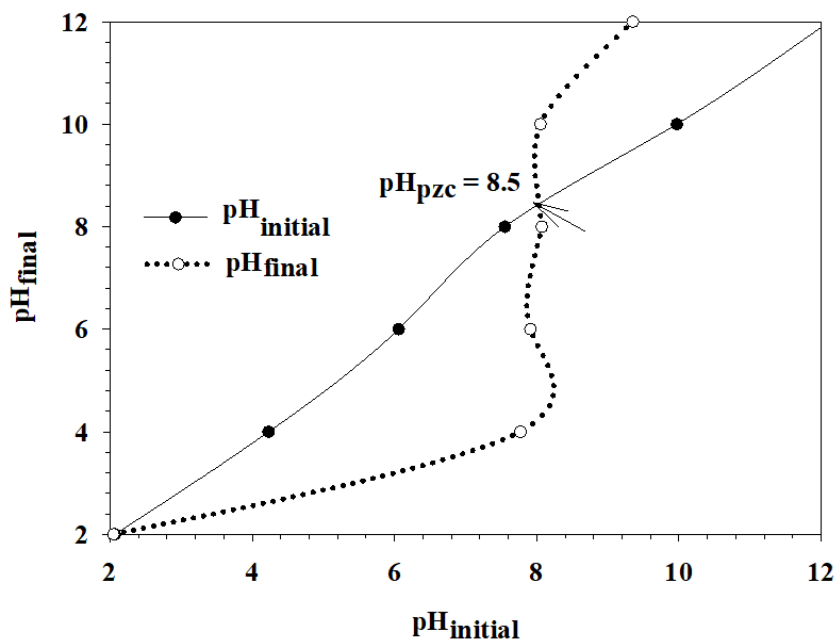


Figure 73. pH point of zero charge (pHpzc) plot of 1 wt. % Mo-1 wt. % W/SynTiO₂ photocatalyst material

The photocatalytic activity performance of Mo-W/SynTiO₂ can be related to the natural (unmodified) pH = 9.87 (Figure 74), IBF pKa value of range 4.9 - 5.2 (Table 19) [222], and the pH_{pzc} of the photocatalyst at 8.5 (Figure 73). At the natural (unmodified) pH = 9.87 condition, the IBF molecules are dissociated and exist in anionic form while the catalyst surface becomes negatively charged. The lack of attractive forces pulling the IBF molecules to the surface of the catalyst will prevail under this condition due to similarity in charges. However, since the anionic form is more promoted than the molecular form at pH > pKa, the degradation of IBF anionic form will be more photocatalytically favoured especially under UV irradiation [299-301]. As the reaction proceeded, the final aqueous suspension media pH value of 7.90 (Table 23) at 240 min irradiation may have played enhancing role on the photocatalytic degradation of IBF as the pH condition at this point now supports attraction of the anionic IBF form and the positively charged catalyst surface based on the IBF pka value and pH_{pzc} of the photocatalyst (Table 19, Figure 73) [222]. The initial pH conditions of 6.5, and 5.5 exhibited similar IBF photocatalytic degradation pattern. As can be seen from Figure 74, the rate constant of pH = 6.5; though, not significant was a bit higher at 0.0027 min⁻¹ than for pH = 5.5 at 0.0023 min⁻¹ where about 60 % initial 10 mg/L IBF concentration and about 47 % initial 10 mg/L IBF concentration was

respectively removed at 240 min irradiation (Figure 74). Though, these initial pH conditions agreed with the 8.5 p_Hpzc of the catalyst and 4.9 pK_a value of IBF to establish an electrostatic force of attraction that will pull the anionic IBF forms to the surface of the positively charged catalyst. This was not the case as it has been reported that at lesser pH dissociation of molecular IBF to its anionic form is not favoured [300-301]. Moreover, the further reduction to lower final pH values (Table 23) of these initial pH conditions contributed to the reduced IBF photocatalytic degradation. In all, pH effect on the enhanced IBF photocatalytic degradation followed such order: pH_{natural} (unmodified) = 9.87 > pH = 6.5 > pH = 5.5 (Figure 74).

Therefore, in order to keep condition natural (unmodified) as much as possible with respect to pH and haven also achieved better photocatalytic activity performance at such pH condition, other test evaluations were performed at natural (unmodified) pH = 9.87.

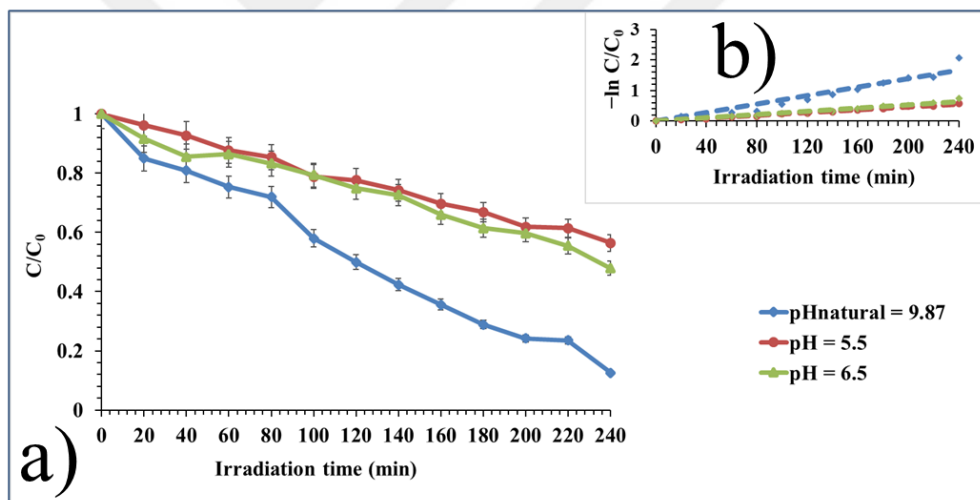


Figure 74. a) pH effect on the photocatalytic degradation efficiency of Mo-W/SynTiO₂ over IBF ($C_0 = 10$ mg/L), and b) corresponding photocatalytic degradation rate constant (k)

4.3.1.2. Effect of Catalyst Dosage and Initial IBF Concentration

At initial pH_{natural} (unmodified) value of 9.87, effect of catalyst dosages of 0.75 g/L, 1.25 g/L, 2 g/L and already investigated 1 g/L was evaluated over 10 mg/L initial IBF concentration. As can be seen from the Figure 75, increase in the catalyst dosage reflected to a decrease in the photocatalytic degradation rate of IBF. This can be attributed to the shielding of certain catalyst amount in suspension hindering adequate penetration of light for adequate photoactivation of the catalyst particles [162, 223]. It can be seen from the Table 23, that the variation between initial and final pH conditions at the tested catalyst dosages maintained a stabilized and not significantly varied final pH values except for 2 g/L catalyst dose with the lesser photocatalytic activity.

Thus, the suppression effect of the catalyst dosage against IBF photocatalytic degradation can be seen to have followed such order: 1 g/L < 0.75 g/L < 1.25 g/L < 2 g/L (Figure 75).

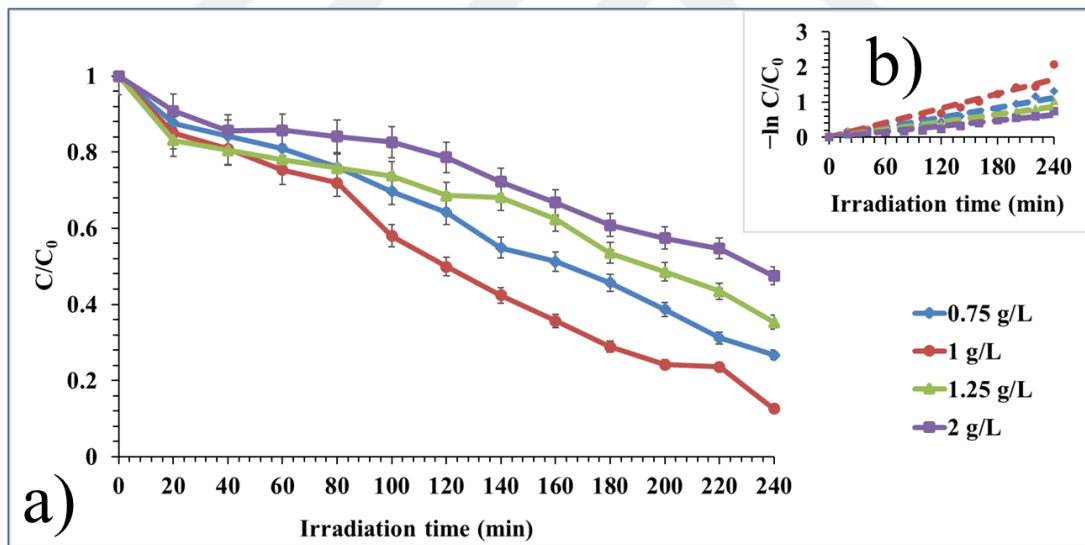


Figure 75. a) Catalyst dosage effect on the photocatalytic degradation efficiency of Mo-W/SynTiO₂ over IBF ($C_0 = 10$ mg/L, initial pH_{natural} = ~ 9.87), and b) corresponding photocatalytic degradation rate constant (k)

On the other hand, the effect of initial IBF concentration was investigated at pH natural (unmodified) condition (Figure 74) and with a 1 g/L catalyst dose (Figure 75) that delivered the better photocatalytic activity performance of all the other tested dosages.

Again, from Figure 76, there was a mixed behaviour in the photocatalytic degradation rate. The photocatalyst removed over 90 % initial 10 mg/L IBF concentration at a rate constant of 0.0069 min^{-1} in comparison to about 73 % removal of initial 5 mg/L IBF concentration at a rate constant of 0.0047 min^{-1} (Figure 76, Table 23). Against 15 mg/L initial IBF concentration, the photocatalyst removed $< 50 \%$ IBF at a rate constant of 0.0019 min^{-1} less than that achieved against 20 mg/L initial IBF concentration where about 51 % removal and at a rate of 0.003 min^{-1} was achieved after 240 min irradiation (Figure 76, Table 23). Though, an increase in initial pollutant concentration has been reported to impede photocatalytic degradation rate as more molar concentration of the pollutant saturate available active photocatalyst site [162, 223].

Notwithstanding, variation in photocatalytic degradation rate between either different catalyst dosages at a particular initial pollutant concentration or vice versa with a mixed behavior outcome has also been reported and attributed to effect due to surface adsorption mechanisms [223]. Variation between the initial and final pH values was not wide as can be seen from Table 23 and maintained almost a stable value at the final point.

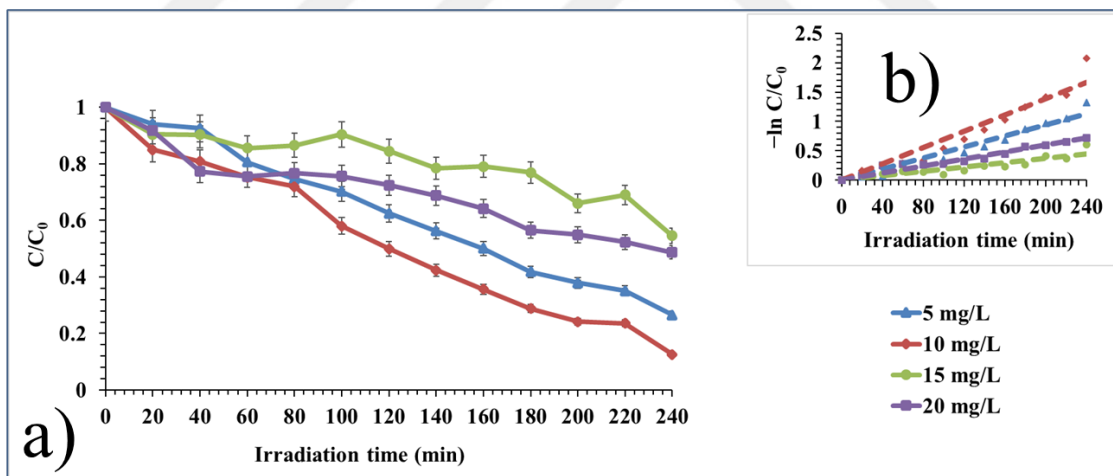


Figure 76. a) Initial IBF concentration effect on the photocatalytic degradation efficiency of 1 g/L Mo-W/SynTiO₂ initial pH_{natural} = ~ 9.87, and b) photocatalytic degradation rate constant (k)

With a better photocatalytic activity performance at initial pH = 9.87, catalyst dosage of 1 g/L and initial IBF concentration of 10 mg/L, the rest test evaluations were carried out with these conditions unless otherwise stated.

4.3.1.3. Effect of Chemical Scavengers

The effect of chemical scavengers in the probation of the reactive species responsible for driving the photocatalytic degradation of IBF was also investigated. 1 mM each of isopropyl alcohol (IPA), benzoquinone (BQ), and ammonium oxalate (AO), were employed as the chemical scavengers for the respective probe of hydroxyl ($\text{HO}\cdot$) radical, superoxide anion ($\text{O}_2^{\cdot-}$) and hole charge (h^+) carrier reactive species [134, 162, 222-223].

As can be seen from Figure 77, all the tested chemical scavengers with respect to no added scavenger impeded the photocatalytic degradation of IBF during the 240 min UV irradiation. In comparison to no added scavenger, IPA suppressed the photodegradation reaction rate with about 80 % of initial 10 mg/L IBF concentration removed while BQ removed about 70 % of same initial IBF concentration. The most suppression effect was observed in the case of AO where in comparison to over 90 % initial 10 mg/L IBF removed after 240 min irradiation, < 50 % removal was achieved (Figure 77). The stability between the initial and final pH conditions (Table 23) of the catalyst suspension media containing the tested chemical scavengers confirms that pH variation effect was minimal towards the selectivity of the tested scavengers with respect to the probed reactive species.

Thus, the suppression effect of the chemical scavengers towards IBF photocatalytic degradation followed the order: AO > BQ > IPA (Figure 77, Table 23).

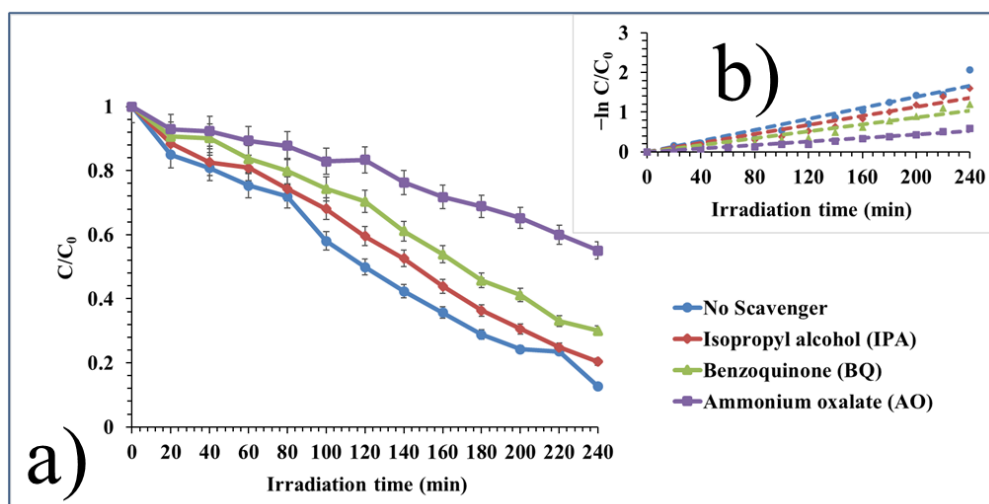


Figure 77. a) Chemical scavenger effect on the photocatalytic degradation efficiency of 1 g/L Mo-W/SynTiO₂ over IBF ($C_0 = 10$ mg/L, initial $\text{pH}_{\text{natural}} = \sim 9.87$), and b) corresponding photocatalytic degradation rate constant (k)

4.3.1.4. Effect of Contaminant Ions (Cations and Anions) and Humic Acid (HA)

Contaminant ion and humic acid effect (HA) on the photocatalytic degradation process were also evaluated. One molar equivalent (1 Meq) concentration each of the tested cations and anions were employed while different concentrations in the range of 1 mg/L – 4 mg/L was used in the case of HA. For the cations, Fe^{3+} , Mg^{2+} , Ca^{2+} , Al^{3+} , and NH_4^+ ions were tested while for the anions, HCO_3^- , CO_3^{2-} , SO_4^{2-} , HPO_4^{2-} , and Cl^- were tested.

As can be seen from Figure 78, in the first 20 min of the 240 min irradiation time window, Fe^{3+} ion upon addition removed over 84 % of the initial 10 mg/L IBF concentration. This sharp rate of removal continued up to 40 min of irradiation and over 90 % initial 10 mg/L IBF concentration was removed; sustained thereafter until the 240 min irradiation with almost complete IBF removal at this time. Al^{3+} assumed the same degradation rate kinetics pattern, however in a more slowly fashion (Figure 78). In the presence of Al^{3+} , about 60 % of the initial 10 mg/L IBF concentration was removed in the first 20 min of the 240 min irradiation. The photocatalytic degradation process sustained the rate of removal but at a much slower kinetic rate pattern in comparison to Fe^{3+} with subsequent IBF removal up to 140 min irradiation time where about 90 % IBF removal was achieved and maintained till the 240 min irradiation time window (Figure 78). Comparatively, in the presence of Fe^{3+} , and Al^{3+} ions, IBF removal rate was enhanced by the photocatalyst with a respective 0.0184 min^{-1} and 0.0142 min^{-1} degradation rate constants as to the 0.0069 min^{-1} achieved by no cation addition (Figure 78). On the contrary, Mg^{2+} , Ca^{2+} , and NH_4^+ exerted suppression effect with respect to no cation addition with respective removal rate of 0.003 min^{-1} , 0.0025 min^{-1} and 0.0022 min^{-1} (Figure 78). Reports have been documented of the inhibitory effects of Fe^{3+} and Al^{3+} ions on the photocatalytic degradation process of organic pollutants with the facilitation of same by Mg^{2+} , Ca^{2+} , and NH_4^+ [298].

However, the outcome in this thesis work is on the contrary and can be attributed to different test evaluation protocol, different photocatalyst and reaction conditions. Moreover, the variation between the initial and final pH condition in the presence of Fe^{3+} , and Al^{3+} ions shifted to much lower final pH points which are acidic proton (H^+) promoting environment that facilitated IBF removal rates in the presence of both ions (Table 23) [134, 222].

On the other hand, in the presence of Mg^{2+} , Ca^{2+} , and NH_4^+ ions, a shift of initial pH value to higher alkaline final pH points was recorded and contributed to the reduced photocatalytic degradation process witnessed in the presence of these ions (Table 23). Thus,

the suppression effect of the photocatalytic process in the presence of cations is of the order: $\text{Fe}^{3+} < \text{Al}^{3+} < \text{Mg}^{2+} < \text{Ca}^{2+} < \text{NH}_4^+$ (Figure 78).

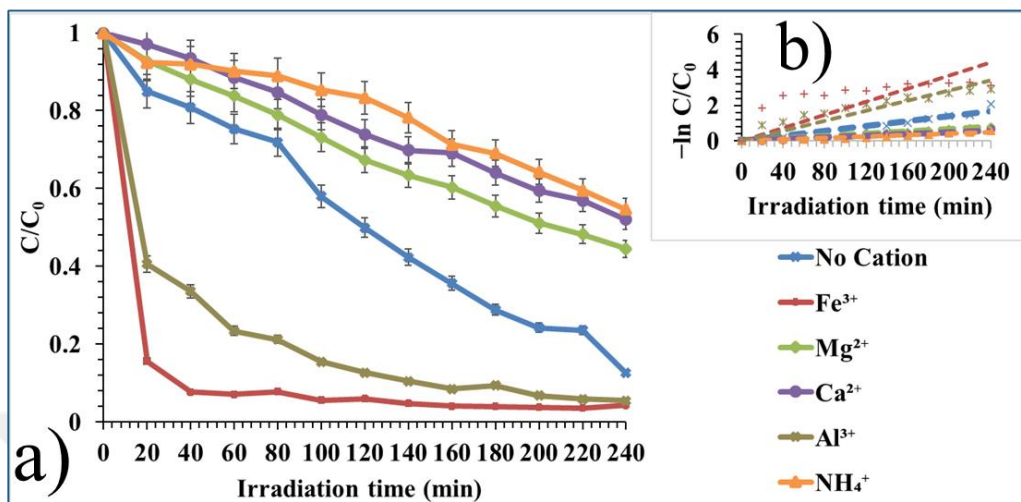


Figure 78. a) Cation effects on the photocatalytic degradation efficiency of 1 g/L Mo-W/SynTiO₂ over IBF ($C_0 = 10$ mg/L, initial $\text{pH}_{\text{natural}} = \sim 9.87$), and b) corresponding photocatalytic degradation rate constant (k)

Concerning the tested anions, except for the Cl^- ion in whose presence there was a little suppression on the photocatalytic degradation process but was not significant and later showed no influence with equal activity performance with no added anion at 240 min irradiation time (Figure 79). In the presence of HCO_3^- , SO_4^{2-} , CO_3^{2-} , and HPO_4^{2-} ions the photocatalytic degradation process was suppressed (Figure 79). This can be attributed to the scavenging capability of these anions towards hydroxyl ($\text{HO}\cdot$) radicals thereby diminishing the photoactivity [298]. Final pH values recorded in the presence of these anions did not to a large extent vary with respect to the initial pH values and maintained alkaline pH condition during the irradiation process (Table 23). The suppression effect exhibited on the photocatalytic degradation process in the presence of the anions is of such order: $\text{Cl}^- < \text{HCO}_3^- \leq \text{SO}_4^{2-} = \text{CO}_3^{2-} = \text{HPO}_4^{2-}$ (Figure 79).

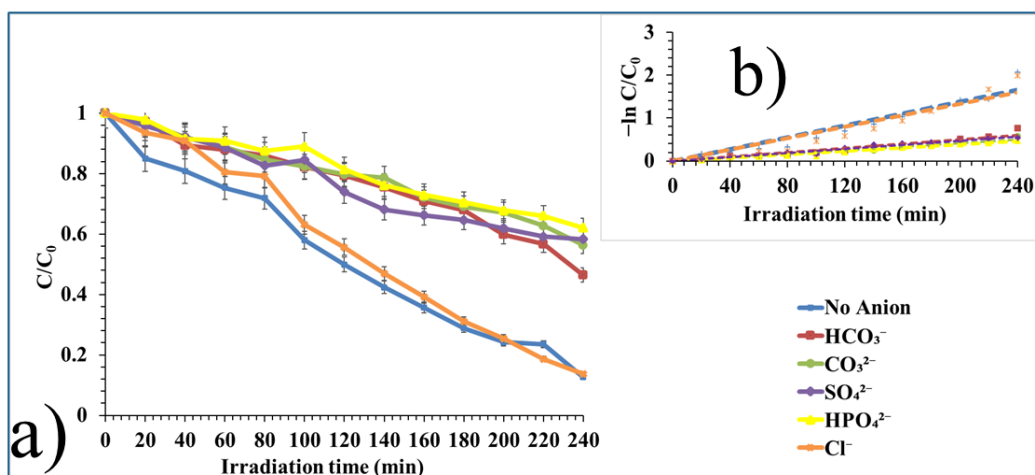


Figure 79. a) Anion effect on the photocatalytic degradation efficiency of 1 g/L Mo-W/SynTiO₂ over IBF ($C_0 = 10$ mg/L, initial $\text{pH}_{\text{natural}} = \sim 9.87$, and b) corresponding photocatalytic rate constant (k)

The effect on the photocatalytic degradation process showed in the presence of humic acid was such that with increase in the HA concentration, the photocatalytic degradation rate kinetics diminished (Figure 80). This can be attributed to the shielding of light penetration effect by HA in photocatalyst suspension media thereby reducing photocatalytic performance activity [134, 162, 223]. The inhibitory effect of the photocatalytic degradation process in the presence of HA occurred in such a trend: 1 mg/L < 2 mg/L < 3 mg/L \sim 4 mg/L (Figure 80). Measured initial pH values in the presence of the tested HA concentration (1mg/L – 4 mg/L) shifted to and maintained lower alkaline final pH values (Table 23).

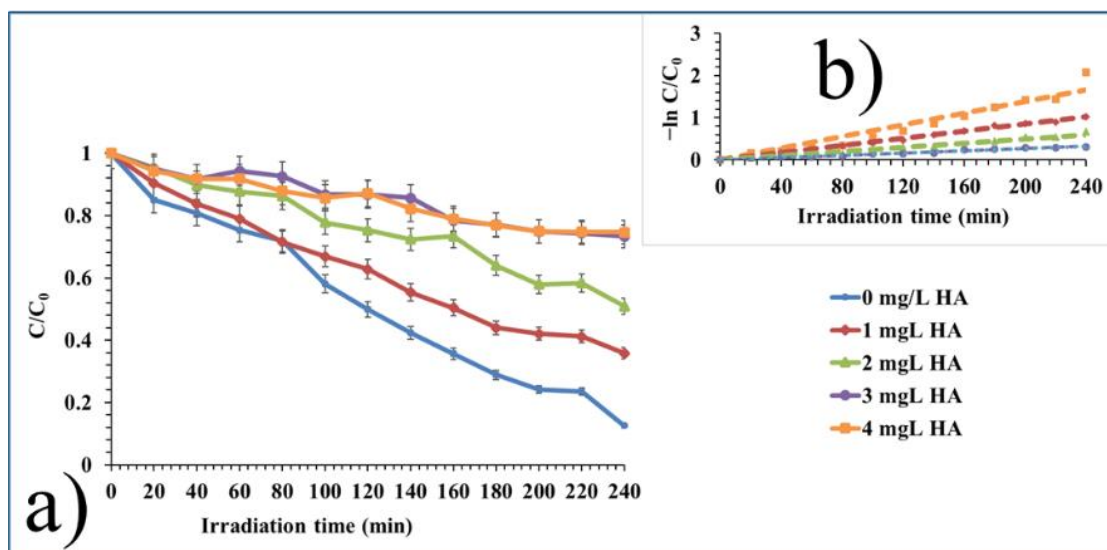


Figure 80. a) Humic acid (HA) effect on the photocatalytic degradation efficiency of 1 g/L Mo-W/SynTiO₂ over IBF ($C_0 = 10$ mg/L, initial $\text{pH}_{\text{natural}} = \sim 9.87$), and b) corresponding photocatalytic degradation rate constant (k)

4.3.1.5. Effect of Hydrogen Peroxide (H₂O₂)

As an external oxidant, hydrogen peroxide (H₂O₂) was added in the concentration range of 1 mM – 4 mM concentrations. As can be seen from Figure 81, H₂O₂ effect on the photocatalytic degradation process was such that with increase in the H₂O₂ concentration, the IBF removal rate by the photocatalyst was the more suppressed. This exhibition can be attributed to the reported scavenging attitude of hydrogen peroxide (H₂O₂) which limits the intensity and availability of photogenerated hydroxyl (HO[•]) radicals in driving the degradation process [223, 298]. The anomaly seen in the presence of 2 mM H₂O₂, where the photocatalytic degradation process was less suppressed compared to 1 mM H₂O₂ up to 220 min irradiation time can be attributed to variations of scavenging attitudes at these two different concentrations (Figure 81). However, this trend can be seen change with progress in irradiation time where at 240 min, and in the presence of 1 mM H₂O₂, the photocatalytic degradation process become much less interfered compared to 2 mM H₂O₂ (Figure 81). Variation between initial and final pH condition in the presence of these H₂O₂ concentrations remained approximately stable (Table 23). In all, such a trend of suppression effect of the photocatalytic degradation process in the presence of the added hydrogen peroxide (H₂O₂) can be observed: 2 mM H₂O₂ < 1 mM H₂O₂ < 3 mM H₂O₂ < 4 mM H₂O₂.

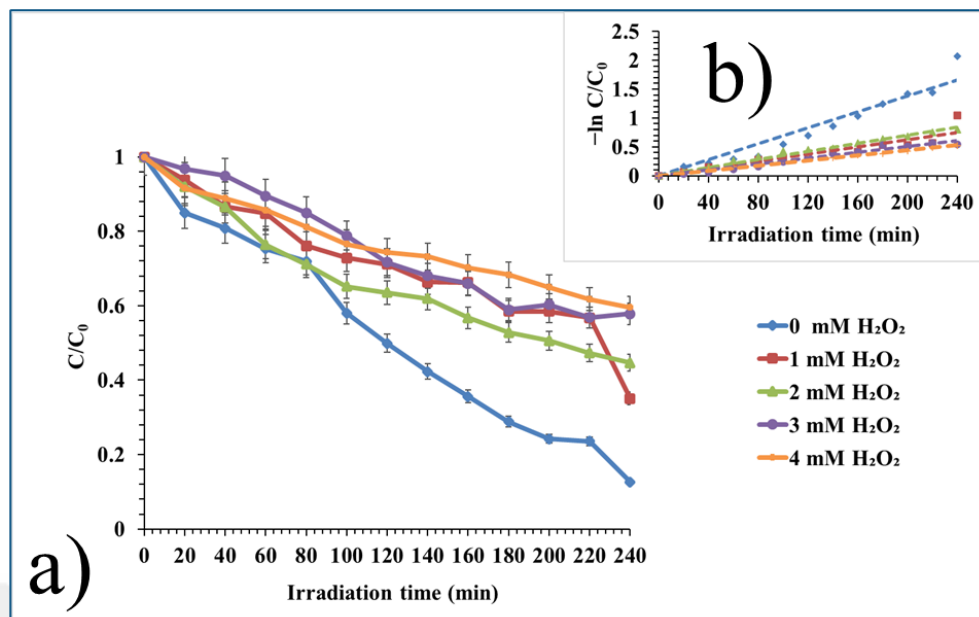


Figure 81. a) Hydrogen peroxide (H_2O_2) effect on the photocatalytic degradation efficiency of 1 g/L Mo-W/SynTiO₂ over IBF ($C_0 = 10$ mg/L, initial $pH_{natural} = \sim 9.87$), and b) corresponding degradation rate constant (k)

As can be seen from Figure 82, dark, photolysis, heat effect without catalyst and heat effect with catalyst under the test condition protocols as already stated did not impact the photocatalytic degradation process of IBF significantly.

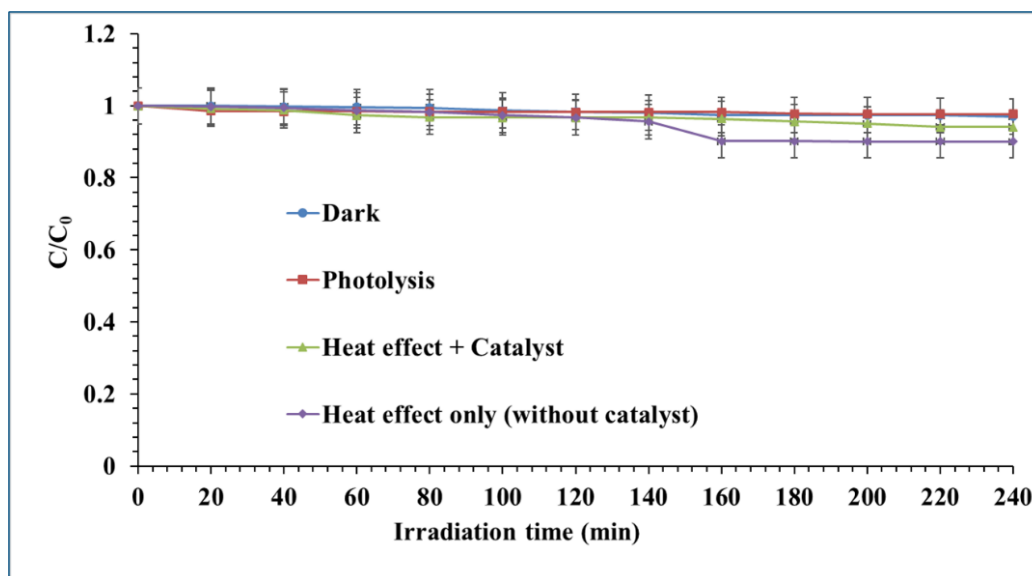


Figure 82. Dark, photolysis, heat effect without catalyst and heat effect with catalyst at test conditions of : 1 g/L Mo-W/SynTiO₂, C₀ = 10 mg/L, initial pH_{natural} = ~ 9.87 where applicable

Table 23 show the parametric indicators for the photocatalytic activity performance of the tested materials over ibuprofen (IBF) based on their degradation rate constant (k), correlation constant (R²), half-life (t_{1/2}), and pH variation condition.

Table 23. Tested photocatalytic parameters for (C₀ = 10 mg/L initial IBF concentration under 365 nm) with 1 g/L catalyst and their associated rate constant (min⁻¹), correlation coefficient (R²), half-life t_{1/2} (min), and initial and final pH values

Test	Degradation rate constant k (min ⁻¹)	R ²	Half-life (t _{1/2}) (min)	pH _{initial}	pH _{final}
Preliminary test for photocatalyst material selection #					
SynTiO ₂	0.0019	0.99	364.74	3.48	2.98
W/SynTiO ₂	0.0023	0.88	301.30	7.8	7.11
Mo/SynTiO ₂	0.0030	0.94	231	9.71	8.00
Mo-W/SynTiO ₂	0.0069	0.97	100.43	9.81	7.45
Selected photocatalyst material: Mo-W/SynTiO ₂					

Continuation of Table 23

pH effect [#]					
pH _{natural} = ~10	0.0069	0.98	100.43	9.87	7.90
pH = 5.5	0.0023	0.99	301.30	5.5	5.36
pH = 6.5	0.0027	0.99	256.67	6.5	6.42
Catalyst dosage effect ^{#, *}					
0.75 g/L	0.0047	0.98	147.45	9.81	8.63
1 g/L	0.0069	0.98	100.43	9.8	8.06
1.25 g/L	0.0036	0.98	192.50	9.82	7.89
2 g/L	0.0027	0.98	256.67	9.85	7.01
Pollutant concentration effect ^{#, *}					
5 mg/L	0.0047	0.98	147.45	9.92	7.57
10 mg/L	0.0069	0.98	100.43	9.82	7.13
15 mg/L	0.0019	0.94	364.74	9.88	7.28
20 mg/L	0.0030	0.98	231.00	9.94	7.78
Chemical scavenger test ^{#, *}					
No scavenger	0.0069	0.98	100.43	9.87	7.84
1 mM IPA	0.0057	0.98	121.58	9.83	8.36
1 mM BQ	0.0043	0.97	161.16	9.85	7.85
1 mM AO	0.0022	0.99	315.00	9.85	8.16
Contaminant ions: cation effect ^{#, *}					
No Cation	0.0069	0.98	100.43	9.88	7.88
1 M Fe ³⁺	0.0184	0.87	37.66	9.86	4.19
1 M Mg ²⁺	0.0033	0.99	210.00	9.82	7.85
1 M Ca ²⁺	0.0025	0.99	277.20	9.85	7.52
1 M Al ³⁺	0.0142	0.96	48.80	9.83	4.17
1 M NH ₄ ⁺	0.0022	0.98	315.00	9.84	7.95
Contaminant ions: anion effect ^{#, *}					
No Anion	0.0069	0.98	100.43	9.85	7.86
1 M HCO ₃ ⁻	0.0025	0.97	277.20	9.88	8.75
1 M CO ₃ ²⁻	0.0021	0.99	330.00	9.82	9.06
1 M SO ₄ ²⁻	0.0024	0.99	288.75	9.90	8.21

Continuation of Table 23

1 M HPO ₄ ²⁻	0.0019	0.99	364.74	9.85	7.62
1 M Cl ⁻	0.0067	0.96	103.43	9.84	8.38
Humic acid (HA) effect ^{#, *}					
0 mg/L HA	0.0069	0.98	100.43	9.85	7.87
1 mg/L HA	0.0042	0.99	165.00	9.84	7.68
2 mg/L HA	0.0025	0.99	277.20	9.86	7.78
3 mg/L HA	0.0013	0.99	533.08	9.85	7.56
4 mg/L HA	0.0014	0.99	495.00	9.85	7.48
Hydrogen peroxide (H ₂ O ₂) effect ^{#, *}					
0 mM H ₂ O ₂	0.0069	0.98	100.43	9.88	7.95
1 mM H ₂ O ₂	0.0031	0.95	223.55	9.83	7.44
2 mM H ₂ O ₂	0.0035	0.99	198.00	9.86	7.77
3 mM H ₂ O ₂	0.0025	0.99	277.20	9.91	7.78
4 mM H ₂ O ₂	0.0974	0.92	7.11	9.89	7.84
[#] Tests performed under 365 nm near UV-vis irradiation for preliminary stage and others with related initial pH _{natural} (unmodified) condition, [*] other test conditions performed at initial pH _{natural} (unmodified) condition					

4.3.1.6. Possible Photocatalytic Degradation Process Mechanism

From the insight of the chemical scavenger probation test for the reactive species responsible for the photocatalytic degradation process of IBF (Section 4.3.1.3), such a degree of the reactive species participation: $h^+ > O_2^- > HO\cdot$ is portrayed (Figure 77)

Based on this outcome, the photogenerated hole charge (h^+) carrier played a prominent role in the photocatalytic degradation process while superoxide anion (O_2^-), and hydroxyl radical ($HO\cdot$) were also involved. Thus, a classical photodegradation mechanism where all the basic reactive species are involved is proposed in the degradation of IBF. As can be seen from the Figure 83, upon the photoirradiation of the Mo-W/SynTiO₂, electrons (e^-) are knocked off the photocatalyst material and by complementarity there is the generation of hole charge carriers (h^+). The photogenerated electrons drift towards the conduction band

(CB), interacts with surface adsorbed oxygen and by reduction form superoxide anion ($O_2^{\cdot-}$) specie.

Correspondingly, the hole charge carriers (h^+) at the valence band (VB) interacts with surface adsorbed water molecule (H_2O) and by oxidation form hydroxyl radical ($HO\cdot$) specie. The photogenerated charges e^-/h^+ and their related formed superoxide anion ($O_2^{\cdot-}$), and hydroxyl radical ($HO\cdot$) species are now available as reactive oxygen species (ROS) entities for the degradation of IBF (Figure 83).

In support of the proposed mechanism is also the energy band level potentials obtained via Mulliken function (Equation 85, Equation 86, and Table 17) which favours the charge transfer energetics of the photodegradation process of IBF. The derived CB edge potential (- 0.94 eV) (Table17), of the photocatalyst material is negative enough when compared to the $E^{\circ}_{red.}(O_2/O_2^{\cdot-})$ value of (- 0.046 eV) on the normal standard hydrogen electrode (SHE). Therefore, the formation of superoxide anion ($O_2^{\cdot-}$) via single electron reduction pathway of the surface adsorbed O_2 at the CB energy level is favoured (Figure 83).

On the other hand, the derived VB edge potential (2.10 eV) (Table 17) in comparison to the $E^{\circ}_{ox.}(OH^-/HO\cdot)$ of value (1.99 eV) on the normal standard hydrogen electrode (SHE) is favoured with a higher energy potential for the formation of hydroxyl radical ($HO\cdot$) through the indicated pathway (Figure 83). The formation of superoxide anion ($O_2^{\cdot-}$) via $O_2 + H^+/O_2^{\cdot-}$ pathway at the VB potential edge (Figure 83) is also favoured given that the required $E^{\circ}_{ox.}$ Potential value (0.682 eV) for its formation on the normal standard hydrogen electrode (SHE) relative to the derived VB edge potential (2.10 eV) (Table17, Figure 83) is higher in favour of its formation also at this level.

Furthermore, the reported respective potential values of W^{+6}/W^{+5} and Mo^{+6}/Mo^{+5} redox systems at - 0.03 V and + 0.4 V are more higher values than the one derived for the base $SynTiO_2$ in this thesis (- 0.34 eV) and in agreement with reported literature value for TiO_2 potential (Table 17) [107].

Therefore, the W^{+6}/W^{+5} and Mo^{+6}/Mo^{+5} redox systems of the photocatalyst material stands favoured in capturing electrons from the base TiO_2 ; as such facilitating efficient charge transfer and separation processes that compensates prolonged life time of photogenerated reactive species for improved performance efficiency (Table 17, Figure 83).

Connoting all these information, such a reaction mechanism where basically all the photogenerated charges and related species are involved in the photocatalytic degradation process of IBF is proposed (Figure 83).

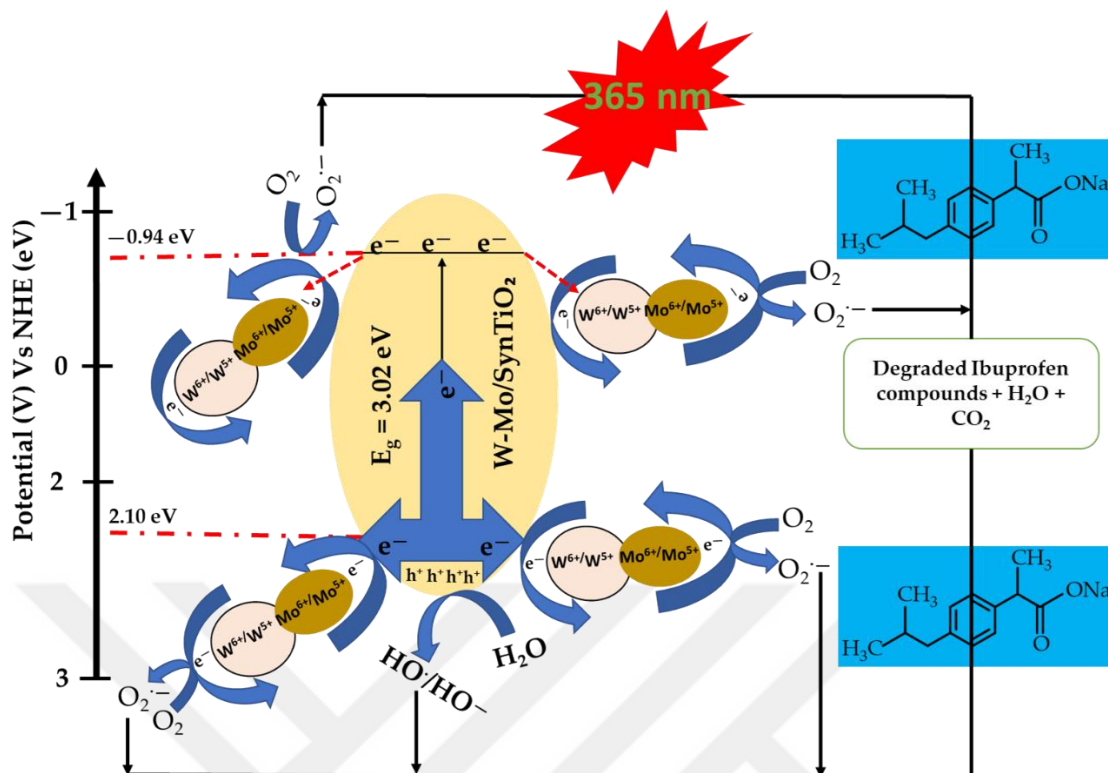


Figure 83. Proposed photocatalytic degradation process mechanism for the removal of IBF by Mo-W/SynTiO₂

4.3.2. Photocatalyst Material Test Evaluation Over Caffeine (CAF)

In testing the photocatalytic activity performance of the synthesized TiO₂ series and its decorated forms towards the degradation of caffeine (CAF), molybdenum decorated TiO₂ (Mo/SynTiO₂) was employed as the best performing photocatalyst material. The other series sample materials following preliminary test (results not shown) were not photocatalytically active towards CAF degradation. From Figure 84, over 80 % initial 5 mg/L CAF concentration was removed after 360 min under 365 nm near UV-Vis irradiation at ~ 6.50 initial pH condition (Table 24). In comparison to the unmodified SynTiO₂ (Figure 84) which was not active towards CAF degradation for 360 min irradiation, Mo/SynTiO₂ was investigated for various other test condition effect on the photocatalytic performance activity.

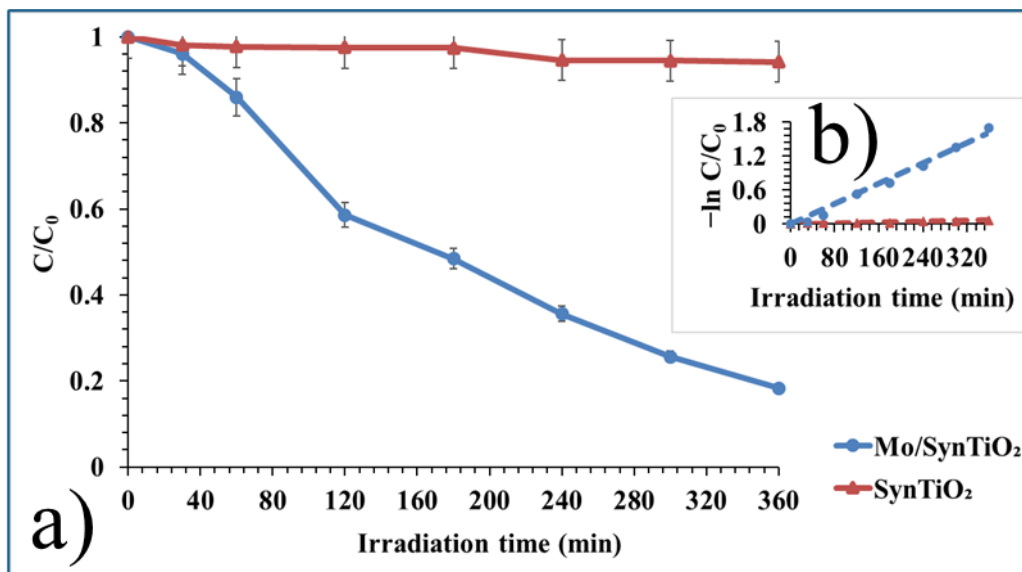


Figure 84. a) Preliminary test for the photocatalytic degradation of caffeine ($C_0 = 5$ mg/L, initial pH_{natural} (unmodified)) under 365 nm irradiation with SynTiO₂ and Mo/SynTiO₂ decorated form, and b) corresponding photocatalytic degradation rate constant (k)

4.3.2.1. Effect of pH

4.3.2.1.1. pH Point of Zero Charge (pH_{pzc}) Value

pH being such a crucial parameter in heterogeneous photocatalysis was investigated of its effect on the photocatalytic degradation process of CAF. Firstly, the pH point of zero charge (pH_{pzc}) of the photocatalyst material was determined at 7.9 (Figure 85) and used in the interpretation of the pH effect on the photocatalytic degradation process of CAF with respect to its pK_a value of (10.4) (Table 19).

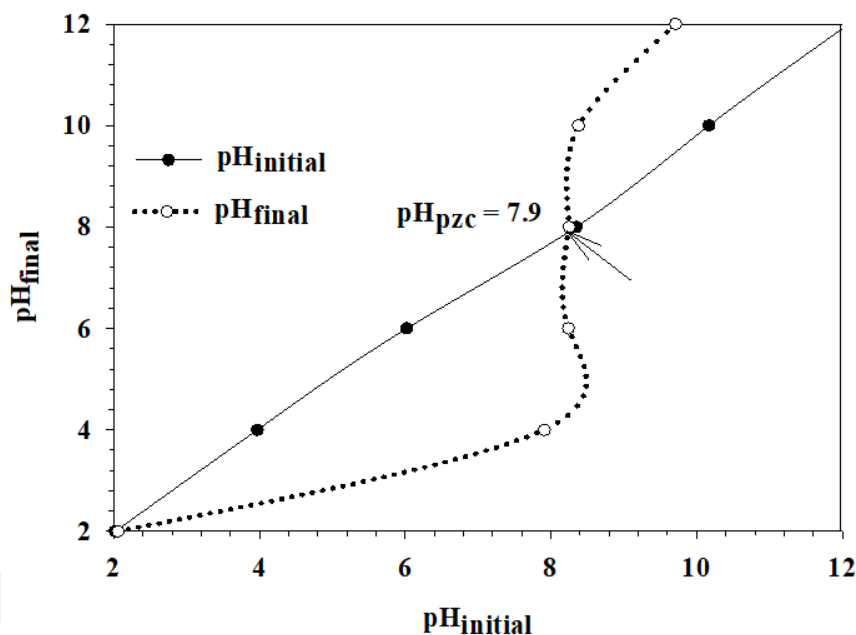


Figure 85. pH point of zero charge (pHpzc) plot of 2 wt. % Mo/SynTiO₂ photocatalyst material

Apart from the ~ 6.50 initial pH condition at which the preliminary test was performed, other initial pH values = 9, and 4 were also investigated. As can be seen from Figure 86, the least performance of the photocatalyst material occurred at initial pH = 4; where < 20 % of 5 mg/L initial CAF was removed at 360 min irradiation. This outcome can be attributed to the fact that the caffeine molecules at this initial pH condition are protonated as it is below its pK_a value of 10.4 with the catalyst surface positively charged as it is again below the pH_{pzc} at 7.9 (Table 19, Figure 86). Thus, there is an established repulsive force between the protonated caffeine molecules in the suspension media and the positively charged catalyst surface limiting required catalyst surface contact for CAF degradation. Moreover, it is reported that at low acidic pH condition, photocatalytic degradation of caffeine is inhibited by interfering adsorption process mechanism, photocatalyst instability and decomposition amongst other limiting factors [162]. A little shift to moderately acidic final pH of ~ 5 (Table 24) did not influence the photocatalytic degradation process outcome up to the 360 min irradiation time window. At the initial natural (unmodified) pH = ~ 6.5, about 90 % of 5 mg/L initial CAF was removed at 360 min irradiation (Figure 86). However, the caffeine molecule remains also the same at the initial natural (unmodified) pH = ~ 6.5 with respect to the pH_{pzc} (7.9) and caffeine pK_a (10.4).

The observed photocatalytic performance activity at this pH condition can be attributed to the enhanced surface modification properties of the photocatalyst material at this pH condition and by inference regardless of pH modification as this is a natural (unmodified) pH condition [162, 274]. The initial pH = 9 condition saw the photocatalyst with even an improved activity performance in comparison to both the natural (unmodified) initial pH = ~ 6.5 and initial pH = 4. About 94 % of initial 5 mg/L CAF concentration was achieved after 360 min irradiation at initial pH = 9 (Figure 86). This can be attributed to the more favoured attraction of the protonated caffeine molecules to the negatively charged catalyst surface by virtue of the respective values of pKa (10.4) and pH_{pzc} (7.9) (Table 19, Figure 85) [134, 162, 222, 274]. Moreover, the non-exclusivity of the photocatalytic degradation of caffeine and other organic pollutants via hydroxyl radical (HO \cdot) can also be suggested to have risen from the improved photocatalyst activity performance at the alkaline pH values of 6.5 and 9 as such environment enhances hydroxide ion (HO $^-$) generation to drive degradation processes as well [162].

The maintained final pH values around the initial pH alkaline promoting environment (Table 24) confirms the sustained improved photoactivity performance of the catalyst at these points while though with a moderate shift to final pH = 4.73 (Table 24), the initial pH = 4 condition remained acidic and unfavourable for improved photocatalytic degradation of caffeine (Figure 86).

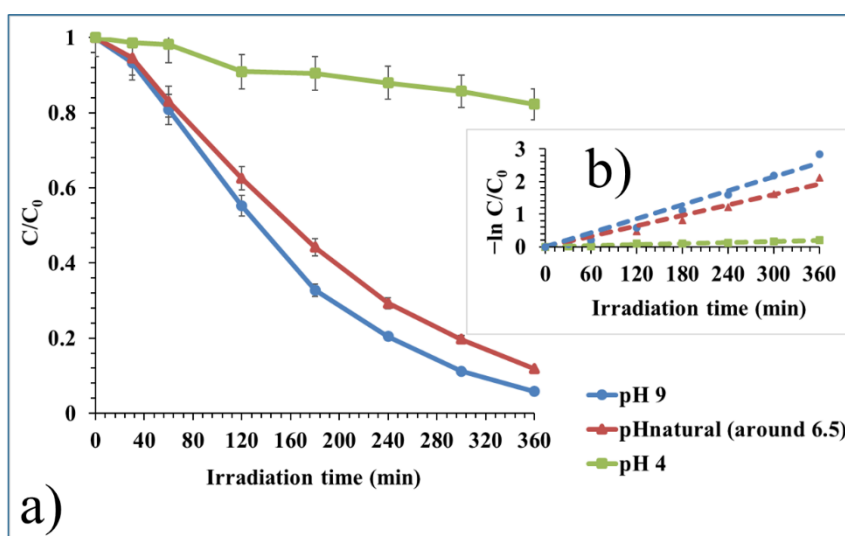


Figure 86. a) pH effect on the photocatalytic degradation efficiency of Mo/SynTiO $_2$ over CAF ($C_0 = 5$ mg/L), and b) corresponding photocatalytic degradation rate constant (k)

In order not alter to a large extent, the photocatalytic reaction suspension media by shifting the pH working condition through adjustments using HCl and or NaOH, other test conditions preferably were carried out at initial natural (unmodified) pH = ~ 6.5.

4.3.2.2. Effect of Catalyst Dosage and Initial CAF Concentration

Catalyst dosage effect as can be seen from Figure 87 on the photocatalytic degradation process of CAF was such that with increase in catalyst dose, photocatalyst activity performance improved. Additionally, to 1 g/L catalyst dose, 0.5 g/L, 0.75 g/L and 1.25 g/L were investigated. The 1.25 g/L dose showed though not significant improved photocatalyst activity performance with respect to 1 g/L where at 360 min irradiation, about 88 % of 5 mg/L initial CAF was removed with respect to about 83 % removal for the 1 g/L catalyst dose (Figure 87). Retarded rate of degradation was witnessed of 0.75 g/L and 0.5 g/L as respective ~ 70 % and 54 % initial 5 mg/L CAF concentration was removed after 360 min irradiation. Higher removal rate obtained at higher doses of the catalyst has been reported and attributed to increase in photocatalyst surface active sites that help facilitate photocatalytic degradation process than at low doses [162, 223]. Variation between initial and final pH values of suspension media was minimal (Table 24). Thus, the enhancing effect of investigated photocatalyst dosages is of the order: 1.25 g/L \geq 1 g/L > 0.75 g/L > 0.5 g/L (Figure 87).

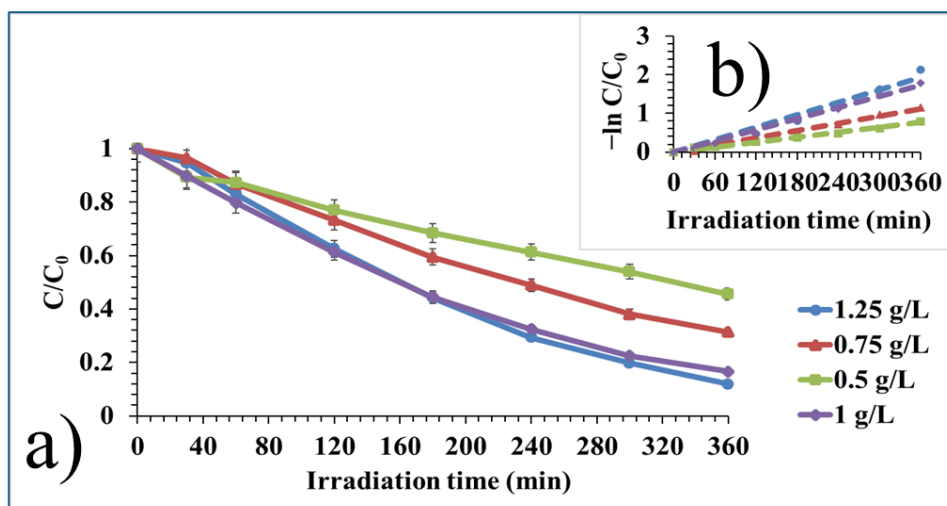


Figure 87. a) Catalyst effect on the photocatalytic degradation efficiency of Mo/SynTiO₂ over CAF ($C_0 = 5$ mg/L, initial pH_{natural} = ~ 6.5), and b) corresponding photocatalytic degradation constant (k)

On the other hand, in addition to already employed 5 mg/L initial CAF concentration, other initial CAF concentrations of 10 mg/L, 15 mg/L, and 20 mg/L were also investigated. As can be seen from Figure 88, increase in initial pollutant concentration decreases the photocatalytic activity performance of the photocatalyst material in the degradation of caffeine. This is attributed to the irreversible saturation of active surface photocatalyst sites at higher initial pollutant concentrations [162, 223]. The equal activity performance exhibited by the photocatalyst at initial CAF concentrations of 10 mg/L and 15 mg/L where about 75 % removal was recorded in comparison to the over 80 % removal of initial 5 mg/L CAF concentration can be related to similarity in catalyst surface adsorption mechanisms at those concentrations [223]. The lowest photocatalytic activity performance was of the 70 % removal recorded at initial 20 mg/L CAF concentration. Final pH values of the initial tested CAF concentrations were reduced a bit to lower moderately alkaline values and were stabilized (Table 24). The suppression effect on the photocatalytic activity performance over the tested initial CAF concentration followed such order: 5 mg/L < 10 mg/L = 15 mg/L < 20 mg/L (Figure 88).

Haven obtained on the average better photocatalyst activity performance at initial natural (unmodified) pH with 1 g/L catalyst dosage and 5 mg/L initial CAF concentration, these conditions were adopted and employed for the rest of the test effect evaluations.

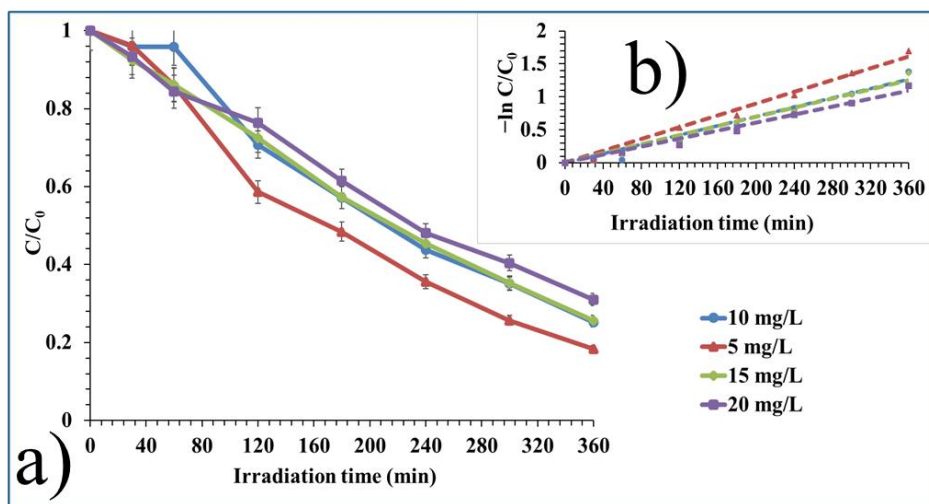


Figure 88. a) Catalyst dosage effect on the photocatalytic degradation efficiency of Mo/SynTiO₂ over CAF ($C_0 = 5$ mg/L, initial pH_{natural} = ~ 6.5), and b) corresponding photocatalytic degradation rate constant (k)

4.3.2.3. Effect of Chemical Scavengers

For the probation of reactive species responsible for the photocatalytic degradation process of caffeine, chemical scavenger test was performed. 1 mM each of isopropyl alcohol (IPA), ammonium oxalate (AO), and benzoquinone (BQ) were employed for the respective detection of hydroxyl radical ($\text{HO}\cdot$), superoxide anion ($\text{O}_2^{\cdot-}$) and hole charge (h^+) carrier reactive species [134, 162, 222-223]. As can be seen from Figure 89, the presence of BQ in the reaction medium for the first 80 min irradiation exposure, saw a faster rate of photocatalytic degradation kinetics in comparison to IPA, AO and no scavenger addition. During this time, almost 20 % of initial 5 mg/L CAF was removed. In the remaining 280 min irradiation time, the photocatalytic degradation kinetics in the presence of BQ and in comparison, to no added scavenger was $\sim 0.005 \text{ min}^{-1}$ with over 80 % initial 5 mg/L CAF removal each (Table 24, Figure 89). In the case of IPA, and AO there was a more distinguished suppression effect with respective ~ 75 % and ~ 72 % initial 5 mg/L CAF removal at 360 min irradiation (Figure 89).

The non-selectivity of BQ towards superoxide anion ($\text{O}_2^{\cdot-}$) can be linked to the shift of the final pH value in presence of BQ to lower pH values for both IPA and AO in comparison to no added scavenger (Table 24). Moreover, the possible interaction of hydroxyl radical ($\text{HO}\cdot$) with BQ, thereby limiting its availability for superoxide anion ($\text{O}_2^{\cdot-}$)

) scavenging to deliver the expected suppression effect has been reported [295-296]. Thus, the presence of BQ in the reaction media for the probation of superoxide anion ($O_2^{\cdot-}$) cannot be outrightly dismissed but masked by the photogenerated hydroxyl radical (HO^{\cdot}). As such, the suppression effect order exhibited on the photocatalytic degradation process of CAF by the photocatalyst followed thus: $AO > IPA > BQ \leq$ No Scavenger (Figure 89).

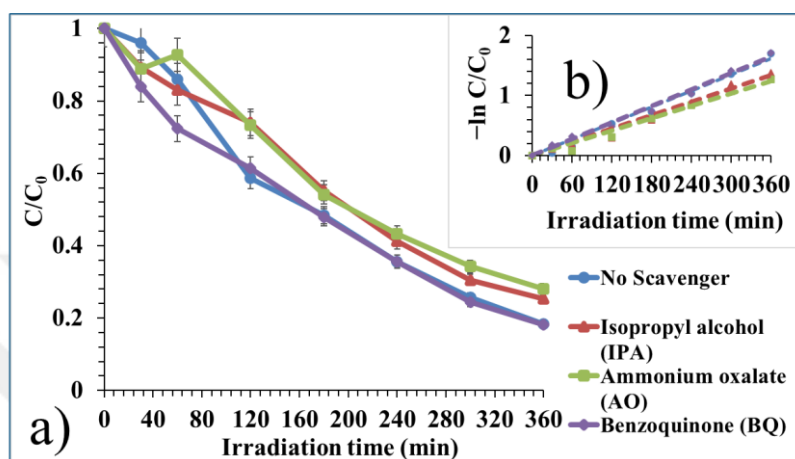


Figure 89. a) Initial CAF concentration effect on the photocatalytic degradation efficiency of 1 g/L Mo/SynTiO₂ (initial pH_{natural} = ~ 6.5), and b) corresponding photocatalytic degradation rate constant (k)

4.3.2.4. Effect of Contaminant Ions (Cations and Anions) and Humic Acids (HA)

The effect of contaminant ions, as well as humic acid, was also investigated. One molar equivalent (1 Meq) concentration each of NH_4^+ , Fe^{3+} , Mg^{2+} , Al^{3+} , and Ca^{2+} ions were employed for the cation effect while HPO_4^{2-} , HCO_3^- , CO_3^{2-} , SO_4^{2-} , and Cl^- ions of one molar equivalent (1 Meq) concentration each were employed for the anion effect. For the humic acid (HA), a range of 1 mg/L – 4 mg/L concentration was employed to investigate its effect on the photocatalytic degradation process of caffeine.

From the depicted graph in Figure 90, in the presence of Fe^{3+} , over 90 % of the initial 5 mg/L CAF was removed by the photocatalyst at 30 min of irradiation time. The photocatalytic activity performance further enhanced up to the 360 min irradiation time window in the presence of Fe^{3+} with almost complete removal of the initial 5 mg/L CAF concentration in comparison to about 88 % removal at this time with no cation addition (Figure 90). Though Fe^{3+} has been reported to show inhibitory effects on the photocatalytic

[298]. The exhibited contrary outcome in this case can be attributed to different test evaluation protocol, different photocatalyst and reaction conditions. Moreover, the variation between the initial and final pH condition in the presence of Fe shifted to a much lower final pH value which is acidic proton (H^+) promoting environment that facilitated CAF removal rates (Table 24) [134, 222]. In the presence of Mg^{2+} ion, a suppression effect was not significant with about 80 % CAF removal at 360 min irradiation (Figure 90). NH_4^+ and Ca^{2+} ions also suppressed the photocatalytic degradation rate compared to no added cation with respective removals of about 70 % and 65 % at 360 min irradiation. A higher suppression effect on the photocatalytic process occurred in the presence of Al^{3+} with about 30 % removal of initial 5 mg/L CAF concentration. Though in contrary to report, the exhibited suppression effect by the presence of Mg^{2+} , NH_4^+ and Ca^{2+} ions in comparison to no added cation is due to variation in photocatalyst material, suspension reaction media, and test condition [298]. Moreover, Mg^{2+} , NH_4^+ , and Ca^{2+} ions have equally been reported to exhibit no influence on photocatalytic degradation of some organic pollutants in some cases and in others retardation of the process [298]. The initial and final pH conditions of the reaction media in the presence of these ions were moderate and did not vary widely (Table 24). Despite final pH shift to a more acidic proton (H^+) photocatalytic performance enhancing condition (Table 24), Al^{3+} exhibited a suppression effect on the photocatalytic degradation process due to reported reason of its precipitation on the catalyst surface that ends up blocking photoactivity [298]. The suppression effect exhibited by the added cations on the photocatalytic degradation process followed such order: $Al^{3+} > Ca^{2+} > NH_4^+ > Mg^{2+} \gg Fe^{3+} \ll$ No cation (Figure 90).

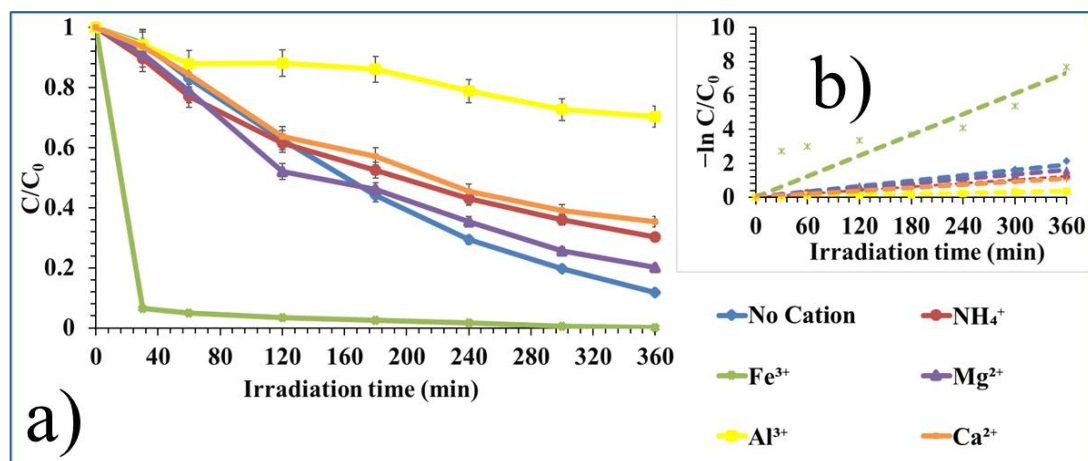


Figure 90. a) Cation effect on the photocatalytic degradation efficiency of 1 g/L Mo/SynTiO₂ over CAF ($C_0 = 5$ mg/L, initial pH_{natural} = ~ 6.5), and b) corresponding photocatalytic degradation rate constant (k)

In the presence of the tested anions, the photocatalytic degradation process was suppressed by all the anions except for HCO_3^- which showed a slight non-significant increase with just about 90 % removal of initial 5 mg/L CAF concentration approximately same percentage removal with no added anion at 360 min irradiation time (Figure 91). The rest of SO_4^{2-} , HPO_4^{2-} , and CO_3^{2-} ions exerted suppression effect on the photocatalytic process but not as more significant as Cl^- ion with respective CAF removals of ~ 85 %, ~ 81 %, and ~ 77 % for the trio in comparison to ~ 67 % for the Cl^- at 360 min irradiation (Figure 91). The slight but not significant enhancement in the presence of HCO_3^- is attributed to the co-existence of both HCO_3^- and CO_3^{2-} as ion buffer system with a synergistic contribution towards the enhanced photocatalytic activity performance in the presence of HCO_3^- [162]. This occurrence is favoured by the initial pH condition of both ions at which point the added CO_3^{2-} is effectively absent (Table 24) [162]. However, at more advanced alkaline final pH (Table 24), the CO_3^{2-} is now proportionately present showing the displayed suppression effect reported due to its scavenging attitude for hydroxyl radical ($\text{HO}\cdot$) and also a doubly charged ion with intense scavenging attribute for that matter just as SO_4^{2-} , HPO_4^{2-} (Figure 91) [162, 298]. At advanced final pH for the present HCO_3^- ion which also is reported as a hydroxyl radical ($\text{HO}\cdot$) ion scavenger, suppression due to this attribute was not effected or rather in effect but minimal due to its mono charged ion form of HCO_3^- that led to its lower scavenging attribute to impede the photodegradation process [162]. Inclusively the presence of Cl^- ion and those of SO_4^{2-} , HPO_4^{2-} , and CO_3^{2-} showed suppression effect also due to their competitive adsorption tendencies in the active centres of the photocatalyst material (Figure

91). Therefore, suppression effects exhibited on the photocatalytic degradation process in the presence of anions occurred in the following order: $\text{Cl}^- > \text{CO}_3^{2-} > \text{HPO}_4^{2-} > \text{SO}_4^{2-} > \text{HCO}_3^- \geq \text{No Anion}$ (Figure 91).

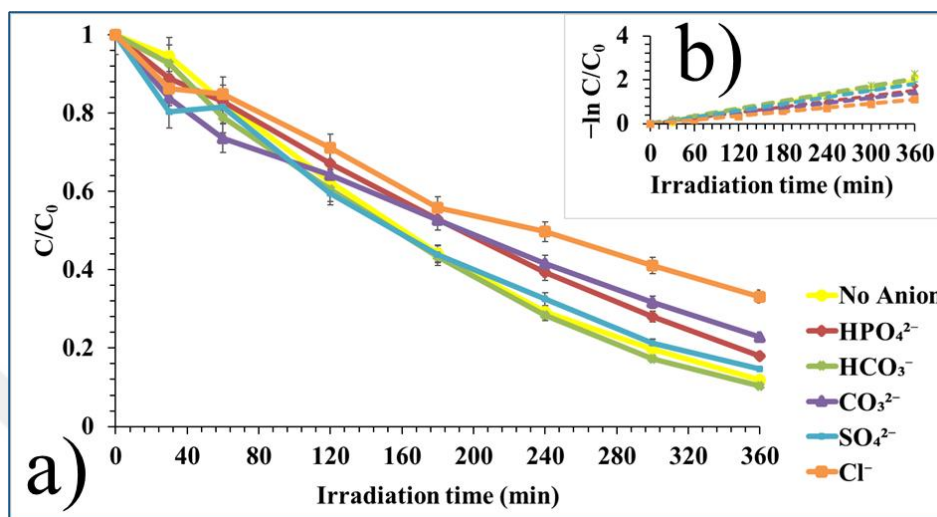


Figure 91. a) Anion effect on the photocatalytic degradation efficiency of 1 g/L Mo/SynTiO over CAF ($C_0 = 5$ mg/L, initial $\text{pH}_{\text{natural}} = \sim 6.5$), and b) corresponding photocatalytic degradation rate constant (k)

In the presence of 1 mg/L HA, there was no effect over the photocatalytic degradation process of CAF (Figure 92). Photocatalytic activity performance remained approximately the same in the presence of 1 mg/L HA in comparison to 0 mg/L HA with equal about 88 % removal of the initial 5 mg/L CAF concentration (Figure 92). The 2 mg/L HA, 3 mg/L HA, and 4 mg/L HA suppressed the photocatalytic degradation process and the suppression effect increased with increase in HA concentration due to shielding effect preventing adequate photoirradiation of reaction suspension media in the presence of HA [134, 162, 223]. Final pH conditions of the reaction media in the presence of the added HA except for 0 mg/L HA shifted to moderately acidic condition and maintained similar values across at this pH level (Table 24). Exhibited suppression effect on the photocatalytic degradation process of CAF in the presence of the added HA concentrations occurred as such: 4 mg/L HA > 3 mg/L HA > 2 mg/L HA > 1 mg/L HA \sim 0 mg/L HA (Figure 92).

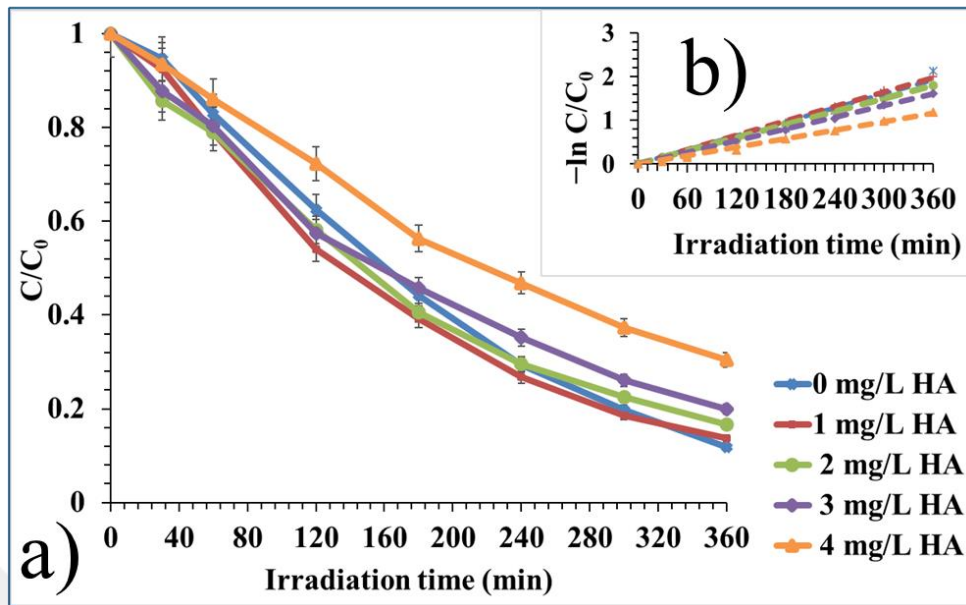


Figure 92. a) Humic acid (HA) effects on the photocatalytic degradation efficiency of 1 g/L Mo/SynTiO₂ over CAF ($C_0 = 5$ mg/L, initial pH_{natural} = ~ 6.5), and b) corresponding photocatalytic degradation rate constant (k)

4.3.2.5. Effect of Hydrogen Peroxide (H₂O₂)

In the case of hydrogen peroxide (H₂O₂) and at the added concentration level of 1 mM – 4 mM each, suppression effect was exhibited and increased on the photocatalytic degradation process as can be seen in the Figure 93 from a lower 1 mM H₂O₂ to higher 4 mM H₂O₂ [Figure 93]. It has been reported that with some photocatalyst materials and under certain reaction conditions, hydrogen peroxide scavenges hydroxyl radical (HO \cdot) which in turn impedes photocatalytic degradation process of organic pollutants [223, 298]. Final pH values in the presence of the externally added hydrogen peroxide (H₂O₂) oxidant maintained except for the 0 mM H₂O₂ weakly acidic values during the 360 min irradiation (Table 24). Suppression effect in the presence of the added hydrogen peroxide (H₂O₂) occurred in such order: 1 mM H₂O₂ < 2 mM H₂O₂ < 3 mM H₂O₂ < 4 mM H₂O₂ (Figure 93).

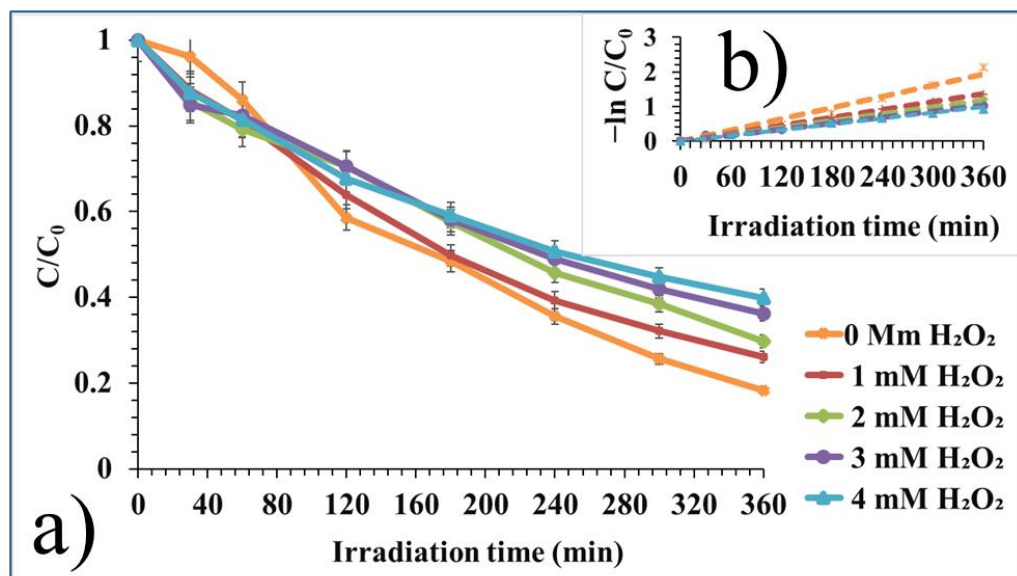


Figure 93. a) Hydrogen peroxide (H₂O₂) effect on the photocatalytic degradation efficiency of Mo/SynTiO₂ over CAF ($C_0 = 5$ mg/L, initial pH_{natural} = ~ 6.5), and b) corresponding photocatalytic degradation rate constant (k)

Dark, photolysis, heat effect without catalyst and heat effect with catalyst under the test condition protocols as already stated did not impact the photocatalytic degradation process of CAF significantly as depicted in Figure 94.

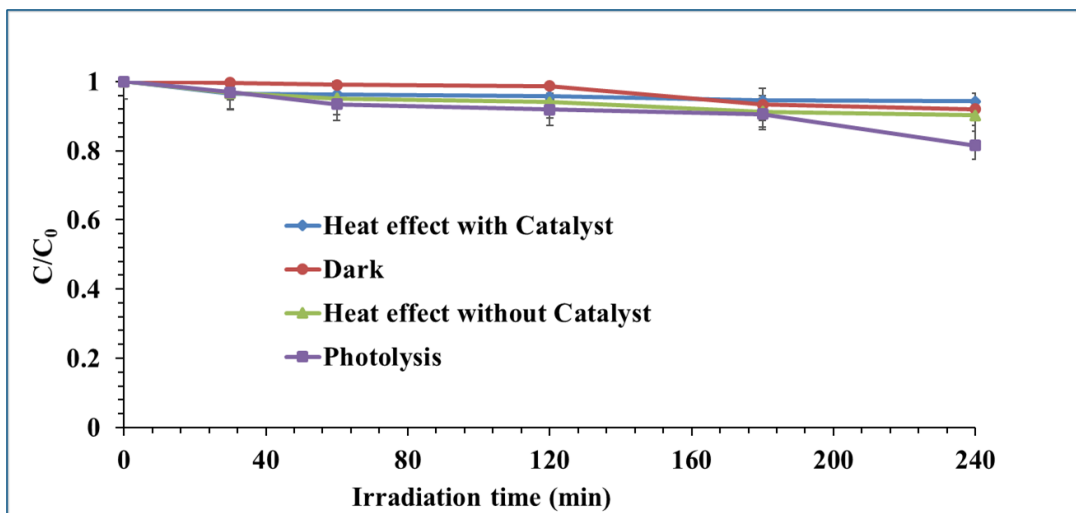


Figure 94. a) Dark, photolysis, heat effect without catalyst and heat effect with catalyst under test conditions of 1 g/L Mo/SynTiO₂, C₀ = 5 mg/L, and initial pH_{natural} (unmodified) = ~ 6.5 where applicable

Table 24 show the parametric indicators for the photocatalytic activity performance of the tested materials over caffeine (CAF) based on their degradation rate constant (k), correlation constant (R²), half-life (t_{1/2}), and pH variation condition.

Table 24. Tested photocatalytic parameters at (C₀ = 5 mg/L CAF concentration under 365 nm at 1 g/L catalyst) with associated rate constant k (min⁻¹), correlation coefficient (R²), half-life t_{1/2} (min), and initial and final pH values

Test	Degradation rate constant k (min ⁻¹)	R ²	Half-life (t _{1/2}) (min)	pH _{initial}	pH _{final}
Photocatalyst material evaluation with respect to control [#]					
SynTiO ₂	0.0002	0.95	3465	3.23	3.09
Mo/SynTiO ₂	0.0045	0.99	154	6.45	6.00
2 wt. % Mo/SynTiO ₂					
pH effect [#]					

Continuation of Table 24

pH _{natural} = around 6.50	0.0054	0.99	128.33	6.53	6.52
pH = 4	0.0005	0.99	1386	4.32	4.73
pH = 9	0.0071	0.99	97.61	9.06	7.38
Catalyst dosage effect ^{#, *}					
0.5 g/L	0.0021	0.99	330	6.48	6.46
0.75 g/L	0.0031	0.99	223.55	6.53	6.47
1 g/L	0.0048	0.99	144.38	6.50	6.49
1.25 g/L	0.0054	0.97	128.33	6.58	6.50
Pollutant concentration effect ^{#, *}					
5 mg/L	0.0045	0.99	154	6.47	6.27
10 mg/L	0.0035	0.99	198	6.50	6.36
15 mg/L	0.0035	0.99	198	6.55	6.38
20 mg/L	0.0030	0.99	231	6.57	6.47
Chemical scavenger test ^{#, *}					
No scavenger	0.0045	0.99	154	6.53	6.45
1 mM IPA	0.0037	0.99	187.30	6.48	6.45
1 mM BQ	0.0046	0.99	150.65	6.55	6.27
1 mM AO	0.0035	0.99	198	6.55	6.50
Contaminant ions: cation effect ^{#, *}					
No Cation	0.0054	0.99	128.33	6.52	6.44
1 M Fe ³⁺	0.0203	0.93	34.14	6.52	3.36
1 M Mg ²⁺	0.0045	0.99	154	6.53	6.20
1 M Ca ²⁺	0.0031	0.99	223.55	6.5	5.95
1 M Al ³⁺	0.0010	0.98	693	6.57	3.78
1 M NH ₄ ⁺	0.0034	0.99	203.82	6.5	5.97
Contaminant ions: anion effect ^{#, *}					
No Anion	0.0054	0.99	128.33	6.53	6.47
1 M HCO ₃ ⁻	0.0057	0.99	121.58	6.57	9.97
1 M CO ₃ ²⁻	0.0039	0.99	177.69	6.67	11.04

Continuation of Table 24

1 M SO ₄ ²⁻	0.005	0.99	138.60	6.52	6.38
1 M HPO ₄ ⁻	0.0043	0.99	161.16	6.41	7.89
1 M Cl ⁻	0.0030	0.99	231	6.54	6.00
Humic acid (HA) effect ^{#, *}					
0 mg/L HA	0.0054	0.99	128.33	6.53	6.48
1 mg/L HA	0.0055	0.99	126	6.52	6.16
2 mg/L HA	0.0050	0.99	138.60	6.47	6.06
3 mg/L HA	0.0044	0.99	157.50	6.55	6.05
4 mg/L HA	0.0032	0.99	216.56	6.54	6.28
Hydrogen peroxide (H ₂ O ₂) effect ^{#, *}					
0 mM H ₂ O ₂	0.0054	0.99	128.33	6.51	6.49
1 mM H ₂ O ₂	0.0038	0.99	182.37	6.47	6.05
2 mM H ₂ O ₂	0.0033	0.99	210	6.47	6.28
3 mM H ₂ O ₂	0.0029	0.99	238.97	6.52	6.12
4 mM H ₂ O ₂	0.0027	0.99	256.67	6.44	5.82
[#] Tests performed under 365 nm near UV-vis irradiation/ preliminary stage and at related initial pH _{natural} (unmodified) condition, [*] other test conditions performed at initial pH _{natural} (unmodified) condition					

4.3.2.6. Possible Photocatalytic Degradation Process Mechanism

In the light of the chemical scavenger probe test (Section 4.3.2.3), such a degree of the reactive species participation as such: $h^+ > HO \cdot > O_2^{\cdot -}$ was exhibited (Figure 89). Based on this outcome, the photogenerated hole charge (h^+) carrier played a prominent role in the photocatalytic degradation process while hydroxyl radical ($HO\cdot$) and superoxide anion ($O_2^{\cdot -}$) were also involved to an extent. As such, a classical photodegradation mechanism where all the basic reactive species were either directly or indirectly involved is proposed in the degradation process of CAF. As can be seen from the Figure 95, upon the photoirradiation of the Mo/SynTiO₂, electrons (e^-) are knocked off the photocatalyst material and

correspondingly hole charge carriers (h^+) are generated. The photogenerated electrons drifted towards the conduction band (CB), interacts with surface adsorbed oxygen and by reduction form superoxide anion ($O_2^{\cdot -}$) specie. However, these species might not have been involved in the photocatalytic degradation of caffeine at the CB level via the normal single electron reduction pathway of the surface adsorbed O_2 due to reason earlier stated.

Correspondingly, the hole charge carriers (h^+) at the valence band (VB) interacts with surface adsorbed water molecule (H_2O) and by oxidation form hydroxyl radical ($HO\cdot$) specie. The photogenerated charges e^-/h^+ and their related formed superoxide anion ($O_2^{\cdot -}$), and hydroxyl radical ($HO\cdot$) species are now available as reactive oxygen species for the degradation of CAF (Figure 95). Therefore, rather the superoxide anion ($O_2^{\cdot -}$) formed at CB energy level involving in the photocatalytic degradation of caffeine, it is proposed that the one formed at around the introduced fermi level above VB energy level and close to the CB via ($O_2 + H^+/O_2^{\cdot -}$) pathway was the one that generated the superoxide anion that participated in the degradation of caffeine.

In support of the proposed mechanism is also the energy band level potentials obtained via Mulliken function (Equation 85, Equation 86, and Table 17) which favours the charge transfer energetics of the photodegradation process of CAF. The derived VB edge potential (2.29 eV) (Table 17) in comparison to the $E^{\circ}_{ox.}$ ($OH^-/HO\cdot$) of value (1.99 eV) on the normal standard hydrogen electrode (SHE) is favoured with a higher energy potential for the formation of hydroxyl radical ($HO\cdot$) (Scheme 4). The formation of superoxide anion ($O_2^{\cdot -}$) via $O_2 + H^+/O_2^{\cdot -}$ pathway at the VB potential edge (Figure 95) is also favoured given that the required $E^{\circ}_{ox.}$ Potential value (0.682 eV) for its formation on the normal standard hydrogen electrode (SHE) relative to the derived VB edge potential (2.29 eV) (Table 17, and Figure 95) is highly favoured for its formation at this level.

Furthermore, the reported potential value of Mo^{+6}/Mo^{+5} redox system at +0.4 V is much higher than the one derived for the base $SynTiO_2$ in this thesis (- 0.34 eV) and in agreement with reported literature value for TiO_2 potential (Table 17) [107]. Therefore, the Mo^{6+}/Mo^{5+} redox system of the photocatalyst material stands favoured in capturing electrons from the base TiO_2 thereby, facilitating efficient charge transfer and separation processes (Table 17, and Figure 95).

Connecting all these information, a reaction mechanism where basically all the photogenerated charges and related species are involved in the photocatalytic degradation process of CAF is proposed (Figure 95).

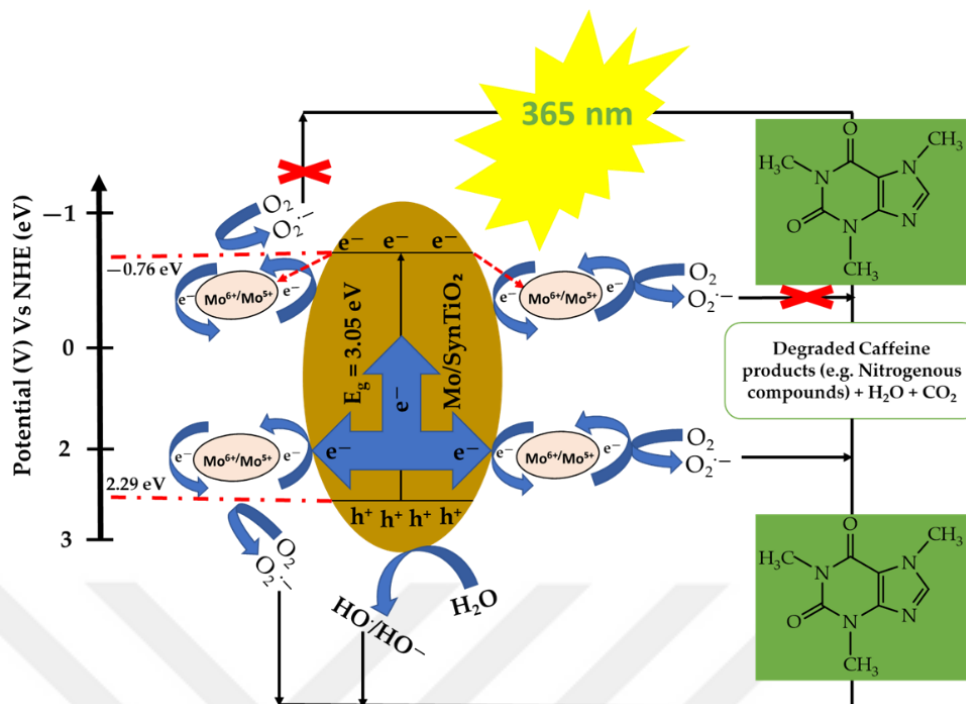


Figure 95. Proposed photocatalytic degradation process mechanism for the removal of CAF by Mo/SynTiO₂

4.3.3. Photocatalytic Material Test Evaluation Over Carbamazepine (CBZ)

On preliminary basis, the SynTiO₂ and decorated forms were also deployed under 365 nm irradiation for the photocatalytic degradation of carbamazepine. From Figure 96, both the Mo/SynTiO₂ and W/SynTiO₂ photocatalyst materials at 60 min of UV irradiation and under initial pH_{natural} (unmodified) condition, removed over 90 % of initial 10 mg/L CBZ while the Mo-W/SynTiO₂ achieved about 88 % CBZ removal. By 120 min irradiation, CBZ was completely removed by the modified photocatalyst materials in comparison to the unmodified SynTiO₂ which during the irradiation period remain non photoactive (Figure 96).

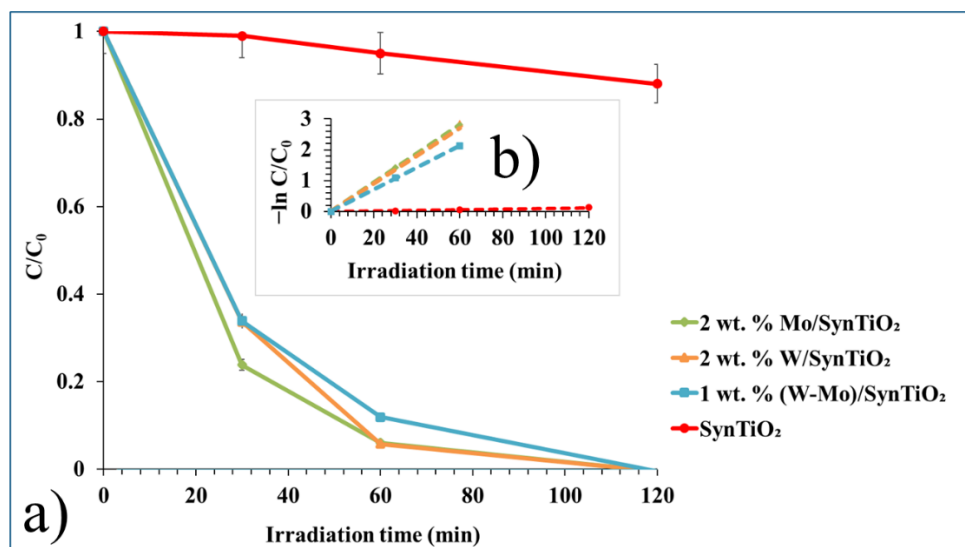


Figure 96. a) Photocatalytic degradation activity performance of 1 g/L each of Mo and or W decorated SynTiO₂ under 365 nm against CBZ ($C_0 = 10$ mg/L at their respective initial pH_{natural} (unmodified) condition (Table 25), and b) corresponding photocatalytic degradation rate constant (k)

At 450 nm irradiation, the modified photocatalyst materials under initial pH_{natural} (unmodified) condition exhibited photoactivity (Figure 97). Mo/SynTiO₂ and W/SynTiO₂ achieved respectively the same amount of over 60 % removal of the initial 10 mg/L CBZ concentration after 4 h irradiation time window while Mo-W/SynTiO₂ achieved over 50 % removal in comparison to the non-photoactive unmodified SynTiO₂. While the decorated SynTiO₂ exhibited impressive photocatalytic performance towards CBZ under UV irradiation, they were also photoactive in the degradation of CBZ under visible light irradiation exposure. Initial and final pH conditions of the photocatalyst material suspensions varied in a range of more acidic final pH values especially in the case of the Mo modified photocatalyst materials due to its reported increase surface acidity property feature which enhances its surface oxygen interaction for photocatalytic activity improvement (Table 25) [109, 111, 280].

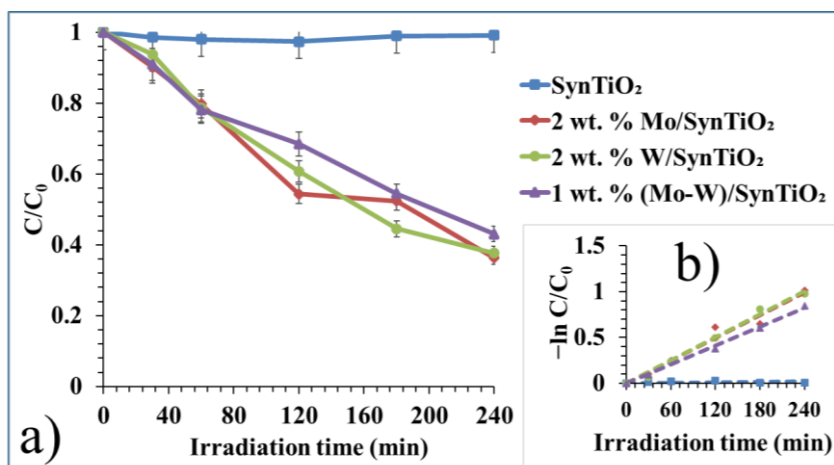


Figure 97. a) Photocatalytic degradation activity performance of 1 g/L each of Mo and or W decorated SynTiO₂ under 450 nm against CBZ ($C_0 = 10$ mg/L at their respective initial pH_{natural} (unmodified) condition (Table 25)), and b) corresponding photocatalytic degradation rate constant (k)

Table 25 show the parametric indicators for the photocatalytic activity performance of the tested materials over carbamazepine (CBZ) based on their degradation rate constant (k), correlation coefficient (R^2), half-life ($t_{1/2}$), and pH variation condition.

Table 25. Tested photocatalytic parameters for ($C_0 = 10$ mg/L initial CBZ concentration under 365 nm and 450 nm with 1 g/L catalyst) and their associated rate constant k (min^{-1}), correlation coefficient (R^2), half-life $t_{1/2}$ (min), and their initial and final pH values

Test	Degradation rate constant k (min^{-1})	R^2	Half-life ($t_{1/2}$) (min)	pH _{initial}	pH _{final}
Synthesized photocatalyst material test ^{#, □}					
SynTiO ₂	0.0010	0.97	693	3.33	3.03
W/SynTiO ₂	0.0452	0.99	15.33	7.78	7.20
Mo/SynTiO ₂	0.0470	0.99	14.74	6.12	5.40
Mo-W/SynTiO ₂	0.0356	0.99	19.47	9.93	4.87
Synthesized photocatalyst material test ^{*, □}					

Continuation of Table 25

SynTiO ₂	0.0010	0.99	8152.94	3.29	3.05
W/SynTiO ₂	0.0042	0.99	165	7.75	7.22
Mo/SynTiO ₂	0.0041	0.99	169.02	5.88	5.38
Mo-W/SynTiO ₂	0.0034	0.99	203.82	9.74	4.75
# Tests performed under 365 nm near UV-vis irradiation, * Tests performed under 450 nm visible light irradiation, and [□] initial pH _{natural} (unmodified) condition					

Haven tested the photocatalyst materials in suspension and investigated profoundly various parametric factors effects on the photocatalytic degradation processes of ibuprofen (IBF), caffeine (CAF), and carbamazepine (CBZ), the fabricated α -Al₂O₃ ceramic substrate as support for the W/HRTiO₂ photocatalyst material was employed for the photocatalytic degradation of IBF, CAF, and CBZ in the immobilized form.

4.4. Photocatalyst Test Over Immobilized W/HRTiO₂ on α -Al₂O₃ Ceramic Support

The HRTiO₂ haven delivered a more uniformly homogeneous topcoat layer on the ceramic support (Figure 22), the W decorated form of HRTiO₂ with an impressive photocatalytic activity performance over the investigated CECs compounds was employed for the supported photocatalyst test. The coating procedure as outlined in (Section 3.8) for a 1 wt. % coat suspension of (2 wt. % W/HRTiO₂) was used in the deposition of ~ 0.005 g of the photocatalyst material. This amount is 12 times smaller than that applied for the suspension photocatalyst tests at 1 g/L realized from 0.06 g photocatalyst powder material in 60 mL working volume. Thus, there is no comparability in terms of photocatalyst activity performance due to differences in catalyst amount. In order to ensure that the disk shape support was properly submerged in the pollutant containing reactor cell, same 60 mL suspension test working volume was maintained. Again, to compensate to a certain extent issue of reactor contents mass transfer which due to the photocatalyst material confinement

is limited, an extended irradiation exposure time window of 360 min for an initial 5 mg/L concentration of the tested CECs compounds was considered.

As shown in Figure 98, immobilized W/HRTiO₂ photocatalyst showed an enhanced photoactivity where almost 100 % of the initial 5 mg/L CECs compounds (IBF, CAF and CBZ) were removed under 365 nm irradiation at initial natural (unmodified) pH condition after 360 min exposure time.

Subsequently, removal rates by the photocatalyst over CAF and CBZ were still impressive recording for the 2nd and 3rd cycles of reuse respective removals of ~ 88 %, ~ 84 %, and ~ 90 %, ~ 88 % of the initial 5 mg/L concentration at 360 min irradiation (Fig 98b, and c). In the case of IBF, a rather low removal rate was recorded for the 2nd and 3rd cycle reuse with respective ~ 31 %, and ~ 25 % removals of the initial 5 mg/L concentration at 360 min irradiation time (Figure 98c).

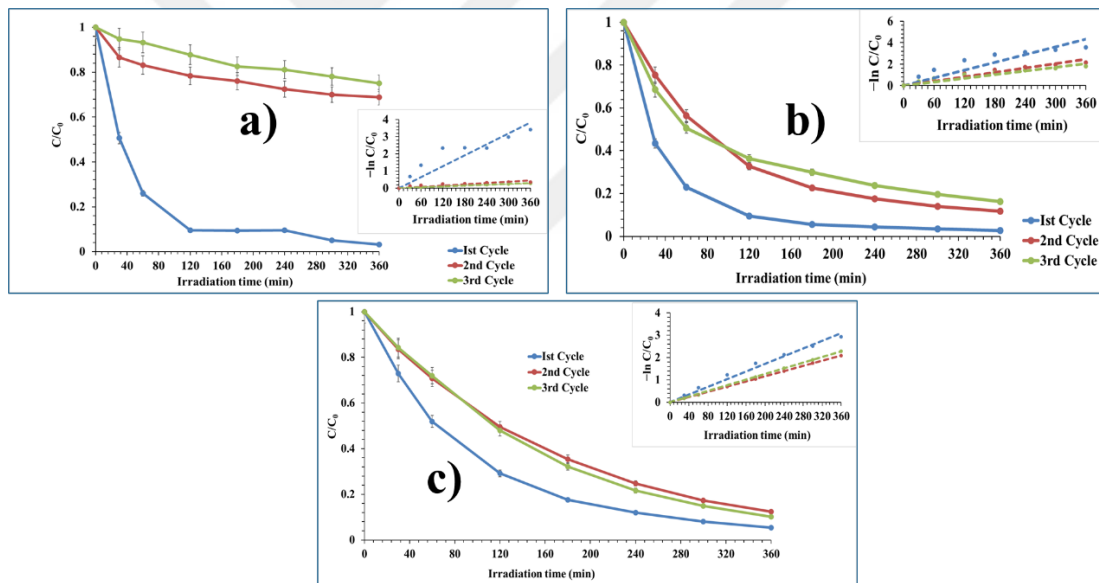


Figure 98. a) Photocatalytic degradation activity performance of immobilized 0.005 g W/HRTiO₂ on ceramic support showing in general 3 cycle test runs and their related degradation rate constant k (inset) for a) IBF, b) CAF, and c) CBZ ($C_0 = 5$ mg/L, initial pH_{natural} (unmodified) values (Table 26), and under 365 nm irradiation

The low % removal observed of the photocatalyst over IBF in 2nd and 3rd reusage cycles was an attribute of surface adsorption mechanism effects between the IBF molecules and photocatalyst surface with respect to the pKa value (4.52-4.9) and the pH_{pzc} (4.4) of the photocatalyst material which based on the initial and final pH condition of the 1st cycle test promoted photoactivity but lacked in the subsequent 2nd and 3rd cycle (Table 19, Figure 44, and Table 26). On the contrary, the more sustained activity performance over CAF and CBZ for the entire 3 cycle reusage was due to maintained force of attraction between the organic substrate molecules and the pH_{pzc} of the photocatalyst supported by their initial and final pH conditions which continuously facilitated the photodegradation process (Table 19, Figure 44, and Table 26).

While the immobilized photocatalyst sustained a higher photoactivity over 3 cycles of reusage at least for CAF and CBZ, the photostability of the topcoat structure was also maintained as can be seen from the XRD measurement obtained of ceramic topcoat W/HRTiO₂ and treated at 600 °C for adhesion (Figure 99a). In comparison to the unmodified base HRTiO₂ both the untreated and heat treated at 600 °C, the tested W/HRTiO₂ retained the pristine TiO₂ crystalline phase structure after the 3 successive cycle test runs (Figure 27, and Figure 99a). The α -Al₂O₃ phase of the ceramic support material showed typical phase reflections with an overlapping anatase TiO₂ {101} phase reflection of the W/HRTiO₂ overlay with the other anatase and rutile phases still prominent, intense, and defined after the cycle runs confirming minimal surface topcoat alterations (Figure 99a).

In support, FTIR spectra of the 600 °C heat treated recycled W/HRTiO₂ overlay in comparison to the non-heat treated HRTiO₂ (unmodified), and non-heat-treated W/HRTiO₂ were matched by material content functional groups and typified their respective as expected chemical bond profiles already outlined (Section 3.92, Figure 25, and Figure 99b).

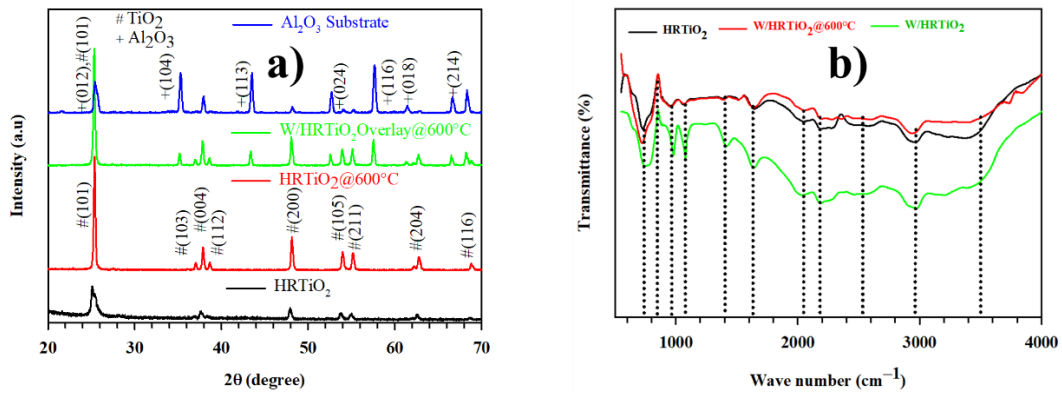


Figure 99. Surface morphological characteristics obtained of a) XRD measurement, and b) FTIR spectra of tested ceramic supported W/HRTiO₂ photocatalysts after 3 cycle photocatalytic test runs

Effect of dark reaction with the photocatalyst material and the tested CECs contents as well as photolysis in the presence of uncoated ceramic support and CECs compounds did minimally impact the photodegradation process outcome (Figure 100).

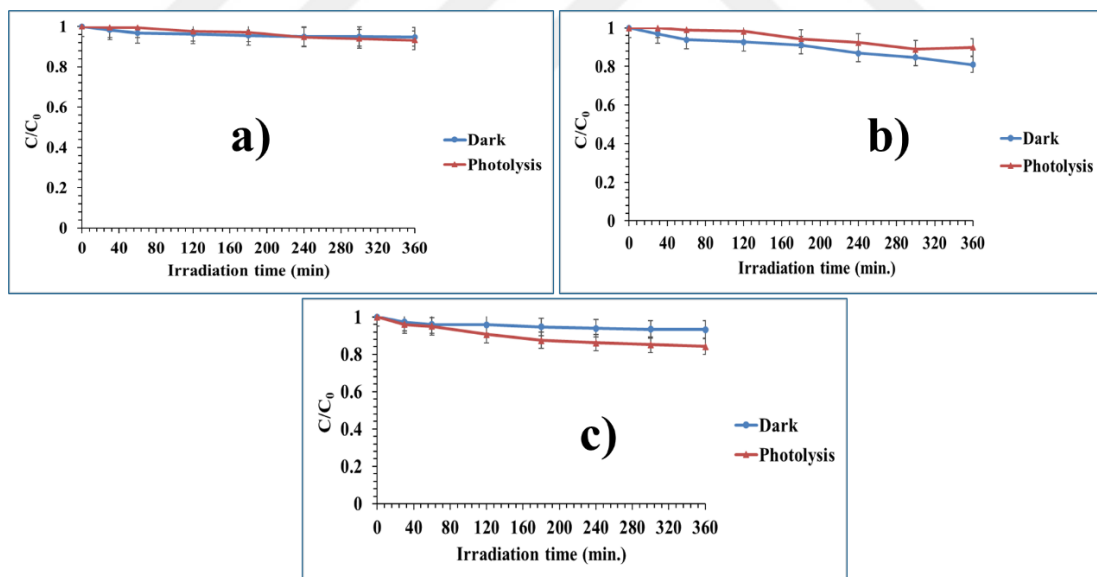


Figure 100. Dark effect on the W/HRTiO₂ overlay on ceramic support, and photolysis effect of uncoated ceramic support only over the degradation of a) IBF, b) CAF, and c) CBZ with conditions: ($C_0 = 5$ mg/L each, initial pH_{natural}(unmodified) condition (Table 26)), and under 365 nm irradiation

Table 26 show the parametric indicators for the photocatalytic activity performance of the tested materials during the 3-cycle test runs over ibuprofen (IBF), caffeine (CAF), and carbamazepine (CBZ) based on their degradation rate constant (k), correlation coefficient (R^2), half-life ($t_{1/2}$), and initial and final pH condition.

Table 26. Parametric indicators for the photocatalytic activity performance of ceramic supported W/HRTiO₂ over IBF, CAF, and CBZ and their associated degradation rate constant k (min⁻¹), correlation coefficient constant (R^2), half-life $t_{1/2}$ (min), and initial and final pH values

Cycle test runs	Degradation rate constant k (min ⁻¹)	R^2	Half-life ($t_{1/2}$) (min)	pH _{initial}	pH _{final}
0.005 g W/HRTiO ₂ on ceramic support Vs 5 mg/L initial Ibuprofen concentration ^{#, □}					
Ist Cycle	0.0107	0.94	64.77	5.13	9.09
2nd Cycle	0.0013	0.93	533.08	5.11	8.26
3rd Cycle	0.0009	0.99	770	5.13	7.74
0.005 g W/HRTiO ₂ on ceramic support Vs 5 mg/L initial Caffeine concentration ^{#, □}					
Ist Cycle	0.0120	0.94	57.75	5.49	8.37
2nd Cycle	0.0068	0.98	101.91	5.45	8.40
3rd Cycle	0.0057	0.97	121.58	5.47	7.44
0.005 g W/HRTiO ₂ on ceramic support Vs 5 mg/L initial Carbamazepine concentration ^{#, □}					
Ist Cycle	0.0086	0.99	80.58	5.57	7.74
2nd Cycle	0.0058	1	119.48	5.52	7.39
3rd Cycle	0.0063	0.99	110	5.50	7.33
[#] Tests performed under 365 nm near UV-vis irradiation, and [□] initial pH _{natural} (unmodified condition)					

5. CONCLUSION

In this thesis, there was the demonstration of worked α - Al_2O_3 ceramic substrate as a support for W modified TiO_2 . Commercially available huntsman TiO_2 marketed under the portfolio name HR- tioxide (HRTiO_2) was selected and used for the first time as the base TiO_2 photocatalyst material instead of the commonly used and available TiO_2 like P25 (Degussa), Ishihara UV 100: Sachtleben Homikat UV 100, PC50: Millennium TiONA PC50, A100: Ishihara Sangyo etc.

By series of dispersion and stability studies of the HRTiO_2 powder suspension, a 0.005 g delivered a better homogeneous and uniformly distributed topcoat layer on ceramic following structural and surface morphological controls. The HRTiO_2 and sol-gel process synthesized TiO_2 (SynTiO_2) were as two different TiO_2 powder materials decorated by sonochemical method with W and or Mo dopants to obtain sets of modified TiO_2 with a 2 wt. % either of the dopants in the mono decorated form and 1 wt. % each of the dopants contents in the decorated form.

Obtained materials were characterized for structural, morphological, textural, and optical properties. Thereafter in suspension and as part of the modification outcome in the improvement of the TiO_2 based photocatalysts materials; 2 wt % W/ HRTiO_2 degraded 96 % of initial 50 mg/L IBF concentration, ~ 76 % of initial 100 mg/L CAF concentration, and ~ 100 % and 88 % of respective initial 50 mg/L and 100 mg/L CBZ concentrations after 1 h and at 365 nm irradiation, under natural (unmodified) initial pH conditions.

Modified TiO_2 (HRTiO_2 and SynTiO_2) base materials (doped and or doped/sensitized) also showed enhanced performance activity under 450 nm irradiation. Various parameteric effects on the photocatalytic degradation process were also investigated and reaction mechanisms proposed accordingly.

Approximately 0.005 g (W/ HRTiO_2) immobilized on ceramic support removed on average 90 % of 5 mg/L initial IBF, CAF, and CBZ concentrations and sustained over 80 % removal for CAF and CBZ at 360 min of 365 nm irradiation under natural (unmodified) pH conditions. After 3 cycle test runs, XRD and FTIR measurement outcome showed topcoat surface stability.

In conclusion, the as prepared materials can have potential application in the abatement of CECs contaminated water sources while also eliminating the polishing stage encountered in secondary wastewater effluent through the use of supported photocatalyst.

6. RECOMMENDATION

Global water pollution challenge continue to receive wider attention aimed at ameliorating and restoring uncontaminated water status. Part of this effort has been in the area of TiO₂ based photocatalysis where various semiconductor materials have been studied for their photocatalytic activity enhancing properties on their host components. In this regard, several strategies ranging from heteroatom doping to semiconductor oxide coupling, to heterojunction fabrications, to dye sensitizations, to surface morphology controls including hybrid nanostructured materials development have been employed to achieve narrow semiconductor band gap, retard photogenerated electron-hole pair (e⁻/h⁺) charge recombination, facilitate photocatalyst contaminant reaction ratio, and enhance efficient energy cultivation within the UV-visible spectrum.

Great advancement has been made of adopting various methods including the one focused in this thesis towards engineered TiO₂/semiconductor based photocatalyst materials for performance enhancement engaging one or combinations of these modification strategies. However, several areas are worth deepening investigation in order to realize practical performance photocatalysis.

On this note and as a matter of future perspective, the following areas should be addressed: 1) More simple, less solvent input (preferably non-toxic and environmentally friendly), little or no precious metal precursor materials, and less energy intensive synthesis method should be considered for the development of photocatalyst materials. 2) Elaborate and comprehensive investigation into the mechanism of charge transfer process involved in semiconductor composite photocatalysts materials. 3) Further investigation in understanding deeply the electron (e⁻) charge transfer mechanism of phthalocyanine (Pc) molecules incorporated into host materials with the aim of improving the activity performance photocatalytically is needed. Improvement of their water solubility and thermal stability should be considered more. 4) More focus in the area of recoverable photocatalyst system and the effective realization of their practical deployment for real wastewater treatment is needed. 5) Nonetheless, further studies are needed on the identification of degraded end products of investigated parent organic compounds ascertaining their fate with a subsequent deeper knowledge of their toxicological effects to humans, animals and the environment.

7. REFERENCES

1. Rasheed, T., Li, C., Bilal, M., Yu, C. and Iqbal, H., M., Potentially Toxic Elements and Environmentally Related Pollutant Recognition Using Colorimetric and Ratiometric Fluorescent Probes, Science of the Total Environment, 640 (2018a) 174-193.
2. Gavrescu, M., Behaviour of Persistent Pollutants and Risks Associated with Their Presence in the Environment-Integrated Studies, Environmental Engineering and Management Journal, 8, 6 (2009) 1517-1531.
3. Fisher, M., M. and Eugster, E. A., What is in Our Environment that Effects Puberty?, Reproductive Toxicology, 44 (2014) 7-14.
4. EL-Shahawi, M., S., E., Hamza, A., Bahammakh, A., S. and Al-Saggaf, W., T., An Overview on the Accumulation, Transformations, Toxicity, and Analytical Methods for the Monitoring of Persistent Organic Pollutants, Talanta, 80 (2010) 1587-1597.
5. UNESCO/Berghahn Books, The United Nations World Water Report 3: Water in a Changing World, Paris/New York, 2009.
6. Schwazernbach, R., P., Egli, T., Hofstetter, T., B., Gunten, U., von. and Wehrli, B., Global Water Pollution and Human Health, Annual Review of Environment and Resources, 35 (2010) 109-136.
7. Geissen, V., Mol, H., Klumpp, E., Umlauf, G., Nadal, M., van der Ploeg, M., van de Zee, S., E., A., T., M. and Ritsema, C., J., Emerging Pollutants in the Environment: A Challenge for Water Resource Management, International Soil and Water Conservation Research, 3 (2015) 57-65.
8. Petrovic, M. and Barcelo, D., Application of Liquid Chromatography/Quadruple-Time-of-Flight Mass Spectrometry (LC-QqTOF-MS) in the Environment Analysis, Journal of Mass Spectrometry, 41(2006) 1259-1267.
9. Richardson, S., D., Water Analysis: Emerging Contaminants and Current Issues. Analytical Chemistry, 81(2009) 4645-4677.
10. Richardson, S., D. and Ternes, T. A., Water Analysis: Emerging Contaminants and Current Issues, Analytical Chemistry, 83 (2011) 4614-4648.
11. Pal, A., Gin, A., Y-C. and Reinhard, M., Impacts of Emerging Organic Contaminants on Freshwater Resources: Review of Recent Occurrences, Sources, Fate and Effects, Science of the Total Environment, 408 (2010) 6062-6069.
12. Lindsey, M., E., Meyer, M. and Thurman, E., M., Analysis of Trace Levels of Saffinamide and Tetracycline Antimicrobials in Groundwater and Surface Water Using Solid-Phase Extraction and Liquid Chromatography/Mass Spectroscopy. Analytical Chemistry, 73 (2001) 4640-4646.

13. <https://www.norman-network.net> Emerging Substances. October 1, 2021.
14. Yan, Y., OK, Y., S., Kim, K.-H., Kwon, E., E. and Tsang, Y., F. Occurrences and Removal of Pharmaceuticals and Personal Care Products (PPCPs) in Drinking Water and Water/Sewage Treatment Plants: A Review, Science of the Total Environment, 596 (2017) 303-320.
15. Tiedeken, E., J., Tahar, A., McHugh, B. and Rowan, N., J. Monitoring, Sources, Receptors, and Control Measures for Three European Union Watch List Substances of Emerging Concern in Receiving Waters- A 20 Year Systematic Review, Science of the Total Environment, 574 (2017) 1140-11673.
16. Barbosa, M., O., Moreira, N., F., F., Ribeiro, A., R., Pereira, M., F., R. and Silva, A., M., T., Occurrence and Removal of Organic Micropollutants: An Overview of the Watch List of EU Decision 2015/495, Water Resources, 94 (2016) 257-279.
17. Rasheed, T., Bilal, M., Nabeel, F., Adeel, M. and Iqbal, H., M., N., Environmentally Related Contaminants of High Concern: Potential Sources and Analytical Modalities for Detection, Quantification, and Treatment, Environment International, 122 (2019) 52-66.
18. Liu, J.-L. and Wong, M.-H., Pharmaceuticals and Personal Care Products (PPCPs): A Review on Environmental Contamination in China, Environmental International, 59 (2013) 208-224.
19. Souza, J.-, C., G., Ribeiro, A., R., Barbosa, M., O., Pereira, M., F., R., Silva, A., M., T., A Review on Environmental Monitoring of Water Organic Pollutants Identified by EU Guidelines, Journal of Hazardous Materials, 344 (2018) 146-162.
20. Diaz-Cruz, M., S. and Barcelo, D., Trace organic Chemicals Contamination in Ground Water Recharge, Chemosphere, 72 (2008) 333-342.
21. Burge, I., J., Keller, M., Buser, H-R., Muller, M., D. and Poiger, T., Saccharin and Other Artificial Sweeteners in Soils: Estimated Inputs from Agricultural and House Degradation, and Leaching to Groundwater, Environmental Science Technology, 45 (2011) 615-621.
22. Einsiedl, F., Radke, M. and Maloszewski, P., Occurrence and Transport of Pharmaceuticals in a Karst Groundwater System Affected by Domestic Wastewater Treatment Plants, Journal of Contaminant Hydrology, 117 (2010) 26-36.
23. Holm, J., V., Rugge, K., Bjerg, P. and Christensen, H., Occurrence and Distribution of Pharmaceutical Organic Compounds in the Groundwater Downgradient of a Landfill (Grindsted, Denmark), Environmental Science and Technology, 28 (1995) 1415-1420.
24. Eckel, W., P., Ross, B. and Isensee, R., K., Pentobarbital Found in Ground Water, Ground Water, 5 (1993) 801-804.

25. Shore, L., S. and Shemesh, M., Naturally Produced Steroid Hormones and Their Release into the Environment, Pure and Applied Chemistry, 75 (2003) 1859-1871.
26. Watanabe, N., Harter, T., H. and Bergamaschi, B., A., Environmental Occurrence and Shallow Ground Water Detection of the Antibiotic Monensin from Dairy Farms, Journal of Environmental Quality, 37 (78-85).
27. Kummerer, K., The Presence of Pharmaceuticals in the Environment due to Human Use-Present Knowledge and Future Challenges, Journal of Environmental Management, 90 (2009) 2354-2366.
28. Swartz, W., C., H., Reddy, S., Benotti, M., J., Yin, H., F., Barber, L., B., Brownawell, B., J. and Rudel, R., A., Steroid Estrogens, Nonylphenol Ethoxylate Metabolites, and Other Wastewater Contaminants in Groundwater Affected by a Residential Septic System on Cape Cod, MA, Environmental Science and Technology, 40 (2006) 4894-4902.
29. Verstraeten, I., M., Fetterman, G., S., Meyer, M., T., Bullen, T. and Sebree, S., K., Use of Tracers and Isotopes to Evaluate Vulnerability of Water in Domestic Wells to Septic Waste, Ground Water Monitoring and Remediation, 25 (2005) 107-117.
30. He, K., Soares, A., D., Adejumo, H., Mc Diamird, M., Squibb, K. and Blaney, L., Detection of a Wide Variety of Human and Veterinary Fluoroquinolone Antibiotics in Municipal Wastewater and Wastewater-Impacted Surface Water, Journal of Pharmaceutical and Biomedical Analysis, 106 (2015) 136-143.
31. Vasquez, M., I., Lambrianides, A., Scheneider, M., Kummerer, K. and Fatta-Kassinos, D., Environmental Side Effects of Pharmaceutical Cocktails Effects: What We Know and What We Should Know, Journal of Hazardous Materials, 279 (2014) 169-189.
32. Ribeiro, C., Ribeiro, A., R. and Tiritan, M., E., Occurrence of Persistence Organic Pollutants in Sediments and Biota from Portugal Vs European Incidence: A Critical Overview, Journal of Environmental Science and Health B, 51 (2016) 143-153.
33. Stuart, M., Lapworth, D., Crane, E. and Hart, A., Review of Risks from Potential Emerging Contaminants in UK Underground Water, Science of the Total Environment, 416 (2102) 1-21.
34. Radovic, T., Grujic, S., Petkovic, A., Dimkic, M. and Lausevic, M., Determination of Pharmaceuticals and Pesticides in Rivers Sediments and Corresponding Surface and Groundwater in the Danube River and Tributaries in Serbia, Environmental Monitoring Assessment, 187 (2015) 4092.
35. Gorito, A., M., Ribeiro, A., R., Almedia, C., M., R. and Silva, A., M., T., A Review on the Application of Constructed Wetlands for the Removal of Priority Substances and Contaminants of Emerging Concern Listed in Recently Launched EU Legislation, Environmental Pollution, 227 (2017) 428-443.

36. Fatta-Kassinos, D., Meric, S. and Nikolaou, A., Pharmaceutical Residues in Environmental Waters and Wastewater: Current State of Knowledge and Future Research, Archives of Environmental Contamination and Toxicology, 399 (2011) 251-275.
37. Vieno, N. and Sillanpaa, M., Fate of Diclofenac in Municipal Wastewater Treatment Plant- A Review, Environmental International, 69 (2014) 28-39.
38. <http://www.un.org/sustainabledevelopment/water-and-sanitation> Clean Water and Sanitation. October 2, 2021.
39. United Nations General Assembly (UNGA), The Human Right to Water and Sanitation, Resolution 64/292, United Nations, New York, 2010.
40. United Nations General Assembly (UNGA), Transforming Our World, The 2020 Agenda for Sustainable Development, United Nations, 2015.
41. Official Journal of the European Union, Establishing a Framework for Community Action in the Field of Water Policy 317. (2000/60/EC) 23.10.2000, 1-72.
42. Technical Guidance for Deriving Environmental Quality Standards, European Communities, Common Implementation Strategy for the Water Framework Directive 27. (2000/60/EC), 2001.
43. Directives 2008/105/EC of the European Parliament and of the Council of 16 December 2008 on Environmental Quality Standards in the Field of Water Policy, Amending and Subsequently Repealing Council Directives, 82/176/EEC, 83/513/EEC, 84/156/EEC, 84/491/EEC, 86/280/EEC and Amending Directive 2000/60/EC of the Council, Official Journal of the European Union, 348 (2008) 84-97.
44. Conference of Plenipotentiaries, Stockholm Convention on Persistent Organic Pollutants, Secretariate of the Stockholm on Persistent Organic Pollutants, (2001).
45. Directive 2013/39/EU of the European Parliament and of the Council of 12 August 2013 Amending Directives 2000/60/EC and 2008/105/EC as Regards Priority Substances in the Field of Water Policy, Official Journal of the European Union, 226 (2013) 1-17.
46. Decision 495/2015/ EU 20 of March 2015 Establishing a Watch List of Substances for Union-Wide Monitoring in the Field of Water Policy Pursuant to Directive 2008/105/EC of the European Parliament and of the Council, Official Journal of European Union, 78 (2015) 40-42.
47. Houtman, C., J., Emerging Contaminants of Surface Waters and their Relevance for the Production of Drinking Water in Europe, Journal of Integrated Environmental Science, 7 (2010) 271-295.

48. Bouissou-Schurtz, C., Houeto, P., Guerbet, M., Bachelot, M., Casellas, C., Mauclaire, A.-C., Panetier, P., Delval, C. and Masset, D., Ecological Risk Assessment of the Presence of Pharmaceutical Residues in a French National Water Survey, Regulatory Toxicology and Pharmacology, 69 (2014) 296-303.
49. La Farre, M., Perez, S., Kantiani, L. and Barcelo, D., Fate and Toxicity of Emerging Pollutants, their Metabolites and Transformation Products in the Aquatic Environment, Trends in Analytical Chemistry, 27, 11 (2008) 991-1007.
50. Rizzo, L., Malato, S., Antayali, D., Beretsou, V., G., Dolic, M., B., Gernjak, W., Heath, E., Ivancev-Tumbas, I., Karaolia, P., Lado Ribeiro, A., R., Mascolo, G., McArdell, C., S., Schaar, H., Silva, A., M., T. and Fatta-Kassinos, D., Consolidated Vs New Advanced Methods for the Removal of Contaminants of Emerging Concern from Urban Wastewater, Science of the Total Environment, 655 (2019) 986-1008.
51. Bui, X., T., Vo, T., P., Ngo, H., H., Guo, W., S. and Nguyen, T., T., Multicriteria Assessment of Advanced Treatment Technologies for Micropollutant Removal at Large-Scale Application, Science of the Total Environment, 563-564 (2016) 1050-1067
52. Ahmed, M., B., Zhou, J., L., Ngo, H., H., Guo, W., Thomaidis, N., S. and Xu, J., Progress in the Biological and Chemical Treatment Technologies for Emerging Contaminant Removal from Wastewater: A Critical Review, Journal of Hazardous Materials, 323 (Part A), 274-298.
53. Shamas, N., K. and Wang, L., K., Ozonation. In: Wang, L., K., Hung, Y.-T., Shamas, N., K., Eds., Physicochemical Treatment Processes, Humana Press, New Jersey, 2005.
54. Rice, R., G., Century 21- Pregnant with Ozone, Ozone Science and Engineering, 24 (2002) 1-15.
55. Sun, B., Guan, X., Fang, J. and Tratnyek, P., G., Activation of Manganese Oxidants with Bisulphite for Enhanced Oxidation of Organic Contaminants: The Involvement of Manganese (III), Environmental Science and Technology, 49, 20 (2015) 12414-12424.
56. Poyatos, J., M., Munio, M., M., Almecija, M., C., Torres, J., C., Hontoria, E. and Osorio, F., Advanced Oxidation Processes for Wastewater Treatment: State of the art, Water Air and Soil Pollution, 205 (2010) 187-204.
57. Bokare, A., D. and Choi, W., Review of Iron-Free Fenton -Like Systems for Activating H₂O₂ in Advanced Oxidation Processes, Journal of Hazardous Materials, 275 (2014) 121-135.
58. Mahamuni, N., N. and Adewuyi, Y., G., Advanced Oxidation Processes (AOPs) Involving Ultrasound for Wastewater Treatment: A Review with Emphasis on Cost Estimation, Ultrasonics Sonochemistry, 17 (2010) 990-1003.

59. Oturan, M., A. and Aaron, J., J., Advanced Oxidation Processes in Water/Wastewater Treatment I: Principles and Applications. A Review, Critical Reviews in Environmental Science and Technology, 44 (2014) 2577-2641.
60. Esteves, B., M., Rodrigues, C., S., D. and Madeira, L., M., Wastewater Treatment by Heterogeneous Fenton-Like Processes in Continuous Reactors. In Applications of Advanced Oxidation Processes (AOPs) in Drinking Water Treatment, Gil, A., Galeano, L., A., Vicente, M., A., Eds., Springer International Publishing, Cham, 2019.
61. Stakinakis, A., S., Use of Selected Advanced Oxidation Processes (AOPs) for Wastewater Treatment – A Mini Review, Global Nest Journal, 10 (2008) 376-385.
62. Domeno, C., Rodriguez-Lafuente, A., Martos, J., Bilbao, R. and Nerin, C., VOC Removal and Deodorization of Effluent Gases from an Industrial Plant by Photo-Oxidation, Chemical Oxidation, and Ozonation, Environmental Science Technology, 44 (2010) 2585-2591.
63. Liu, G., Ji, J., Huang, H., Xie, R., Feng, Q., Shu, Y., Zhan, Y., Fang, R., He, M. and Lui, S., et al., UV/H₂O₂: An Efficient Aqueous Advanced Oxidation Process for VOCs Removal, Chemical Engineering Journal, 324 (2017) 44-50.
64. Krzemieniewski, M., Debowski, M., Janczukowicz, W. and Pesta, J., Effect of Sludge Conditioning by Chemical Methods with Magnetic Field Application, Polish Journal of Environmental Studies, 12 (2003) 595-605.
65. Al Momani, F., A., Potential Use of Solar Energy for Waste Activated Sludge Treatment, International Journal of Sustainable Engineering, 6 (2013) 82-91.
66. Shannon, M., A., Bohn, P. W., Elimelech, M., Georgiadis, J., G., Marinas, B., J. and Mayes, A., M., Science and Technology for Water Purification in the Coming Decades, Nature, 452 (2008) 301-310.
67. Toor, R. and Mohseni, M., UV-H₂O₂ Based AOP and its Integration with Biological Activated Carbon Treatment for DBP Reduction in Drinking Water, Chemosphere, 66 (2007) 2087-2095.
68. Comninellis, C., Kapalka, A., Malato, S., Parsons, S., A. and Mantzavinos, I., P., D., Advanced Oxidation Processes for Water Treatment: Advances for R&D, Journal of Chemical Technology and Biotechnology, 83 (2008) 769-776.
69. Brigada, R., J., Consider Fenton's Chemistry for Wastewater Treatment, Chemical Engineering Processing, 91 (1995) 62-66.
70. Legrini, O., Oliveros, E. and Braun, A., M., Photochemical Processes for Water Treatment, Chemical Review, 93 (1993) 671-698.

71. Rosenfeldt, E., J., Chen, P., J., Kullman, S. and Linden, K., G., Destruction of Estrogenic Activity in Water Using UV Advanced Oxidation, Science of the Total Environment, 377 (2007) 105-113.
72. Skoumal, M., Cabot, P.-L., Centellas, F., Arias, C., Rodriguez, R., M., Garrido, J., A. and Brillas, E., Mineralization of Paracetamol by Ozonation Catalyzed with Fe²⁺, Cu²⁺ and UVA Light, Applied Catalysis B Environment, 22 (2006) 228-240.
73. Haber, F. and Weiss, J., The Catalytic Decomposition of Hydrogen Peroxide by Iron Salts, Proceedings of the Royal Society of London, Series A, Mathematical and Physical Sciences, 147 (1934) 332-351.
74. Gogate, P., R. and Pandit, A., B., A Review of Imperative Technologies for Wastewater Treatment I: Oxidation Technologies at Ambient Conditions, Advances in Environmental Research, 8 (2004), 501-551.
75. Ikehata, K., Jodeiri Naghashkar, N. and Gamal El-Din, M., Degradation of Aqueous Pharmaceuticals by Ozonation and Advanced Oxidation Processes: A Review, Ozone Science and Engineering, 28 (2006) 358-414.
76. Trapido, M., Epold, I., Bolobajev, J. and Dulova, N., Emerging Micropollutants in Water/Wastewater: Growing Demand on Removal Technologies, Environmental Science and Pollution Research, 21, 21 (2014) 12217-12222.
77. Rioja., N., Beguria, P., Penas, F., J. and Zorita, S., Competitive Removal of Pharmaceuticals from Environmental Waters by Adsorption and Photocatalytic Degradation, Environmental Science and Pollution Research, 21, 19 (2014) 11168-11177.
78. Rodrigues, C., S., D., Neto, A., R., Duda, R., M., de Oliveira, R., A., Boaventura, R., A., R. and Madeira, L., M., Combination of Chemical Coagulation, Photo-Fenton Oxidation and Biodegradation for the Treatment of Vinasse from Sugar Cane Ethanol Distillery, Journal of Cleaner Production, 142 (2017) 3634-3644.
79. Rice., R., G. and Netzer, A., Handbook of Ozone Technology and Applications, Volume 1, Ann Arbor Science Publishers, Butterworths, 1982.
80. Shu, Z., Bolton, J., R., Belosevic, M. and El Din, M., G., Photodegradation of Emerging Micropollutants Using the Medium -Pressure UV/H₂O₂ Advanced Oxidation Process, Water Research, 47 (2013) 2881-2889.
81. Klamerth, N., Malato, S., Maldonado, M., I., Aguera, A. and Fernandez-Alba, A., R. Application of Photo-Fenton as a Tertiary Treatment of Emerging Contaminants in Municipal Wastewater, Environmental Science Technology, 44 (2010) 1792-1798.
82. Ferro, G., Polo-Lopez, M., I., Martinez-Piernas, A., Fernandez-Ibanez, P., Aguera, A. and Rizzo, L., Cross-Contamination of Residual Emerging Contaminants and Antibiotic Resistant Bacteria in Lettuce Crops and Soil Irrigated with Wastewater

- Treated by Sunlight /H₂O₂, Environmental Science Technology, 49 (2015) 11096-11104.
83. Byrne, C., Subramanian, G. and Pillai, S., C., Recent Advances in Photocatalysis for Environmental Applications, Journal of Environmental Chemical Engineering, 6 (2018) 3531-3555.
 84. Miranda-Garcia, N., Maldonado, M., I., Coronado, J. and Malato, S., Degradation Study of 15 Emerging Contaminants at Low Concentration by Immobilized TiO₂ in a Pilot Plant, Catalysis Today, 15, 1 (2010) 107-113.
 85. Miranda-Garcia, N., Suarez, S., Sanchez, B., Coronado, J., M., Malato, S. and Maldonado, M., I., Photocatalytic Degradation of Emerging Contaminants in Municipal Wastewater Treatment Plant Effluents Using Immobilized TiO₂ in a Solar Pilot Plant, Applied Catalysis B: Environmental, 103, 3-4 (2011) 294-301.
 86. Bouafia-Chergui, S., Zemmouri, H., Chabani, M., and Bensmaili, A., TiO₂-Photocatalyzed Degradation of Tetracycline: Kinetic Study, Adsorption Isotherms, Mineralization and Toxicity Reduction, Desalination and Water Treatment, (2015) 1-8.
 87. Ananpattarachai, J. and Kajitvichyankul, P., Photocatalytic Degradation of p,p'-D-DT Under UV and Visible Light Using Interstitial N-Doped TiO₂, Journal of Environmental Science and Health- Part B Pesticides, Food Contaminants, and Agricultural Wastes, 50, 4 (2015) 247-260.
 88. Yola, M., L., Eren, T. and Atar, N., A Novel Efficient Photocatalyst Based TiO₂ Nanoparticles Involved Boron Enrichment Waste for Photocatalytic Degradation of Atrazine, Chemical Engineering Journal, 250 (2014) 288-294.
 89. Shetty, R., Chavan, V., B., Kulkarni, P., S., Kulkarni, B., D. and Kamble, S., P., Photocatalytic Degradation of Pharmaceuticals Pollutants Using N-Doped TiO₂ Photocatalyst: Identification of CFX Degradation Intermediates. Indian Chemical Engineer, (2016) 1-23.
 90. Cruz, M., Gomez, C., Duran-Valle, C., J., Pastrana-Martinez, L., M., Faria, J., L. and Silva, A., M., T., et al., Bare TiO₂ and Graphene Oxide TiO₂ Photocatalyst on the Degradation of Selected Pesticides and Influence of the Water Matrix, Applied Surface Science, 416 (2017) 1013-1021.
 91. Ollis, D., F. and Al-Ekabi, H. Photocatalytic Purification and Treatment of Water and Air, Elsevier, Amsterdam, 1993.
 92. Wei, T., Y. and Wan, C., C., Kinetics of Photocatalytic Oxidation of Phenol on TiO₂ Surface, Journal of Photochemistry and Photobiology A: Chemistry, 69 (1992) 241-247.

93. Schneider, J., Matsuoka, M., Takeuchi, M., Zhang, J., L., Horiuchi, Y., Anpo, M. and Bahnemann, D., W., Understanding of TiO₂ Photocatalysis: Mechanisms and Materials, Chemical Review, 114 (2014) 9919-9986.
94. Pelaez. M., Nolan, N., T., Pillai, S., C., Seery, M., K., Falaras, P., Kontos, A., G., Dunlop, P., S., M., Hamilton, J., W., J., Byrne, J., A. and O'Shea, K., et al., A Review on the Visible Light Active Titanium Dioxide Photocatalysts for Environmental Applications, Applied Catalysis B- Environmental, 125 (2012) 331-349.
95. Tong, H., Ouyang, S., X., Bi, Y., P., Umezawa, N., Oshikiri, M. and Ye, J., H., Nano-Photocatalytic Materials: Possibilities and Challenges, Advance Material, 24 (2012) 229-251.
96. Mills, A. and LeHunte, S., An Overview of Semiconductor Photocatalysis, Journal of Photochemistry and Photobiology A Chemistry, 108 (1997) 1-35.
97. Ge, J., Zhang, Y., Heo, Y.-J. and Park, S.-J., Advanced Design and Synthesis of Composite Photocatalysts for the Remediation of Wastewater: A Review, Catalyst, 9 (2019) 122.
98. Dhand, V., Mittal, G., Rhee, K., Y., Park, S., J. and Hui, D., A Short Review on Basalt Fibre Reinforced Polymer Composites, Composites Part B: Engineering, 73 (2015) 166-180.
99. Azeez, A., A., Rhee, K., Y., Park, S., J. and Hui, D., Epoxy Clay Nanocomposites-Processing, Properties and Applications: A Review, Composite Part B: Engineering, 45 (2013) 308-320.
100. Bronstein, H., Nielsen, C., B., Schroeder, B., C. and McCulloch, I., The Role of Chemical Design in the Performance of Organic Semiconductors, Natural Reviews Chemistry, 4 (2020) 66-77.
101. Jiang, D., Otitoju, T., A., Ouyang, Y., Shoparwe, N., F., Wang, S., Zhang, A. and Li, S., A Review on the Metal Ions Modified TiO₂ for Photocatalytic Degradation of Organic Pollutants, Catalysts, 11 (2021), 1039.
102. Kumar, S., G. and Rao Koteswara, K., S., R., Comparison of Modification Strategies Towards Enhanced Charge Carrier Separation and Photocatalytic Degradation Activity of Metal Oxide Semiconductors (TiO₂, WO₃, ZnO), Applied Surface Science, 391 (2017) 124-148.
103. Friedmann, D., Hakki, A., Kim, H., Choi, W. and Bahnemann, D., Heterogeneous Photocatalytic Organic Synthesis: State-of-The-Art and Future Perspectives, Green Chemistry, 18 (2016) 5391.
104. Uddin, MD.-S., Salam, MD.-A., Habib, MD.-S., Ahmed, K., Hossain, T. and Nasrin, P., Various Material Development Strategies for Suitable Catalysts of Photo Catalytic Water Splitting to Green Fuel H₂: A Critical Review, Material Science Research India, 18, 2 (2021) 108-142.

105. Salimi, M., Esrafil, A., Gholami, M., Jafari, A., J., Kalantary, R., R., Farzadkia, M., Kermani, M. and Sobhi, H., R., Contaminants of Emerging Concern: A Review of New Approach in AOP Technologies, Environmental Monitoring Assessment, 189 (2017) 414.
106. Dal Santo, V. and Naldoni, A., Titanium Dioxide Photocatalysis, Catalysis, 8 (2018) 591.
107. Park, H., Park, Y., Kim, W. and Choi, W., Surface Modification of TiO₂ Photocatalyst for Environmental Applications, Journal of Photochemistry and Photobiology C: Photochemistry Reviews, 15 (2013) 1-20.
108. Perovic., K., dela Rosa, F., M., Kovacic, M., Kusic, H., Stangar, U., L., Fresno, F., Dionysiou, D., D. and Bozic, A., L., Recent Achievements in Development of TiO₂-Based Composite Photocatalytic Materials for Solar Driven Water Purification and Water Splitting, Materials, 13 (2020) 1338.
109. Khan, H. and Berk, D., Characterization and Mechanistic Study of Mo⁺⁶ and V⁺⁵ Co-doped TiO₂ as a Photocatalyst, Journal of Photochemistry and Photobiology A Chemistry, 294 (2014) 96-109.
110. Xu, H., Liao, J., Yuan, S., Zhao, Y., Zhang, M., Wang, Z. and Shi, L., Tuning the Morphology, Stability and Photocatalytic Activity of TiO₂ Nanocrystal Colloids by Tungsten Doping, Material Research Bulletin, 51 (2014) 326-331.
111. Yang, H., Li, X., Wang, A., Wang, Y. and Chen, Y., Photocatalytic Degradation of Methylene Blue by MoO₃ Modified TiO₂ Under Visible Light, Chinese Journal of Catalysis, 35 (2014) 140-147.
112. Dunnill, C., W. and Parkin, I., P., Nitrogen -doped TiO₂ Thin Films: Photocatalytic Applications for Healthcare Environments, Dalton Transactions, 40 (2011) 1635-1640.
113. Liu, G., Wang, L., Z., Yang, H., M. and Lu, G., Q., Titania-Based Photocatalyst-Crystal Growth, Doping and Heterostructuring. Journal of Materials Chemistry, 20 (2010) 831-843.
114. Ashi, R., Morikawa, T., Irie, H. and Ohwaki, T., Nitrogen-Doped Titanium Dioxide as Visible-Light-Sensitive Photocatalyst: Designs, Developments, and Prospects. Chemical Review, 114 (2014) 9824-9852.
115. Mittal, A., Mari, B., Sharma, S., Kumari, V., Maken, S., Kumari, K. and Kumar, N., Non-metal Modified TiO₂: A Step Towards Visible Light Photocatalysis, Journal of Materials Science: Materials in Electronics, 30 (2019) 3186-3207.

116. Kalid, N., R., Ahmed, E., Hong, Z., Zhang, Y. and Ahmad, M., Nitrogen Doped TiO₂ Nanoparticles Decorated on Graphene Sheets for Photocatalysis Application, Current Applied Physics, 12, 6 (2012) 1485-1492.
117. Salah, N., Hameed, A., Aslam, M., Abdel-Wahab, M., S., Babkair, S., S. and Bahabri, F., S., Flow Controlled Fabrication of N Doped ZnO Thin Films and Estimation of Their Performance for Sunlight Photocatalytic Decontamination of Water, Chemical Engineering Journal, 291 (2016) 115-127
118. Ribao, P., Rivero, M., J. and Ortiz, I., Enhanced Photocatalytic Activity Using GO/TiO₂ Catalyst for The Removal of DCA Solution, Environmental Science and Pollution Research, 25 (2018) 34893-34902.
119. Cordero-Garcia, A., Guzman-Mar, J., L., Hinojosa-Reyes, L., Ruiz-Ruiz, E. and Hernandez-Ramirez, A., Effect of Carbon Doping on WO₃/TiO₂ Coupled Oxide and Its Photocatalytic activity on Diclofenac Degradation, Ceramics International, 42, 8 (2016) 9796-9803.
120. Grabowska, E., Zaleska, A., Sobczak, J., W., Gazda, J. and Hupka, J., Boron-doped TiO₂: Characteristics and Photoactivity Under Visible Light, Procedia Chemistry, 1, 2 (2009) 1553-1559.
121. Li, D., Haneda, H., Hishita, S., Ohashi, N. and Labhsetwar, N., K., Flourine -doped TiO₂ Powders Prepared by Spray Pyrolysis and Their Improved Photocatalytic Activity for Decomposition of Gas -Phase Acetaldehyde, Journal of Flourine Chemistry, 126, 1 (2005) 69-77.
122. Anucha, C., B., Altin, I., Fabbri, D., Degirmencioglu, I., Calza, P., Magnacca, G., Stathopoulos, V., N. and Bacaksiz, E. Synthesis and Characterization of B/NaF and Silicon Phthalocyanine-Modified TiO₂ and an Evaluation of Their Photocatalytic Removal of Carbamazepine, Separations, 7 (2020) 71.
123. Zhou, S., W., Peng, P., Liu, J., Tang, Y., H., Meng, B. and Peng, Y., X., Investigation on the Electronic Structures and Optical Performances of Si-S Codoped Anatase TiO₂ by First-Principles Calculation, Physics Letters A, 380, 16 (2016) 1462-1468.
124. Wang, F., Li, F., Zhang, L., Zeng, H., Sun, Y., Zhang, S. and Xu, X., S-TiO₂ with Enhanced Visible-Light Photocatalytic Activity Derived from TiS₂ in Deionized Water, Materials Research Bulletin, 87 (2017) 20-26.
125. Jin, C., Zheng, R., Y., Guo, Y., Xie, J., L., Zhu, Y., X. and Xi, Y., C., Hydrothermal Synthesis and Characterization of Phosphorus-Doped TiO₂ with High Photocatalytic Activity for Methylene Blue Degradation, Journal of Molecular Catalysis, 313, 1-2 (2009) 44-48.
126. Jiang. H., Liu, Y., Li, Y. and Wang, H., Synergistic Effects of Lanthanum, Nitrogen and Phosphorus Tri-Doping on Visible -Light Photoactivity of TiO₂ by Microwave-Hydrothermal Process, Journal of Rare Earths, 34, 6 (2016) 604-613.

127. Kumaresan, L., Prabhu, A., Palanichamy, M., Arumugam, E. and Murugesan, V., Synthesis and Characterization of Z^{4+} , La^{3+} and Ce^{3+} Doped Mesoporous TiO_2 : Evaluation of Their Photocatalytic Activity, Journal of Hazardous Materials, 186, 2-3 (2011) 1183-1192.
128. Macias-Tamez, R., Villanueva-Rodriguez, M., Ramos-Delgado, N., A., Maya-Trevino, L. and Hernandez-Ramirez, A., Comparative study of the Photocatalytic Degradation of the Herbicide 2,4-D Using WO_3/TiO_2 and Fe_2O_3/TiO_2 as Catalyst, Water Air and Soil Pollution, 228 (2017) 379.
129. Mugunthan, E., Saidutta, M., B. and Jagadeeshbabu, P., E., Visible Light Assisted Photocatalytic Degradation of Diclofenac Using TiO_2-WO_3 Mixed Oxide Catalyst, Environmental Nanotechnological Monitoring and Management, 10 (2018) 322-330
130. Arce-Sarria, A., Machuca-Martinez, F., Bustillo-LeCompte, C., Hernandez-Ramirez, A. and Colina-Marquez, J., Degradation and Loss of Antibacterial Activity of Commercial Amoxicillin with TiO_2/WO_3 -Assisted Solar Photocatalysis, Catalysis, 8 (2018) 222.
131. Cordero-Garcia, A., Turnes Palomino, G., Hinojosa-Reyes, L., Guzman-Mar, J., L., Maya-Tevino, L, Hernandez-Ramirez, A., Photocatalytic Behaviour of WO_3/TiO_2-N for Diclofenac Degradation Using Simulated Solar Radiation as an Activation Source, Environmental Science Pollution Research, 24 (2017) 4613-4624.
132. Shi, Y., Yang, Z., Wang, B., An, H., Chen, Z. and Cui, H., Adsorption and Photocatalytic Degradation of Tetracycline Hydrochloride Using a Palygorskite-Supported Cu_2O-TiO_2 Composite, Applied Clay Science, 119 (2016) 311-320.
133. Hu, Z., Wang, X., Dong, H., Li, S., Li, X. and Li, L., Efficient Photocatalytic of Tetrabromodiphenyl Ethers and Simultaneous Hydrogen Production by TiO_2-Cu_2O Composite Films in N_2 atmosphere: Influencing Factors, Kinetics and Mechanisms, Journal of Hazardous Material, 340 (2017) 1-15.
134. Anucha, C., B., Altin, I., Bacaksiz, E., Kucukomeroglu, T., Belay, M., H. and Stathopoulos, V., N., Enhanced Photocatalytic Activity of $CuWO_4$ Doped TiO_2 Photocatalyst Towards Carbamazepine Removal Under UV Irradiation, Separations, 8 (2021) 25.
135. Sud, D. and Siyal, A., Investigations on the Phase Transformation, Optical Characteristics, and Photocatalytic Activity of Synthesized Heterostructured Nonporous $Bi_2O_3-TiO_2$, Journal of Chinese Chemical Society, 63 (2016) 776-783.
136. Sood, S., Mehta, S., K., Sinha, A., S., K. and Kansal, S., K., Bi_2O_3/TiO_2 Heterostructures: Synthesis, Characterization and Their Application in Solar Mediated Photocatalyzed Degradation of an Antibiotic, Ofloxacin, Chemical Engineering Journal, 290 (2016) 45-52.
137. Chen, Y., Wu, Q., Wang, J. and Song, Y., The Fabrication of Magnetic Recyclable Nitrogen-Doped Titanium Dioxide /Calcium Ferrite /Diatomite Heterojunction

- Nanocomposite for Improved Visible-Light-Driven Degradation of Tetracycline, Journal of Chemical Technology and Biotechnology, 94 (2019) 2702-2712.
138. Wu, Q. and Zhang, Z., The Fabrication of Magnetic Recyclable Nitrogen Modified Titanium Dioxide/Strontium Ferrite/Diatomite Heterojunction Nanocomposite for Enhanced Visible-Light-Driven Photodegradation of Tetracycline, International Journal of Hydrogen Energy, 44 (2019) 8261-8272.
 139. Chen, Y. and Liu, K., Fabrication of Magnetically Recyclable Ce/N Co-Doped TiO₂/NiFe₂O₄/Diatomite Ternary Hybrid: Improved Photocatalytic Efficiency Under Visible Irradiation, Journal of Alloy Compounds, 697 (2017) 161-173.
 140. Nguyen, T., B. and Doong, R., A., Heterostructured ZnFe₂O₄/TiO₂ Nanocomposites with a Highly Recyclable Visible-Light Response for Bisphenol A Degradation, RSC Advances, 7 (2017), 50006-50016.
 141. Mirmasoomi, S., R., Mehdipour Ghazi, M. and Galedari, M., Photocatalytic Degradation of Diazinon Under Visible Light Using TiO₂/Fe₂O₃ Nanocomposite Synthesized by Ultrasonic-Assisted Impregnation method, Separation and Purification Technology, 175 (2017) 418-427.
 142. Moniz, S., J., A., Shevlin, S., A., An, X., Guo, Z., X. and Tang, J. Fe₂O₃-TiO₂ Nanocomposites for Enhanced Charge Separation and Photocatalytic Activity, Chemistry A European Journal, 20 (2014) 15571-15579.
 143. Li, R., Liu, J., Jia, Y. and Zhen, Q. Photocatalytic Degradation Mechanism of Oxytetracyclines Using Fe₂O₃-TiO₂ Nanopowders, Journal of Nanoscience and Nanotechnology, 17 (2017) 3010-3015.
 144. Li, R., Jia, Y., Wu, J. and Zhen, Q., Photocatalytic Degradation and Pathway of Oxytetracycline in Aqueous Solution by Fe₂O₃-TiO₂ Nanopowder , RSC Advances, 5 (2015) 40764-40771.
 145. Lu, C., Guan, W., Zhang, G., Ye, L., Zhou, Y. and Zhang, X., TiO₂/Fe₂O₃/CNTs Magnetic Photocatalyst: A fast and Convenient Synthesis and Visible -Light-Driven Photocatalytic Degradation of Tetracycline, Micro and Nano Letters, 8 (2013) 749-752
 146. Zheng, X., Fu, W., Kang, F., Peng, H. and Wen, J., Enhanced Photo-Fenton Degradation of Tetracycline Using TiO₂-Coated α -Fe₂O₃ Core-Shell Heterojunction, Journal of Industrial and Engineering Chemistry, 68 (2018) 14-23.
 147. Li, W., Ding, H., Ji, H., Dai, W., Guo, J. and Du, G., Photocatalytic Degradation of Tetracycline Hydrochloride via CdS-TiO₂ Heterostructure Composite Under Visible Light Irradiation, Nanomaterials, 8 (2018) 415.
 148. Kandi, D., Behera, A., Martha, S., Naik, B. and Parida, K., M., Quantum Confinement Chemistry of CdS QDs Plus Hot Electron of Au Over TiO₂ Nanowire Protruding to Be Encouraging Photocatalyst Towards Nitrophenol Conversion and

- Ciprofloxacin Degradation, Journal of Environmental Chemical Engineering, 7 (2019) 102821.
149. Kanur, A., Umar, A., Anderson, W, A. and Kansal, S., K., Facile Synthesis of CdS/TiO₂ Nanocomposite and Their Catalytic Activity for Ofloxacin Degradation Under Visible Illumination, Journal of Photochemistry and Photobiology A Chemistry, 360 (2018) 34-43.
150. Luo, L., Long, J., Zhao, S., Dai, J., Ma, L., Wang, H., Xia, L., Shu, L. and Jiang, F., Effective Visible-Light-Driven Photocatalytic Degradation of 17 α -Ethinylestradiol by Crosslinked CdS Nano-Rod/TiO₂ (B) Nano-Belt Composite, Process Safety and Environmental Protection, 130 (2019) 77-85.
151. Jiang, Y., Zhang, M., Xin, Y., Chai, C. and Chen, Q., Construction of Immobilized CuS/TiO₂ Nanobelts Heterojunction Photocatalyst for Photocatalytic Degradation of Enrofloxacin: Synthesis, Characterization, Influencing Factors and Mechanism Insight, Journal of Chemical Technology and Biotechnology, 94 (2019) 2219-2228.
152. Chen, Q., Wu, S. and Xin, Y., Synthesis of Au-CuS-TiO₂ Nanobelts Photocatalyst for Efficient Photocatalytic Degradation of Antibiotic Oxytetracycline, Chemical Engineering Journal, 302 (2016) 377-387.
153. Kumar, N., Bhadwal, A., S., Mizaikoff, B., Singh, S. and Kranz, C., Electrochemical Detection of and Photocatalytic Performance of MoS₂/TiO₂ Nanocomposite Against Pharmaceutical Contaminant: Paracetamol, Sensing and Bio-Sensing Research, 24 (2019) 100288.
154. Irandost, M., Akbarzadeh, R., Pirsaeheb, M., Asadi, A., Mohammadi and Sillanpaa, M., Fabrication of Highly Visible Active N, S Co-doped TiO₂@MoS₂ Heterojunction with Synergistic Effect for Photocatalytic Degradation of Diclofenac: Mechanisms, Modelling and Degradation Pathway, Journal of Molecular Liquids, 291 (2019) 111342.
155. Kovacic, M., Kopicic, N., Kusic, H. and Bozic, A., L., Solar Driven Degradation of 17 β -Estradiol Using Composite Photocatalytic Materials and Artificial Irradiation Source: Influence of Process and Water Matrix Parameters, Journal of Photochemistry and Photobiology A Chemistry, 361 (2018) 48-61.
156. Kovacic, M., Papac, J., Kusic., H., Karamanis, P. and Loncaric, A., Degradation of Polar and Non-Polar Pharmaceutical Pollutants in Water by Solar Assisted Photocatalysis Using Hydrothermal TiO₂-SnS₂. Chemical Engineering Journal, 382 (2019) 122826.
157. Wang, Y., Yu, H., Liu, Y., Qu, J., Zhu, S. and Huo, M., A Nanocomposite Comprised of Ti³⁺ Doped TiO₂ Nanotubes and Ag₃PO₄ Quantum Dots with Enhanced Photocatalytic Activity Under Visible Light, Materials Letters, 240 (2019) 35-38.
158. Du, J., Ma, S., Yan, Y., Li, K., Zhao, F. and Zhou, J., Corn-Silk Templated Synthesis of TiO₂ Nanotube Arrays with Ag₃PO₄ Nanoparticles for Efficient Oxidation of

Organic Pollutants and Pathogenic Bacteria Under Solar Light, Colloids and Surfaces A: Physicochemical and Engineering Aspects, 572 (2019) 237-249.

159. Lui, J., Xie, F., Li, R., Li, T., Jia, Z., Wang, Y., Wang, Y., Zhang, X. and Fan, C., TiO₂-x/Ag₃PO₄ Photocatalyst: Oxygen Vacancy Dependent Visible Light Photocatalytic Performance and BPA Degradative Pathway, Materials Science in Semiconductor Processing, 97 (2019) 1-10.
160. Kaur, A., Salunke, D., B., Umar, A., Mehta, S., K., Sinha, A., S., K. and Kansal, S., K., Visible Light Driven Photocatalytic Degradation of Fluoroquinolone Levofloxacin Drug Using Ag₂O/TiO₂ Quantum Dots: Mechanistic Study and Degradation Pathway, New Journal of Chemistry, 41 (2017) 12079-12090.
161. Guo, J., Ma, Q., Deng, X., Cui, Y., Zhang, H., Cheng, X., Li, X., Xie, M. and Cheng, Q., Fabrication of Ag₂O/TiO₂-Zeolite Composite and Its Enhanced Solar Light Photocatalytic Performance and Mechanism for Degradation of Norfloxacin, Chemical Engineering Journal, 308 (2017) 818-826.
162. Anucha, C., B., Altin, I., Bacaksiz, E., Stathopoulos, V., N., Polat, I., Yasar, A. and Yuksel, O., F., Silver Doped Zinc Stannate (Ag-ZnSnO₃) for the Photocatalytic Degradation of Caffeine Under UV Irradiation, Water, 13 (2021) 1290.
163. Hao, X., Li, M., Zhang, L., Wang, K. and Liu, C., Photocatalyst TiO₂/WO₃/GO Nanocomposite with High Efficient Photocatalytic Performance for BPA Degradation Under Visible Light and Sola Light Illumination, Journal of Industrial and Engineering Chemistry, 55 (2017) 140-148.
164. Wang, G., Chen, Q., Xin, Y., Liu, Y., Zhang, Z., Hu, C. and Zhang, B., Construction of Graphene-WO₃/TiO₂ Nanotube Array Photoelectrodes and Its Enhanced Performance for Photocatalytic Degradation of Dimethyl Phthalate, Electrochimica Acta, 222 (2016) 1903-1913.
165. Bigin Simsek, E., Kilic, B., Aşgin, M. and Akan, A., Graphene Oxide Based Heterojunction TiO₂-ZnO Catalyst with Outstanding Photocatalytic Performance for Bisphenol-A, Ibuprofen and Flurbiprofen. Journal of Industrial and Engineering Chemistry, 59 (2018) 115-126.
166. Feng, J., Wang, Y., Hou, Y. and Li, L., Hierarchical Structured ZnFe₂O₄@RGO@TiO₂ Composite as Powerful Visible Light Catalyst for Degradation of Fulvic Acid, Journal of Nanoparticle Research, 19 (2017) 178.
167. Luo, L., J., Li, J., Dai, J., Xia, L., Barrow, C., J., Wang, H., Jegatheesan, J. and Yang, M., Bisphenol A Removal on TiO₂-MoS₂-Reduced Graphene Oxide Composite by Adsorption and Photocatalysis, Process Safety and Environmental Protection, 112 (2017) 274-279.
168. Wang, W., Han, Q., Zhu, Z., Zhang, L., Zhong, S. and Liu, B., Enhanced Photocatalytic Degradation Performance of Organic Contaminants by Heterojunction Photocatalyst BiVO₄/TiO₂/RGO and Its Compatibility on Four

- Different Tetracycline Antibiotics, Advanced Powder Technology, 30 (2019) 1882-1896.
169. Yang, Z., Yan, J., Lian, J., Xu, H., She, X. and Li, H., g-C₃N₄ Nanocomposites for Degradation of Ciprofloxacin Under Visible Light Irradiation, ChemistrySelect, 1 (2016) 5679-5685.
 170. Li, G., Nie, X., Gao, Y. and An, T., Can Environmental Pharmaceuticals be Photocatalytically Degraded and Completely Mineralized in Water Using g-C₃N₄/TiO₂ Under Visible Light Irradiation? - Implications of Persistent Toxic Intermediates, Applied Catalysis B Environment, 180 (2016) 726-732.
 171. Yu, S., Wang, Y., Sun, F., Wang, R. and Zhou, Y. Novel mpg-C₃N₄/TiO₂ Nanocomposite Photocatalytic Membrane Reactor for Sulfamethoxazole Photodegradation, Chemical Engineering Journal, 337 (2018) 183-192.
 172. Wang, W., Fang, J., Shao, S., Lai, M. and Lu, C., Compact and Uniform TiO₂@g-C₃N₄ Core-Shell Quantum Heterojunction for Photocatalytic Degradation of Tetracycline Antibiotics, Applied Catalysis B Environmental, 217 (2017) 57-64.
 173. Chen, Y., Lu, W., Shen, H., Gu, Y., Xu, T., Zhu, Z., Wang, G. and Chen, W., Solar Driven Efficient Degradation of Emerging Contaminants by g-C₃N₄-Shielding Polyester fibre/TiO₂ Composites, Applied Catalysis B Environmental, 258 (2019) 117960.
 174. Li, C., Sun, Z., Zhang, W., Yu, C. and Zheng, S. Highly Efficient g-C₃N₄/TiO₂/Kaolinite Composite with Novel Three-Dimensional Structure and Enhanced Visible Light Responding Ability Towards Ciprofloxacin and Saureus, Applied Catalysis B Environmental, 220 (2018) 272-282.
 175. Xie, X., Chen, C., Wang, X., Li, J. and Naraginti, S., Efficient Detoxification of Triclosan by a S-Ag/TiO₂@g-C₃N₄ Hybrid Photocatalyst: Process Optimization and Bio-Toxicity Assessment, RSC Advances, 9 (2019) 20439-20449.
 176. Song, J., Wu, X., Zhang, M., Liu, C., Yu, J., Sun, G., Si, Y. and Ding, B., Highly Flexible, Core-Shell Heterostructured, and Visible-Light-Driven Titania-Based Nanofibrous Membranes for Antibiotic Removal and E. coli Inactivation, Chemical Engineering Journal, 379 (2020) 122269.
 177. Yang, L., Bai, X., Shi, J., Du, X., Xu, L. and Jin, P., Quasi-Full-Visible-Light Absorption by D35-TiO₂/g-C₃N₄ for Synergistic Persulfate Activation Towards Efficient Photodegradation of Micropollutants, Applied Catalysis B Environment, 256 (2019) 117759.
 178. Su, Y., Chen, P., Wang, F., Zhang, Q., Chen, T., Wang, Y., Yao, K., Lv, W. and Liu, G., Decoration of TiO₂/g-C₃N₄ Z-Scheme by Carbon Dots as a Novel Photocatalyst with Improved Visible-Light Photocatalytic Performance for the Degradation of Enrofloxacin, RSC Advances, 7 (2017) 34096-34103.

179. Nie, Y., C., Yu, F., Wang, L., C., Xing, Q., J., Liu, X., Pei, Y., Zou, J., P., Dai, W., L., Li, Y. and Suib, S., L., Photocatalytic Degradation of Organic Pollutants Coupled with Simultaneous Photocatalytic H₂ Evolution Over Graphene Quantum Dots/Mn-N-TiO₂/g-C₃N₄ Composite Catalysts: Performance and Mechanism, Applied Catalysis B Environment, 227 (2018) 312-321.
180. Jo, W., K., Adinaveen, T., Vijaya, J., J. and Sagaya Selvam, N., C., Synthesis of MoS₂ Nanosheet Supported Z-Scheme TiO₂/g-C₃N₄ Photocatalyst for the Enhanced Photocatalytic Degradation of Organic Water Pollutants, RSC Advances, 6 (2016) 10487-10497.
181. Tahir, M., B., Sagir, M. and Shahzad, K., Removal of Acetyl Salicylate and Methyl-Theobromine from Aqueous Environment Using Nano-Photocatalyst WO₃-TiO₂@g-C₃N₄ Composite, Journal of Hazardous Materials, 363 (2019) 205-213.
182. McFarland, E., W. Catalysis by Doped Oxides, Chemical Reviews, 113, 6 (2013) 4391-4427.
183. Pandis, P., K., Perros, D., E. and Stathopoulos, V., N., Doped Apatite-Type Lanthanum Silicates in CO Oxidation Reaction, Catalysis Communication, 114 (2018) 98-103.
184. Goula, M., A., Charisiou, N., D., Pandis, P., K. and Stathopoulos, V., N., A Ni/Apatite-Type Lanthanum Silicate Supported Catalyst in Glycerol Steam Reforming Reaction, RSC Advances, 6 (2016) 78954-78958.
185. Damaskinos, C., M., Vasiliades, M., A., Stathopoulos, V., N. and Efstathiou, A., M., The Effect of CeO₂ Preparation Method on the Carbon Pathways in the Dry Reforming Reaction of Methane on Ni/CeO₂ Studied by Transient Techniques, Catalysts, 9, 7 (2019) 621.
186. Stathopoulos, V., N., Belessi, V., C., Costa, C., N., Neophytides, S., Falaras, P., Efstathiou, A., M. and Pomonis, P., J., Catalytic Activity of High Surface Area Mesoporous Mn-Based Mixed Oxides for the Deep Oxidation of Methane and Lean-NO_x Reduction, Studies in Surface Science and Catalysis, 130 (2000) 1529-1534.
187. Salmas, C., E., Stathopoulos, V., N., Pomonis, P., J. and Androutsopoulos, G., P., Pore Structure -Chemical Composition Interactions of New High Surface Area Manganese Based Mesoporous Materials. Materials Preparation, Characterization and Catalytic Activity, Langmuir, 18, 2 (2002) 423-432.
188. Janczarek, M. and Kowalska, E., On the Origin of Enhanced Photocatalytic Activity of Copper-Modified Titania in the Oxidative Reaction Systems, Catalysts, 7 (317) 2017.
189. Serpone, N., Maruthamuthu, P., Pichat, P., Pelizzetti, E. and Hidaka, H., Exploiting the Interparticle Electron Transfer Process in the Photocatalyzed Oxidation of Phenol, 2-Chlorophenol and Pentachlorophenol: Chemical Evidence for Electron and

- Hole Transfer Between Coupled Semiconductors, Journal of Photochemistry and Photobiology A Chemistry, 85 (1995) 247-255.
190. Bessekhoud, Y., Robert, D. and Weber, J., V., Bi₂Si₃/TiO₂ and CdS Heterojunctions as an Available Configuration for Photocatalytic Degradation of Organic Pollutant, Journal of Photochemistry and Photobiology A Chemistry A, 163 (2004) 569-580.
 191. Low, J., Yu, J., Jaroniec, M., Wageh, S. and Al-Ghamdi, A., A., Heterojunction Photocatalysts, Advanced Materials, 29 (2017) 1601694.
 192. Baek, J., H., Kim, B., J., Han, G., Hwang, S., W., Kim, D., R., Cho, I., S and Jung, H., S., BiVO₄/WO₃/SnO₂ Double-Heterojunction Photoanode with Enhanced Charge Separation and Visible -Transparency for Bias-Free Solar -Water Splitting with a Perovskite Solar Cell, ACS Applied Materials and Interfaces, 29 (2017) 1601694.
 193. Uddin, M., T., Nicolas, Y., Olivier, C., Toupance, T., Servant, L., Muller, M., M., Kleebe, H., J., Zeigler, J. and Jaegermann, W., Nanostructured SnO₂-ZnO Heterojunction Photocatalyst Showing Enhanced Photocatalytic Activity for the Degradation of Organic Dyes, Inorganic Chemistry, 51 (2012) 7764-7773.
 194. Shirmadi, A., Teridi, M., A., M., Azimi, H., R., Basirun, W., J., Jamali-Sheini, F. and Yousefi, R., Enhanced Photocatalytic Performance of ZnSe/PANI Nanocomposites for Degradation of Organic and Inorganic Pollutants, Applied Surface Science, 462 (2018) 730-738.
 195. Lee, C., H., Lee, G., H., van der Zande, A., M., Chen, W., C., Li, Y., L., Han, M., Y., Cui, X., Arefe, G., Nuckolls, C. and Heinz, T., F., et al., Atomically Thin p-n Junctions with van der Waals Heterointerfaces, Nature Nanotechnology, 9 (2014) 676-681.
 196. Kawazoe, H., Yanagi, H., Ueda, K. and Hosono, H., Transparent p-Type Conducting Oxides: Design and Fabrication of p-n Heterojunctions, Materials Research Society Bulletin, 25, (2000), 28-36.
 197. Lu, M., X., Shao, C., L., Wang, K., X., Lu, N., Zhang, P., Zhang, M., Y., Li, X., H. and Liu, Y., C., p-MoO₃ Nanostructures/n-TiO₂ Nanofibre Heterojunctions: Controlled Fabrication and Enhanced Photocatalytic Properties, ACS Applied Material Interfaces, 6 (2014) 9004-9012.
 198. Zhang, Y. and Park, S., J. Formation of Hollow MoO₃/SnS₂ Heterostructured Nanotubes for Efficient Light-Driven Hydrogen Production, Journal of Materials Chemistry A, 6 (2018) 20304-20312.
 199. Wen, X., J., Niu, C., G., Zhang, L., Zeng, G., M. Novel p-n Heterojunction BiOI/CeO₂ Photocatalyst for Wider Spectrum Visible-Light Photocatalytic Degradation of Refractory Pollutants, Dalton Transactions, 46 (2017) 4982-4993.

200. Marshal, R., Photocatalysis: Semiconductor Composites: Strategies for Enhancing Charge Carrier Separation to Improve Photocatalytic Activity, Advanced Functional Materials, 24 (2014) 2420.
201. Wei, Z., D., Zhao, Y., Fan, F., T. and Li, C., The Property of Surface Heterojunction Performed by Crystal Facets for Photogenerated Charge Separation, Computational Material Science, 153 (2018) 28-35.
202. Yu, J., G., Low, J., X., Xiao, W., Zhou, P. and Jaroniec, M., Enhanced Photocatalytic CO₂-Reduction Activity of Anatase TiO₂ by Coexposed {001} and {101} Facets, Journal of American Chemical Society, 136 (2014) 8839-8842.
203. Gao, S., J., Wang, Wang, W., Ni, Y., R., Lu, C., H. and Xu, Z., Z., Facet-Dependent Photocatalytic Mechanisms of Anatase TiO₂: A New Sight on the Self-Adjusted Surface Heterojunction, Journal of Alloy Compounds, 647 (2015) 981-988.
204. Lu, J., Wu, J., Xu, W., X., Cheng, H., Q., Qi, X., M., Li, Q., W., Zhang, Y., A., Guan, Y., Ling, Y. and Zhang, Z., Room Temperature Synthesis of Tetragonal BiOI Photocatalyst with Surface Heterojunction Between (001) Facets and (110) Facets, Materials Letters, 219 (2018) 260-264.
205. Li, H., J., Tu, W., G. and Zhou, Z., G., Z-Scheme Photocatalytic Systems for Promoting Photocatalytic Performance: Recent Progress and Future Challenges, Advanced Science, 3 (2012) 12.
206. Wu, X., S., Hu, Y., D., Wang, Y., Zhou, Y., S., Han, Z., H., Jin, X., L. and Chen, G., In Situ Synthesis of Z-Scheme Ag₂CO₃/Ag/AgNCO Heterojunction Photocatalyst with Enhanced Stability and Photocatalytic Activity, Applied Surface Science, 464 (2019) 108-114.
207. Lu, X., Y., Che, W., J., Hu, X., F., Wang, Y., Zhang, A., T., Deng, F., Luo, S., L. and Dionysiou, D., D., The Facile Fabrication of Novel Visible-Light -Driven Z-Scheme CuInS₂/Bi₂WO₆ Heterojunction with Intimate Interface Contact by In Situ Hydrothermal Growth Strategy for Extraordinary Photocatalytic Performance, Chemical Engineering Journal, 356 (2019) 819-829.
208. Leary, R., and Westwood, A., Carbonaceous Nanomaterials for the Enhancement of TiO₂ Photocatalysis, Carbon, 49 (2011) 741-772.
209. Li, J., Liu, K., Xue, J., Xue, G., Sheng, X., Wang, H., Huo, P. and Yan, Y., CQDs Precluded Carbon-Incorporated 3D Burger-Like Hybrid ZnO Enhanced Visible-Light-Driven Photocatalytic Activity and Mechanism Implication, Journal of Catalysis, 369 (2019) 450-461.
210. Zhao, F., F., Rong, Y., F., Wan, J., M., Hu, Z., W., Peng, Z., Q. and Wang, B., High Photocatalytic Performance of Carbon Quantum Dots/TNTs Composites for Enhanced Photogenerated Charges Separation Under Visible Light. Catalysis Today, 315 (2018) 162-170.

211. Long, B., Huang, Y., C., Li, H., B., Zhao, F., Y., F., Rui, Z., B., Liu, Z., L., Tong, Y., X., and Ji, H., B., Carbon Dots Sensitized BiOI with Dominant {001} Facets for Superior Photocatalytic Performance, Industrial and Engineering Chemistry Research, 54 (2015) 12788-12794.
212. Di, J., Li, S., X., Zhao, Z., F., Huang, Y., C., Jia, Y, and Zheng, H., J., Biomimetic CNT@TiO₂ Composite with Enhanced Photocatalytic Properties, Chemical Engineering Journal, 281 (2015) 60-68.
213. Miribangul, A., Ma, X., L., Zeng, C., Zou, H., Wu, Y., H., Fan, T., P. and Su, Z., Synthesis of TiO₂/CNT Composites and Its Photocatalytic Activity Toward Sudan (I) Degradation, Photochemistry and Photobiology, 92 (2016) 523-527.
214. Xu, Y.G., Liu, J., Xie, M., Jing, L., Q., Xu, H., She, X., J., Li, H., M. and Xie, J., M., Construction of Novel CNT/LaVO₄ Nanostructures for Efficient Antibiotic Photodegradation, Chemical Engineering Journal, 357 (2019) 487-497.
215. Police, A., K., R., Chennaiahgari, M., Boddula, R., Vattikuti, S., V., P., Mandari, K., K. and Chan, B., Single -Step Hydrothermal Synthesis of Wrinkled Graphene Wrapped TiO₂ Nanotubes for Photocatalytic Hydrogen Production and Supercapacitor Applications, Materials Research Bulletin, 98 (2018) 314-321.
216. Balandin, A., A., Ghosh, S., Bao, W., Calizo, I., Teweldebrhan, D. and Miao, F., et al., Superior Thermal Conductivity of Single -Layer Graphene, Nano Letters, 8, 3 (2008) 902-7.
217. Martin, J., Akerman, N., Ulbricht, G., Lohmann, T., Smet, Jv. and Von Klitzing, K., et al., Observation of Electron-Hole Puddles in Graphene Using a Scanning Single-Electron Transistor, Nature Physics, 4, 2 (2008) 144-8.
218. Lu, Y., Ma, B., Yang, Y., Huang, E., Ge, Z., Zhang, T., Zhang, S., Li, L., Guan, N. Ma, and Y., et al., Hight Activity of Hot Electrons from Bulk 3D Graphene Materials for Efficient Photocatalytic Hydrogen Production, Nano Research, 10 (2017) 1662-1672.
219. Zhang, H., Lv, X., J., Li, Y., M., Wang, Y. and Li, J., H., P25-Graphene Composite as a High Performance Photocatalyst. ACS Nano, 4 (2010) 380-386.
220. Isari, A., A., Payan, A., Fattahi, M., Jorfi, S. and Kakavandi, B., Photocatalytic Degradation of Rhodamine B and Real Textile Wastewater Using Fe-Doped TiO₂ Anchored on Reduced Graphene Oxide (Fe-TiO₂/rGO): Characterization and Feasibility, Mechanism and Pathway Studies, Applied Surface Science, 462 (2018) 549-564.
221. Yang, Q., Dong, L., Su, R., Hu, B., Wang, Z., Jin, Y., Wang, Y., Besenbacher., F. and Dong, M., Nanostructured Heterogeneous Photo-Catalysts for Hydrogen Production and Water Splitting: A Comprehensive Insight, Applied Materials Today, 17 (2019) 159-182.

222. Anucha, C., B., Altin, I., Bacaksiz, E., Degirmencioglu, I., Kucukomeroglu, T., Yilmaz, S. and Stathopoulos, V., N., Immobilized TiO₂/ZnO Sensitized Copper (II) Phthalocyanine Heterostructure for the Degradation of Ibuprofen Under UV Irradiation, Separations, 8 (2021) 24.
223. Anucha, C., B., Altin, I., Biyiklioglu, Z., Bacaksiz, E., Polat, I. and Stathopoulos, V., N., Synthesis, Characterization, and Photocatalytic Evaluation of Manganese (III) Phthalocyanine Sensitized ZnWO₄ (ZnWO₄MnPc) for Bisphenol A Degradation under UV Irradiation, Nanomaterials, 10 (2020) 2139.
224. Zhao, W., Sun, Y. and Castellano, F., N., Visible -Light Induced Water Detoxification Catalyzed by Pt II Dye Sensitized Titania, Journal of American Chemical Society, 130 (2008) 12566-67.
225. Han, L., Islam, A. and Chen, H., et al., High-Efficiency Dye-Sensitized Solar Cell with a Novel Co-Adsorbent, Energy and Environmental Science, 5 (2012) 6057-6060.
226. Ji, J., M., Zhou, H. and Kim, H., K., Rational Design Criteria for D-II-a Structured Organic and Porphyrin Sensitizers for Highly Efficient Dye-Sensitized Solar Cells, Journal of Materials Chemistry A, 6 (2018) 14518-14545.
227. Wu, Q., Cao, J., Wang, J., Liu, Y., Zhao, Y., Wang, H., Liu, Y., Huang, H., Liao, F., Shao, M. and Kang, Z., A Metal-Free Photocatalyst for Highly Efficient Hydrogen Peroxide Photoproduction in Real Seawater, Nature Communications, 12 (2021) 483.
228. Chen, X.-F. and Denis, K., P., Ng., β -Cyclodextrin-Conjugated Phthalocyanine as Water-Soluble and Recyclable Sensitizers for Photocatalytic Applications, Chemical Communications, 57, 29 (2021) 3567-3570.
229. Sakthivel, S., Shankar, M., Palanichamy, M., Arabindoo, B., Bahnemann, D. and Murugesan, V., Enhancement of Photocatalytic Activity by Metal Deposition: Characterisation and Photo Efficiency of Pt, Au, and Pd Deposited on TiO₂ Catalyst, Water Research, 38, 13 (2004) 3001-8.
230. Wang, C., Y., Zhang, X., Song, X., N., Wang, W., K. and Yu, H., Q., Novel Bi₁₂O₁₅C₁₆ Photocatalyst for the Degradation of Bisphenol A Under Visible-Light Irradiation, ACS Applied Materials Interfaces, 8 (2016) 5320-5326.
231. Jiang, W., J., Zhu, Y., F., Zhu, G., X., Zhang, Z., J., Chen, X., J. and Yao, W., Q., Three-Dimensional Photocatalyst with a Network Structure, Journal of Materials Chemistry A, 5 (2017) 5661-5679.
232. Wan, W., C., Zhang, R., Y., Ma, M., Z. and Zhou, Y., Monolithic Aerogel Photocatalysts: A Review, Journal of Materials Chemistry A, 6 (2018) 754-775.
233. Pierre, A., C. and Pajonk, G., M., Chemistry of Aerogels and Their Applications, Chemical Review, 102 (2002) 4243-4265.

234. Heiligtag, F., J., Rossell, M., D., Suess, M., J. and Niederberger, M., Template-Free Co-Assembly of Performed Au and TiO₂ Nanoparticles into Multicomponent 3D Aerogels, Journal of Materials Chemistry, 21 (2011) 16893-16899.
235. Srikanth, B., Goutham, R., Narayan Badri, R., Ramprasath, A., Gopinath, K., P. and Sankaranarayanan, A., R., Recent Advancements in Supporting Materials for Immobilized Photocatalytic Applications in Wastewater Treatment, Journal of Environmental Management, 200 (2017) 60-78.
236. Miranda-Garcia, N., Suarez, S., Maldonado, M., I., Malato, S. and Sanchez, B., Regeneration Approaches for TiO₂ Immobilized Photocatalyst Used in the Elimination of Emerging Contaminants in Water, Catalysis Today, 230 (2014) 27-34.
237. Dong, Y., Tang, D. and Li, C., Photocatalytic Oxidation of Methyl Orange in Water Phase by Immobilized TiO₂-Carbon Nanotube Nanocomposite Photocatalyst, Applied Surface Science, 296 (2014b) 1-7.
238. Ramasundaram, S., Seid, M., G., Choe, J., W., Kim, E.-J., Chung, Y., C., Cho, K., Lee, C. and Hong, S., W., Highly Reusable TiO₂ Nanoparticle Particle Photocatalyst by Direct Immobilization on Steel Mesh via PVDF Coating, Electrospraying, and Thermal Fixation. Chemical Engineering Journal, 306 (2016) 344-351.
239. Vereb, G., Ambrus, Z., Pap, Z., Mogyorosi, K., Dombi, A., and Hernadi, K., Immobilization of Crystallized Photocatalyst on Ceramic Paper by Titanium (IV) Ethoxide and Photocatalytic Decomposition of Phenol, Reaction, Kinetics and Mechanisms, Catalysis, 113 (2014) 293-303.
240. Sabri, N., A., Nawi, M., A. and Nawawi, W., I., Porous Immobilized C Coated N Doped TiO₂ Containing In-situ Generated Polyenes for Enhanced Visible Light Photocatalytic Activity, Optical Materials Amsterdam, 48 (2015) 258-266.
241. Lin, L., Wang, H. and Xu, P., Immobilized TiO₂-Reduced Graphene Oxide Nanocomposites on Optical Fibres as High Performance Photocatalysts for Degradation of Pharmaceuticals, Chemical Engineering Journal, 310, 2 (2016) 389-398.
242. Ray, S. and Lalman, J., A., Fabrication and Characterization of an Immobilized Titanium Dioxide (TiO₂) Nanofibre Photocatalyst, Materials Today: Proceedings, 3 (2016) 1582-1591.
243. Yadini, A., El Saufi, H., Dunlop, P., S., M., Byrne, J., A., Azzouzi, M. and El Hajjaji, S.-El., Supported TiO₂ on Borosilicate Glass Plates for Efficient Photocatalytic Degradation of Fenamiphos, Journal of Catalysis, 6 (2014) 1-8.
244. Akerdi, A., G., Bahrami, S., H., Arami, M. and Pajootan, E., Photocatalytic Discolouration of Acid Red 14 Aqueous Solution Using Titania Nanoparticles Immobilized on Graphene Oxide Fabricated Plate, Chemosphere, 159 (2016) 293-299.

245. Ghoreishian, S., M., Badii, K., Norouzi, M. and Malek, K., Effect of Gold Plasma Pre-treatment on Photocatalytic Activity of 3D Fabric Loaded with Nano Photocatalysts: Response Surface Methodology, Applied Surface Science, 365 (2016) 252-262.
246. Razak, S., Nawi, M., A. and Haitham, K., Fabrication, Characterization and Application of Reusable Immobilized-PANI Photocatalyst Plate for The Removal of Reactive Red 4 Dye, Applied Surface Science, 319 (2014) 90-98.
247. Nadarajan, R., Wan Abu Bakar, W., A., Ali, R. and Ismail, R., Photocatalytic Degradation of 1,2-Dichlorobenzene Using Immobilized TiO₂ TiO₂/SnO₂/WO₃ Photocatalyst Under Visible Light: Application of Response Surface Methodology, Arabian Journal of Chemistry, 11 (2018) 34-47.
248. Zeng, J., Liu, S., Cai, J. and Zhang, L., TiO₂ Immobilized in Cellulose Matrix for Photocatalytic Degradation of Phenol Under Weak UV Light Irradiation, Journal of Physical Chemistry C, 114 (2010) 7806-7811.
249. Shaykhi, Z., M. and Zinatizadeh, A., A., L., Statistical Modelling of Photocatalytic Degradation of Synthetic Amoxicillin Wastewater (SAW) in an Immobilized TiO₂ Photocatalytic Reactor Using Response Surface Methodology (RSM), Journal of The Taiwan Institute of Chemical Engineers, 45 (2014) 1717-1726.
250. Teixeira, S., Martins, P., M., Lanceros-Mendez, S., Kuhn, K. and Cuniberti, G., Reusability of Photocatalytic TiO₂ and ZnO Nanoparticles Immobilized in Poly (vinylidene difluoride)-Co-Trifluoro Ethylene, Applied Surface Science, 384 (2016) 497-504.
251. Rhouta, B., Bouna, L., Maury, F., Senocq, F., Lafont, M.-C., Jada, A., Amjoud, M. and Daoudi, L., Surfactant-Modifications of Na⁺-Beidellite for The Preparation of TiO₂-Bd Supported Photocatalysts: II Physico-Chemical Characterization and Photocatalytic Properties, Applied Clay Science, 115 (2015) 266-274.
252. Ohji, T. and Fukushima, M., Macro-porous ceramics: Processing and Properties. International Materials Reviews, 57, 2 (2012) 115-131.
253. Elma, M., Yacou, C., Wang, D., Smart, S. and Diniz da Costa, J., Micro-porous Silica Based Membranes for Desalination, Water, 4, 3 (2012) 629-649.
254. Xu, J., Chang, C. and Gao, C., Performance of a Ceramic Ultra-filtration Membrane System in Pre-treatment to Seawater Desalination, Separation and Purification Technology, 75, 2 (2010) 165-173.
255. Ylker, E., Separation of Whey Components by Using Ceramic Composite Membranes, Desalination, 189, 1-3 (2006) 87-91.
256. Mirales-Cuevas, S., Oller, I., Aguera, A., Sanchez Perez, J., A., Sanchez-Moreno, R. and Malato, S., Is the Combination of Nanofiltration Membranes and AOPs for

- Removing Microcontaminants Cost Effective in Real Municipal Wastewater Effluents? *Environmental Science: Water Research Technology*, 2 (2016) 511-520.
257. Lu, Q., Dong, X., Zhu, Z. and Dong, Y., Environment Oriented Low Cost Porous Mullite Ceramic Membrane Supports Fabricated from Coal Gangue and Bauxite, *Journal of Hazardous Materials*, 273 (2014) 136-145.
258. Tsuru, T., Nano/Sub-Nano Tuning of Porous Ceramic Membranes for Molecular Separation, *Journal of Sol-Gel Science Technology*, 46 (2008) 349-361.
259. Segal, D., Chemical Synthesis of Ceramic Materials, *Journal of Material Chemistry*, 7 (1997) 1297-1305.
260. Li, K., Ceramic Membranes for Separation and Reaction, First Edition, John Wiley and Sons Inc., New Jersey, 2007.
261. Amin, Sh., K., Abdallah, H., A., M., Roushdy, M., H. and El-Sherbiny, S., A., An Overview of Production and Development of Ceramic Membranes, *International Journal of Applied Engineering Research*, 11, 12 (2016) 7708-7721.
262. Sonawane, R., Hegde, S. and Dongare, M., Preparation of Titanium (IV) Oxide Thin film Photocatalyst by Sol-Gel Dip Coating, *Material Chemistry and Physics*, 77 (2003) 744-750.
263. Vaiano, V., Sacco, O., Sannino, D. and Ciambelli, P., Nanostructured N-Doped TiO₂ Coated on Glass Spheres for the Photocatalytic Removal of Organic Dyes Under UV or Visible Light Irradiation, *Applied Catalysis B: Environmental*, 170 (2015) 153-161.
264. Cao, S., Liu, B., Fan, L., Yue, Z., Liu, B. and Cao, B., Highly Antibacterial Activity of N-Doped TiO₂ Thin films Coated on Stainless Steel Brackets Under Visible Light Irradiation, *Applied Surface Science*, 309 (2014) 119-127.
265. Zuo, J., Deposition of Ag Nanostructures on TiO₂ Thin films by RF Magnetron Sputtering, *Applied Surface Science*, 256 (2010) 7096-7101.
266. Scheirs, J., Compositional and Failure Analysis of Polymers: A Practical Approach, First Edition, John Wiley and Sons Ltd., Chichester, 2000.
267. Exposito, A., J., Patterson, D., A., Mansor, W.S, W., Monteagudo, J., M., Emanuelson, E., Sanmartin, I. and Duran, A., Antipyrene Removal by TiO₂ Photocatalyst Based on Spinning Disc Reactor Technology, *Journal of Environmental Management*, 187 (2017) 504-512.
268. Molina, R., Segura, Y., Martinez, F. and Melero, J., A., Immobilization of Active and Stable Goethite Coated-Films by a Dip -Coating Process and Its Application for Photo-Fenton Systems, *Chemical Engineering Journal*, 203 (2012) 212-222.
269. www.huntsman.com/products, Huntsman, October 26, 2021.

270. Furlani, E., Aneggi, E., de Leitenburg, C. and Maschio, S., High Energy Ball Milling of Titania and Titania-Ceria Mixtures, Powder Technology, 254 (2014) 591-596.
271. Kuentz, M., and Rothlisberger, D., Sedimentation Analysis of Aqueous Microsuspensions Based on Near Infrared Transmission Measurements During Centrifugation Determination of a Suitable Amount of Gelling Agent to Minimize Settling in the Gravitational Field, Sciences Techniques et Pratiques Pharmaceutiques Sciences, 12, 6 (2002) 391-396.
272. Aviles-Garcia, O., Espino-Valencia, J., Romero-Romero, R., Rico-Cerda, J., L, Arroyo-Albiter, M., Solis-Casados, D., A. and Natividad-Rangel, R., Enhanced Photocatalytic Activity of Titania by Co-Doping with Mo and W, Catalysts, 8 (2013) 631.
273. Zener, B., Matoh, L., Carraro, G., Miljevc, B. and Korsec, R., C., Sulfur-Nitrogen- and Platinum-Doped Titania Thin Films with High Catalytic Efficiency Under Visible-Light Illumination, Beilstein Journal of Nanotechnology, 9 (2018) 1629-1640.
274. Elhalil, A., Elmoubarki, R., Machrouhi, A., Sadiq, M., Abdenouni, S., Qourzal, S. and Barka, N., Photocatalytic Degradation of Caffeine by ZnO-ZnAl₂O₄ Nanoparticles Derived from LDH Structure, Journal of Environmental Chemical Engineering, 5 (2017) 3719-3726.
275. Husain, S., T., Siddiqa, A., Siddiq, M. and Ali, S., Iron -Doped Titanium Dioxide Nanotubes: A Study of Electrical, Optical and Magnetic Properties, Journal of Nanoparticle Research, 13 (2013) 6517-6525.
276. Li, B., Zhao, Z., Gao, F., Wang, X. and Qiu, J., Mesoporous Microspheres Composed of Carbon-Coated TiO₂ Nanocrystals with Exposed {001} Facets for Improved Visible Light Photocatalytic Activity, Applied Catalysis B: Environmental, 147 (2014) 958-964.
277. Li, S. and Jena, P., Origin of The Anatase to Rutile Conversion of Metal-Doped TiO₂, Physical Review B, 79 (2009) 201204.
278. Inturi, S., N., R., Boningari, T., Suidan, M. and Smirniotis, P., G., Visible-Light-Induced Photodegradation of Gas Phase Acetonitrile Using Aerosol-Made Transition Metal (V, Cr, Fe, Mn, Mo, Ni, Cu, Y, Ce, and Zr) Doped TiO₂, Applied Catalysis B: Environmental, 144 (2014) 333-342.
279. Luo, S-Y., Yan, B-X. and Shen, J., Enhancement of Photoelectric and Photocatalytic Activities: Mo Doped TiO₂ Thin Films Deposited By Sputtering, Thin Solid Films, 522 (2012) 361-365.
280. Chaudhari, S., M., Gawal, P., M., Sane, P., K., Sontakke, S., M. and Nemade, P., R., Solar Light-Assisted Photocatalytic Degradation of Methylene Blue with Mo/TiO₂:

- A Comparison with Cr- and Ni-Doped TiO₂, Research on Chemical Intermediates, 44 (2018) 3115-3134.
281. Gong, J., Yang, C., Pu, W. and Zhang, J. Liquid Phase Deposition of Tungsten Doped TiO₂ Films for Visible Light Photoelectrocatalytic Degradation of Dodecylbenzenesulfonate, Chemical Engineering Journal, 167 (2011) 190-197.
282. Belver, C., Han, C., Rodriguez, J., J. and Dionysiou, D., D., Innovative W-Doped Titanium Dioxide Anchored on Clay for Photocatalytic Removal of Atrazine, Catalysis Today, 280 (2017) 21-28
283. Prabhu, N., Agilan, S., Muthukumarasamy, N. and Senthikumar, C., K., Effect of Temperature on The Structural and Optical Properties of WO₃ Nanoparticles Prepared by Solvol Thermal Method Method, Digest Journal of Nanomaterials and Biostructures, 8, 4 (2013) 1483-1490.
284. Tavallaei, H., Jafarpour, M., Feizpour, F., Rezaeifard, A. and Farrokhi, A., A Cooperative Effect in a Novel Bimetallic Mo-V Nanocomplex Catalyzed Selective Aerobic C-H Oxidation, ACS Omega, 4 (2019) 3601-3610.
285. Liu, G., Liu, S., Lu, Q., Sun, H. and Xiu, Z., BiVO₄/Cobalt Pthalocyanine (CoPc) Nanofiber Heterostructures: Synthesis, Characterization and Application in Photodegradation of Methylene Blue, RSC Advances, 4 (2014) 53402-53406.
286. Xie, Z., Shuang, S., Ma, L., Zhu, F., Liu, X. and Zhang, Z., Annealing Effect on Photoelectrochemical and Photocatalytic Performance of TiO₂ Nanorods, RSC Advances, 7 (2017) 51382.
287. Kumar, S., Mote, V., D., Prakash, R. and Kumar, D., X-ray Analysis of α -Al₂O₃ Particles by Williamson-Hall Methods, Materials Focus, 5, 6 (2016) 545.
288. Stefa, S., Lykaki, M., Fragkoulis, D., Binas, V., Pandis, P., K., Stathopoulos, V., N. and Konsolakis, M., Effect of the Preparation Method on the Physicochemical Properties of the CO Oxidation Performance of Nanostructured CeO₂/TiO₂, Processes, 8 (2020) 847.
289. Lykaki, M., Stefa, S., Carabiniero, S., A., C., Pandis, K., Stathopoulos, V., N. and Konsolakis, M., Facet-Dependent Reactivity of Fe₂O₃/CeO₂ Nanocomposites: Effects of Ceria Morphology on CO Oxidation, Catalyst, 9 (2019) 371.
290. Meng, L., Zhang, X., Tang, Y., Su, K. and Kong, J., Hierarchically Porous-Silicon-Carbon-Nitrogen Hybrid Materials Towards Highly Efficient and Selective Adsorption of Organic Dyes, Scientific Report, 5 (2015) 7910.
291. Miao, Y., Zhai, Z., Jiang, L., Shi, Y., Yang, Z., Duan, D., Zhen, K. and Wang, J., Facile and New Synthesis of Cobalt Doped Mesoporous TiO₂ with High Visible-Light Performance, Powder Technology, 266 (2014) 365-371.

292. Thommes, M., Kaneko, K., Neimark, A., V., Olivier, J., P., Rodriguez-Reinoso, F., Rouquerol, J. and Sing, K., S., W., Physisorption of Gases with Special Reference to The Evaluation of Surface Area and Pore Size Distribution (IUPAC Technical Report), Pure and Applied Chemistry, 87, 9-10 (2015) 1051-1069.
293. Kubelka, P. and Munk, F., Ein Beitrag zur Optik der Farbanstriche, Zeitschrift fur Physik, 12 (1931) 593-601.
294. Murali, A., Sarswat, P., K. and Free, M., L., Minimizing Electron -Hole Recombination Through Band-gap Engineering in Novel ZnO-CeO₂-rGO Ternary Nanocomposite for Photoelectrochemical and Photocatalytic Applications. Environmental Science Pollution Research, 27 (2020) 25042-25056.
295. Schuchmann, M., N., Bothe, E., von Sonntag, J. and von Sonntag, C., Reaction of OH Radical with Benzoquinone in Aqueous Solutions. A Pulse Radiolysis Study, Journal of The Chemical Society, Perkins Transaction, 2 (1998) 791-796.
296. Veltwisch, D. and Asmus, K.-D., On the Reaction of Methyl and Phenyl Radicals with p-Benzoquinone in Aqueous Solution, Journal of The Chemical Society, Perkins Transaction, 2 (1998) 1147-1152.
297. Zhao, C., Pelaez, M., Dionysiou, D., D., Pillai, S., C., Byrne, J., A. and O'Shea, K., E., UV and Visible Light Activated Photocatalysis of 6-Hydroxymethyl Uracil, a Model Compound for the Potent Cyanotoxin Cylindrospermopsin, Catalysis Today, 224 (2014) 70-76
298. Kudlek, E., Dudziak, M. and Bohdziewicz, J., Influence of Inorganic Ions and Organic Substances on the Degradation of Pharmaceutical Compound in Water Matrix, Water, 8 (532) 532.
299. Chiona, J., Kosslick, H., Fischer, C., Flechsig, G., U., Frunza, L. and Schulz, A., Photocatalytic Decomposition of Pharmaceutical Ibuprofen Pollutions in Water Over Titania Catalyst, Applied Catalysis B: Environmental, 129 (2013) 589-534.
300. Iovino, P., Chianese, S., Canzano, S., Prisciandaro, M. and Musmara, D., Degradation of Ibuprofen in Aqueous Solution with UV Light: The Effect of Reactor Volume and pH, Water Air Soil Pollution, 227 (2016) 194.
301. Iovino, P., Chianese, S., Canzano, S., Prisciandaro, M. and Musmara, D., Degradation of Ibuprofen in Aqueous Solutions, Water Air Soil Pollution, 23 (2016) 22993-23004.

CURRICULUM VITAE

Chukwuka Bethel ANUCHA graduated from Abia State Senior Science School Ihie, in 1996. He received his B.Sc. from the University of Port Harcourt, Rivers State 2004 at second class honours. After graduation, he taught in a high school in 2005/2006 in the northern part of Nigeria for his National Youth Service. Upon completion of his youth service, he continued teaching and spent some years in the chemical industry for a period spanning 2007 to 2013. He left high school teaching/industry work in 2014 to pursue master's degree under Erasmus Mundus scholarship. After completing his master's degree in Chemistry co-jointly awarded by the University of Barcelona, Spain and the University of Algarve, Faro, Portugal at Excellent grade in 2016, he went back to work in a chemical company in Italy for a year in 2017.

In 2018, he was recruited as an early-stage researcher (ESR) under Marie Skłodowska-Curie Action (MSCA) Innovative Training Networks (ITN) awarded by the European Union (EU) commission and implemented within the Framework Programme for Research and Innovation Horizon 2020 Scheme for the AQUAlity project- 765860 to which Karadeniz Technical University KTU, Trabzon, Turkey was an institution member of the AQUAlity project consortia. While working as an ESR, he pursued and obtained his Ph.D. in Chemistry at Department of Chemistry, KTU in 2022.